



## Site U1558<sup>1</sup>

### Contents

- 1 Background and objectives
- 4 Operations
- 9 Stratigraphic unit summary
- 12 Sedimentology
- 25 Igneous petrology
- 42 Alteration petrology
- 64 Biostratigraphy
- 74 Paleomagnetism
- 86 Age model and mass accumulation rates
- 91 Physical properties and downhole measurements
- 113 Geochemistry
- 127 Microbiology
- 132 References

### Keywords

International Ocean Discovery Program, IODP, *JOIDES Resolution*, Expedition 390, Expedition 393, Expedition 390C, South Atlantic Transect, Biosphere Frontiers, Earth Connections, Mid-Atlantic Ridge, Site U1558

### Core descriptions

### Supplementary material

### References (RIS)

### MS 390393-106

Published 23 January 2024

Funded by NSF OCE1326927

D.A.H. Teagle, J. Reece, T.J. Williams, R.M. Coggon, J.B. Sylvan, E.R. Estes, G.L. Christeson, E. Albers, C. Amadori, T.M. Belgrano, T. D'Angelo, N. Doi, A. Evans, G.M. Guérin, M. Harris, V.M. Hojnacki, G. Hong, X. Jin, M. Jonnalagadda, D. Kuwano, J.M. Labonte, A.R. Lam, M. Latas, W. Lu, P. Moal-Darrigade, S.F. Pekar, C. Robustelli Test, J.G. Ryan, D. Santiago Ramos, A. Shchepetkina, A. Villa, S.Y. Wee, S.J. Widlansky, M. Aizawa, C. Borrelli, J.D. Bridges, E.J. Carter, J. Dinarès-Turell, J.D. Estep, W.P. Gilhooly III, L.J.C. Grant, M.R. Kaplan, P.D. Kempton, C.M. Lowery, A. McIntyre, C.M. Routledge, A.L. Slagle, M. Takada, L. Tamborrino, Y. Wang, K. Yang, W. Kurz, M. Prakasam, L. Tian, T. Yu, and G. Zhang<sup>2</sup>

<sup>1</sup>Teagle, D.A.H., Reece, J., Williams, T.J., Coggon, R.M., Sylvan, J.B., Estes, E.R., Christeson, G.L., Albers, E., Amadori, C., Belgrano, T.M., D'Angelo, T., Doi, N., Evans, A., Guérin, G.M., Harris, M., Hojnacki, V.M., Hong, G., Jin, X., Jonnalagadda, M., Kuwano, D., Labonte, J.M., Lam, A.R., Latas, M., Lu, W., Moal-Darrigade, P., Pekar, S.F., Robustelli Test, C., Ryan, J.G., Santiago Ramos, D., Shchepetkina, A., Villa, A., Wee, S.Y., Widlansky, S.J., Aizawa, M., Borrelli, C., Bridges, J.D., Carter, E.J., Dinarès-Turell, J., Estep, J.D., Gilhooly, W.P., III, Grant, L.J.C., Kaplan, M.R., Kempton, P.D., Lowery, C.M., McIntyre, A., Routledge, C.M., Slagle, A.L., Takada, M., Tamborrino, L., Wang, Y., Yang, K., Kurz, W., Prakasam, M., Tian, L., Yu, T., and Zhang, G., 2024. Site U1558. In Coggon, R.M., Teagle, D.A.H., Sylvan, J.B., Reece, J., Estes, E.R., Williams, T.J., Christeson, G.L., and the Expedition 390/393 Scientists, South Atlantic Transect. *Proceedings of the International Ocean Discovery Program, 390/393*: College Station, TX (International Ocean Discovery Program). <https://doi.org/10.14379/iodp.proc.390393.106.2024>

<sup>2</sup>**Expedition 390/393 Scientists' affiliations.**

## 1. Background and objectives

Site U1558 (30°53.7814'S, 24°50.4822'W; proposed Site SATL-43A) is in the central South Atlantic Ocean at a water depth of ~4334 meters below sea level (mbsl) ~1067 km west of the Mid-Atlantic Ridge (see Figure **F1** and Tables **T1**, **T2**, all in the Expedition 390/393 summary chapter [Coggon et al., 2024c]) on crust that formed at a slow half spreading rate of ~19.5 mm/y (Kardell et al., 2019; Christeson et al., 2020) (see Figure **F7** in the Expedition 390/393 summary chapter [Coggon et al., 2024c]). With an estimated age of 49.2 Ma, Site U1558 is the second oldest location of the South Atlantic Transect (SAT) campaign (International Ocean Discovery Program [IODP] Expeditions 390C, 395E, 390, and 393).

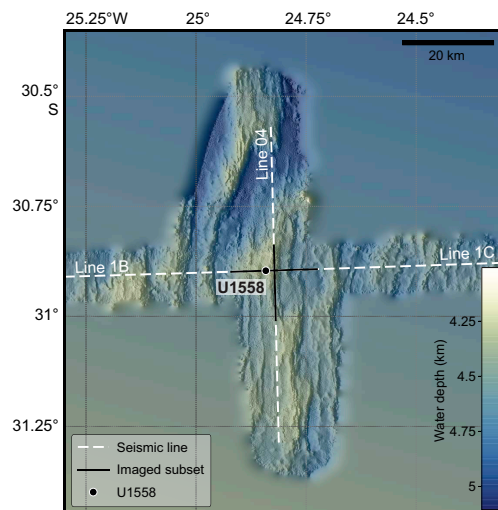
### 1.1. Geologic setting

Site U1558 is located on the main approximately east–west (085) Crustal Reflectivity Experiment Southern Transect (CREST) crossing Line 1B/1C at Common Depth Point 3252 about 1.9 km west of the north–south–trending (355) CREST Seismic Line 04 (Figures **F1**, **F2**) (Reece et al., 2016; Reece and Estep, 2019). Interpretation of multichannel seismic and ocean-bottom seismograph data in this region suggests that the ocean crust at the site is slightly thinner (~5.5 km; Christeson et al., 2020) than normal ocean crust ( $6.15 \pm 0.93$  km; Christeson et al., 2019). At a water depth of 4334 m, Site U1558 is significantly shallower (~450 m) than predicted by simple lithospheric cooling models (see Figure **F4** in the Expedition 390/393 summary chapter [Coggon et al., 2024c]) (e.g., Parsons and Sclater, 1977; Korenaga and Korenaga, 2008; Marty and Cazenave, 1989). This difference presumably reflects the location of this site on a relatively elevated feature on the rugged faulted terrain of the western flank of the southern Mid-Atlantic Ridge.

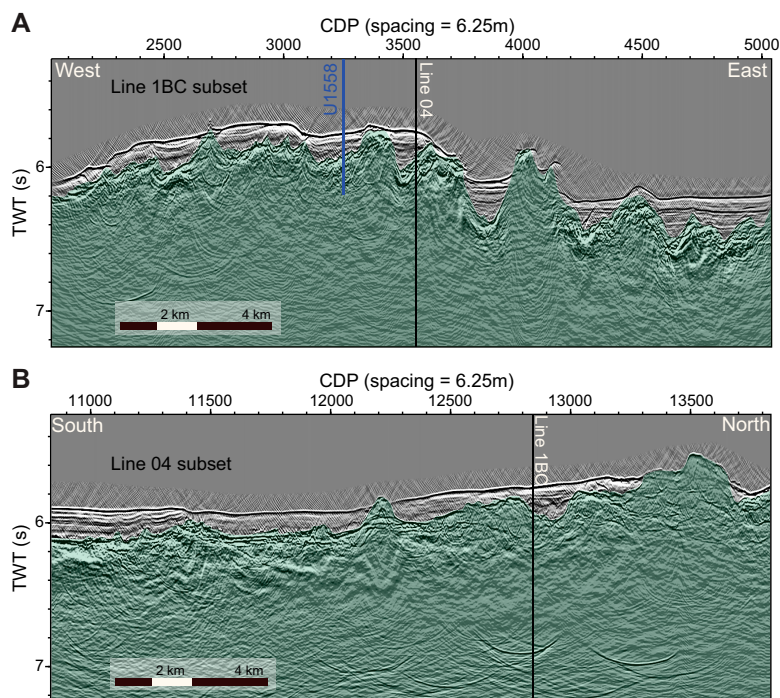
Site U1558 sits in a ~1 km wide sediment-filled subbasin on top of an irregular, near north–south–trending (355), ~20 km wide, 500 m high basement ridge elevated above the regional seafloor (Figures **F1**, **F2**, **F3**). This basement ridge is one of many subparallel and 30–40 km long ridges, although it is significantly higher than the neighboring 100–200 m high basement ridges. On the east–west seismic profile CREST Line 1B/1C, a number of these 1 km wide subbasins are imaged across the basement ridge, each filled with ~150 to ~270 m of sediment (Figure **F2A**) to a range of bathymetric levels between 4300 and 4700 mbsl (Figure **F1**). The subbasins are separated by base-

ment highs, most of which are draped by sediments, resulting in almost continuous sediment cover across the ridge. However, some basement high points remain emergent or covered by only thin sedimentary cover. The basement ridge Site U1558 is located on deepens to the north into a ~5000 m deep basin (Figure F1).

Seismic observations suggest that the ocean crust at Site U1558 has a sediment cover of 167 m (Reece et al., 2016; Reece and Estep, 2019), which is close to the global average overburden thickness for basement of this age (~150 m; Spinelli et al., 2004) and the reported mean sediment thickness encountered along CREST Seismic Line 1B for crustal ages between 48 and 63 Ma (132 m;



**Figure F1.** Bathymetric map of 49 Ma SAT study area showing location of Site U1558 and CREST multichannel seismic (MCS) Reflection Lines 1B/1C and 04 (Christeson and Reece, 2020). Seismic reflection profiles were acquired during CREST cruise (Reece et al., 2016). Solid black lines = location of wide-angle MCS profiles for which seismic images are shown in Figure F2.



**Figure F2.** CREST multichannel seismic (MCS) reflection profiles on ~49 Ma crust showing local basement topography, Site U1558 (blue line). A. West–east Line 1B/1C that crosses Line 04 approximately 1.9 km east of Site U1558. B. North–south Line 04. Black lines = intersections of MCS reflection profiles. CDP = common depth point, TWT = two-way traveltime.



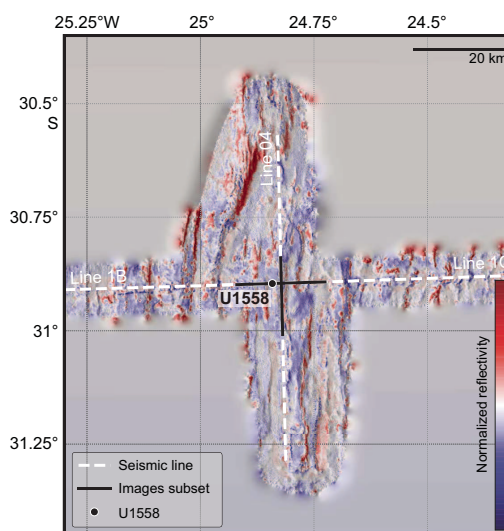
Estep et al., 2019). However, a recent sedimentation thickness global synthesis suggests that ~50 Ma ocean crust should host between 200 and 360 m of sediment (cf. Olson et al., 2016; Straume et al., 2019, and references therein).

Backscatter reflections from multibeam profiles (Figure F3) reveal that a significant proportion of the seafloor near Site U1558 returns strong reflections and is either unsedimented or hosts only thin, discontinuous sediment cover. This may allow ventilation of the volcanic rocks of the upper ocean crust through the ingress of seawater and egress of seawater-derived low-temperature hydrothermal fluids, with consequent impacts on heat flow, sediment pore waters, basement hydrothermal alteration, and microbial communities in both the marine sediments and underlying basalts.

Site U1558 was first occupied during engineering Expedition 390C, during which Hole U1558A was cored using the advanced piston corer (APC) and extended core barrel (XCB) systems to a total depth of 163.9 meters below seafloor (mbsf), penetrating the entire sediment succession and ~4.5 m into basement (Figure F5; Table T1) (see Table T2 and Figure F15, both in the Expedition 390/393 summary chapter [Coggon et al., 2024c]) (Estes et al., 2021). After operations in Hole U1558A were complete, a reentry system and casing was supposed to be installed into basement in the next hole. However, the drill string could not be disconnected from the reentry system using the Dril-Quip running tool because the hard rock inhibited the complete transfer of weight off of the tool. After two failed attempts in Holes U1558B and U1558C, a reentry system with 13 $\frac{3}{8}$  inch casing was finally installed to 146.1 mbsf in Hole U1558D about 10 m above the estimated basement depth (instead of into basement) and 21 m above the actual sediment/basement interface in this hole (~167 mbsf) (Figure F4). The basement/sediment interface is irregular at the site and varies more than 15 m between Holes U1558A (~159 mbsf), U1558D (~167 mbsf), and U1558F (~176 mbsf) (see Table T2 in the Expedition 390/393 summary chapter [Coggon et al., 2024c]). The age of Site U1558 was predicted to be ~49.2 Ma based on CREST site survey magnetic data (Kardell et al., 2019). However, preliminary biostratigraphy analysis of cores sampled during Expedition 390C suggest that the lowermost sediments in Hole U1558A are middle to late Eocene (~42 Ma), suggesting a long period of little or no sedimentation.

## 1.2. Objectives

The operational objectives at Site U1558 during Expedition 393 were to (1) core the entire sediment section and a few meters into basement with the APC/XCB system in Hole U1558F to collect



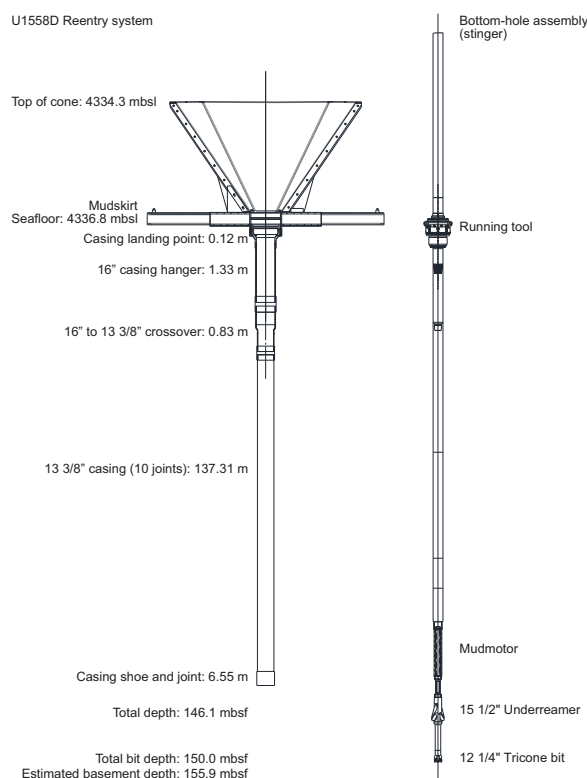
**Figure F3.** Backscatter reflections from Site U1558 region collected during CREST site survey cruise (Reece et al., 2016; Reece and Estep, 2019; Christeson et al., 2020). Red = higher normalized reflectivity values, blue = lower normalized reflectivity values. Solid black lines = locations of wide-angle multichannel seismic profiles for which seismic images are shown in Figure F2.

material that addresses the paleoceanographic, paleoclimate, and microbiological objectives of the SAT expeditions; (2) core 250 m into basement with the rotary core barrel (RCB) system in Hole U1558D to collect material that addresses the petrologic, geochemical, and microbiological objectives of the SAT expeditions; and (3) collect wireline geophysical logging data through the basement sections.

## 2. Operations

Site U1558 was previously occupied in November 2020 during Expedition 390C with objectives to confirm the depth to basement by coring, conduct gas safety measurements, and set a reentry system consisting of a reentry cone and 13% inch casing (Estes et al., 2021). Hole U1558A was cored with the APC and XCB systems to 163.9 mbsf, finding the sediment/basement contact at 158.9 mbsf. Holes U1558B and U1558C marked unsuccessful attempts to drill in and release the reentry system using the Dril-Quip running tool. While lowering the reentry system for Hole U1558D (Figure F4), the reentry cone and mud skirt became detached from the casing and fell to the seafloor the right way up and within a few meters of the intended location. The drill bit and casing assembly were lowered through the cone and drilled into Hole U1558D, setting the casing shoe at 146.1 mbsf and the base of the hole at 150.0 mbsf.

During Expedition 393, three holes were cored at Site U1558 (Table T1; Figure F5). Hole U1558E consisted of one APC core that missed the mudline. Hole U1558F was cored with the APC/XCB system to 177.2 mbsf, with the sediment/basement contact at 176.0 mbsf. In Hole U1558D, the sediment/basement contact was found at 166.8 mbsf and the volcanic sequence was cored with the RCB system to 370.2 mbsf (203.4 meters subbasement [msb]). Unfortunately, while withdrawing the bit out of Hole U1558D to prepare for wireline logging, the reentry cone and some casing were pulled out the seafloor by the bottom-hole assembly (BHA), ending operations in that hole. The cased SAT holes were intended to be legacy holes for potential future deepening or other operations, but this is no longer possible at this site. This also precluded wireline logging of the volcanic sequences.



**Figure F4.** Reentry system, Hole U1558D (Estes et al., 2021).

**Table T1.** Core summary, Site U1558. DRF = drilling depth below rig floor, DSF = drilling depth below seafloor, CSF = core depth below seafloor, CSF-A = core depth below seafloor, Method A. Core type: H = advanced piston corer (APC), F = half-length APC (HLAPC), R = rotary core barrel (RCB), X = extended core barrel (XCB), numeric core type = drilled interval. ROP = rate of penetration. (Continued on next two pages.) [Download table in CSV format.](#)

Hole U1558A	Hole U1558B	Hole U1558C
Expedition: 390C	Expedition: 390C	Expedition: 390C
Latitude: 30°53.7728'S	Latitude: 30°53.7707'S	Latitude: 30°53.7761'S
Longitude: 24°50.4970'W	Longitude: 24°50.4843'W	Longitude: 24°50.4942'W
Water depth (m): 4336.87	Water depth (m): 4336.81	Water depth (m): 4336.86
Date started (UTC): 12 Nov 2020; 1630 h	Date started (UTC): 15 Nov 2020; 0610 h	Date started (UTC): 18 Nov 2020; 1900 h
Date finished (UTC): 15 Nov 2020; 0610 h	Date finished (UTC): 18 Nov 2020; 1900 h	Date finished (UTC): 21 Nov 2020; 0956 h
Time on hole (days): 2.57	Time on hole (days): 3.53	Time on hole (days): 2.62
Seafloor depth DRF (m): 4348.1	Seafloor depth DRF (m): 4348.1	Seafloor depth DRF (m): 4348.1
Seafloor depth est. method: APC Calculated	Seafloor depth est. method: TAGGED	Seafloor depth est. method: TAGGED
Rig floor to sea level (m): 11.23	Rig floor to sea level (m): 11.29	Rig floor to sea level (m): 11.24
Penetration DSF (m): 163.9	Penetration DSF (m): 161.1	Penetration DSF (m): 162.7
Cored interval (m): 163.9	Cored interval (m): 0	Cored interval (m): 0
Recovered length (m): 138.69	Recovered length (m): 0	Recovered length (m): 0
Recovery (%): 84.62	Recovery (%): 0	Recovery (%): 0
Drilled interval (m): 0	Drilled interval (m): 161.1	Drilled interval (m): 162.7
Drilled interval (N): 0	Drilled interval (N): 1	Drilled interval (N): 1
Total cores (N): 19	Total cores (N): 0	Total cores (N): 0
APC cores (N): 11		
XCB cores (N): 8		
<b>Hole U1558D</b>	<b>Hole U1558D</b>	<b>Hole U1558E</b>
Expedition: 390C	Expedition: 393	Expedition: 393
Latitude: 30°53.7814'S	Latitude: 30°53.7814'S	Latitude: 30°53.7922'S
Longitude: 24°50.4822'W	Longitude: 24°50.4822'W	Longitude: 24°50.4822'W
Water depth (m): 4334.44	Water depth (m): 4334.42	Water depth (m): 4336.84
Date started (UTC): 21 Nov 2020; 0956 h	Date started (UTC): 28 Jun 2022; 0035 h	Date started (UTC): 25 Jun 2022; 1130 h
Date finished (UTC): 23 Nov 2020; 2256 h	Date finished (UTC): 05 Jul 2022; 0524 h	Date finished (UTC): 26 Jun 2022; 0515 h
Time on hole (days): 2.54	Time on hole (days): 7.2	Time on hole (days): 0.74
Seafloor depth DRF (m): 4345.7	Seafloor depth DRF (m): 4345.7	Seafloor depth DRF (m): 4348.1
Seafloor depth est. method: TAGGED	Seafloor depth est. method: Tag	Seafloor depth est. method: Offset
Rig floor to sea level (m): 11.26	Rig floor to sea level (m): 11.28	Rig floor to sea level (m): 11.26
Penetration DSF (m): 150	Penetration DSF (m): 370.2	Penetration DSF (m): 9.5
Cored interval (m): 0	Cored interval (m): 220.2	Cored interval (m): 9.5
Recovered length (m): 0	Recovered length (m): 100.8	Recovered length (m): 9.97
Recovery (%): 0	Recovery (%): 45.78	Recovery (%): 104.95
Drilled interval (m): 150	Drilled interval (m): 0	Drilled interval (m): 0
Drilled interval (N): 1	Drilled interval (N): 0	Drilled interval (N): 0
Total cores (N): 0	Total cores (N): 38	Total cores (N): 1
	RCB cores (N): 38	APC cores (N): 1
<b>Hole U1558F</b>		
Expedition: 393		
Latitude: 30°53.7923'S		
Longitude: 24°50.4757'W		
Water depth (m): 4337.27		
Date started (UTC): 26 Jun 2022; 0515 h		
Date finished (UTC): 28 Jun 2022; 0035 h		
Time on hole (days): 1.81		
Seafloor depth DRF (m): 4348.5		
Seafloor depth est. method: Mudline		
Rig floor to sea level (m): 11.23		
Penetration DSF (m): 177.2		
Cored interval (m): 174.2		
Recovered length (m): 164.33		
Recovery (%): 94.33		
Drilled interval (m): 3		
Drilled interval (N): 1		
Total cores (N): 23		
APC cores (N): 9		
HLAPC cores (N): 9		
XCB cores (N): 5		

Core	Core on deck date	Core on deck time UTC (h)	Top depth drilled DSF (m)	Bottom depth drilled DSF (m)	Advanced (m)	Top depth cored CSF (m)	Bottom depth recovered CSF-A (m)	Recovered length (m)	Curated length (m)	Recovery (%)	Sections (N)	Real ROP (m/h)
390C-U1558A-												
1H	13 Nov 2020	0630	0.0	3.4	3.4	0.0	3.47	3.47	3.47	102	4	0.0
2H	13 Nov 2020	0750	3.4	12.9	9.5	3.4	7.48	4.08	4.08	43	4	114.0
3H	13 Nov 2020	0855	12.9	22.4	9.5	12.9	22.27	9.37	9.37	99	8	114.0
4H	13 Nov 2020	1010	22.4	31.9	9.5	22.4	32.39	9.99	9.99	105	8	114.0
5H	13 Nov 2020	1125	31.9	41.4	9.5	31.9	39.88	7.98	7.98	84	7	114.0



**Table T1 (continued).** (Continued on next page.)

Core	Core on deck date	Core on deck time UTC (h)	Top depth drilled DSF (m)	Bottom depth drilled DSF (m)	Advanced (m)	Top depth cored CSF (m)	Bottom depth recovered CSF-A (m)	Recovered length (m)	Curated length (m)	Recovery (%)	Sections (N)	Real ROP (m/h)
6H	13 Nov 2020	1235	41.4	50.9	9.5	41.4	51.06	9.66	9.66	102	8	114.0
7H	13 Nov 2020	1405	50.9	60.4	9.5	50.9	60.09	9.19	9.19	97	8	114.0
8H	13 Nov 2020	1515	60.4	69.9	9.5	60.4	69.59	9.19	9.19	97	8	114.0
9H	13 Nov 2020	1625	69.9	75.9	6.0	69.9	75.93	6.03	6.03	101	5	72.0
10H	13 Nov 2020	1930	75.9	85.4	9.5	75.9	85.71	9.81	9.81	103	8	5.4
11H	13 Nov 2020	2330	85.4	94.9	9.5	85.4	94.50	9.10	9.10	96	7	3.8
12X	14 Nov 2020	0220	94.9	103.9	9.0	94.9	100.10	5.20	5.20	58	5	15.4
13X	14 Nov 2020	0400	103.9	113.5	9.6	103.9	111.61	7.71	7.71	80	7	23.0
14X	14 Nov 2020	0530	113.5	123.1	9.6	113.5	120.66	7.16	7.16	75	6	19.2
15X	14 Nov 2020	0710	123.1	132.7	9.6	123.1	129.82	6.72	6.72	70	6	19.2
16X	14 Nov 2020	0850	132.7	142.3	9.6	132.7	140.19	7.49	7.49	78	6	19.2
17X	14 Nov 2020	1050	142.3	151.9	9.6	142.3	149.58	7.28	7.28	76	6	14.4
18X	14 Nov 2020	1450	151.9	161.5	9.6	151.9	158.54	6.64	6.64	69	6	4.1
19X	14 Nov 2020	1850	161.5	163.9	2.4	161.5	164.39	2.62	2.89	109	3	1.0
Hole U1558A totals:					163.90			138.69	138.96	85		
390C-U1558B-												
11	18 Nov 2020	0200	0.0	161.1			*****Drilled from 0.0 to 161.1 mbsf*****				0	14.5
390C-U1558C-												
11	20 Nov 2020	0300	0.0	162.7			*****Drilled from 0.0 to 162.7 mbsf*****				0	18.2
390C-U1558D-												
11	23 Nov 2020	0650	0.0	150.0			*****Drilled from 0.0 to 150.0 mbsf*****				0	0.0
393-U1558E-												
1H	26 Jun 2022	0515	0.0	9.5	9.5	0.0	9.98	9.97	9.98	105	8	0.0
393-U1558F-												
1H	26 Jun 2022	0645	0.0	4.0	4.0	0.0	4.03	4.03	4.03	101	4	0.0
2H	26 Jun 2022	0820	4.0	13.5	9.5	4.0	14.04	10.04	10.04	106	8	114.0
3H	26 Jun 2022	0945	13.5	23.0	9.5	13.5	23.11	9.61	9.61	101	8	114.0
4I	26 Jun 2022	1000	23.0	26.0			*****Drilled from 23.0 to 26.0 mbsf*****				0	36.0
5H	26 Jun 2022	1100	26.0	35.5	9.5	26.0	34.73	8.73	8.73	92	7	57.0
6H	26 Jun 2022	1210	35.5	45.0	9.5	35.5	44.76	9.26	9.26	97	8	57.0
7H	26 Jun 2022	1340	45.0	54.5	9.5	45.0	54.96	9.96	9.96	105	8	114.0
8H	26 Jun 2022	1445	54.5	64.0	9.5	54.5	64.56	10.06	10.06	106	8	114.0
9H	26 Jun 2022	1550	64.0	72.7	8.7	64.0	72.70	8.70	8.70	100	7	104.4
10H	26 Jun 2022	1740	72.7	86.9	14.2	72.7	83.05	10.35	10.35	73	8	56.8
11F	26 Jun 2022	1920	86.9	91.6	4.7	86.9	91.13	4.23	4.23	90	4	14.1
12F	26 Jun 2022	2035	91.6	96.3	4.7	91.6	96.57	4.97	4.97	106	5	18.8
13F	26 Jun 2022	2135	96.3	101.0	4.7	96.3	101.05	4.75	4.75	101	5	56.4
14F	26 Jun 2022	2240	101.0	105.7	4.7	101.0	105.93	4.93	4.93	105	5	56.4
15F	26 Jun 2022	2345	105.7	110.4	4.7	105.7	110.53	4.83	4.83	103	5	56.4
16F	27 Jun 2022	0050	110.4	115.1	4.7	110.4	115.29	4.89	4.89	104	5	56.4
17F	27 Jun 2022	0155	115.1	119.8	4.7	115.1	119.13	4.03	4.03	86	4	56.4
18F	27 Jun 2022	0300	119.8	124.5	4.7	119.8	124.90	5.10	5.10	109	5	70.5
19F	27 Jun 2022	0450	124.5	129.2	4.7	124.5	129.34	4.84	4.84	103	5	282.0
20X	27 Jun 2022	0700	129.2	138.9	9.7	129.2	136.67	7.47	7.47	77	6	19.4
21X	27 Jun 2022	0835	138.9	148.6	9.7	138.9	147.29	8.39	8.39	86	7	16.6
22X	27 Jun 2022	0950	148.6	158.3	9.7	148.6	157.63	9.03	9.03	93	7	23.3
23X	27 Jun 2022	1120	158.3	168.0	9.7	158.3	167.00	8.70	8.70	90	7	19.4
24X	27 Jun 2022	1355	168.0	177.2	9.2	168.0	175.43	7.43	7.43	81	6	6.5
Hole U1558F totals:					174.20			164.33	164.33	94		
393-U1558D-												
2R	28 Jun 2022	2020	150.0	156.8	6.8	150.0	151.89	1.89	1.89	28	3	16.3
3R	28 Jun 2022	2305	156.8	166.5	9.7	156.8	158.18	1.38	1.38	14	2	12.9
4R	29 Jun 2022	0255	166.5	171.3	4.8	166.5	168.03	1.44	1.53	30	2	2.2
5R	29 Jun 2022	0650	171.3	176.2	4.9	171.3	175.94	4.41	4.64	90	4	2.1
6R	29 Jun 2022	1150	176.2	185.9	9.7	176.2	184.09	7.84	7.89	81	6	2.6
7R	29 Jun 2022	1725	185.9	195.6	9.7	185.9	193.28	6.86	7.38	71	6	2.4
8R	29 Jun 2022	2345	195.6	205.3	9.7	195.6	198.33	3.00	2.73	31	2	2.2
9R	30 Jun 2022	0325	205.3	210.1	4.8	205.3	208.89	3.51	3.59	73	3	2.4
10R	30 Jun 2022	0730	210.1	215.0	4.9	210.1	214.67	4.40	4.57	90	4	2.1
11R	30 Jun 2022	1300	215.0	224.7	9.7	215.0	222.31	7.12	7.31	73	6	2.4
12R	30 Jun 2022	1720	224.7	234.4	9.7	224.7	228.52	3.65	3.82	38	3	3.2
13R	30 Jun 2022	1955	234.4	239.3	4.9	234.4	237.93	3.19	3.53	65	3	4.2
14R	30 Jun 2022	2305	239.3	244.1	4.8	239.3	241.60	2.00	2.30	42	2	4.4
15R	01 Jul 2022	0410	244.1	253.8	9.7	244.1	249.87	5.17	5.77	53	4	3.1
16R	01 Jul 2022	0720	253.8	258.7	4.9	253.8	256.48	2.37	2.68	48	2	2.9
17R	01 Jul 2022	1005	258.7	263.5	4.8	258.7	260.47	1.56	1.77	33	2	3.8
18R	01 Jul 2022	1335	263.5	268.4	4.9	263.5	266.74	3.23	3.24	66	3	2.6

## 2.1. Transit

The ship completed the 508 nmi transit from Site U1559 to Site U1558 in 46.5 h (1.9 days), arriving on site at 1125 h on 25 June 2022. The ship was switched to dynamic positioning mode, beginning operations at Site U1558.

## 2.2. Hole U1558E

An APC/XCB BHA was assembled and deployed to 4321 meters below rig floor (mbrf). A pipe “pig” was circulated down through the drill pipe to remove any rust from the extra ~1300 m of pipe required to reach the seafloor at Site U1558, compared to the shallower Site U1559 drilled previously. Heavy weather and sea conditions delayed the start of coring in Hole U1558E by 3 h while waiting for the ship’s heave to subside. The ship was positioned 20 m south of Hole U1558D (Figure F5). At 0440 h on 26 June 2022, Core 393-U1558E-1H penetrated 9.5 m and recovered 9.97 m (105%), but there was no mudline. Therefore, Hole U1558E was terminated at 0515 h.

Table T1 (continued).

Core	Core on deck date	Core on deck time UTC (h)	Top depth drilled DSF (m)	Bottom depth drilled DSF (m)	Advanced (m)	Top depth cored CSF (m)	Bottom depth recovered CSF-A (m)	Recovered length (m)	Curated length (m)	Recovery (%)	Sections (N)	Real ROP (m/h)
19R	01 Jul 2022	1630	268.4	273.2	4.8	268.4	270.91	2.00	2.51	42	2	3.8
20R	01 Jul 2022	1900	273.2	278.1	4.9	273.2	275.20	1.68	2.00	34	2	4.5
21R	01 Jul 2022	2215	278.1	282.9	4.8	278.1	280.49	2.12	2.39	44	2	3.6
22R	02 Jul 2022	0120	282.9	287.8	4.9	282.9	286.19	3.16	3.29	64	3	3.5
23R	02 Jul 2022	0445	287.8	292.6	4.8	287.8	289.96	2.01	2.16	42	2	2.7
24R	02 Jul 2022	0720	292.6	297.5	4.9	292.6	293.93	1.07	1.33	22	1	4.2
25R	02 Jul 2022	1025	297.5	302.3	4.8	297.5	299.74	2.05	2.24	43	2	3.0
26R	02 Jul 2022	1325	302.3	307.2	4.9	302.3	303.80	1.35	1.50	28	1	3.3
27R	02 Jul 2022	1605	307.2	312.0	4.8	307.2	308.69	1.17	1.49	24	1	4.4
28R	02 Jul 2022	1840	312.0	316.9	4.9	312.0	312.94	0.85	0.94	17	1	6.5
29R	02 Jul 2022	2100	316.9	321.7	4.8	316.9	318.15	0.90	1.25	19	1	7.2
30R	02 Jul 2022	2350	321.7	326.6	4.9	321.7	322.45	0.54	0.75	11	1	6.5
31R	03 Jul 2022	0255	326.6	331.4	4.8	326.6	329.28	2.51	2.68	52	2	3.2
32R	03 Jul 2022	0540	331.4	336.3	4.9	331.4	333.22	1.50	1.82	31	2	3.9
33R	03 Jul 2022	0835	336.3	341.1	4.8	336.3	337.80	1.40	1.50	29	1	3.6
34R	03 Jul 2022	1125	341.1	346.0	4.9	341.1	342.60	1.41	1.50	29	1	4.2
35R	03 Jul 2022	1415	346.0	350.8	4.8	346.0	347.69	1.55	1.69	32	2	4.4
36R	03 Jul 2022	1725	350.8	355.7	4.9	350.8	354.13	2.68	3.33	55	3	3.7
37R	03 Jul 2022	2050	355.7	360.5	4.8	355.7	359.84	3.53	4.14	74	3	3.0
38R	03 Jul 2022	2345	360.5	365.4	4.9	360.5	362.75	1.69	2.25	34	2	5.3
39R	04 Jul 2022	0315	365.4	370.2	4.8	365.4	368.40	2.61	3.00	54	2	3.2
Hole U1558D totals:					220.20			100.80	109.75	46		

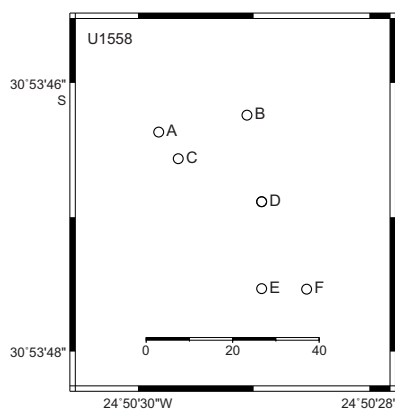


Figure F5. Map of holes drilled at Site U1558. Scale is in meters.

### 2.3. Hole U1558F

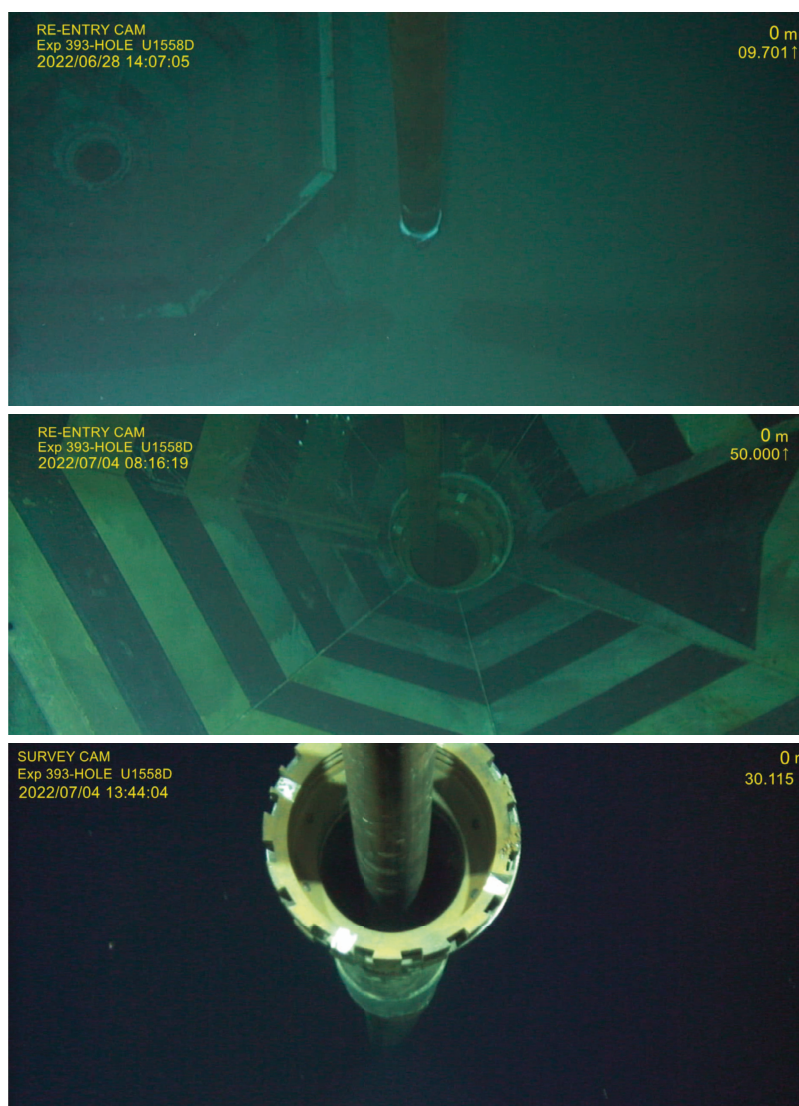
The ship was offset 10 m east of Hole U1558E (50 m southeast of Hole U1558A; Figure F5), and we started Hole U1558F at 0610 h on 26 June 2022. Coring started with the full-length APC system, and a seafloor depth of 4337.3 mbsl was established based on the mudline in Core 393-U1558F-1H. After Core 3H, we drilled ahead 3 m in an effort to fill gaps in the stratigraphy recovered from Hole U1558A during Expedition 390C. APC coring continued through Core 10H at 86.9 mbsf, where 80,000 lb of overpull was required to free the barrel, marking APC refusal depth. All full-length APC cores were oriented, and the advanced piston corer temperature (APCT-3) tool was deployed for Cores 3H, 6H, and 10H. Unfortunately, the advance in Core 10H was overdrilled by 4.7 m, and core is missing from Hole U1558F from 82.2 to 86.9 mbsf. The half-length APC (HLAPC) was deployed for Cores 11F–19F. Core 19F needed to be freed by drilling over the core barrel at 129.2 mbsf, marking HLAPC refusal depth. The XCB coring system was deployed for Cores 20X–24X. The driller noted a formation change at 176.0 mbsf (the basement contact), and drilling was terminated at 177.2 mbsf approximately 1.2 m into volcanic rocks. Cores 1H–24X penetrated from 0 to 177.2 mbsf and recovered 164.3 m (94%). The drill string was recovered to the ship, and the drill bit cleared the rotary table at 0035 h on 28 June, ending Hole U1558F.

### 2.4. Hole U1558D

We then made up the RCB BHA with a new TransCo C-4 RCB bit and following a slip and cut, lowered it to Hole U1558D, where a reentry system had been installed in November 2020 during Expedition 390C. Guided by the subsea camera video feed, the ship maneuvered over the hole. At first, the bit entered the center of the cone, but it soon met resistance; the bit did not pass down into the casing and had to be pulled back above the cone. In retrospect, this was the first indication that there would be trouble with casing in this hole. The second attempt was successful, and the bit reentered Hole U1558D at 1505 h on 28 June 2022. We lowered the bit to the depth of the existing hole (150 mbsf) and started coring at 1845 h. The existing hole is designated as drilled interval 390C-U1558D-11. Cores 393-U1558D-2R and 3R penetrated from 150 to 166.5 mbsf and recovered 3.27 m (20%) of sediment. The sediment/basement contact was determined to be at 166.8 mbsf based on an abrupt slowing of the rate of penetration at that depth while starting to drill Core 4R. Coring continued, at first alternating between full- and half-length cores based on the rate of penetration and core recovery, and switching exclusively to half-length cores from Core 16R. Perfluorocarbon tracer was run on all cores. Core 39R reached a healthy 203.4 m into volcanic rock, and coring was stopped to enable wireline logging. Basement Cores 4R–39R sampled from 166.8 to 370.2 mbsf, recovered 97.53 m of core (~48%), and took 5.0 days to drill.

At 0330 h on 4 July, we set back the top drive and pulled the bit up to 126.3 mbsf, observing 20,000 lb of drag. At 0445 h, we deployed the subsea camera to observe the bit release and guide reentry in preparation for downhole logging. We pulled the bit out of the hole to 4317 mbsl, 17 m above the seafloor. However, at 0615 h the drill pipe was observed by the subsea camera to be still inside the reentry cone, with the cone much higher up than it should be. The extra weight on the drill string confirmed that the cone and some, perhaps all, casing had been pulled out of the hole by the BHA. From 0730 to 0830 h, we attempted unsuccessfully to free the casing by pushing into the seafloor. We raised the camera back up to the ship, and from 1030 to 1100 h we attempted to free the drill string from the casing by rotation. During this process, a weight decrease of 30,000 lb was observed on the hook load indicator, showing that at least part of the casing had come free. The subsea camera was deployed again, and at 1345 h we observed that the cone had fallen away and that some of the BHA drill collars appeared to be bent but the casing hanger and casing crossover were still attached (Figure F6). The decision was made to retrieve the drill string and deal with any casing at the surface. When the drill string reached surface, the casing hanger and casing were no longer attached and must have fallen away while being raised. The bit cleared the rotary on the rig floor at 0215 h on 5 July. We disassembled the BHA, examined it for damage, and set aside the bottom three drill collars, one of which was slightly bent. After 65.4 h drilling time, the C-4 bit had only minor wear, with a few worn teeth at the top of the roller cones. We then secured the rig floor for transit and raised the thrusters, ending operations in Hole U1558D and at Site U1558. The original operations plan included running three downhole logging tool strings in Hole U1558D,





**Figure F6.** Camera feed photographs showing casing hanger and casing stuck on drill string, Hole U1558D.

but they could not be undertaken. Unfortunately, Hole U1558D is no longer a legacy hole for potential future operations. At 0530 h on 5 July, we started the 227 nmi transit to Site U1583 (proposed Site SATL-33B).

### 3. Stratigraphic unit summary

At Site U1558, we recovered 158.9 and 176.5 m of sediment in Holes U1558A and U1558E, respectively, before RCB coring in Hole U1558D penetrated 203.5 m of volcanic formations from the uppermost ocean crust (total depth of 370.3 mbsf). The cores recovered from the four holes (U1558A and U1558D–U1558F) comprise two major sedimentary units (Figure F7) overlying five basement units (Figure F8). These lithostratigraphic units are numbered from the top of the hole, with units in the sedimentary section designated by Roman numerals (e.g., I and II) and units in the basement (volcanic units) designated by Arabic numerals (e.g., 1 and 2); subunits are designated with letters (e.g., IA, IB, 2A, and 2B).

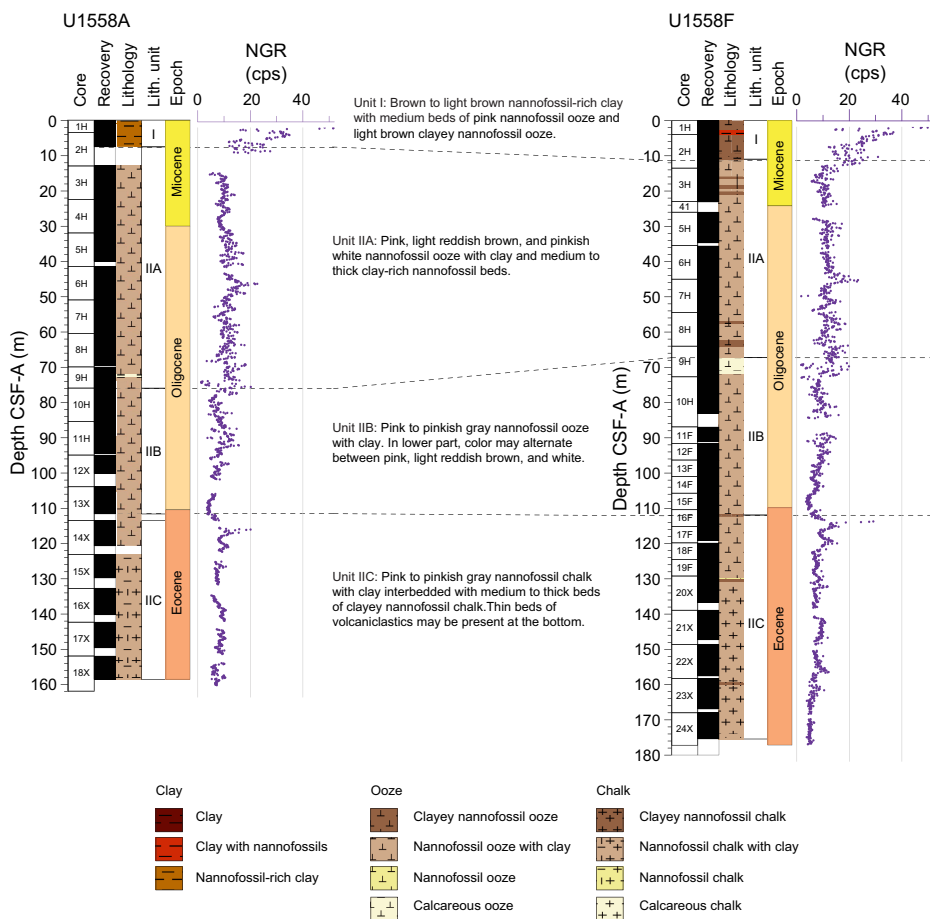
### 3.1. Sediment units

A near-complete 159–176 m thick sequence of siliciclastic and biogenic sediments was recovered from two sediment holes cored at Site U1558 (Holes U1558A and U1558F), principally comprising brown Early Miocene nannofossil-rich clay overlying pinkish middle Eocene to Early Miocene nannofossil ooze and chalk with clay and foraminifera.

Two sedimentary lithostratigraphic units (I and II) are defined at Site U1558 (Figure F7; Table T2). Unit I is composed of up to 10.11 m of Pleistocene to Early Miocene brown and reddish brown nannofossil-rich clay containing varying amounts of foraminifera and sponge spicules and subordinate nannofossil ooze with clay and foraminifera. Unit II is composed of up to 165.32 m of middle Eocene to Early Miocene biogenic sediments consisting primarily of pink, pinkish white, pinkish gray, and light brown nannofossil ooze and chalk with varying amounts of clay and foraminifera. Unit II is divided into three subunits based on their composition (clay, CaCO<sub>3</sub>, and foraminifera content) and color. Differences in constituent mineral assemblages between the units and with increasing burial depth are relatively subtle. There is a discernible increase in CaCO<sub>3</sub> content with a concomitant decrease in clay content downhole. In lower portions of the sediment section, nannofossil ooze is moderately consolidated and is termed “chalk.” Overall, clay content decreases downhole.

### 3.2. Volcanic sequences

In Hole U1558D, we drilled ~203 m of mid-ocean-ridge basalt (MORB) and intersected two distinct volcanic sequences separated by a ~1 m thick layer of indurated calcareous sedimentary

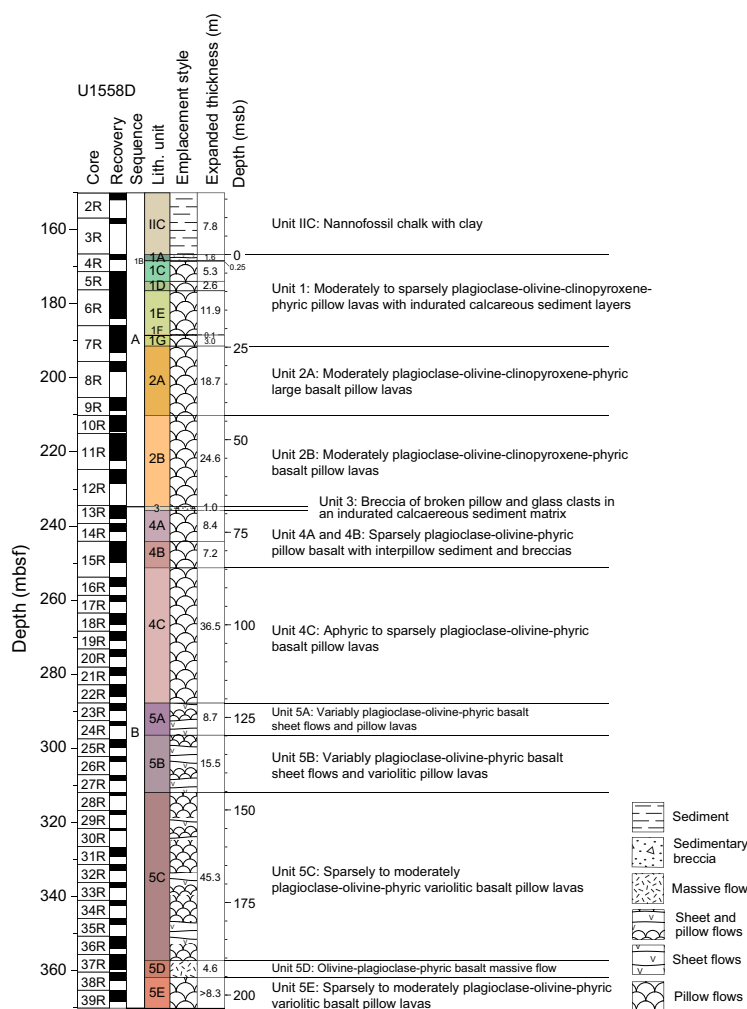


**Figure F7.** Lithostratigraphic summary of sedimentary units and correlation of full sediment sequences, Holes U1558A and U1558F. For epochs, see Age model and mass accumulation rates. For unit contact depths and thicknesses, see Table T2. Dashed lines = correlation between units. cps = counts per second.

breccia with volcanic debris that possibly indicates a hiatus in volcanism at this site on the order of tens of thousands of years (Figure F8; Table T5). The upper Sequence A (166.55–234.64 mbsf) includes volcanic Lithostratigraphic Units 1 and 2, which are moderately to highly plagioclase-olivine-clinopyroxene phyric microcrystalline basaltic lava mostly emplaced as lava pillows of varying comfort (diameter = 10–130 cm). Extremely sparse but distinctive green clinopyroxene

**Table T2.** Sedimentary units and subunits, contacts, and thicknesses, Site U1558. \* = sediment/basement contact. [Download table in CSV format.](#)

Unit	Hole	Depth (mbsf)	Thickness (m)	Age	Core, section, interval (cm)	Lithologic summary
I	390C-U1558A	0–7.48	>7.48	Early Miocene	1H-1, 0, to 2H-CC, 26	Brown (7.5YR 5/3-4/3) and light brown (7.5YR 6/4) nannofossil-rich clay with 20–40 cm thick beds of light brown (7.5YR 6/4) clayey nannofossil ooze.
	393-U1558E	0–9.98	9.98		1H, 0, to 1H-CC, 18	
	393-U1558F	0–10.96	10.96		1H-1, 0, to 2H-5, 94	
IIA	390C-U1558A	12.90–75.93	>62.43	Early Miocene to late Oligocene	3H-1, 0, to 9H-CC, 13	Nannofossil ooze with clay varying in color from pink (5YR 7/3), (7.5YR 6/4) light reddish brown, to pinkish white (5YR 8.5/2) with decimeter-thick beds of light reddish brown (5YR 5/3) clayey nannofossil ooze.
	393-U1558F	10.11–67.17	56.21		2H-5, 94, to 9H-3, 16	
IIB	390C-U1558A	75.93–113.84	37.91	early Oligocene	10H-1, 0, to 14X-1, 34	Pink (5YR 7/4) to pinkish white (5YR 8/2) nannofossil ooze with clay with several thin beds of white calcareous ooze.
	393-U1558F	67.17–111.90	44.73		9H-3, 16, to 16H-2, 0	
IIC	390C-U1558A	113.84–158.54	44.60	late to middle Eocene	14X-1, 34, to 18X-CC, 37	Nannofossil ooze/chalk with clay with decimeter beds of clayey nannofossil ooze/chalk.
	393-U1558D	150.38–158.16	7.78		2R-1, 0, to 2R-1, 100	
	393-U1558F	111.90–175.43*	63.53		16H-2, 0, to 24X-CC, 29	



**Figure F8.** Lithostratigraphic summary of volcanic units, Hole U1558D. Unit contact depths and thicknesses are expanded to account for <100% recovery (see Table T5 for curated and expanded contact depths).



phenocrysts are a characteristic feature of the Sequence A volcanic rocks. In contrast, the underlying Sequence B (234.65–370.20 mbsf) lacks these green phenocrysts, and its uppermost unit contains abundant interflow sediments and breccias, suggestive of a buried seafloor horizon. This change in phenocryst assemblage indicates that some aspect of the magmatic system changed between eruptive sequences. However, lava geochemistry as assessed by Cr/Ti ratios measured directly on the cores by portable X-ray fluorescence (pXRF) is relatively consistent downhole with little evidence for fractionated series apart from Unit 4, which has higher Cr concentrations than the other lava units.

### 3.3. Sediment/basement interface

Expeditions 390C and 393 recovered basement in Holes U1558A, U1558D, and U1558F, with the shallowest basalts recovered at depths between 158.44 and 175.29 mbsf. Hole U1558A continuously recovered a contact between nannofossil ooze and the top of a pillow lava flow, which, together with the other sites, suggests the sediments directly overlie lava flows at Site U1558. One small piece of indurated calcareous sediment was recovered above the interface in Hole U1558D, but sediments above the basement were otherwise unlithified. For stratigraphic correlation between SAT sites and with other sections of upper ocean crust recovered by scientific ocean drilling, we have defined a site sediment/basement interface depth for each of the SAT sites. The depth at which basement was encountered during drilling of the deepest hole, U1558D, was 166.8 mbsf (drilling depth below seafloor [DSF] scale) and is taken as the site interface depth at Site U1558.

## 4. Sedimentology

Two of the six holes at Site U1558 cored the entire sediment section: (1) Hole U1558A was cored during Expedition 390C (October–December 2020; Estes et al., 2021) and recovered 158.9 m of sediments, and (2) Hole U1558F was cored during Expedition 393 and recovered 176 m of sediments. Hole U1558D recovered 8.18 m of sediments above the sediment/basement interface before RCB coring of basement rocks, and Hole U1558E missed the mudline and recovered only one core (9.97 m) of sediments. The recovered sediments were described during Expedition 393 and predominantly consist of nannofossil ooze/chalk with clay and nannofossil-rich clay (in the upper 10 m) of Early Miocene to middle Eocene age.

The sediments were divided into two lithostratigraphic units (I and II; youngest to oldest) (Figures [F9](#), [F10](#), [F11](#), [F13](#), [F14](#)). Unit II is divided into three subunits (IIA–IIC) based on relative changes in the amount of clay and CaCO<sub>3</sub>, physical and biogenic sedimentary structures, and physical properties of the sediments.

It should be noted that some sedimentary intervals have slight color and bioturbation intensity differences between Holes U1558A, U1558D, U1558E, and U1558F. Hole U1558A was described about ~18 months after it was drilled in December 2020; therefore, any differences in the sediment coloration are due to oxidation and drying. As for biogenic structures, bioturbation intensity is higher in recently drilled Holes U1558D–U1558F compared to bioturbation intensity in Hole U1558A. It is assumed that such disparity is due to sediments drilled during Expedition 393 being fresher, resulting in better lithologic contrasts and visibility of trace fossils.

### 4.1. Unit descriptions

#### 4.1.1. Unit I

Intervals: 390C-U1558A-1H, 0 cm, to 2H-CC, 26 cm; 393-U1558E-1H, 0 cm, to 1H-CC, 18 cm;  
393-U1558F-1H, 0 cm, to 2H-5, 94 cm

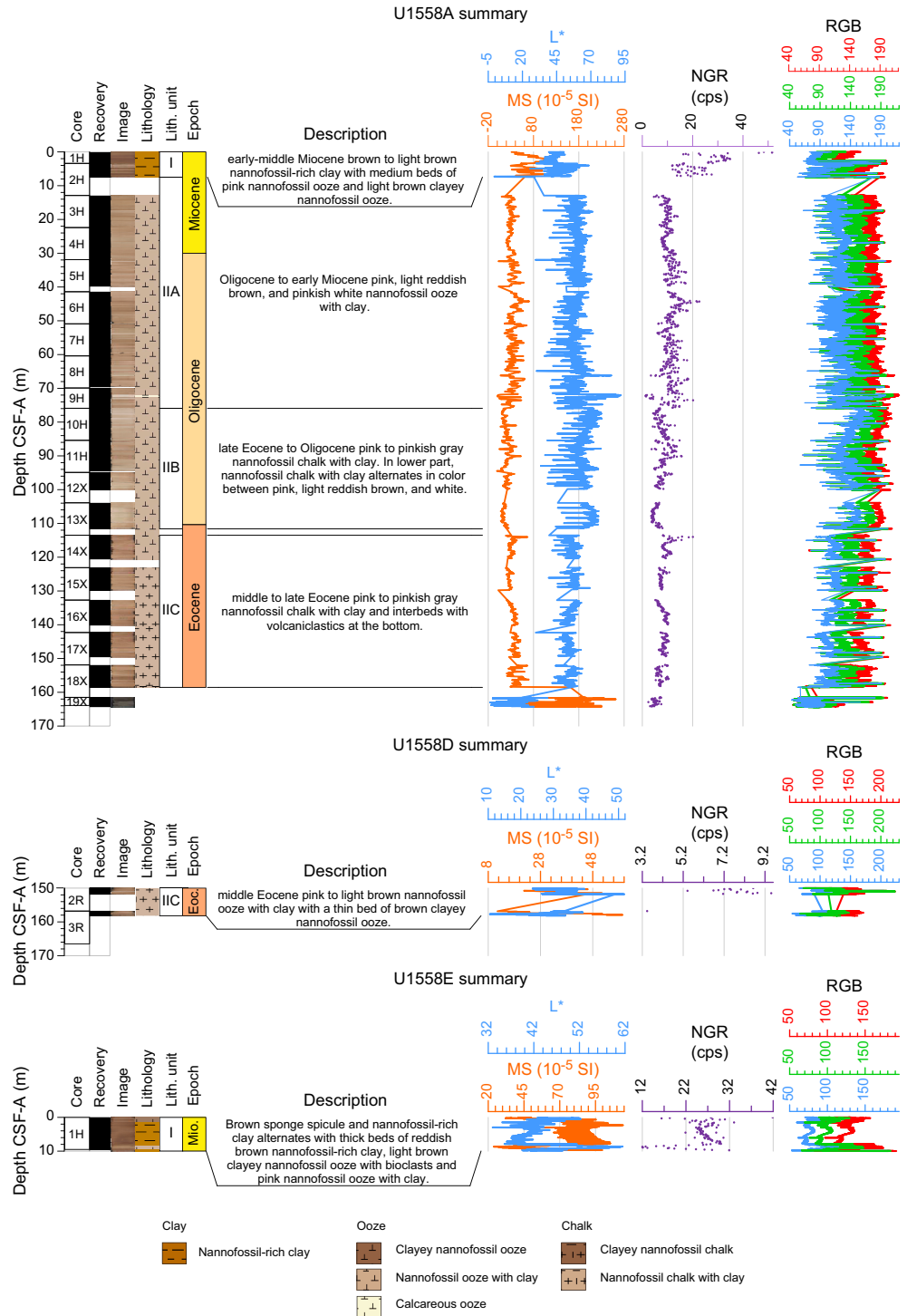
Depths: Hole U1558A = 0–7.5 m core depth below seafloor, Method A (CSF-A); Hole U1558E  
= 0–10.0 m CSF-A; Hole U1558F = 0–11.0 m CSF-A

Thickness: Hole U1558A = 7.5 m; Hole U1558E = >10.0 m; Hole U1558F = 11.0 m

Age: Early Miocene

Lithology: alternating nannofossil ooze with nannofossil-rich clay with foraminifera

Lithostratigraphic Unit I is composed of alternating layers of nannofossil ooze and nannofossil-rich clay (Figures F9, F10, F11, F12). The nannofossil ooze varies in clay content, ranging from clayey nannofossil ooze to nannofossil ooze with clay, reflected in the sediment color, ranging from dark reddish gray to reddish brown, brown, and light brown (Figures F9, F10). The nannofossil-rich clay contains varying amounts of foraminifera and sponge spicules. Overall, clay content decreases downhole throughout Unit I (Figures F9, F13). Hole U1558A is dominated by nannofossil-rich clay with a few up to 40 cm thick beds of nannofossil ooze in the bottom 3.5 m of



**Figure F9.** Lithologic summaries, Holes U1558A, U1558D, U1558E, and U1558F. For epochs, see Age model and mass accumulation rates. cps = counts per second, RGB = red-green-blue. (Continued on next page.)

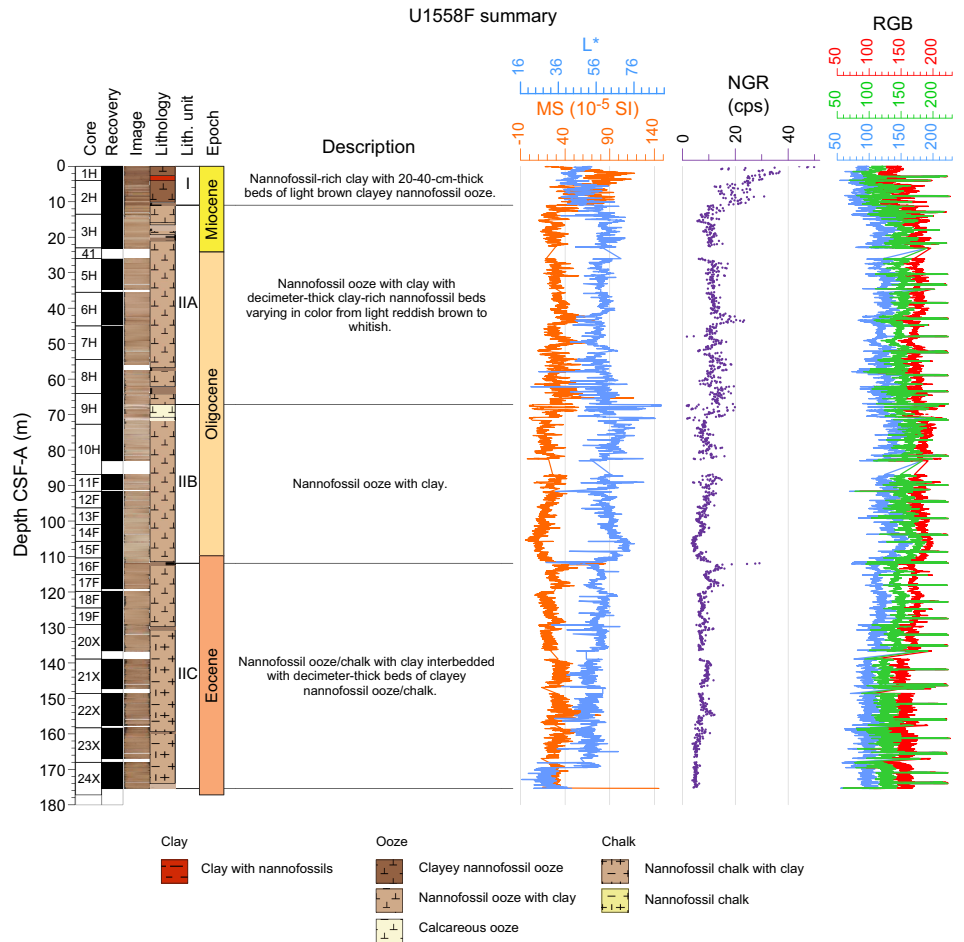


Figure F9 (continued).

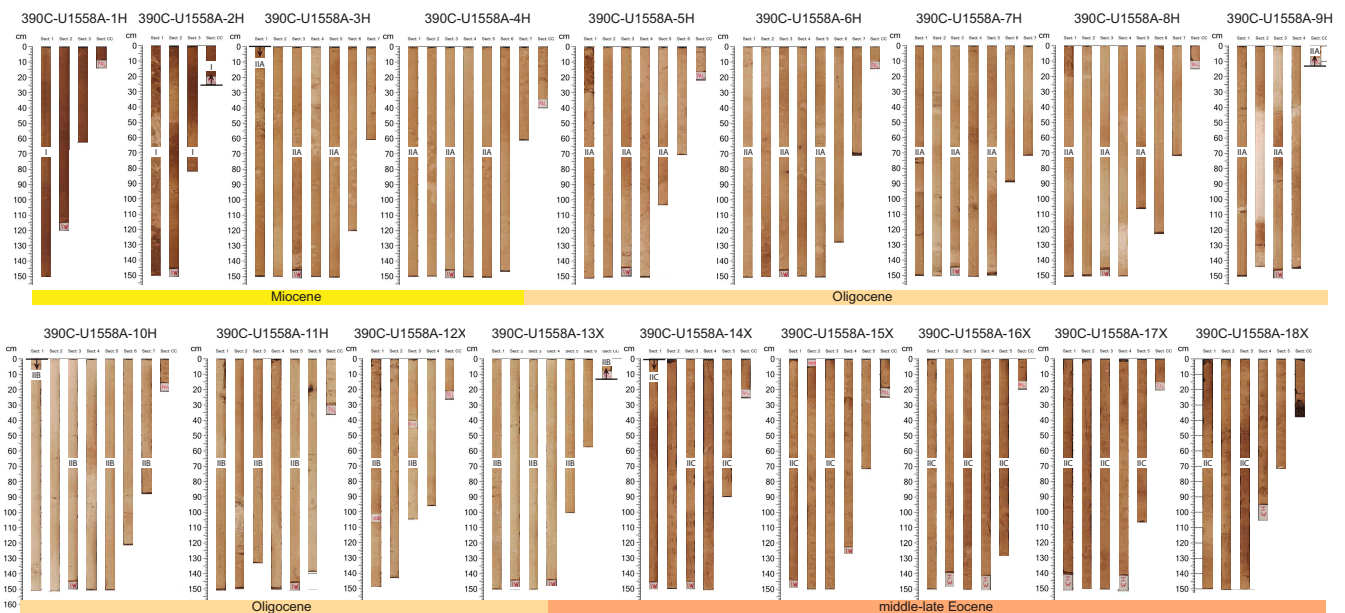


Figure F10. Core composite photographs with ages and units, Holes U1558A and U1558F. (Continued on next page.)



Unit I. In contrast, Hole U1558F is dominated by nannofossil ooze with a few up to 40 cm thick beds of nannofossil-rich clay in the upper 4 m of Unit I.

Lithologic contacts in Unit I are typically gradational, bioturbated, and horizontal and rarely sub-angular. Mottling is the dominant sedimentary structure where bedding is not present. Even though biogenic mottling is common, distinct ichnofossils can be identified in decimeter-thick intervals, including but not limited to *Zoophycos*, *Planolites*, *Palaeophycus*, *Thalassinoides*, *Skolithos*, *Arenicolites*, and *Chondrites*. Bioturbation intensity ranges between absent and complete (bioturbation index [BI] = 0–6) but is mostly common to high (BI = 3–4). Ichnofossil diversity is commonly 2–5 ichnogenera, with the maximum diameter ranging 1–20 mm (Figure F14). The boundary between Units I and II is marked by a decrease in clay content (Figure F10) based on a lightening in sediment color (i.e., higher luminosity/lightness [L\*]; Figure F15), a decrease in magnetic susceptibility (MS) and natural gamma radiation (NGR) values (Figure F9), as well as a higher CaCO<sub>3</sub> content. This boundary was not recovered in Hole U1558A.

The primary minerals identified with bulk X-ray diffraction (XRD) in Unit I include calcite, quartz, plagioclase, and clay minerals such as illite, kaolinite, and smectite (Figures F16, F17; Tables T3, T4). Calcite and quartz form the dominant peaks, with calcite being the largest. The characteristic double peak of plagioclase indicates that it is a significant component of Unit I. The typical mineral composition of Unit I is as follows: 38–62 wt% calcite (supported by 20–47 wt% CaCO<sub>3</sub>; see **Geochemistry**), 27–43 wt% total clay minerals, 6–9 wt% feldspar, and 4–10 wt% quartz (Figure

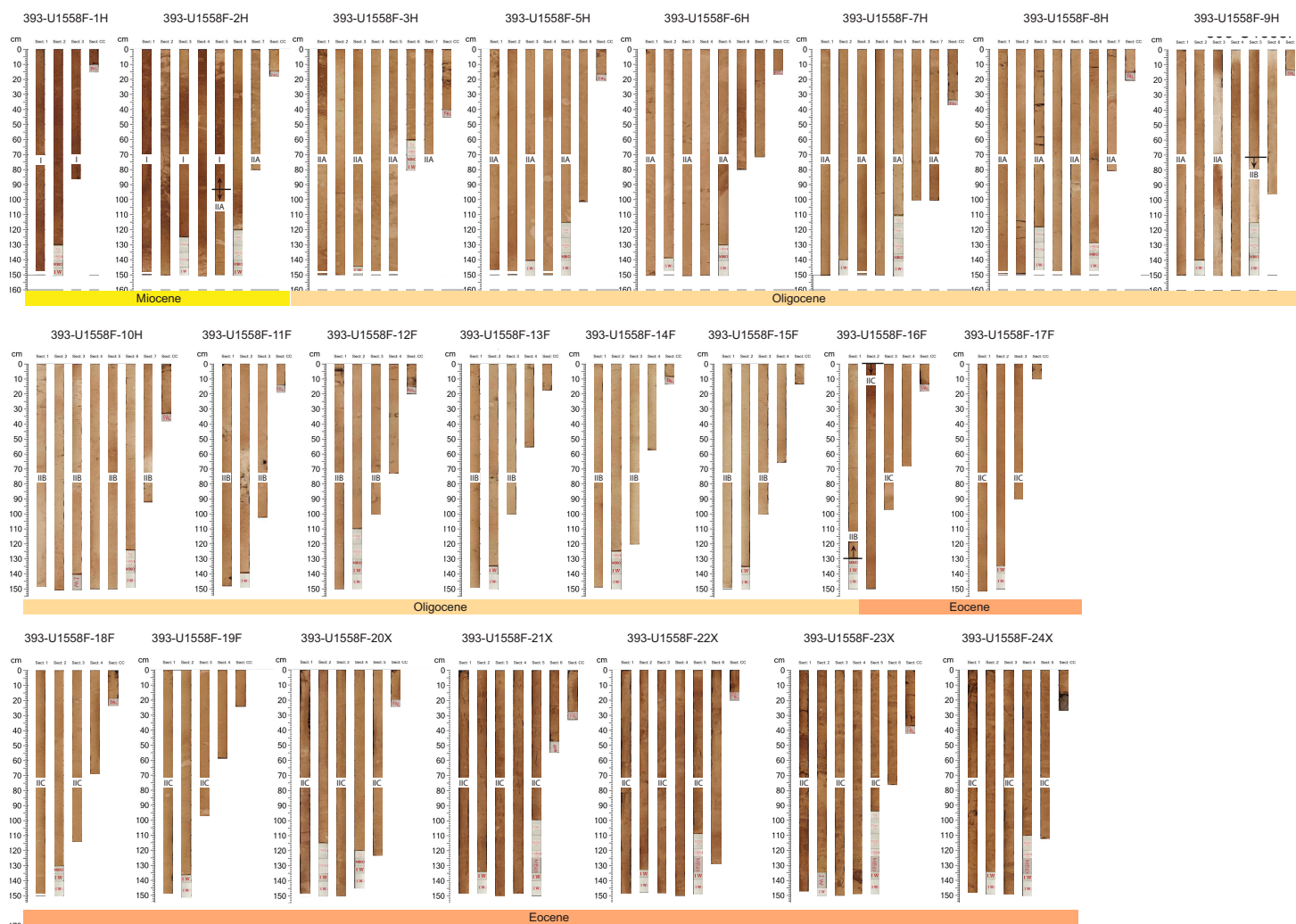
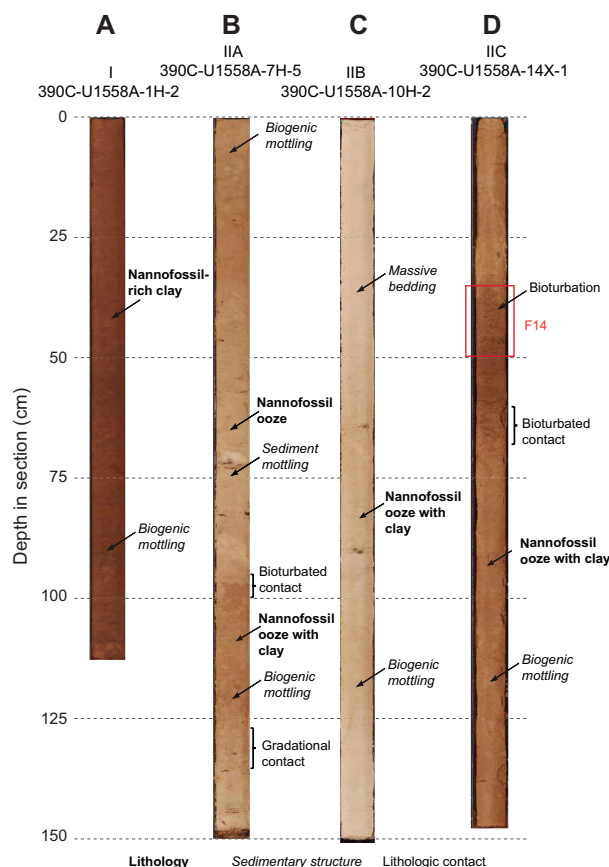
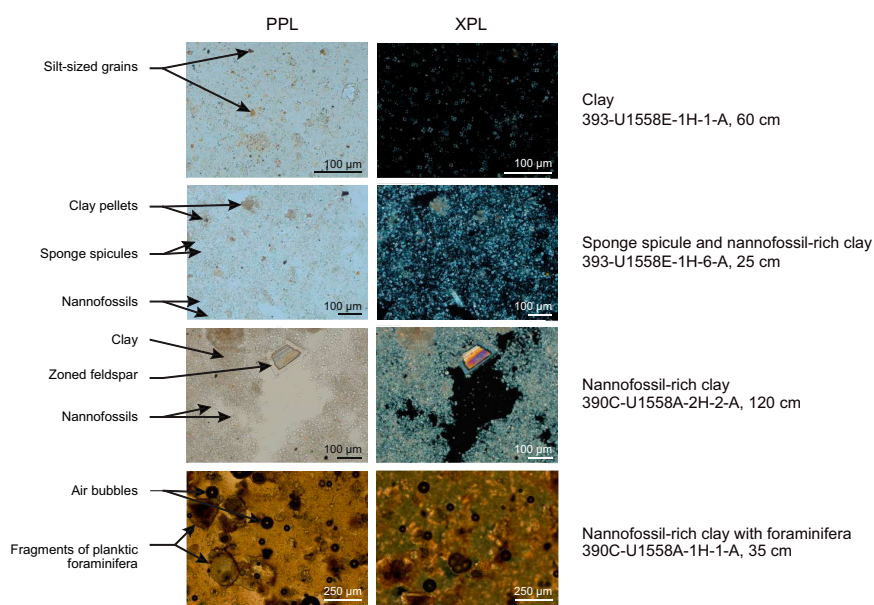


Figure F10 (continued).



**Figure F11.** Typical lithologies of each unit, Site U1558. A. Unit I nannofossil-rich clay with foraminifera and nannofossil ooze with varying clay content. B. Subunit IIA nannofossil ooze with clay interbedded with clayey nannofossil ooze. C. Subunit IIB nannofossil ooze with clay. D. Subunit IIC nannofossil chalk with clay.



**Figure F12.** Smear slide photomicrographs showing principal sediment types, Site U1558. Nannofossil-rich clay and nannofossil ooze/chalk. PPL = plane polarized light, XPL = cross-polarized light. (Continued on next page.)

**F17**; Table **T4**). In this deep marine environment, the relatively large amounts of clay and feldspar indicate a terrigenous influx of airborne material and dissolution of some calcite.

#### 4.1.2. Unit II

Intervals: 390C-U1558A-3H-1, 0 cm, to 18X-CC, 28 cm; 393-U1558D-2R-1, 0 cm, to 3R-CC, 16 cm; 393-U1558F-2H-5, 94 cm, to 9H-5, 72 cm

Depths: Hole U1558A = 12.9–158.5 m CSF-A; Hole U1558D = 150.4–158.2 m CSF-A; Hole U1558F = 11.0–175.4 m CSF-A

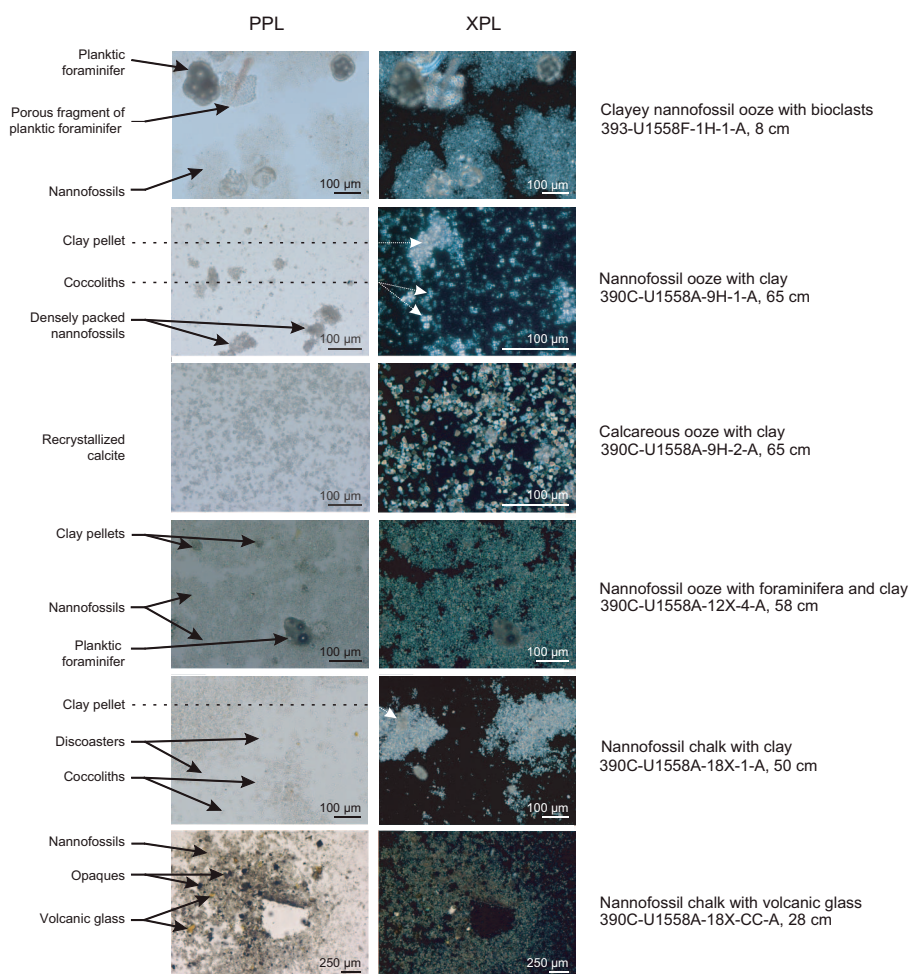
Thickness: Hole U1558A = 145.6 m; Hole U1558D = >7.8 m; Hole U1558F = 164.5 m

Age: Early Miocene to middle Eocene

Lithology: nannofossil ooze transitioning into nannofossil chalk with varying amounts of clay and foraminifera

Lithostratigraphic Unit II is composed of nannofossil ooze overlying nannofossil chalk, both with varying amounts of clay (Figures **F9**, **F10**, **F11**, **F13**). The transition from nannofossil ooze to nannofossil chalk occurs at the top of Cores 390C-U1558A-15X and 393-U1558F-20X. In general, Unit II has <10% of foraminifera. There are no discernible breaks in the lithology, and no hiatuses were identified (see **Biostratigraphy**).

Lithologic contacts in Unit II are typically gradational to bioturbated, horizontal to subhorizontal, and rarely curved. Sediments are massive to mottled. Trace fossils are observed in decimeter-thick intervals and commonly include *Thalassinoides*, *Planolites*, *Palaeophycus*, *Skolithos*, *Chondrites*, and more rarely *Arenicolites*, *Cylindrichnus*, *Zoophycos*, and *Phycosiphon*. Bioturbation intensity



**Figure F12 (continued).**

ranges between absent and intense (BI = 0–5) and is predominantly sparse to common (BI = 1–3). Ichnofossil diversity ranges 1–5 and is commonly 2–3, with the maximum diameter ranging 3–30 mm (Figure F14). XRD data indicate a uniform mineralogy of Unit II (Figures F16, F17; Tables T3, T4). Calcite dominates the mineral assemblage with terrigenous minerals such as quartz, plagioclase, and clay minerals constituting minor components of this unit. However, slight variations in relative peak intensities exist, especially in kaolinite, illite, and smectite, indicating changes in clay mineral contents.

Unit II is divided into three subunits that are described below.

**4.1.2.1. Subunit IIA**

Intervals: 390C-U1558A-3H-1, 0 cm, to 9H-CC, 13 cm; 393-U1558F-2H-5, 94 cm, to 9H-3, 16 cm

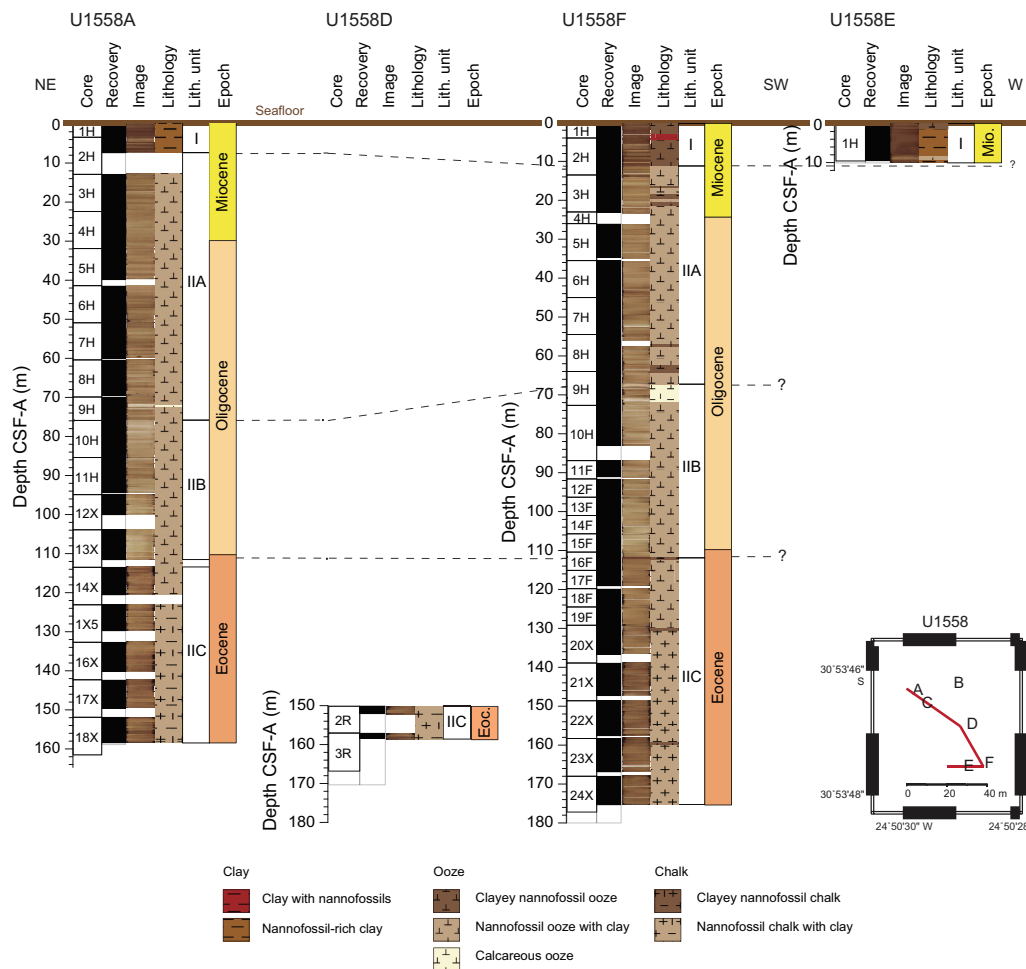
Depths: Hole U1558A = 12.9–75.9 m CSF-A; Hole U1558F = 11.0–67.2 m CSF-A

Thickness: Hole U1558A = 63.0 m; Hole U1558F = 56.2 m

Age: Early Miocene to late Oligocene

Lithology: nannofossil ooze with clay interbedded with clayey nannofossil ooze

Subunit IIA predominantly consists of nannofossil ooze with clay interbedded with clayey nannofossil ooze. The amount of clayey nannofossil ooze appears to be slightly higher in Hole U1558F compared to the amount in Hole U1558A. Color banding at the meter scale is present in most of Subunit IIA, ranging from pink and pinkish white to light brown (Figure F10). Quasicyclic pat-

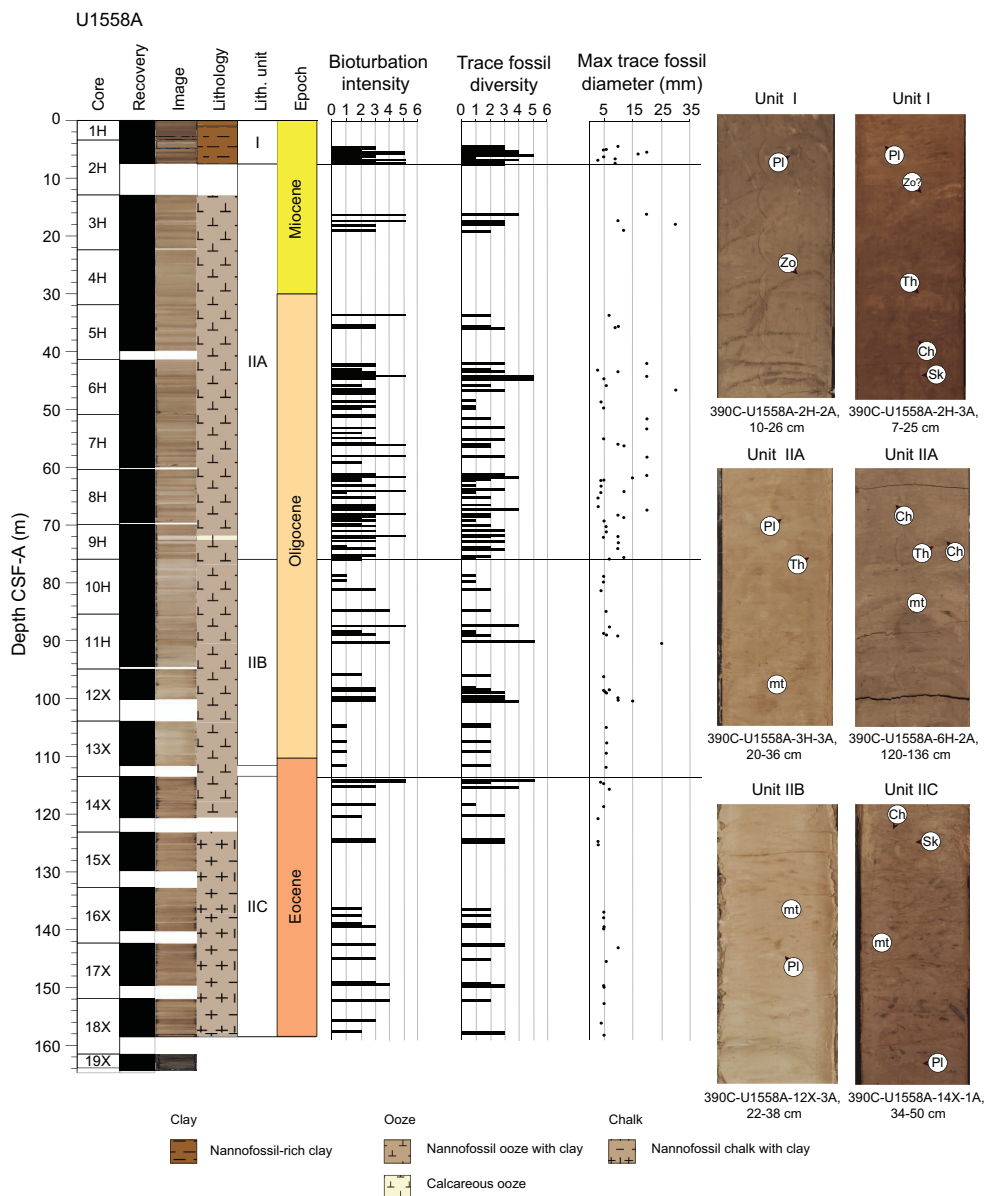


**Figure F13.** Lithologic correlation of sediment holes, Site U1558. For epochs, see Age model and mass accumulation rates. Dashed lines = correlation between units. Bottom right: sketched map (not to scale) showing positions of each hole relative to one another.



terns at the meter scale are also seen in MS and NGR data within this interval (Figure F9). A few decimeter-thick intervals of inclined laminations located between horizontal beds appear in Sections 393-U1558F-6H-1 and 6H-2 as well as in Section 8H-6. We suggest that these sedimentary structures represent localized soft-sediment deformation, as supported by magnetic fabric data (see Paleomagnetism).

The contacts between the beds are typically gradational and bioturbated. Massive bedding and mottling are the dominant sedimentary structures. Biogenic mottling is common, with the following ichnogenera identified: *Thalassinoides*, *Planolites*, *Palaeophycus*, *Skolithos*, and more rarely *Arenicolites*, *Zoophycos*, *Chondrites*, and *Phycosiphon*. Bioturbation intensity varies throughout the unit. It is generally higher (BI = 1–5) in the upper (~10–20 m CSF-A) and lower (~42–76 m CSF-A) parts of Subunit IIA and lower (BI = 1–3) in the middle part (~20–42 m CSF-A) of the subunit. Ichnofossil diversity ranges 1–5, commonly constituting 2–3. The maximum ichnofossil diameter ranges 3–30 mm (Figure F14).



**Figure F14.** Characterization of bioturbation signatures and core photographs of typical trace fossil assemblages for each unit, Holes U1558A and U1558D–U1558F. For epochs, see Age model and mass accumulation rates. Zo = *Zoophycos*, Pl = *Planolites*, Th = *Thalassinoides*, Ch = *Chondrites*, Sk = *Skolithos*, Pa = *Palaeophycus*, mt = biogenic mottling, Ar = *Arenicolites*, He = *Helminthopsis*. (Continued on next two pages.)



The mineral composition of Subunit IIA is 84–91 wt% calcite, 8–13 wt% total clay minerals, 1–2 wt% quartz, and 1 wt% feldspar (Figures F16, F17; Tables T3, T4).

The boundary between Subunits IIA and IIB occurs in Section 393-U1558F-2H-5, 94 cm, and between Cores 390C-U1558A-9H and 10H based on a visual decrease in clay content (Figure F10), brightening in sediment color (i.e., higher  $L^*$ ; Figure F15), decreases in MS and NGR values (Figure F9), and higher  $\text{CaCO}_3$  content.

#### 4.1.2.2. Subunit IIB

Intervals: 390C-U1558A-10H-1, 0 cm, to 14X-1, 34 cm; 393-U1558F-9H-3, 16 cm, to 16H-2, 0 cm

Depths: Hole U1558A = 75.9–113.8 m CSF-A; Hole U1558F = 67.2–111.9 m CSF-A

Thickness: Hole U1558A = 37.9 m; Hole U1558F = 44.7 m

Age: early Oligocene

Lithology: nannofossil ooze with clay

Subunit IIB predominantly consists of pink to pinkish gray nannofossil ooze with clay. A few decimeter-thick layers of white recrystallized calcareous ooze appear in Cores 390C-U1558A-11H, 393-U1558F-9H, and 10H. Minor intervals of clayey nannofossil ooze were also observed in Hole U1558F. Subtle color banding at the meter scale is present in the upper 15 m of this subunit. A signature corresponding to this banding is also seen in the MS and NGR data (Figure F9).

Massive bedding is the dominant sedimentary structure, when not obscured by sediment mottling. Dark gray to black specs (millimeter scale), likely composed of sulfide and iron oxides, are sporadically spaced throughout this subunit. Subunit IIB is the least bioturbated subunit. It typically presents sparse to low bioturbation intensity ( $BI = 1-2$ ). Even though biogenic mottling is commonly present, individual biogenic sedimentary structures are

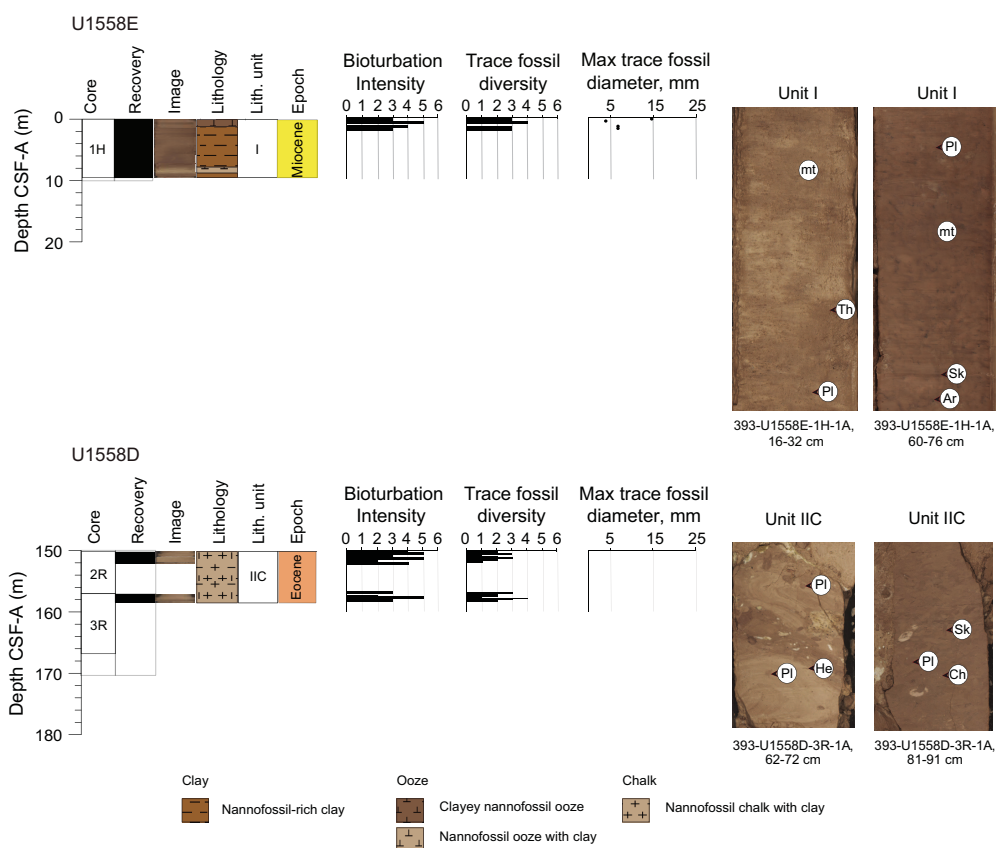


Figure F14 (continued). (Continued on next page.)

visible in several decimeter-thick intervals. The identified ichnofossils are *Planolites*, *Palaeophycus*, *Skolithos*, *Thalassinoides*, *Chondrites*, and rarely *Cylindrichmus* and *Arenicolites*. Trace fossil diversity ranges 1–5 ichnogenera, more commonly constituting 2–3. The maximum trace fossil diameter varies between 5 and 25 mm (Figure F14).

The mineral composition of Subunit IIB based on XRD analysis consists of 90–94 wt% calcite, 5–8 wt% total clay minerals, 1–2 wt% quartz, and 1% feldspar (Figures F16, F17; Tables T3, T4). The higher carbonate content of Subunit IIB compared to Subunits IIA and IIC has been supported by measured CaCO<sub>3</sub> (68–97 wt%; see **Geochemistry**). XRD and carbonate (CARB) data indicate that Subunit IIB is more carbonate rich (CaCO<sub>3</sub> = 84–91 wt%; see **Geochemistry**) than the overlying Subunit IIA.

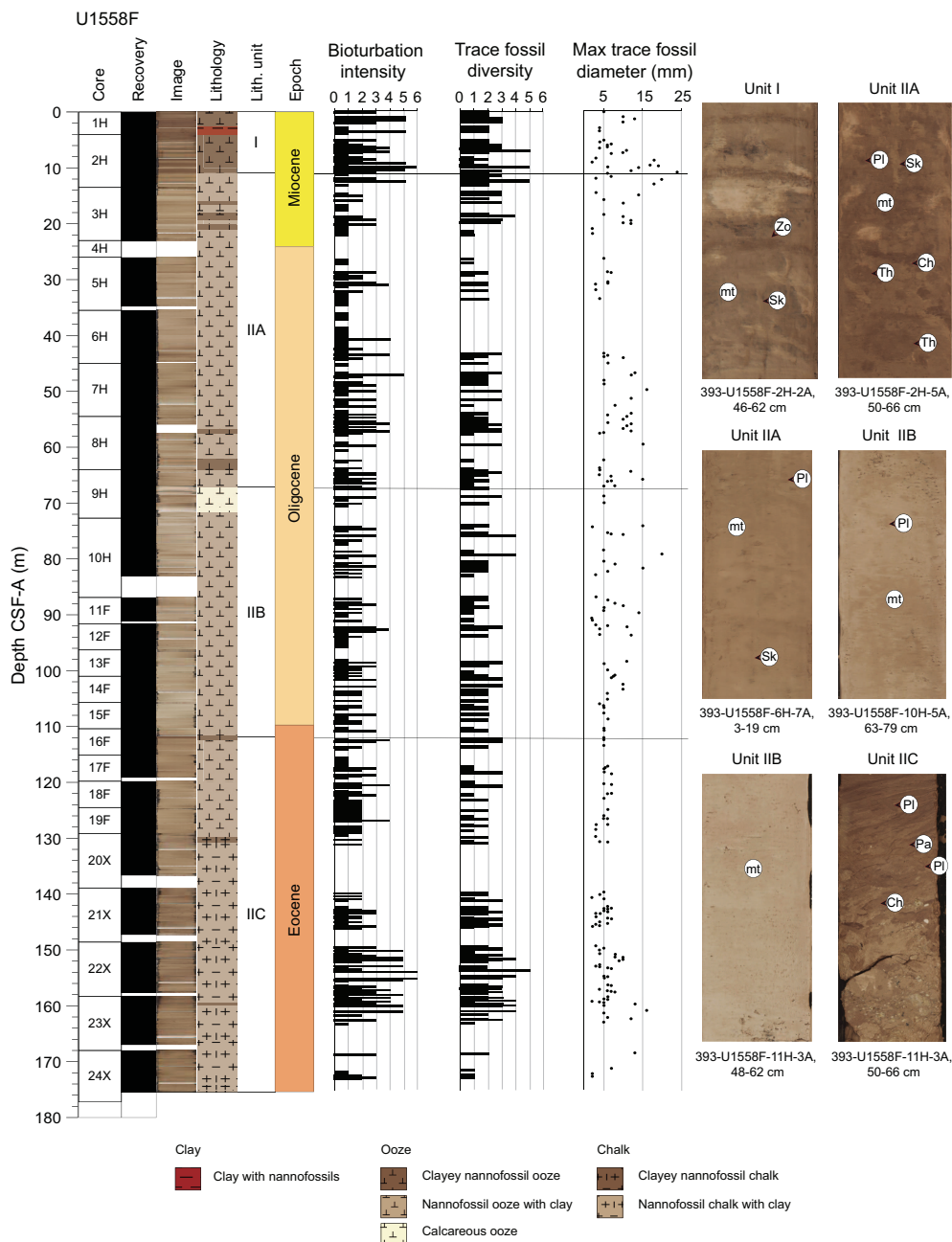


Figure F14 (continued).

The boundary between Subunits IIB and IIC occurs between Cores 390C-U1558A-13X and 14X and at the top of Section 393-U1558F-16H-2. It is recognized by a visual increase in clay content (Figure F10), darkening of sediment color (i.e., lower  $L^*$ ; Figure F15), higher MS and NGR values (Figure F9), as well as lower  $\text{CaCO}_3$  content. This boundary also marks the Eocene/Oligocene boundary (see [Biostratigraphy](#)).

#### 4.1.2.3. Subunit IIC

Intervals: 390C-U1558A-14X-1, 34 cm, to 18X-CC, 37 cm; 393-U1558D-2R-1, 0 cm, 3R-CC, 16 cm; 393-U1558F-16H-2, 0 cm, to 24X-CC, 29 cm

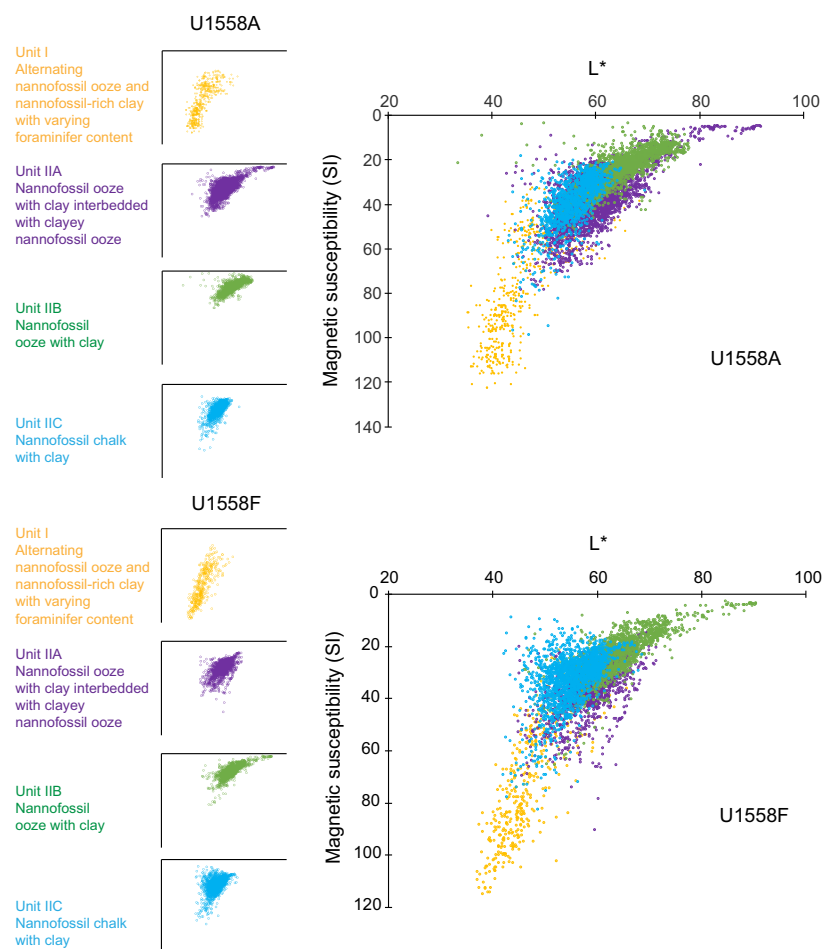
Depths: Hole U1558A = 113.8–158.5 m CSF-A; Hole U1558D = 150.0–158.2 m CSF-A; Hole U1558F = 111.9–175.4 m CSF-A

Thickness: Hole U1558A = 44.6 m; Hole U1558D = 7.8 m; Hole U1558F = 63.5 m

Age: late to middle Eocene

Lithology: nannofossil chalk with clay

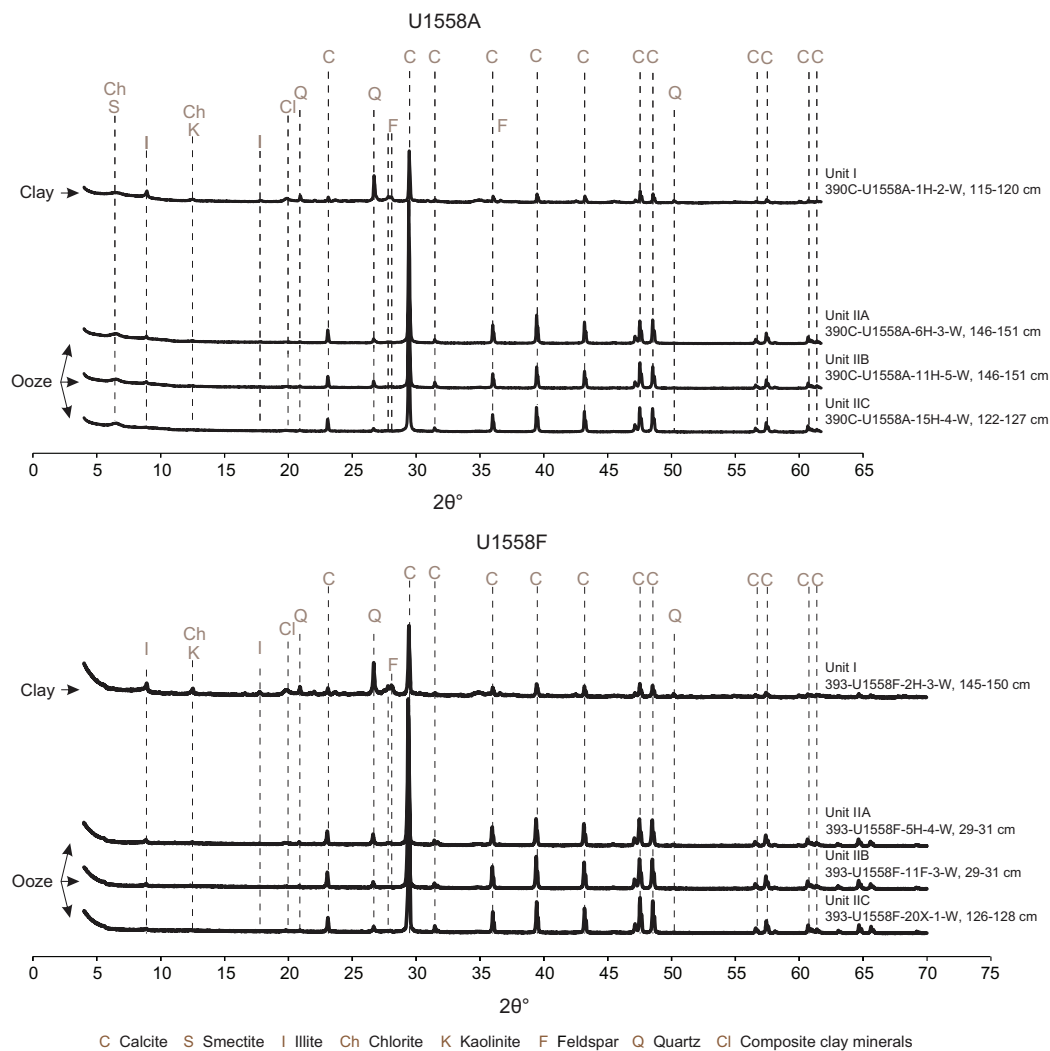
Subunit IIC predominantly consists of pink to pinkish gray nannofossil chalk with clay. At the top of this subunit, a 6 and 16 m thick nannofossil ooze layer overlies the nannofossil chalk in Holes U1558A and U1558F, respectively. Additionally, decimeter-thick intervals of clayey nannofossil chalk and two thin interbeds with volcanic glass ~1 m above the sediment/basement interface are observed in Hole U1558F. In Hole U1558A, the sediment/basement interface occurs within Section 18X-CC based on the first appearance of ferromanganese crust, whereas in Hole U1558F, the sediment/basement contact is abrupt and occurs in Section 24X-CC, 29 cm.



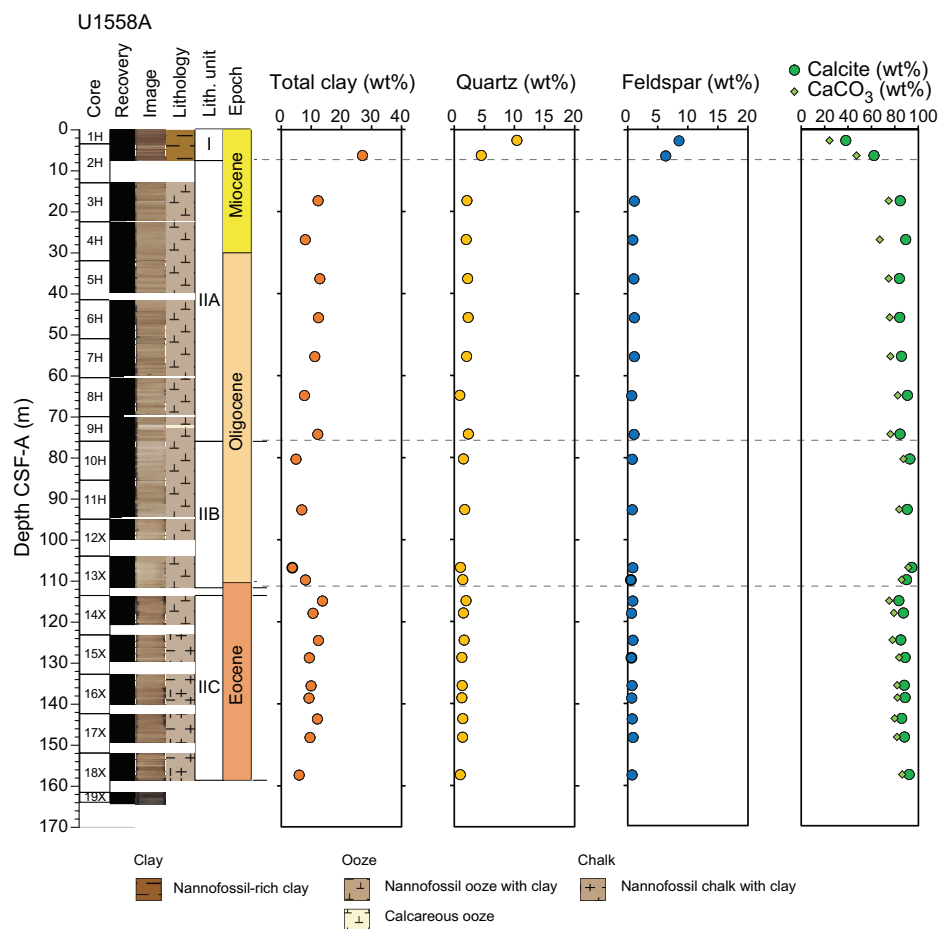
**Figure F15.** Scatter plots of SHMSL MSP and  $L^*$  (reflectance; greater value = lighter), Holes U1558A and U1558F. (See Sedimentology in the Expedition 390/393 methods chapter [Coggon et al., 2024b].) Insets on left: properties of individual subunits with brief descriptions.

Even though moderate to severe drilling disturbances, such as biscuits and fracturing, are common below Sections 390C-U1558A-17X-1 and 393-U1558F-20X-1, the intact sediments preserve intervals that contain thin laminations overlying bioturbation. The most common sedimentary structures in Subunit IIC are mottling and decimeter-scale massive bedding. Thin laminations can be present (e.g., interval 390C-U1558A-15X-2, 5–25 cm). The bedding contacts are described as ranging from bioturbated to irregular, with the surface appearing horizontal to curved. Subunit IIC is characterized by increased biogenic activity, with bioturbation intensity ranging from absent to intense (BI = 0–5) and more commonly low to high (BI = 2–4). Bioturbation intensity is low (BI = 1–2) in the upper part of Subunit IIC (~112–130 m CSF-A), absent in its middle part (BI = 0; ~130–140 m CSF-A), and increases in the lower part (BI = 2–5; ~140–175 m CSF-A). Typical trace fossils include *Chondrites*, *Skolithos*, *Planolites*, *Zoophycos*, and *Nereites/Cosmorhaphes*, with rare *Palaeophycus* and *Helminthopsis*. Trace fossil diversity ranges 1–2 ichnogenera in the upper part of Subunit IIC (~112–130 m CSF-A) and reaches 2–5 ichnogenera in the lower part (~140–175 m CSF-A). A similar trend is observed for the maximum trace fossil size: it increases from 3 to 5 mm in the upper part of Subunit IIC to 5–15 mm in the lower part of Subunit IIC (Figure F14).

The mineral composition of Subunit IIC consists of 83–92 wt% calcite, 6–14 wt% total clay minerals, 1–2 wt% quartz, and 1 wt% feldspar (Figures F16, F17; Tables T3, T4). These XRD results and measured  $\text{CaCO}_3$  amounts (57–86 wt%; see [Geochemistry](#)) support a slightly lower carbonate content in Subunit IIC compared to the overlying Subunit IIB.



**Figure F16.** Representative X-ray diffractograms of bulk sediments, Holes U1558A and U1558F.



**Figure F17.** Downhole changes in mineralogy, including clay, quartz, feldspar, and calcite, based on XRD results and CaCO<sub>3</sub>, Hole U1558A. Values are normalized: total clay minerals (smectite + illite + chlorite + kaolinite) + quartz + feldspar (plagioclase + K-feldspar) + calcite = 100%.

**Table T3.** XRD semiquantitative estimation of main mineralogical components, Hole U1558A. All XRD-derived semiquantitative estimates are tabulated in Table T4. [Download table in CSV format.](#)

Lith. unit	Lithologic description	Depth range CSF-A (m)	Thickness (m)	Calcite (wt%)		Total clays (wt%)		Quartz (wt%)		Feldspar (wt%)	
				Value range	Mean	Value range	Mean	Value range	Mean	Value range	Mean
I	Alternating nannofossil ooze and nannofossil-rich clay with varying foraminifer content	0–7.5	>7.5	38–62	50	27–43	35	4–10	7	6–9	7
IIA	Nannofossil ooze with clay interbedded with clayey nannofossil ooze	12.9–75.9	>62.4	84–91	86	8–13	11	1–2	2	1	1
IIB	Nannofossil ooze with clay	75.9–113.8	37.9	90–94	92	4–8	6	1–2	1	1	1
IIC	Nannofossil chalk with clay	113.8–158.5	44.6	83–92	88	6–14	10	1–2	1	1	1



**Table T4.** XRD semiquantitative estimation of main mineralogical components of all samples, Hole U1558A. [Download table in CSV format.](#)

Core, section, interval (cm)	Top depth CSF-A (m)	Lith. unit	Lithologic description	Total clay (wt%)	Quartz (wt%)	Feldspar (wt%)	Calcite (wt%)
390C-U1558A-							
1H-2, 115–120	2.7	I	Alternating nannofossil ooze and nannofossil-rich clay with varying foraminifer content	43	10	9	38
2H-2, 145–150	6.4			27	4	6	62
3H-3, 146–151	17.4	IIA	Nannofossil ooze with clay interbedded with clayey nannofossil ooze	12	2	1	85
4H-3, 146–151	26.9			8	2	1	89
5H-3, 144–149	36.4			13	2	1	84
6H-3, 146–151	45.9			12	2	1	84
7H-3, 145–150	55.4			11	2	1	86
8H-3, 146–151	64.9			8	1	1	91
9H-3, 146–151	74.3			12	2	1	84
10H-3, 145–150	80.4	IIB	Nannofossil ooze with clay	5	2	1	93
11H-5, 146–151	92.7			7	2	1	91
13X-2, 144–149	106.8			4	1	1	94
13X-4, 144–149	109.8			8	1	1	90
14X-1, 145–150	115.0	IIC	Nannofossil chalk with clay	14	2	1	83
14X-3, 145–150	118.0			11	2	1	87
15X-1, 144–149	124.5			12	2	1	85
15X-4, 122–127	128.8			9	1	1	89
16X-2, 139–149	135.6			10	1	1	88
16X-4, 141–151	138.6			9	1	1	89
17X-1, 140–150	143.7			12	1	1	86
17X-4, 141–151	148.2			10	1	1	88
18X-4, 95–105	157.4			6	1	1	92

## 5. Igneous petrology

Hole U1558D targeted ~49.2 Ma upper oceanic crust along the SAT, reached volcanic basement at 166.8 mbsf, and penetrated a further 203.4 m into igneous rocks, reaching 370.2 mbsf and recovering 97.5 m of basalt for an average basement recovery of 48% (Figure F8; Table T5). In the upper part of the hole, recovery was relatively high, with an average of 73% between Cores 393-U1558D-5R and 11R. Recovery dropped for the remainder of the hole to an average of 40% between Cores 12R and 39R, but within this interval several cores advanced through coarser grained massive lava flows and carbonate sediment-cemented pillows and recovery reached 60%–70%. Overall, this recovery was sufficient for unit boundaries, lava types, and volcanic emplacement styles to be determined with confidence throughout the hole.

Unless stated otherwise, all cores, sections, and intervals refer to Hole U1558D. Depths are described in meters below seafloor (mbsf; on CSF-A scale) and meters subbasement (msb; CSF-A depth minus 166.8 m). Sample, interval, and contact depths are curated depths unless mentioned otherwise. This section documents the lithostratigraphy of the volcanic basement at Site U1558 and then summarizes observations and results for the phenocryst phases, breccias, and igneous chemostratigraphy as measured on split core surfaces by pXRF.

### 5.1. Lithostratigraphic units

The basement volcanic sequence at Site U1558 was divided into two main eruptive sequences (A and B) and five main volcanic and intravolcanic sedimentary units. Unit 1 is divided into seven subunits (1A–1G), Unit 2 is divided into two subunits (2A and 2B), Unit 4 is divided into three subunits (4A–4C), and Unit 5 is divided into five subunits (5A–5E). These units and their thicknesses, emplacement styles, contacts, and lithologic details are summarized in Table T5, illustrated in Figure F8, and documented in detail in this section.

#### 5.1.1. Sediment/basement interface

The shallowest occurrences of volcanic rocks and the deepest occurrences of sediment within the sediment/basement interface for all holes at Site U1558 are summarized in Table T6 and illustrated in Figure F18. Single cores containing both sediment (nannofossil chalk with clay [Subunit

**Table T5.** Volcanic units, contacts, thicknesses, and emplacement styles, Hole U1558D. See the Expedition 390/393 methods chapter (Coggon et al., 2024b) for explanation of expanded and minimum depths and thicknesses. Plag = plagioclase, ol = olivine, cpx = clinopyroxene. (Continued on next page.) [Download table in CSV format.](#)

Sequence	Unit	Upper contact					Unit thickness (m)			Rock type	Flow interior groundmass	Phenocrysts	Evidence for emplacement style	Nature of upper contact
		Core, section, interval (cm)	Curated depth (mbsf)	Curated depth (msb)	Expanded depth DSF (m)	Expanded hole depth (msb)	CSF-A	Minimum	Expanded					
S	IIC	393-U1558D-2R-1, 0	150.38	—	0	—	7.78	—	—	Nannofossil chalk with clay	—	—	—	—
A	1A	4R-1, 5	166.55	0.00	166.80	0.00	0.52	0.47	1.5	Highly plag-ol-cpx-phyric basalt sheet flow	Crypto-crystalline	Plag, Ol, Cpx	Continuous texture over 60 cm bounded by planar chilled margins	Not clearly recovered, uppermost basalt piece has chilled margin intruded by chalky sediment
	1B	4R-1, 57	167.07	0.52	168.29	1.49	0.08	0.08	0.25	Intervolcanic indurated calcareous sediment	—	—	—	Sharp contact; altered volcanic material adhering to sediment
	1C	4R-1, 65	167.15	0.60	168.55	1.75	6.57	2.7	5.3	Highly plag-ol-cpx-phyric basalt pillow lavas	Crypto-crystalline	Plag, Ol, Cpx	Curved glassy margins; continuously recovered pillow lavas	Sharp contact; altered volcanic material adhering to sediment
	1D	5R-2, 98	173.72	7.17	173.86	7.06	2.69	2.1	2.6	Variably plag-ol-cpx-phyric basalt pillow lavas	Crypto-crystalline	Plag, Ol, Cpx	Curved glassy margins; interpillow sediment	Glassy margin at flow top; not continuously recovered
	1E	6R-1, 21	176.41	9.86	176.46	9.66	10.94	8.5	11.9	Moderately to highly plag-ol-cpx-phyric basalt pillow lavas	Crypto-crystalline	Plag, Ol, Cpx	Curved pillow margins, complete pillows, pillow triple junctions	Glassy margin at flow top; not continuously recovered
	1F	7R-2, 40	187.35	20.80	188.33	21.53	0.47	0.07	0.09	Breccia of basalt and glass in indurated calcareous sediment	—	—	Conformable sedimentary hyaloclastite layers in indurated carbonate sediment matrix	Sharp, glassy margin against breccia
	1G	7R-2, 47	187.82	21.26	188.42	21.62	2.25	2.1	3.0	Moderately–highly plag-ol-cpx-phyric basalt pillow lavas	Micro-crystalline	Plag, Ol, Cpx	Curved pillow margins, complete pillows, pillow triple junctions	Sharp, glassy margin in contact with breccia
	2A	7R-4, 24	190.07	23.52	191.38	24.58	20.03	15.9	18.7	Moderately plag-ol-cpx-phyric large basalt pillow lavas	Micro-crystalline	Plag, Ol, Cpx	Subplanar, curved glassy margins; continuous flows 0.5–1.3 m thick	Continuously recovered, doubly chilled margin without intervening sediment
	2B	10R-1, 0	210.10	43.55	210.10	43.30	24.54	20.7	24.6	Moderately plag-ol-cpx-phyric pillow lavas	Crypto-crystalline	Plag, Ol, Cpx	Curved pillow margins, complete pillows, pillow triple junctions	No contact recovered
B	3	13R-1, 24	234.64	68.09	234.73	67.93	0.73	0.75	1.0	Breccia of basalt and glass in indurated calcareous sediment	—	—	Rotated pillow lava clasts and layers of hyaloclastite in sediment matrix	No contact recovered
	4A	13R-1, 97	235.37	68.82	235.75	68.95	8.73	6.6	8.4	Sparsely plag-ol-phyric pillow basalt with interpillow sediments	Crypto-crystalline	Plag, Ol	Curved pillow margins, complete pillows, pillow triple junctions	Breccia sharply overlies glassy pillow margin
	4B	15R-1, 0	244.10	77.55	244.10	77.30	4.27	3.4	7.2	Sparsely plag-ol-phyric basalt pillow lavas with common interpillow breccias	Crypto-crystalline	Plag, Ol	Curved pillow margins, complete pillow lavas	Gradational transition from common to uncommon interpillow sediment
	4C	15R-4, 0	248.37	81.82	251.28	84.48	39.43	35.0	36.5	Aphyric to sparsely plag-ol-phyric basalt pillow lavas	Crypto-crystalline – micro-crystalline	Plag, Ol	Curved pillow margins, complete pillow lavas	Gradational transition to interpillow sediment and breccia-free lavas
	5A	23R-1, 0	287.80	121.25	287.80	121.00	5.85	2.5	8.7	Variably plag-ol-phyric basalt sheet and pillow lavas	Crypto-crystalline – micro-crystalline	Plag, Ol	Planar chilled margins, 1–2 m intervals without glass	Not clearly recovered; possibly gradational over Section 22R-3
	5B	24R-1, 105	293.65	127.10	296.47	129.67	18.35	14.7	15.5	Variably plag-ol-phyric sheet and variolitic pillow lava flows	Micro-crystalline	Plag, Ol	Uncommon chilled margins; long intervals (>0.7 m) continuous grain size without glass	First broken piece of variolitic lava at the upper contact

IIC; see [Sedimentology](#)] or indurated calcareous sediment) as well as basalt were recovered in three of the four holes at Site U1558 (Holes U1558A, U1558D, and U1558F; Figure [F18](#)).

In interval 390C-U1558A-18X-CC, 26–30 cm, a complete, sharp, and apparently conformable sediment/volcanic basement contact was recovered by XCB coring (Figure [F18](#)). Here, the uppermost lava flow is capped by a glassy pillow margin that is altered and incipiently brecciated, in direct contact with the overlying calcareous sediment. The bottom 1–2 cm of sediment is finely laminated and speckled with fragments of variably altered glass. Veins of white sediment cut beneath and above the glassy margin, and a 5 mm thick vein of similarly white sediment cuts the pale brown background sediment 10 cm up from the contact. There is no visual evidence for metalliferous sediment, and the overlying nannofossil chalk with clay reaches a stable background light brownish pink (7.5Y 7/3) that is seen in the other holes after this first few centimeters (Figure [F18B](#)). If this contact had not been continuously recovered, the fragile, unconsolidated glassy margin and sediment with glass fragments probably would have been washed away during drilling, supporting our interpretation of a near-continuous recovery of the sediment/basement interface in Hole U1558A.

The interface was not continuously recovered in Hole U1558D, but unlike the other holes, a 3 cm long piece of indurated calcareous sediment was recovered above the basalt (interval 393-U1558D-4R-1, 0–5 cm). The lack of similar indurated sediment in the better recovered Hole U1558A interface suggests that lithification of the sediments at the interface is laterally discontinuous. Bright white chalky veins cut above and below the upper glassy margin of the shallowest piece of volcanic basement in Hole U1558D (interval 4R-1, 5–12 cm).

Section 393-U1558F-24X-CC recovered sediment and volcanic basement (Figure [F18](#)), but evidence suggests that the interface was not continuously recovered. First, the shallowest piece of volcanic rock is a broken piece without any oxidation or alteration around its edges (Sample 24X-CC, 15–16 cm). This suggests that the piece was freshly broken during drilling because the edges of broken pillow clasts generally display some oxidation. Second, none of the nannofossil chalk is

**Table T5 (continued).**

Sequence	Unit	Upper contact					Unit thickness (m)			Rock type	Flow interior groundmass	Phenocrysts	Evidence for emplacement style	Nature of upper contact
		Core, section, interval (cm)	Curated depth (mbsf)	Curated depth (msb)	Expanded depth DSF (m)	Expanded hole depth (msb)	CSF-A	Minimum	Expanded					
B	5C	28R-1, 0	312.00	145.45	312.00	145.20	45.10	40.5	45.3	Sparsely–moderately plagioclase-phyric variolitic basalt pillow lavas	Crypto-crystalline –micro-crystalline	Plag, Ol	Common glass, curved glassy pillow margins	Not recovered, broken pieces of strongly variolitic pillow lava
	5D	37R-2, 0	357.10	190.55	357.32	190.52	4.03	2.9	4.5	Ol-plagioclase-phyric fine- to medium-grained massive flow	Fine- to medium-grained	Ol, Plag	Gradational textural changes over 3 m with fine- to medium-grained interior	Not completely recovered; top of flow is clearly chilled
	5E	38R-1, 63	361.13	194.58	361.87	195.07	>9.07	>3.9	>8.33	Sparsely–moderately plagioclase-phyric variolitic basalt pillow lavas	Crypto-crystalline –micro-crystalline	Plag, Ol	Common glass, curved pillow margins, interpillow hyaloclastite	Not recovered, first broken variolitic microcrystalline piece
	EOH	39R-2-A	370.20	203.13	—	—	—	—	—	—	—	—	—	—

**Table T6.** Sediment/basement interface depths and descriptions, Site U1558. [Download table in CSV format.](#)

Sediment/basement interface core, section, interval (cm)	Shallowest volcanic piece depth CSF-A (m)	Deepest sediment at interface depth CSF-A (m)	Nature and recovery of sediment/basement interface
390C-U1558A-18X-CC, 27	158.44	161.65	Conformable contact recovered with a fragile altered glassy margin overlaid by laminated nannofossil chalk with suspended altered glassy fragments
393-U1558D-3R-CC, 5	166.55	167.07	Contact poorly recovered, but sediment piece directly overlying volcanic basement is 3 cm thick relatively indurated calcareous sediment
393-U1558F-24X-CC, 15	175.29	175.29	Basalt at interface broken by drilling; true interface not recovered

in contact or adheres to the underlying glassy margin, which itself is freshly broken at its top (Sample 24X-CC, 17 cm). Intravolcanic calcareous sediment within a few meters of the main interface is distinctly more lithified and brighter white than the overlying Subunit IIC light brownish pink nannofossil chalk with clay (e.g., intervals 390C-U1558A-19X-1, 16–18 cm, and 393-U1558D-4R-1, 57–66 cm).

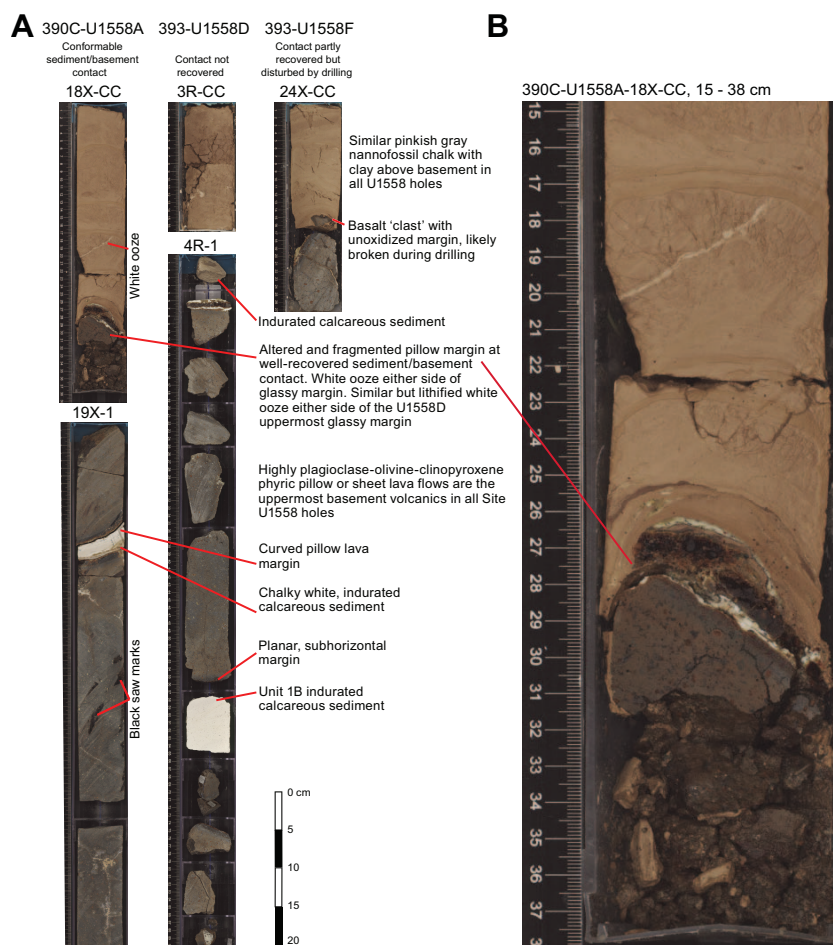
### 5.1.2. Division of volcanic sequences

The volcanic basement in Hole U1558D was divided into two eruptive sequences. This division was made principally based on the presence of distinctive green clinopyroxene phenocrysts in Sequence A, described below, and the presence of an intervening ~1 m thick sedimentary breccia at 234.64 mbsf (69.09 msb), interpreted to have accumulated during a hiatus in volcanism and described in detail as Unit 3 below.

### 5.1.3. Sequence A

Lithology: highly plagioclase-olivine-green clinopyroxene-phyric pillow lavas

Volcanic Sequence A consists of Volcanic Units 1 and 2 that are similar aside from subtle variations in phenocryst abundance, pillow size, and proportion of interpillow sediment. The units in Sequence A are characterized by mostly pillowed lavas with variable pillow thicknesses (20–130 cm) and a moderate to high abundance of plagioclase and olivine phenocrysts together with sparse but distinctive dark olive-green clinopyroxene phenocrysts. Throughout Hole U1558D, including Sequence A, olivine phenocrysts were replaced by either a mixture of clay and Fe oxyhydroxides, pale greenish yellow clay, or calcite (Figure F19A). These pseudomorphic replacements are gener-



**Figure F18.** A. Sediment/volcanic basement interface, Holes U1558A, U1558D, and U1558F. B. Close-up of well-recovered contact, Hole U1558A.



ally recognizable by their distinctive mineralogy and equant, commonly hexagonal habit, and all references to olivine in the following are based on interpretation of such pseudomorphs.

### 5.1.3.1. Subunit 1A

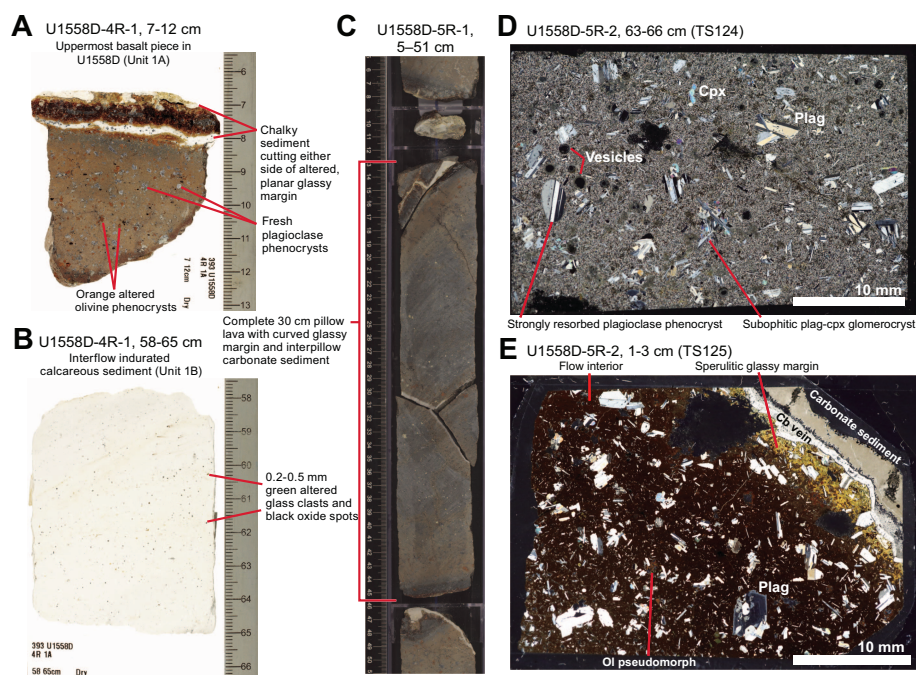
Lithology: highly plagioclase-olivine-clinopyroxene-phyric basalt sheet flow

Subunit 1A consists of a cryptocrystalline basalt sheet flow that is highly plagioclase-olivine-phyric with extremely sparse (<0.5%) but distinctive dark olive-green (5GY 3/4) tabular clinopyroxene phenocrysts. The flow has an expanded thickness of 1.64 m, and its upper contact is the sediment/basement interface at 166.8 mbsf (Table T5). The Subunit 1A flow is interpreted to be a sheet flow because of its thin, planar, subhorizontal glassy margins (Figure F19A).

### 5.1.3.2. Subunit 1B

Lithology: intervolcanic indurated calcareous sediment

Subunit 1B is a 7 cm thick piece of indurated calcareous sediment with Mn oxide spots (Figure F19B; Table T5). The lower edge of the Subunit 1B sediment piece has altered volcanic material adhering to it, showing a sharp lower contact, but the upper margin has been ground during drilling. Micropaleontological analysis of a thin section from Sample 393-U1558D-4R-1, 62–65 cm, revealed the presence of planktic foraminifera tests and their fragments. These foraminifera belong to the common Eocene genera *Subbotina*, *Acarinina*, and *Globigerinatheka* that are consistent with the crustal age of 49.2 Ma. Unfortunately, specimen identification to the species level was not possible, precluding a more refined age estimate or biozone assignment. Analysis of the smear slide from the same sample revealed that Eocene nannofossil taxa were also present, but the assemblage was scarce and poorly preserved, without marker species that would permit precise age determination.



**Figure F19.** Volcanic Unit 1 showing uppermost highly plagioclase (Plag)-olivine (Ol)-clinopyroxene (Cpx) phyric basalt sheet and pillow lava flows, Hole U1558D. A. Shallowest piece of volcanic basement recovered with white calcareous sediment cutting either side of a glassy margin. B. Interlava indurated calcareous sediment interval near sediment/basement interface. C. Completely recovered 30 cm thick pillow lava with curved upper glassy margin and lithified sediment veins in fractures and interpillow space. D. Typical highly phyric basalt (Subunit 1D) with microcrystalline groundmass and vesicles but no fresh olivine (XPL). One ovoid plagioclase crystal shows evidence for resorption. E. Altered glassy pillow lava margin with highly plagioclase-olivine-clinopyroxene phyric interior where olivine is totally altered to clay and Fe oxyhydroxide and groundmass appears to be altered to dark brown clay. Cb = carbonate.



### 5.1.3.3. Subunit 1C

Lithology: highly plagioclase-olivine-clinopyroxene-phyric basalt pillow lavas

Subunit 1C consists of highly plagioclase-olivine-pyroxene-phyric basalt pillow lavas with an expanded thickness of 5.31 m (Figure F19C–F19E; Table T5). The sharp upper contact to the Subunit 1B sediment is partially preserved by the altered volcanic material adhering to its lower surface (Section 393-U1558D-4R-1, 65 cm).

Subunit 1C is lithologically like Subunit 1A, but Subunit 1C is clearly emplaced as pillow lavas (Figure F19C). Two continuously recovered lava pillows have apparent thicknesses of 35 and 60 cm. Indurated calcareous sediment filling interpillow spaces and fractures is common in this subunit (e.g., Figure F19C). A typical highly phyric Subunit 1C chilled glassy margin with adhering interpillow sediment is shown in thin section (Figure F19E).

### 5.1.3.4. Subunit 1D

Lithology: variably plagioclase-olivine-clinopyroxene-phyric basalt pillow lavas

Subunit 1D consists of highly plagioclase-olivine-pyroxene-phyric basalt pillow lavas with some sparsely phyric intervals or flows with a total expanded thickness of 2.6 m (Table T5). Lithologically, Subunit 1D is like Subunits 1A and 1C except for the occurrence of distinct sparsely phyric and even aphyric individual flows in Subunit 1D.

The thin section of a flow interior in Figure F19D shows a typical texture for the highly phyric portions of Subunit 1D. The thin section is representative of other highly phyric Unit 1 basalts. Plagioclase is the dominant phenocryst and, although mostly euhedral, rare examples of clearly resorbed phenocrysts with rounded corners and ovoid shapes were observed in thin section (Figure F19D). Thin sections also reveal the more common presence of clinopyroxene microphenocrysts (<0.5 mm) and glomerocryst components in Unit 1 basalts than apparent from macroscopic observations.

### 5.1.3.5. Subunit 1E

Lithology: moderately to highly plagioclase-olivine-clinopyroxene-phyric basalt pillow lavas

Subunit 1E is the thickest subunit in Unit 1 with an expanded thickness of 11.87 m and consists of well-recovered, moderately plagioclase-olivine-clinopyroxene-phyric basalt pillow lavas with some highly phyric intervals and common interpillow sediment infills (Table T5). The upper contact of Subunit 1E is not sharp or obvious because the volcanic lithology is broadly similar throughout Unit 1 but was placed at a subhorizontal glassy margin (Section 393-U1558D-6R-1, 21 cm). Interpillow carbonate sediments were well recovered throughout Subunit 1E (Figure F20A–F20C). These interpillow sediments exhibit repetitive internal layering of green altered hyaloclastite, commonly packed into the bottom of the interpillow space, with a variably pink to pinkish gray (5Y 8/3 to 7.5Y 7/2) indurated calcareous sediment matrix that increases in proportion upward through the interpillow interstices (Figure F20). These pink sediments commonly contain additional discrete layers of hyaloclastite that are abruptly terminated, and the overlying interpillow space is filled with porcelaneous carbonate material with black (Mn?) oxide layers and dendrites that may be a late sediment or precipitate (Figure F20B, F20C).

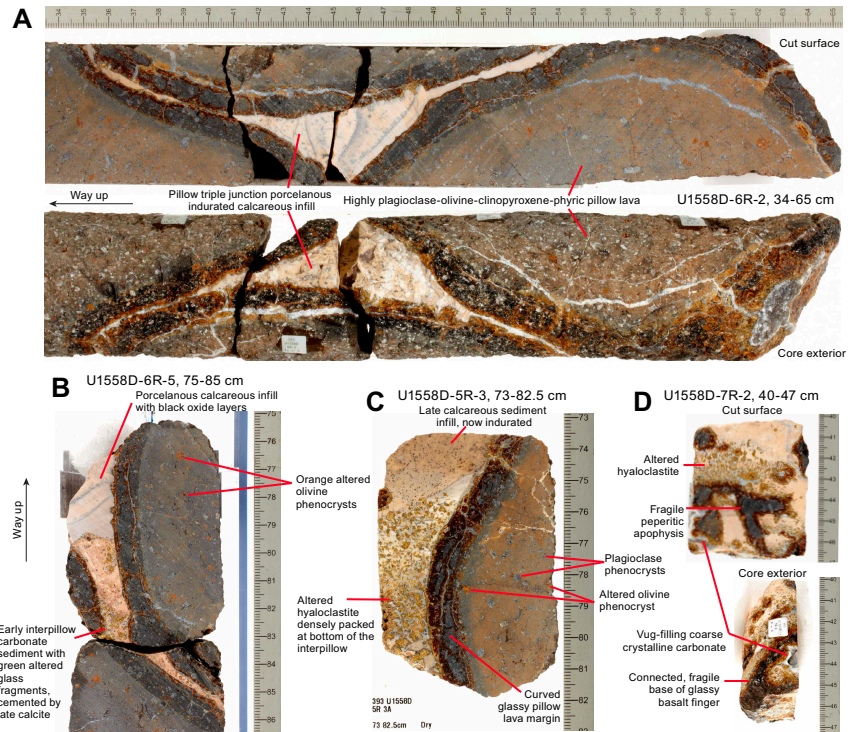
Figure F21 shows a set of typical macro- to microscopic textures for Subunits 1E and 1G, including a green clinopyroxene phenocryst in Subunit 1G that is like other examples in Subunit 1E and the Sequence A basalts, intergrown with plagioclase and altered olivine (Figure F21A). The Subunit 1E glassy pillow margin in Figure F21B contains phenocrysts in both the cryptocrystalline flow interior and glassy selvage. Similar to the macroscopic observations (Figure F20B, F20C), a folded glassy margin filled with altered hyaloclastite overlaid by calcareous sediment is exhibited in Figure F21B.

The pillow flow interiors of Subunit 1E are cryptocrystalline to microcrystalline with randomly oriented plagioclase laths (Figure F21C). The macroscopic observations of millimetric plagioclase, olivine, and clinopyroxene phenocrysts are also evident in thin section, as is the presence of inter-

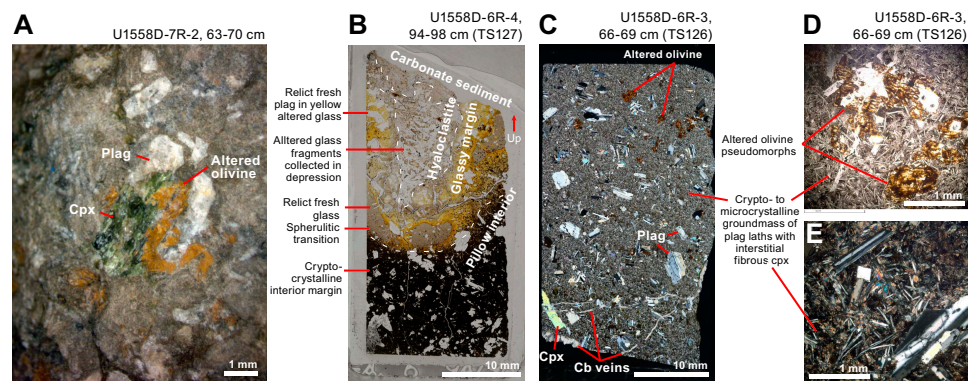
stitial plumose clinopyroxene in the groundmass and the alteration of olivine to either clays and Fe oxyhydroxides or calcite throughout (Figure F21C, F21D).

### 5.1.3.6. Subunit 1F

Lithology: breccia of basalt and glass in indurated calcareous sediment



**Figure F20.** Pillow lava margins and interpillow sediments from near sediment interface Volcanic Unit 1, Hole U1558D. A. Outer core and cut surface images of complete pillow triple junction with 1 cm thick glassy margins and porcelanous calcareous sediment interpillow fill (Subunit 1E). Outer core surface shows highly phyric character of typical Unit 1 lavas. Late carbonate veins cut pillow interior and margin. B. Upright interpillow space sequentially filled by glass fragments that are now altered to green clay in pink indurated calcareous sediment matrix overlaid by paler porcelaneous carbonate with bands of wispy black (Mn?) oxide with dendritic growths (Subunit 1E). C. Similar relationship to B with hyaloclastite densely packed into bottom of sediment-filled interpillow space (Subunit 1E). D. Cut and exterior core surfaces of sediment and hyaloclastite breccia including fragile peperitic injection connected to basalt at base of piece (Subunit 1F).



**Figure F21.** Altered olivine and glass, Hole U1558D. A. Possibly Cr-rich clinopyroxene (Cpx)-(altered) olivine-plagioclase (Plag) microgabbroic glomerocryst (Subunit 1F). B. Partially altered glassy flow margin with hyaloclastite and indurated calcareous sediment infill (Subunit 1E). C–E. Typical igneous texture of Subunit 1E basalts: (C) abundant millimetric plagioclase phenocrysts and lesser amounts of olivine and clinopyroxene phenocrysts; (D) clay and calcite pseudomorphs after olivine; (E) plagioclase phenocrysts and microcrystalline groundmass laths with interstitial plumose clinopyroxene. Cb = carbonate.

Subunit 1F is a ~9 cm thick sedimentary breccia with variably altered glassy clasts and a peperitic injection connected to the wall-rock basalt (interval 393-U1558D-7R-2, 40–47 cm; Figure F20D; Table T5). This thin breccia unit was differentiated to allow any potential differences in lava composition to be examined across what may represent a short hiatus in volcanism. There are two types of breccia clasts: centimeter-sized subangular fresh glass with oxidized rims and millimeter-sized glassy fragments fully altered to a pale olive-green clay. The millimeter-sized fragments form layers that are laterally discontinuous, even at the core scale, one of which coarsens upward (Figure F20D). These clasts are supported by an indurated calcareous sediment matrix. A bifurcated glassy finger connects to the basalt at the base of the piece (Figure F20D). Given how fragile this finger would have been unsupported, it is interpreted to be a peperitic apophysis, injected prior to matrix induration.

#### 5.1.3.7. Subunit 1G

Lithology: moderately to highly plagioclase-olivine-clinopyroxene-phyric basalt pillow lavas

Subunit 1G consists of moderately plagioclase-olivine-clinopyroxene-phyric basalt pillow lavas with some highly phyric intervals that are lithologically like Subunit 1E but with less interpillow sediment. The subunit has an expanded thickness of 3.0 m (Table T5).

#### 5.1.3.8. Subunit 2A

Lithology: moderately plagioclase-olivine-clinopyroxene-phyric large pillow lavas

Subunit 2A consists of moderately plagioclase-olivine-clinopyroxene-phyric basalt pillow lavas with a microcrystalline groundmass and distinctly high individual flow thicknesses, mostly between 50 and 130 cm. The upper contact of Subunit 2A is a doubly chilled margin at Section 393-U1558D-7R-4, 24 cm, and the unit has an expanded thickness of 18.72 m (Table T5).

Subunit 2A is differentiated from Unit 1 by its large pillow sizes and associated coarser, microcrystalline flow interior groundmass and less common glassy margins (Figure F22A). The phenocryst assemblage and character of Unit 2 is similar to Unit 1, including the presence of sparse green clinopyroxene phenocrysts, although on average phenocrysts are less abundant in Unit 2 (Figure F22D). A number of lava pillows were recovered in Subunit 2A, with most pillows having apparent thicknesses of >50 cm and up to 130 cm, much larger than the typical 20–40 cm thickness of pillows in the other units. Given common basal margin dips of ~30°, these apparent pillow thicknesses should be slightly greater than their true thicknesses.

#### 5.1.3.9. Subunit 2B

Lithology: moderately plagioclase-olivine-clinopyroxene-phyric pillow lavas

Subunit 2B consists of moderately to highly plagioclase-olivine-clinopyroxene-phyric basalt pillow lavas with common glassy margins (Figure F22B). The upper contact of Subunit 2B is likely gradational given the similar lithology in Subunit 2A, but it was not clearly recovered. It is defined to be located at Section 393-U1558D-10R-1, 0 cm, giving Subunit 2B an expanded thickness of 24.6 m (Table T5).

The basalt of Subunit 2B is very similar to Subunit 2A, with microcrystalline groundmass and moderately abundant plagioclase, olivine, and clinopyroxene phenocrysts; however, the pillows are of typical or relatively small size (Figure F22B). Phenocrysts include the extremely sparse but distinctive dark olive-green clinopyroxene present throughout Sequence A (Figure F22D). As observed in Unit 1, clinopyroxene phenocrysts tend to have rounded corners or otherwise resorbed rims and commonly occur as glomerocrysts with plagioclase ± olivine (Figure F22E–F22G). Olivine phenocrysts in Unit 2 are generally totally altered to clays both with and without Fe oxyhydroxide, and only rare fresh relict olivine is observable in thin section (Figure F22F).

#### 5.1.4. Sequence B

Lithology: plagioclase-olivine-phyric basalt pillow, sheet, and massive lava flows capped by sedimentary breccia



Volcanic Sequence B consists of sedimentary breccia Unit 3 and underlying Volcanic Units 4 and 5. These volcanic units have plagioclase and olivine phenocrysts but distinctly lack the green clinopyroxene phenocrysts that are present throughout Sequence A. Phenocryst proportions and habits, groundmass grain size, and emplacement style all vary significantly between the Sequence B volcanic units.

#### 5.1.4.1. Unit 3

Lithology: sequence boundary breccia of basalt and glass in indurated calcareous sediment

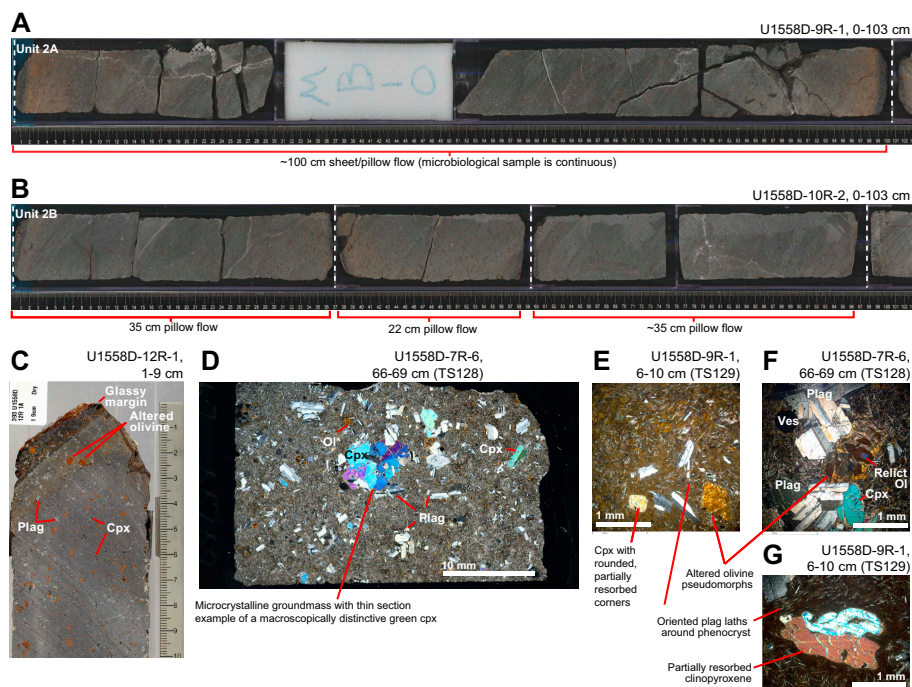
Unit 3 is sedimentary breccia consisting of broken pillow and glass clasts supported in a matrix of layered indurated calcareous sediment (Figure F23A). The upper contact of the Unit 3 breccia was not recovered, but the breccia has a minimum thickness of 75 cm and an expanded thickness of 1 m. At the average sedimentation rate for the Site U1558 basal sediments of 1 cm/ky (see [Age model and mass accumulation rates](#)), the ~30 cm true thickness of carbonate sediment in Unit 3 sedimentary breccia would represent a potential local volcanic hiatus on the order of 30,000 y.

In the Unit 3 breccia, repeating layers show episodic deposition of hyaloclastite layers during this hiatus, but whether that is due to eruptive, current-driven, or downslope transport activity is unclear. The pillow basalt clasts are angular pieces of sparsely phryic pillow basalt from the underlying Unit 4, with some fragile glassy margins protruding from the clasts. Such features indicate that these clasts have not been transported far or at all from seafloor outcrops of the underlying unit.

#### 5.1.4.2. Subunit 4A

Lithology: sparsely plagioclase-olivine-phryic basalt pillow lavas with interpillow sediments

Subunit 4A consists of sparsely plagioclase-olivine-phryic cryptocrystalline pillow basalts with common interpillow breccias and sediment. The upper contact of Unit 4 with the Unit 3 sedimen-



**Figure F22.** Volcanic Unit 2, Hole U1558D. A. Typical large, thick pillow or sheet lava flow (Subunit 2A); note generous continuous microbiological (MBO) sample. B. Three completely recovered small pillows typical of Subunit 2B. C. Highly plagioclase (Plag)-olivine (Ol)-clinopyroxene (Cpx)-phryic basalt glassy pillow margin (Subunit 2B). D. Typical Subunit 2B groundmass, plagioclase and olivine phenocrysts, and exceptionally large clinopyroxene phenocryst. E. Oriented plagioclase laths around phenocrysts. F. Millimetric plagioclase-olivine-clinopyroxene glomerocryst. G. Strongly resorbed clinopyroxene. Ves = vesicle.

tary breccia was continuously recovered at Section 393-U1558D-13R-1, 96 cm, giving Subunit 4A an expanded thickness of 8.4 m (Table T5).

The change from Unit 2 to Subunit 4A basalts is the most significant textural transition in the hole, with Subunit 4A having mostly cryptocrystalline groundmass, sparse phenocryst abundance, and no green clinopyroxene phenocrysts (Figures F23A, F24A, F24C, F25A, F25B). These changes are accompanied by a step upward in average Cr concentrations, indicating Unit 4 is potentially less evolved than the overlying units (see [High-resolution chemostratigraphy](#) below). Figure F25A shows the distinctly finer grained, cryptocrystalline groundmass and the sparsely plagioclase-olivine phyric character of Subunit 4A that is also typical of Subunit 4B.

In addition to these textural and chemical changes, Subunit 4A is characterized by abundant, well-recovered interpillow carbonate sediments and breccias. The clasts in these interpillow breccias generally consist of variably altered glass that has spalled from pillow margins less than a few centimeters away, as shown by the closely fitting curvature of many of these clasts and the adjacent pillow margin (e.g., Figure F24A). Together with the sedimentary breccia in Unit 3 and the change in lava character, these interpillow sediments are interpreted to have infiltrated into the shallow basement subsurface during the volcanic hiatus over which Subunit 4A was exposed at the seafloor. This parallels the younger, near-interface sediments filling the pillow interstices in Unit 1.

#### 5.1.4.3. Subunit 4B

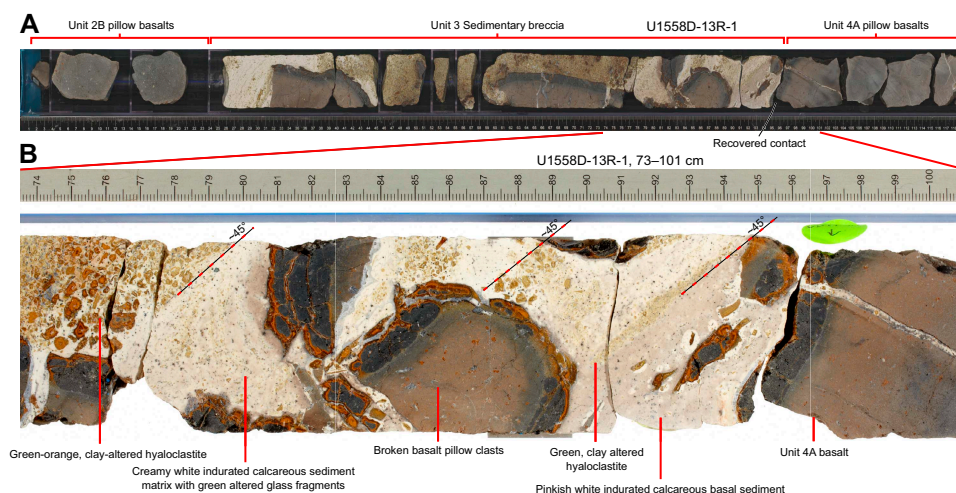
Lithology: sparsely plagioclase-olivine-phyric basalt pillow lavas with interpillow breccias

Subunit 4B is a sparsely plagioclase-olivine-phyric, mostly cryptocrystalline basalt pillow lava unit with jigsaw-fit and interpillow breccias (Figure F24B, F24D), with an expanded thickness of 7.2 m. Subunit 4B is differentiated from Subunit 4a by the less common presence of interpillow sediments and breccias, interpreted as reflecting increasing depth beneath the Unit 3 paleoseafloor horizon. Intense Fe oxyhydroxide alteration of pillow interiors in close proximity to thick (1.5–2 cm) glassy margins are additionally distinctive of Subunit 4B (e.g., Figures F24D, F25C, F25D).

#### 5.1.4.4. Subunit 4C

Lithology: sparsely plagioclase-olivine-phyric to aphyric basalt pillow lavas

Subunit 4C comprises sparsely plagioclase-olivine phyric to aphyric basalt pillow lavas with a distinctive plagioclase lath-dominated microcrystalline groundmass. Recovered cores from this subunit lack the common breccia and interpillow sediment that characterize Subunits 4A and 4B

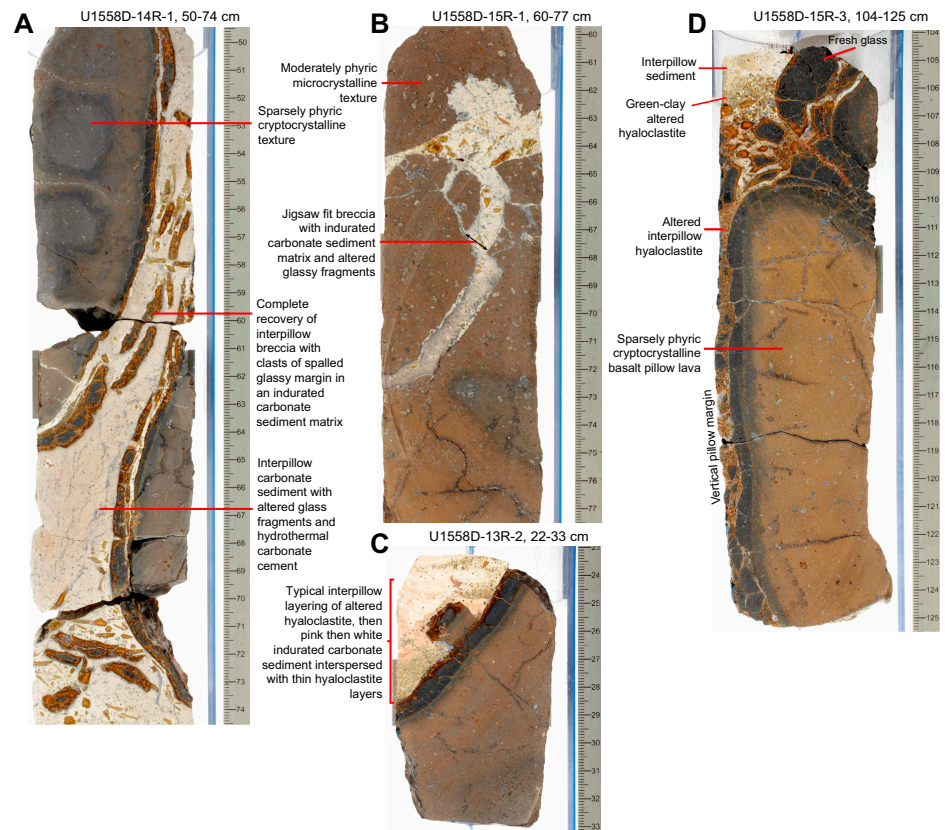


**Figure F23.** Sedimentary breccia at volcanic Sequence A/B boundary in Unit 3, Hole U1558D. A. Entire Unit 3 with rotated clasts of broken Subunit 4A basalts and layers of hyaloclastite in matrix of indurated calcareous sediment. B. Close up of dipping sedimentary layering, different breccia components, and well-recovered lower contact with Subunit 4A.

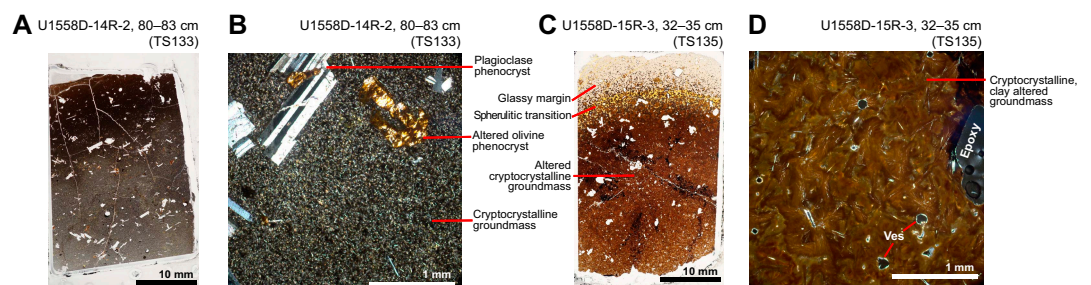


(Figure F26). Subunit 4C has an unrecovered upper contact with Subunit 4B located approximately at Section 393-U1558D-15R-4, 0 cm, and an expanded thickness of 36.5 m, making it the second thickest unit in Hole U1558D.

Common thick glassy margins and relatively small pillow lavas between 15 and 40 cm thick characterize the Subunit 4C lavas. Phenocryst abundance varies from flow to flow but is uniformly low and dominated by 2–4 vol% plagioclase with lesser altered olivine (Figure F26B–F26F). These phenocrysts are set in a microcrystalline groundmass of plagioclase laths with interstitial clinopyroxene that commonly exhibits a plumose texture (Figure F26E, F26F).



**Figure F24.** Exceptionally well recovered interpillow sediments and breccias that characterize Subunits 4A and 4B, Hole U1558D. A. Partly complete pillow triple junction and interpillow sediment breccia with spalled off glassy margin. B. Jigsaw-fit pillow breccia with matrix of indurated calcareous sediment and altered glass fragments. C. Interpillow sediment with typical layering of densely packed hyaloclastite and pink calcareous sediment that becomes paler toward top of oriented piece. D. Long vertical, thick glassy pillow margin and interpillow breccia.



**Figure F25.** Volcanic Subunits 4A and 4B, Hole U1558D. (A) Whole thin section image and (B) photomicrograph near chilled margin showing plagioclase-olivine phyric cryptocrystalline texture. (C) Whole thin section image and (D) photomicrograph of fresh glassy margin, yellow clay-altered spherulitic transition, and strongly altered cryptocrystalline pillow interior. Ves = vesicle.

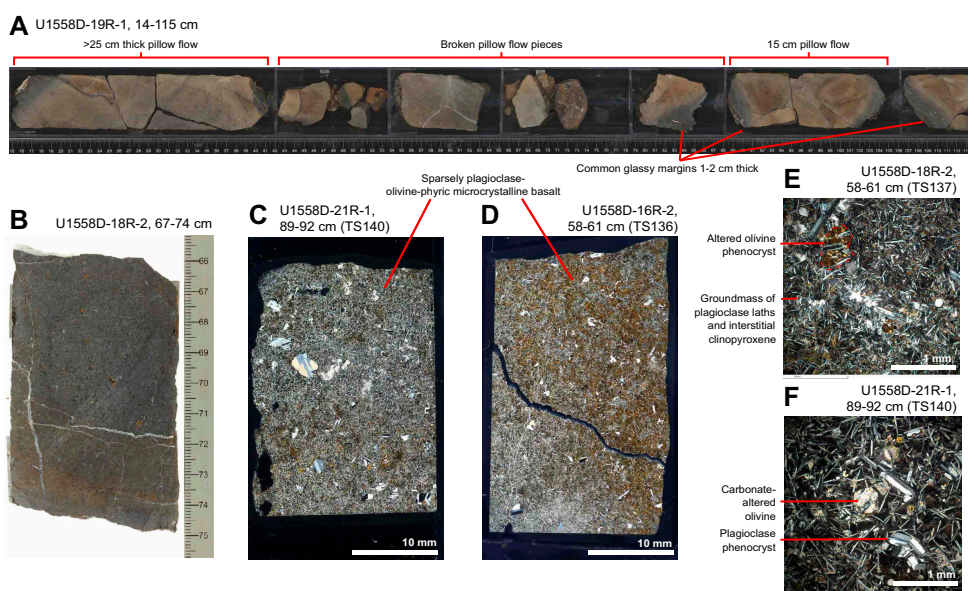
### 5.1.4.5. Subunit 5A

Lithology: variably plagioclase-olivine-phyric basalt sheet and pillow lava flows

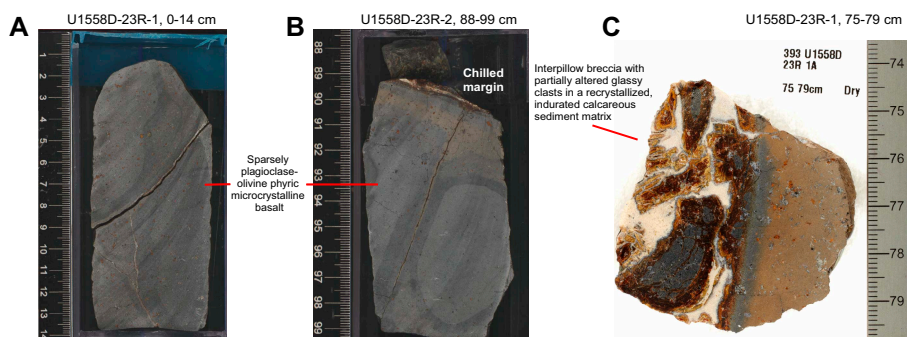
Subunit 5A consists of sparsely to moderately plagioclase-olivine-phyric basalt with a distinctive population of fine (0.2–1 mm) lath-shaped plagioclase phenocrysts in addition to the subequant plagioclase phenocrysts present in Unit 4. The upper contact of Subunit 5A was not clearly recovered but is well defined by pXRF analyses (see [High-resolution chemostratigraphy](#)) and was located at Section 393-U1558D-23R-1, 0 cm, giving an expanded subunit thickness of 8.7 m. Rare planar chilled margins and some long, continuous intervals ( $\leq 1$  m) of microcrystalline lava without glass supports the interpretation of emplacement as sheet flows as well as pillow lavas (Figure [F27A](#), [F27B](#)). One interpillow breccia of angular glassy clasts in an indurated calcareous sediment matrix was recovered from Subunit 5A in interval 393-U1558D-23R-1, 77–87 cm (Figure [F27C](#)).

### 5.1.4.6. Subunit 5B

Lithology: variably plagioclase-olivine-phyric sheet and variolitic pillow lava flows



**Figure F26.** Volcanic Subunit 4C (~37 m thick), Hole U1558D. A. Typical sparsely phyric, small pillow lavas (15–25 cm thick). B. Sparsely phyric microcrystalline pillow interior cut by white veins. C, D. Typical sparsely plagioclase (-olivine) phyric basalt with microcrystalline groundmass textures dominated by modally abundant plagioclase laths 0.1–0.2 mm in length. E. Altered hexagonal olivine phenocryst set in microcrystalline groundmass of plagioclase and interstitial, partly altered, plumose clinopyroxene. F. Calcite pseudomorph after hexagonal olivine microlite and plagioclase set in microcrystalline plagioclase-lath-dominated groundmass.



**Figure F27.** Volcanic Subunit 5A, Hole U1558D. A. Sparsely plagioclase-olivine-phyric flow interior. B. Chilled margin. C. Interpillow breccia of glassy margin clasts and indurated calcareous sediment matrix.



Subunit 5B is generally similar in lithology and emplacement style to Subunit 5A but is differentiated by the presence of pillow flows with mottled or variolitic interiors interlayered with nonvariolitic sheet flows (Figure F28A–F28C). The upper contact of Subunit 5B was not recovered but was located at the shallowest appearance of variolitic lava at Section 393-U1558D-24R-1, 105 cm, giving an expanded subunit thickness of 15.5 m (Table T5).

The varioles and related mottled textures in Subunit 5B are defined by a reduced abundance of plagioclase laths that most commonly surround phenocrysts or glomerocrysts (Figure F28E, F28F). The groundmass inside these varioles is also more altered, appearing browner than the plumose clinopyroxene groundmass outside the varioles.

#### 5.1.4.7. Subunit 5C

Lithology: sparsely to moderately plagioclase-olivine-phyric variolitic basalt pillow lavas

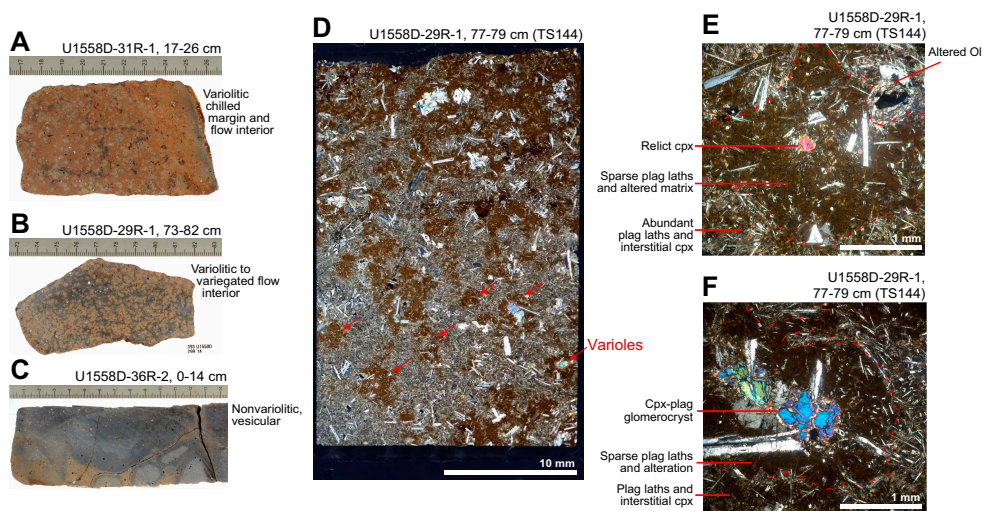
Subunit 5C has a similar phenocryst assemblage and groundmass texture to Subunits 5A and 5B but is dominated by pillow lavas with common glassy, curved margins and a pronounced variolitic flow interior texture. The upper contact of Subunit 5C was not clearly recovered and occurs over discontinuous pieces of broken lava but was located at the onset of more common glassy margins at Section 393-U1558D-28R-1, 0 cm, giving an expanded subunit thickness of 45.3 m and making it the thickest volcanic subunit in Hole U1558D.

The pronounced variolitic texture of Subunit 5C is accentuated by alteration in Subunit 5C (Figure F28A, F28B; see **Alteration petrology**). This texture is presumably quench crystallization related because it is only well developed in pillow lavas and is most pronounced in the interior domains of pillow margins. This could be related to the exceptionally thick glassy margins in Subunit 5C, which commonly exceed 2 cm and transition over <1 cm into altered variolitic pillow interior (Figure F28A).

#### 5.1.4.8. Subunit 5D

Lithology: olivine-plagioclase-phyric fine- to medium-grained basalt massive flow

Subunit 5D is the only clearly defined massive flow in Hole U1558D, with a minimum thickness of 2.9 m and an expanded thickness of 4.6 m. The Subunit 5D upper contact of the massive flow is at Section 393-U1558D-37R-2, 0 cm (Table T5).



**Figure F28.** Volcanic Unit 5, Hole U1558D. A. Strongly variolitic, Fe oxyhydroxide–altered chilled flow margin. B. Variolitic to mottled flow interior in Subunit 5B but also typical of Subunits 5C and 5E. C. Typical nonvariolitic interval of Subunit 5B, sparsely phyric and sparsely vesicular. D. Variolitic texture with brown varioles, mostly surrounding phenocrysts. E. Lack of groundmass plagioclase (plag) and clinopyroxene (cpx) centered on corroded clinopyroxene phenocryst in area of variolitic texture. F. Variolitic texture showing lack of groundmass plagioclase and fresh fibrous clinopyroxene centered on plagioclase-clinopyroxene glomerocryst. Ol = olivine.

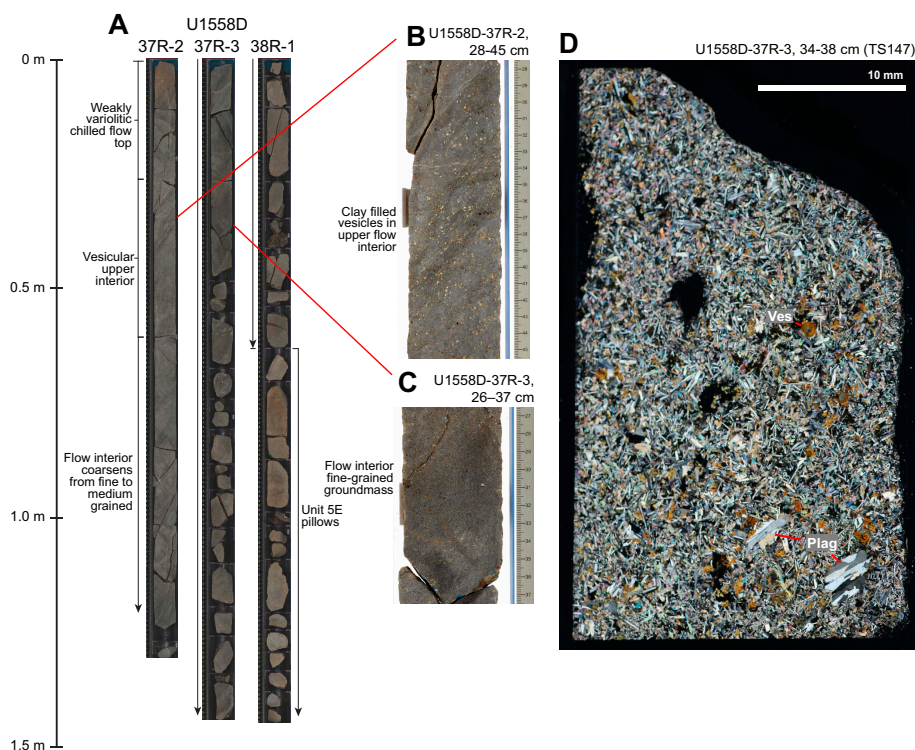
The flow consists of moderately olivine-plagioclase phyric basalt, with olivine phenocrysts being slightly more abundant (~4%) than plagioclase phenocrysts (~2%) (Figure F29C). However, the groundmass contains abundant fine-grained plagioclase laths, such that the plagioclase content in the rock is actually much greater than olivine (Figure F29D).

Glassy margins of the flow were not recovered, but emplacement as a single massive flow is interpreted on the basis of its gradational and asymmetric internal quench texture (Figure F29A). The top ~30 cm of the flow is chilled to a microcrystalline groundmass grain size with subtle variolitic texture that becomes moderately vesicular in the upper flow interior (Figure F29B). The groundmass gradually coarsens from microcrystalline to fine to medium grained toward the bottom of the flow (interval 393-U1558D-37R-3, 50 cm, to 38R-1, 60 cm). These features suggest more rapid cooling on the flow top than the flow bottom, which is more supportive of a flow emplaced on the seafloor than a hypabyssal sill. The vesicular upper interior is interpreted to be formed by volatiles degassing from the nonvesicular lower part of the flow that could not escape through the already chilled flow top (Figure F29B).

#### 5.1.4.9. Subunit 5E

Lithology: sparsely to moderately plagioclase-olivine-phyric variolitic basalt pillow lavas

Subunit 5E is lithologically like Subunit 5C and is interpreted to have formed during the same volcanic episode punctuated by the eruption of the Subunit 5D massive flow. The upper contact of Subunit 5E was not clearly recovered but is located at the first piece of mottled, cryptocrystalline basalt that is texturally distinct from the massive flow at Section 393-U1558D-38R-1, 63 cm. Hole U1558D ends in Subunit 5E at 370.2 mbsf (203.13 msb), giving the unit a minimum thickness of 3.9 m and an expanded thickness of at least 8.3 m. One 2.5 cm thick interpillow breccia was recovered in Subunit 5E, with clasts of angular, variably altered glass in a carbonate-free clay and zeolite matrix (interval 39R-2A, 39–41.5 cm).

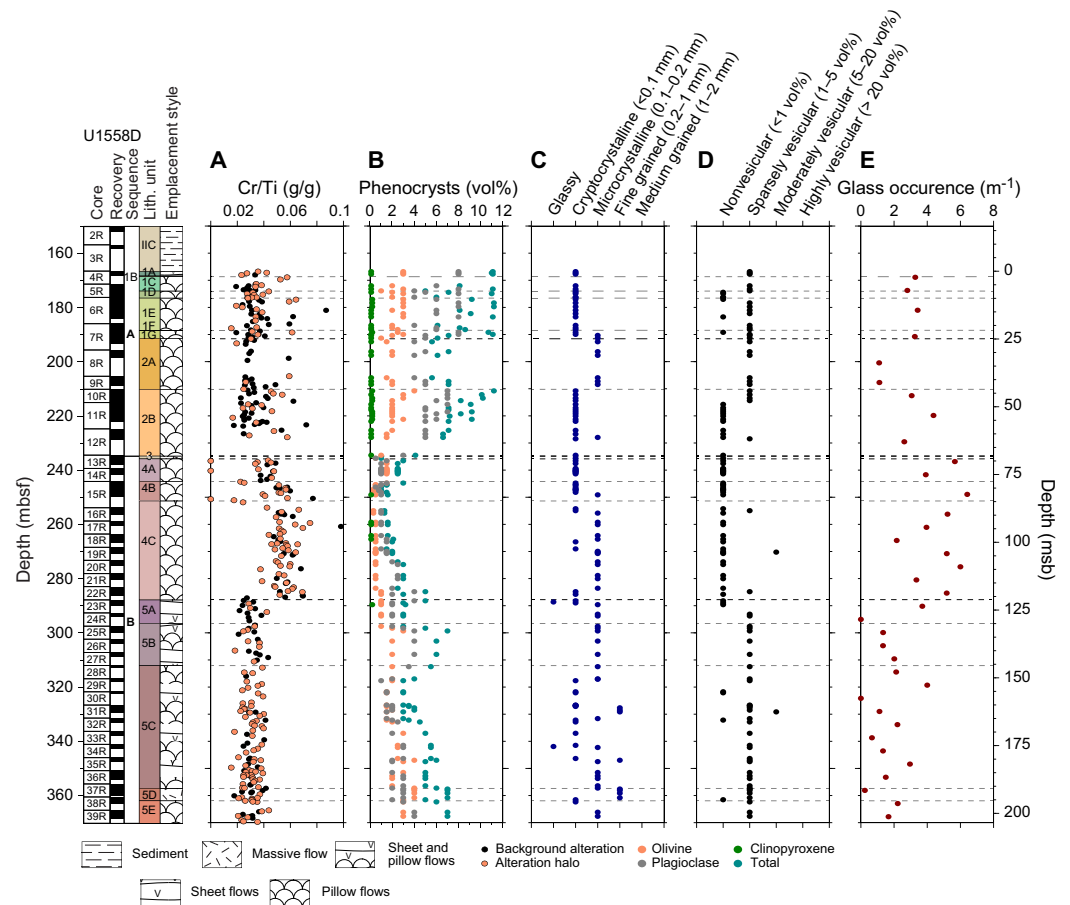


**Figure F29.** Single massive lava flow with minimum thickness of 3 m and expanded thickness of 4.5 m in Volcanic Subunit 5D, Hole U1558D. A. Three sections spanned by texturally gradational massive flow. B. Close up of moderately vesicular upper interior of flow. C, D. Close up of fine-grained flow interior. Plag = plagioclase, Ves = vesicle.

## 5.2. Phenocryst phases

Phenocryst character was a key discriminant of the Site U1558 units (Figure F30), and most of the volcanic rocks recovered have plagioclase-olivine-clinopyroxene-, plagioclase-olivine-, or olivine-plagioclase-phyric phenocryst assemblages with total abundances varying from aphyric to highly phyric levels (Figure F30B). In Figure F30, the aphyric to sparsely phyric character of Subunit 4C is apparent, as is the volumetric dominance of plagioclase over olivine except for short intervals in Subunits 5C–5E.

The presence of extremely sparse but distinct dark olive-green clinopyroxene phenocrysts up to 15 mm is the most characteristic lithologic difference between Sequence A and B basalts (e.g., Figures F21A, F22), and this is reflected in the phenocryst abundances plotted downhole (Figure F30B). Identifying the composition of these green clinopyroxenes requires further microanalytical study; however, if their Cr-diopside-like color is an indication of their high Mg and Cr contents, they may have been sourced from a deep and relatively unfractionated part of the axial magmatic system. In thin section, these clinopyroxenes invariably show some evidence for resorption, such as rounded corners or ovoid or irregular, anhedral shapes (Figure F22E–F22G). Less commonly, plagioclase phenocrysts have also been resorbed (Figure F19D), whereas olivine pseudomorphs always appear to be euhedral. The Sequence A green clinopyroxenes also occur in microgabbroic glomerocrysts with olivine and plagioclase (Figure F21A). Together with their chrome diopside appearance, this strongly indicates these glomerocrysts are cognate and have been transported from a magma chamber or cumulate deeper in the magmatic system. Common resorption textures suggest that the magma that carried these phenocrysts is in disequilibrium with the clinopyroxene and plagioclase in this assemblage, with the magma resorbing minerals in the order



**Figure F30.** Macroscopic core observations, Hole U1558D. A. Cr/Ti ratios from high-resolution pXRF analysis of split core surfaces (see Figure F32 for additional results). B. Phenocryst abundance. C. Flow interior grain size. D. Vesicularity. E. Glass occurrences.



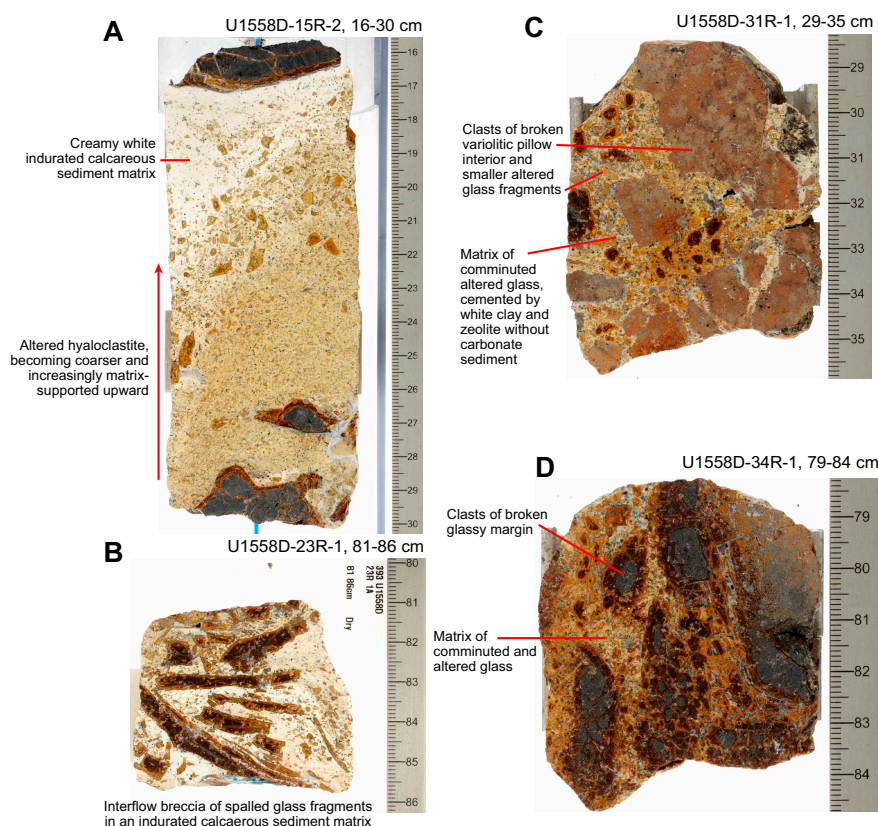
clinopyroxene > plagioclase > olivine, the reverse order of crystallization for typical MORB (Grove et al., 1992).

The absence of green clinopyroxenes in Sequence B, together with its different geochemistry and phenocryst proportions and abundance suggests that it is derived from a different part of the axial magmatic system than Sequence A. This is consistent with the volcanic hiatus of tens of thousands of years thought to separate these sequences, as estimated from the sedimentary breccia thickness and sedimentation rates, as well as the clear step in Cr/Ti composition across the sequence boundary (Figure F30A).

### 5.3. Breccias

Hole U1558D recovered short intervals of different kinds of breccia from most volcanic units. Most of these are interpillow breccias in the interstices between pillow lavas, with the indurated sediment infill apparently making for more cohesive and recoverable rock (Figures F20B, F20C, F24A, F24D). However, breccias with widths across the entire core, too great for interpillow fills, also occur in the hole and are interpreted to be discrete breccia layers (Figures F20D, F23, F31A, F31C).

In volcanic Sequence A and the upper part of Sequence B (Unit 4–Subunit 5A), these breccias invariably have some component of indurated calcareous sediment matrix (e.g., Figures F20B–F20D, F24, F31A). This calcareous sediment component is mostly absent in the lower part of the hole (Subunits 5B–5E), where breccia is more clast supported or jigsaw fit with a matrix of comminuted and altered glass with cementation by clay and zeolite (Figure F31C, F31D).



**Figure F31.** Breccia types, Hole U1558D. A. Sedimentary breccia with altered hyaloclastite and indurated calcareous sediment matrix. B. Interflow breccia with variably altered tabular glassy fragments supported by indurated calcareous sediment. C. Clast-supported breccia of broken pillow interior and glassy clasts with carbonate-free altered and comminuted glass matrix cemented by clay and zeolite. D. Clast-supported interpillow breccia with carbonate-free matrix of altered, comminuted glassy fragments.

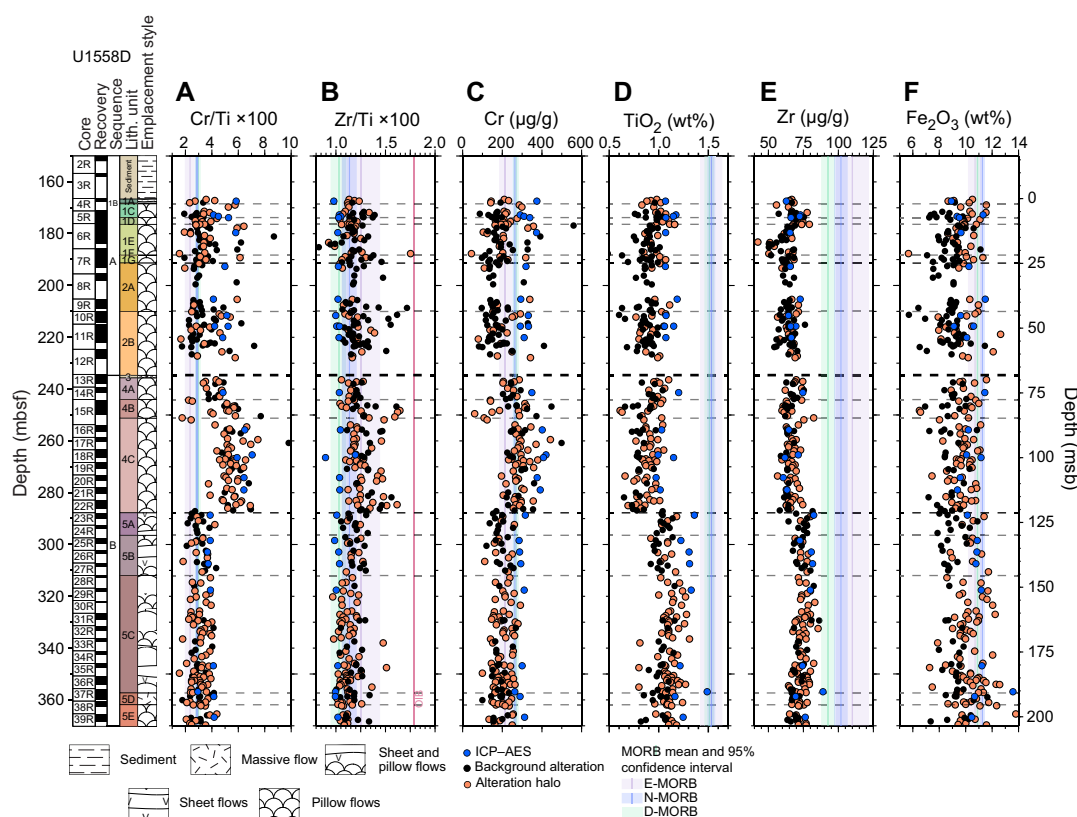
## 5.4. High-resolution chemostratigraphy

We measured 363 locations on the cut surfaces of the archive section halves of Hole U1558D cores by pXRF. Measurements were made at locations with background levels of alteration and also from alteration halos around veins or flow margins (Table T7). This allows both primary igneous compositions and the chemical perturbations by hydrothermal alteration to be considered down-hole.

### 5.4.1. Variation with depth

Figure F32 shows variation in key major element oxides and trace elements with depth for Hole U1558D, both measured by pXRF on split core surfaces (Table T7) and by inductively coupled plasma–atomic emission spectroscopy (ICP-AES) on powdered discrete whole-rock samples (Table T37). These two data sets agree well for most elements, with the ICP-AES powders showing less scatter. The average Cr contents and hence also Cr/Ti ratios, however, are higher for Units 1 and 2 for the ICP-AES results relative to the pXRF, with the ICP-AES-measured Cr being similar to the upper range of the pXRF-measured Cr. Figure F30A and F30B offers a possible explanation for this discrepancy because it coincides with particularly high phenocryst abundance in Units 1 and 2. The pXRF analyses are located where possible over areas of groundmass free of large phenocrysts, which would otherwise strongly and unpredictably affect the results over the ~1 cm<sup>2</sup> analysis area. Avoidance of large, likely Cr-rich green clinopyroxene or Cr-spinel inclusion-bearing olivine phenocrysts may consequently have led to systematically lower Cr contents measured by the pXRF relative to the bulk powder ICP-AES method. Both data sets are still potentially accurate

**Table T7.** Major and trace element geochemistry of basalts determined by pXRF on split core surfaces, Hole U1558D. [Download table in CSV format.](#)



**Figure F32.** A–F. Shipboard split core surface pXRF and ICP-AES whole rock powder analyses of major and trace element concentrations and ratios, Hole U1558D. Total Fe is calculated as Fe<sub>2</sub>O<sub>3</sub>. MORB reference means and 95% confidence intervals from Gale et al. (2013). pXRF data available in Table T7; ICP-AES data available in Table T37. E-MORB = enriched MORB, N-MORB = normal MORB, D-MORB = depleted MORB.

and useful, but this discrepancy requires further investigation and must be kept in mind when interpreting pXRF data for Units 1 and 2 and highly phyric lavas along the SAT in general.

Despite this discrepancy, key major and trace element concentrations and ratios show clear changes across the unit and sequence boundaries, supporting their petrologic definitions described in the previous sections (Figure F32). In particular, high Cr/Ti ratios coupled with generally low concentrations of the incompatible elements Zr and Ti indicate that Unit 4 is less evolved than the other units. This composition evolves to lower Cr/Ti ratios in the upper 10 m of Unit 4, suggesting a transition during the waning stages of the eruption of Sequence B.

There is a subtle increase in Zr/Ti over the Unit 4/5 boundary (Figure F32B). This increase is not apparent in the limited ICP-AES data, so further analysis is required; however, if it is real, the occurrence of elevated Zr/Ti in the apparently less evolved lavas of Unit 4 is difficult to explain within a co-magmatic sequence. Given the greater incompatibility of Zr relative to Ti in the fractionating phases, this change should be in the other direction for different degrees of fractionation from the same parental melt. The change to higher Zr/Ti instead suggests that Unit 4 may have derived from a slightly different, more enriched parental melt than the other units.

In Unit 5, there are no clear differences between the Subunit 5D massive lava flow and the surrounding Subunit 5C and 5E pillow lavas for the elements plotted in Figure F32F. This compositional similarity provides a good opportunity for assessing the influence of contrasting grain size and emplacement style on alteration and the magnetic and physical properties of the lavas. Toward the top of Unit 5 in Subunits 5A and 5B, there is a clear decrease in Ti and subtle increase in Zr concentrations that is not accompanied by a detectable increase in Cr (Figure F32C–F32E).

Apart from slightly higher average values for Unit 4, Zr/Ti ratios are relatively uniform downhole, with ICP-AES-measured compositions scattering around the depleted MORB (D-MORB) mean and pXRF-measured compositions scattering around the normal MORB (N-MORB) mean for all the lavas in Hole U1558D (Figure F32).

## 5.5. Summary

Holes U1558A, U1558D, and U1558F all recovered volcanic basement at Site U1558, but only Hole U1558D advanced deeply into basement. After reaching the sediment/basement interface at 166.8 mbsf, Hole U1558D further advanced to 370.2 mbsf (203.4 mbs), recovering 97.5 m of basement core for a total recovery of 48%, which reached up to 90% in some cores (Table T5).

Hole U1558D intersected two distinct volcanic sequences (A and B) separated by a ~1 m thick sedimentary breccia horizon indicating a hiatus in volcanism at this site potentially on the order of tens of thousands of years. The upper Sequence A (166.55–234.64 mbsf) includes Volcanic Units 1 and 2 that consist of moderately to highly plagioclase-olivine-clinopyroxene-phyric lavas mostly emplaced as pillow lavas of varying size (10–130 cm). Extremely sparse but distinctive dark olive-green clinopyroxene phenocrysts are a characteristic feature of the Sequence A volcanic rocks. Sequence B (234.65–360.20 mbsf) lacks these green clinopyroxene phenocrysts, and its uppermost Unit 4 contains abundant interflow sediments and breccias, suggestive of a buried seafloor horizon, with interesting implications for studying seafloor weathering beneath multiple horizons. This change in phenocryst assemblage indicates some aspect of the magmatic system changed between eruptive sequences. Lava composition assessed by pXRF, particularly for Cr, Ti, and Zr, varies both in a stepwise fashion across petrologically defined unit boundaries and gradually within the units. Zr/Ti ratios are consistent with D-MORB to N-MORB for the lavas at Site U1558.

## 6. Alteration petrology

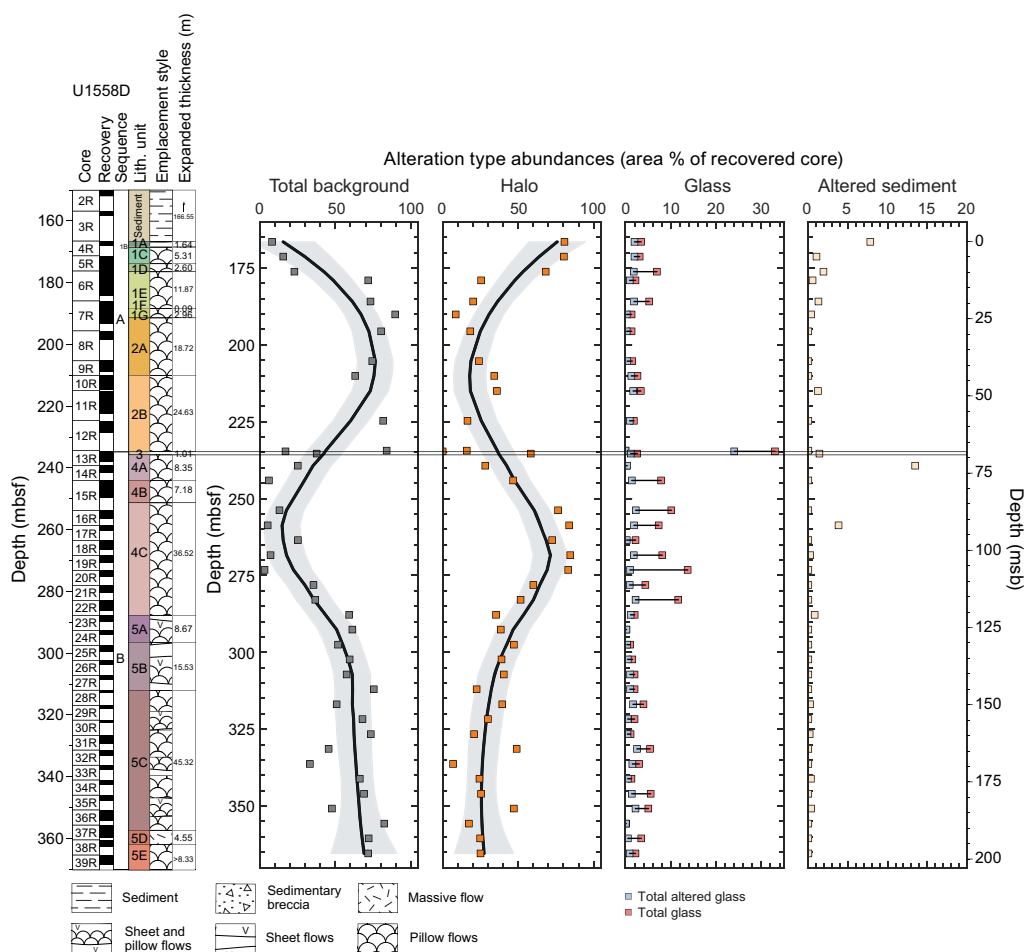
The basement rocks recovered from Site U1558 all preserve evidence of reaction with seawater-derived hydrothermal fluids to varying extents. This alteration is manifested as secondary minerals in three main contexts: (1) replacing interstitial mesostasis and glass, (2) replacing groundmass and phenocrysts, and (3) precipitating in open porosity to partially or completely fill vesicles or fractures to form veins. These three manifestations occur in a range of spatial contexts in Site

U1558 basement, namely background alteration representing fluid/rock reaction that has pervasively permeated the bulk rock and alteration halos that are generally related to previous open porosity that has facilitated more extensive fluid/rock reaction (e.g., around veins and vugs or along igneous margins). In addition, the breccias recovered from Site U1558 also record extensive alteration of clasts and matrix and are cemented by secondary minerals. The replacement minerals, styles, and intensity of alteration, along with the secondary minerals precipitated in veins, vesicles, and breccias provide a record of the hydrothermal alteration taking place across ~50 My of crustal aging. This section focuses on Hole U1558D, although similar alteration features were observed in the basement recovered by XCB coring in Hole U1558A.

Overall, Hole U1558D is characterized by low-temperature alteration with downhole variations in abundances and types of alteration halos and background alteration that are also accompanied by changes in the secondary minerals precipitating in veins (Figure F33).

### 6.1. Alteration of glass

Volcanic glass that occurs along flow margins and as clasts in breccia displays a full spectrum of alteration throughout Hole U1558D, from completely fresh to completely altered. At core section level (the scale of observation), there are no sections where the glass is completely replaced (Figure F33). On average, glass replacement is estimated at 35%–40%, but in Igneous Units 3 and 4 the volcanic glass shows alteration intensities below average. Intervals of fresh glass, several centimeters in length, are not uncommon in Hole U1558D, and interestingly, this fresh glass is commonly



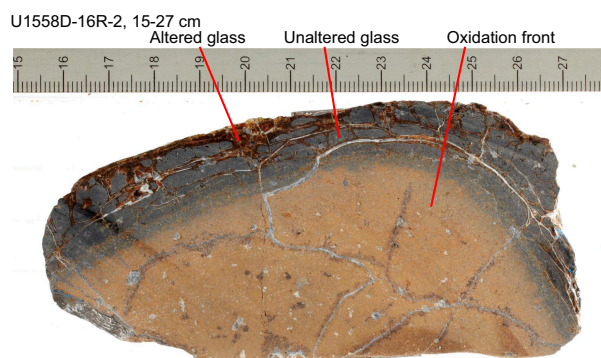
**Figure F33.** Alteration overview showing abundance of background alteration, alteration halos, fresh and altered glass, and altered sediment, Hole U1558D. Data are plotted at individual core level, except where igneous units straddle a core, in which case data are separated by igneous unit. Data are plotted at top of cored intervals. Black trend lines = locally weighted scatter plot smoothing (LOWESS) nonparametric regression, gray shading = 2σ of mean.



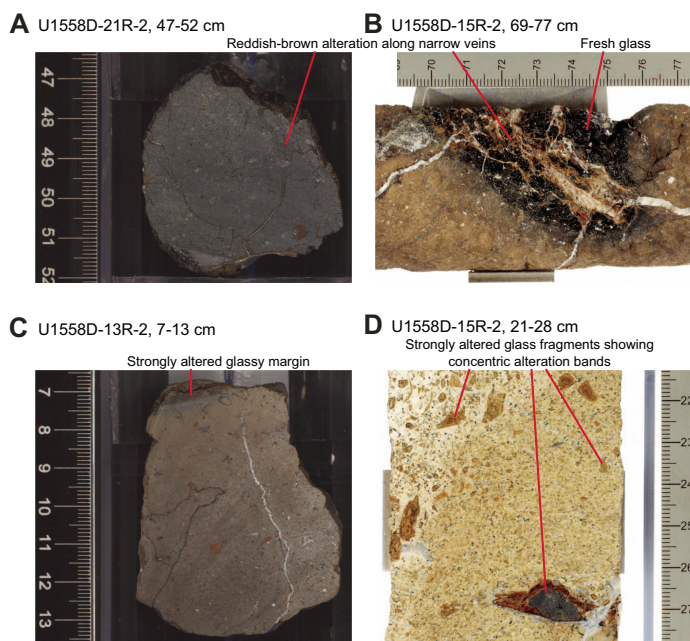
immediately juxtaposed with regions of highly altered and oxidized groundmass (Figure F34). Glass readily alters to clay minerals with a range of colors that correlate with the extent of alteration and progresses from dark brown to reddish brown to pale olive-green, with the latter being the most altered (Figure F35). Incipient alteration of glass begins with the development of brown to orange alteration halos around veins, but as reactions progress the glass alters to progressively lighter colors (Figure F36). This progression is also recognized by the development of concentric alteration bands (Figure F35D). In the sedimentary breccias, the smallest clasts of volcanic glass (<5 mm) are generally completely altered to pale olive-green (5Y 6/4) clay minerals (Table T8).

## 6.2. Background alteration

Background alteration is present throughout Hole U1558D and occurs in four types: gray background, orange speckled background, mixed brown-gray background, and mottled gray chilled margin alteration.



**Figure F34.** Thick glassy margin, Hole U1558D. Glass is mostly unaltered, but thin layer of clay has formed along outermost surface as well as along network of narrow veins. Orange halo alteration is pervasive throughout pillow interior.



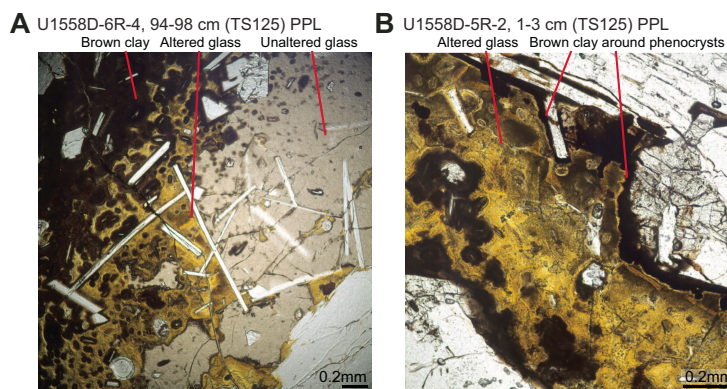
**Figure F35.** Degrees of volcanic glass alteration, Hole U1558D. A. Mostly unaltered, centimeter-sized glass piece with alteration limited to external surface of piece and small (submillimetric) veins. B. Glassy margin where glass is mostly fresh but altered orange-brown along network of veins. C. Strongly altered glassy margin formed against highly altered cryptocrystalline groundmass in pillow basalt. D. Glass fragments in breccia showing concentric alteration, varying from reddish orange to pale olive-green.



### 6.2.1. Gray background

Gray background alteration is present throughout most of Hole U1558D and represents the least altered rocks in this hole and across the SAT. Gray background is uniform in appearance, generally showing GLEY 1 5/N color (Figure F37). Locally, gray background represents up to 70% of a recovered core, and on average occupies 20% of recovered cores (Figure F38).

In thin section, gray background alteration is characterized by the pseudomorphic replacement of mesostasis and minor amounts of groundmass to brown clays (likely Mg-saponite), whereas any phenocrysts are mostly fresh. Vesicles in gray background are partially to fully filled with clays, Fe oxyhydroxides, and calcium carbonate. Some olivine phenocrysts are replaced by creamish clay minerals (Figure F37). In the vicinity of carbonate vesicles, some plagioclase and olivine phenocrysts and groundmass are pseudomorphically replaced by calcium carbonate (Figure F37).



**Figure F36.** Degrees of volcanic glass alteration, Hole U1558D. A. Some glass is locally unaltered and remains isotropic but much is partially altered to brown clay  $\pm$  Fe oxyhydroxides with plagioclase laths unaffected by alteration. B. Volcanic glass completely altered to brown clay  $\pm$  Fe oxyhydroxides. Clay coats phenocryst rims.

**Table T8.** XRD results for mineral separates, Hole U1558D. [Download table in CSV format.](#)

Core, section, interval (cm)	Top depth CSF-A (m)	Bottom depth CSF-A (m)	Minerals identified (semiquantitative% proportion)	Sampling note
393-U1558D-				
4R-1, 28–31	166.78	166.81	Phillipsite-Na (100%)	Vug with prismatic crystals in orange-speckled background
5R-1, 127–144	172.57	172.74	Calcite (64%), phillipsite-Na (36%)	Vein (within MBIO sample)
5R-4, 30–31	175.39	175.40	Calcite-magnesian (100%), additional minor clay peaks	Vein on chilled margin
6R-1, 81–82	177.01	177.02	Calcite (65%), phillipsite-Na (29%), chabazite-Ca zeolite (6%), additional minor peaks	Vein within pillow oxidation front
6R-2, 72–74	178.38	178.40	Calcite-magnesian (100%), additional minor zeolite peaks	Vug in interpillow sediment
6R-3, 101–103	180.04	180.06	Phillipsite-Na (100%), additional minor clay peaks	Vein in glassy margin
6R-4, 71–73	181.18	181.20	Calcite (69%), phillipsite-Na (31%)	Vein in glassy margin
7R-2, 36–39	187.71	187.74	Calcite-magnesian (100%)	Carbonate close to pink cement of interpillow breccia
7R-2, 40–41	187.75	187.76	Calcite-magnesian (100%), additional minor clay peaks (montmorillonite?)	Pink cement of interpillow breccia
7R-2, 42–43	187.77	187.78	Anorthite (50%), sepiolite (28%), calcite-magnesian (22%), additional minor peaks (tal?)	Altered clasts in interpillow breccia
11R-5, 62–64	221.41	221.43	Sepiolite (91%), gobbinsite zeolite (9%)	Vein in glassy margin
13R-1, 29–31	234.69	234.71	Calcite (100%), additional minor clay peaks (montmorillonite?)	White sediment of interpillow breccia
13R-1, 55–58	234.95	234.98	Calcite (97%), koeneneite (3%), additional peaks (phillipsite?)	Altered clasts in interpillow breccia
14R-1, 42–48	239.72	239.78	Calcite (100%)	Interpillow sediment
15R-4, 62–73	248.99	249.10	Calcite-magnesian (100%), additional minor clay peaks (montmorillonite?)	White vein in flow interior
17R-2, 38–61	260.12	260.35	Phillipsite-Na (40%), albite (35%), calcite-magnesian (25%)	White vein in oxidation front
20R-2, 33–44	274.75	274.86	Phillipsite-Na (100%)	White vein in glass
21R-1, 15–30	278.25	278.40	Calcite-magnesian (100%)	Vein in chilled margin
23R-1, 74–81	288.54	288.61	Calcite-magnesian (100%), additional minor clay peaks (montmorillonite?)	Interpillow breccia matrix
29R-1, 7–17	316.97	317.07	Phillipsite-Na (100%), additional strong clay peaks (smectite)	Interpillow breccia matrix
31R-1, 31–33	326.91	326.93	Anorthite (100%), additional minor peaks (phillipsite?)	Interpillow breccia matrix
32R-1, 7–13	331.47	331.53	Zeolite (tschernichite?, 56%), albite (36%), calcite-magnesian (8%)	Fracture surface
34R-1, 78–85	341.88	341.95	Phillipsite-Na (100%), additional minor clay peaks (montmorillonite?)	Cement in interpillow breccia
35R-1, 28–34	346.28	346.34	Phillipsite-Na (98%), sepiolite (2%)	Cement in brecciated glassy margin
39R-2, 35–43	367.25	367.33	Calcite-magnesian (39%), phillipsite-Na (61%)	Cement in interpillow breccia

### 6.2.2. Orange speckled background

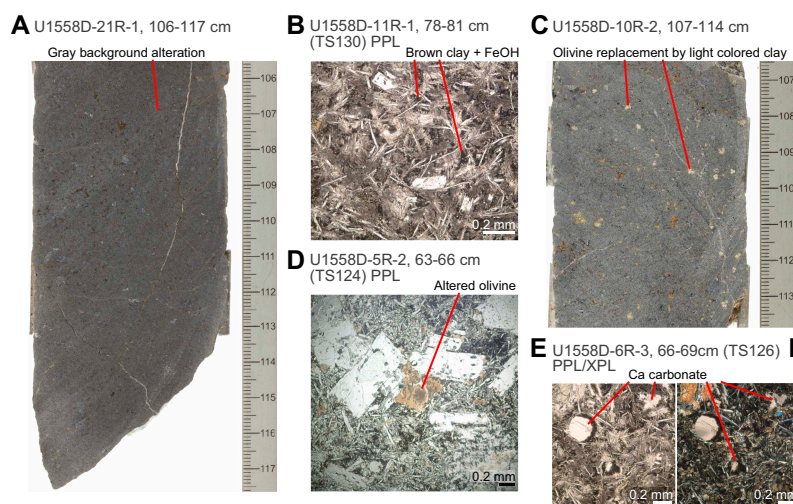
Orange speckled background is a variant of gray background where the olivine phenocrysts are partially to completely replaced by orange clays and Fe oxyhydroxides (Figure F39). The groundmass remains the same uniform gray background as seen in hand sample (GLEY 1 5/N) and thin section (Figure F39). The alteration of olivine to orange clays and Fe oxyhydroxides is not unique to this background alteration type and is found elsewhere in the hole. This type of olivine alteration also occurs within various halo types (Figure F39C, F39D) and within the mixed brown-gray background alteration. It is distinguished here as a separate alteration type because it represents a progression of the uniform background alteration. The orange speckled alteration is most common in Subunit 1E through to Unit 2 (Figure F38) where olivine phenocrysts are abundant. This relationship is less strong deeper in the hole such as in Unit 5.

### 6.2.3. Mixed brown-gray background

Mixed brown-gray background alteration is characterized by mixed background colors but is generally more brown (10YR 6/2 light brownish gray) than gray (GLEY 1 5/N). This alteration type shows a range of textures, from patchy to well-developed variolitic textures (Figure F40). This alteration type occurs in Unit 5 (Figure F38) where clear variolitic textures become a common feature. When a variolitic texture is present, the brown alteration forms <1–2.5 mm radiating areas surrounding varioles that have undergone extensive replacement to brown clay minerals that form an interconnected network of groundmass alteration that gives the characteristic patchy to mottled appearance (Figure F40). The examples where the variolitic texture is not well developed (e.g., interval 393-U1558D-31R-1, 81–108 cm) show the same color but without clear radial clusters of brown alteration, giving a more patchy appearance and likely represents variations in primary igneous textures. The mixed brown-gray background alteration has the highest alteration intensity (percentage replacement) of the three background alteration types, with 65%–75% secondary minerals compared to 15%–30% for most gray background samples and 18%–50% for most orange speckled background samples.

### 6.2.4. Mottled gray chilled margin background

Chilled margins are commonly associated with mottled gray alteration located between the glassy margin and the interior of the flow. These mottled gray chilled margins are not always present at chilled margins but occur irregularly throughout Hole U1558D (e.g., Sample 38R-2, 0–13 cm; Figure F41). This region varies in width from absent up to 1–2 cm, but most commonly it occurs as a thin 2–3 mm band. In the wider examples, the mottled appearance is more evident because of greater alteration of the varioles.



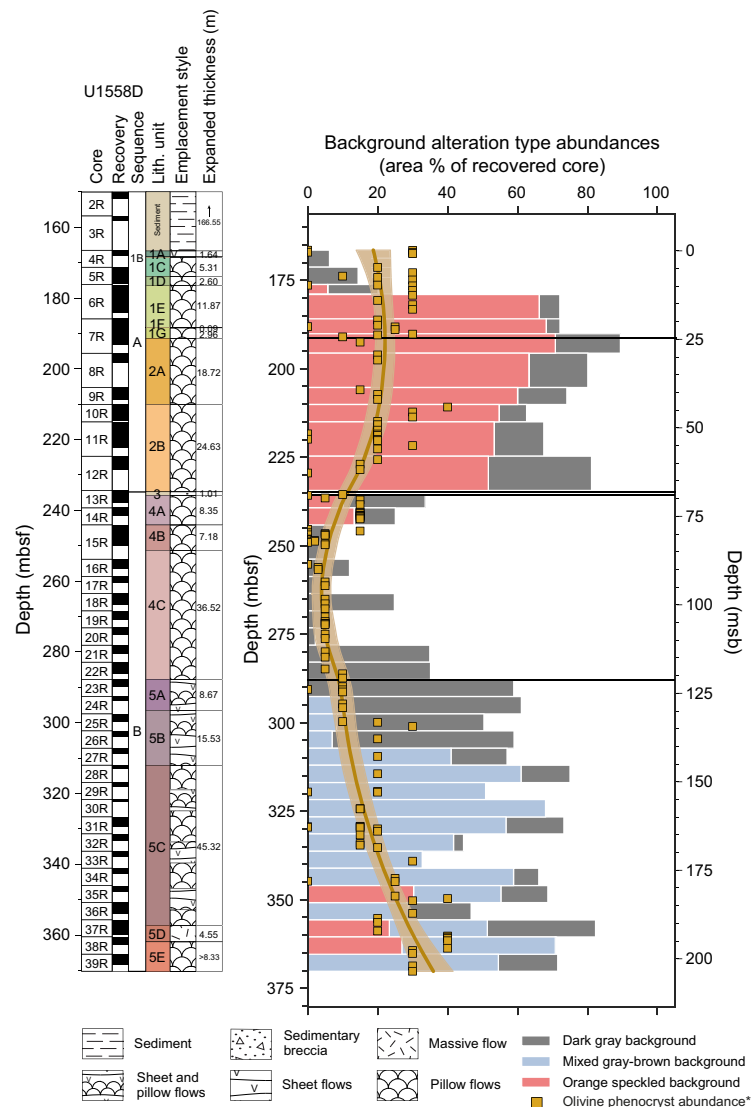
**Figure F37.** Gray background alteration, Hole U1558D. A. Core piece that has undergone limited alteration. B. Background alteration. Groundmass is replaced by brown clay  $\pm$  Fe oxyhydroxides. C. Core piece showing similar gray background to A but replacement of olivine phenocrysts by light-colored clay. D. Light brown clay that replaced olivine phenocryst. E, F. Calcium carbonate replacing groundmass; vesicle (upper left) is also filled with carbonate.

### 6.3. Alteration halos

Alteration halos are ubiquitous in Hole U1558D and occur in a range of colors, thicknesses, and textures (Figure F42). Halos surround recovered veins and chilled margins. In some instances, halos consume whole pieces and have no clear association to recovered veins or margins, although this is likely an artifact of recovery. Halo types are distinguished primarily on the dominant color that reflects the secondary groundmass minerals formed, leading to four main halo types. Textural and color variation within the types are discussed below.

#### 6.3.1. Dark gray halos

Dark gray halos are the least abundant halo type, occurring in only 10 of the 39 cores from Hole U1558D. They are largely absent between 225 and 280 mbsf, and none are found in Unit 4. They are distinguished by their uniform dark gray color (GLEY 15/N dark gray), and they predominantly occur bordering veins, although some examples formed adjacent to pillow margins (Figure F43). When they border veins, the dark gray halos are on average 3–4 mm wide. In the majority of occurrences (72%), dark gray halos occur together with light brownish gray halos. In thin section, the dark gray halos are characterized by the presence of yellow-brown clays that replace mesostasis and groundmass minerals and commonly fill vesicles (Figure F44). Dark gray halos are com-



**Figure F38.** Downhole distribution of background alteration types calculated on section unit scale, Hole U1558D. Olivine phenocryst abundance (\*) shown for context and plotted as olivine phenocryst abundance (area%) × 10.



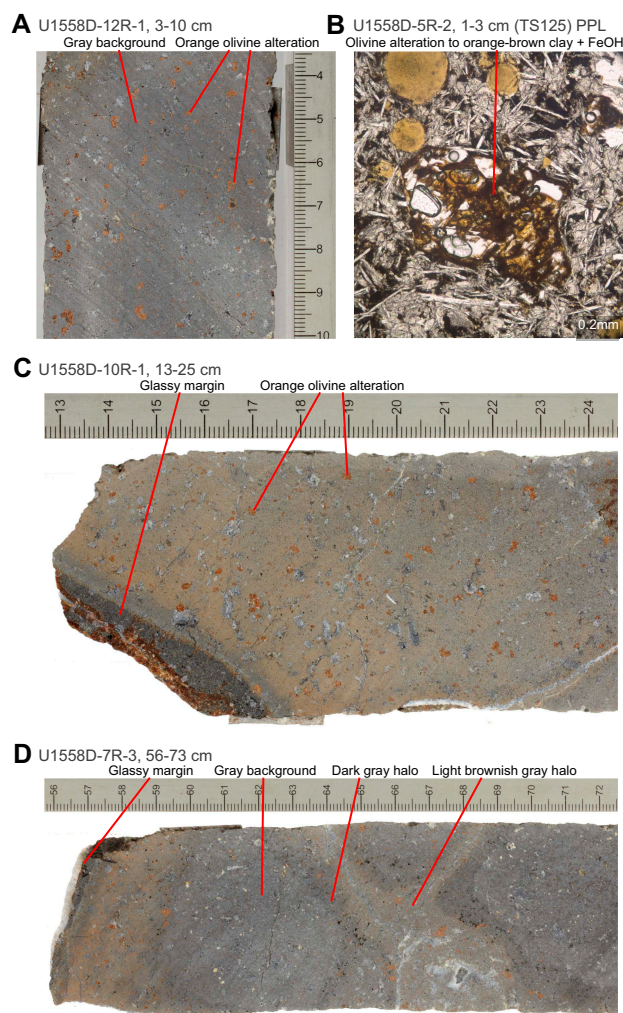
monly overprinted by the other halo types (Figure F43) and appear to represent the earliest forming halo type.

### 6.3.2. Light brownish gray halos

Light brownish gray halos occur in 20 of the 39 cores and are present in all igneous units, although they are absent for a significant part of Unit 4 (241.1–287.8 mbsf; Figure F42). They are light brownish gray (10YR 6/2 light brownish gray), which is the same color as the mixed brown-gray background (Figure F43). In Volcanic Sequence A, this halo type mostly occurs paired with dark gray halos around veins, where the light brownish gray (average 4 mm half-width) occurs closest to the vein indicating that they are overprinting the dark gray halos. They also occur as halos around vugs. In Unit 5 (Sequence B), some light brownish gray halos are associated with the variolitic mixed brown-gray background alteration, where they form larger halos (4–10 mm) but are not associated with dark gray halos. Because of the patchy to variolitic appearance of the background, the light brownish gray halos in this interval also show patchy texture.

### 6.3.3. Brown halos

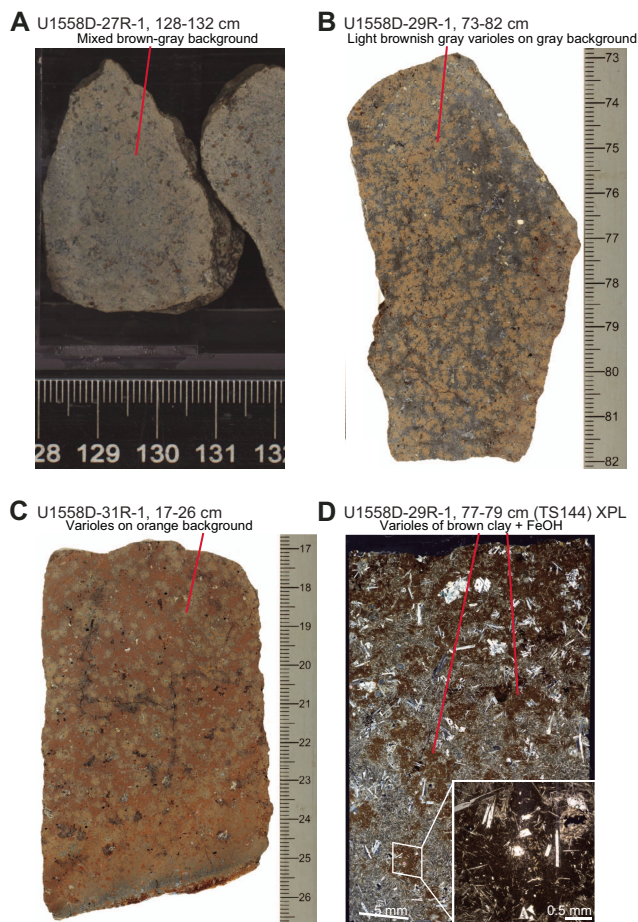
Brown halos are found throughout Hole U1558D and show varying abundances and intensities (Figure F42). This halo type also occurs in Hole U1558A XCB cores. Brown halos occur bordering



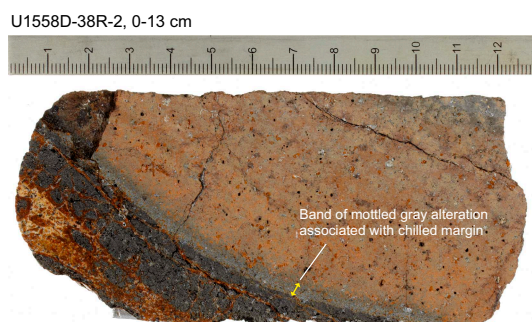
**Figure F39.** Orange speckled background, Hole U1558D. A. Altered olivine phenocrysts appear as orange spots in gray background. B. Pseudomorphic replacement of olivine by orange-brown clay  $\pm$  Fe oxyhydroxides. C. Orange speckled alteration of olivine in highly oxidized groundmass from interior of glassy pillow margin. D. Orange speckled alteration as in C occurring in oxidized rim of pillow margin as well as in vein halos; olivine phenocrysts in gray background are altered to light-colored clay.



veins and as more altered groundmass regions within chilled margins (mostly pillow margins; Figure F45). These halos, when bordering veins, display a very broad size range (0.5–45 mm wide), and on average they are the widest halo type to border veins (average = 9 mm; Table T9). Brown halos developed from chilled margins generally extend up to 40 mm into the host rock where they show sharp and diffuse boundaries (Figure F45). The intensity of alteration is reflected by the variations in the depth of brown coloration from 7.5YR 5/2 brown, 7.5YR 5/3 brown, 7.5YR 3/3 dark brown, 5YR 6/6 brown, to 5YR 3/1 very dark gray. The 7.5YR 5/2 and 7.5YR 5/3 browns are the



**Figure F40.** Mixed brown-gray background, Hole U1558D. A. Mixed brown-gray background without variolitic texture. B. Pronounced patchy to variolitic alteration texture on gray background. C. Pronounced patchy to variolitic alteration texture on orange halo and orange pillow margin alteration zone. D. Patchy alteration to brown clay ± Fe oxyhydroxides. Inset shows close up of area highlighted by white box with replacement of groundmass and plagioclase microphenocrysts.



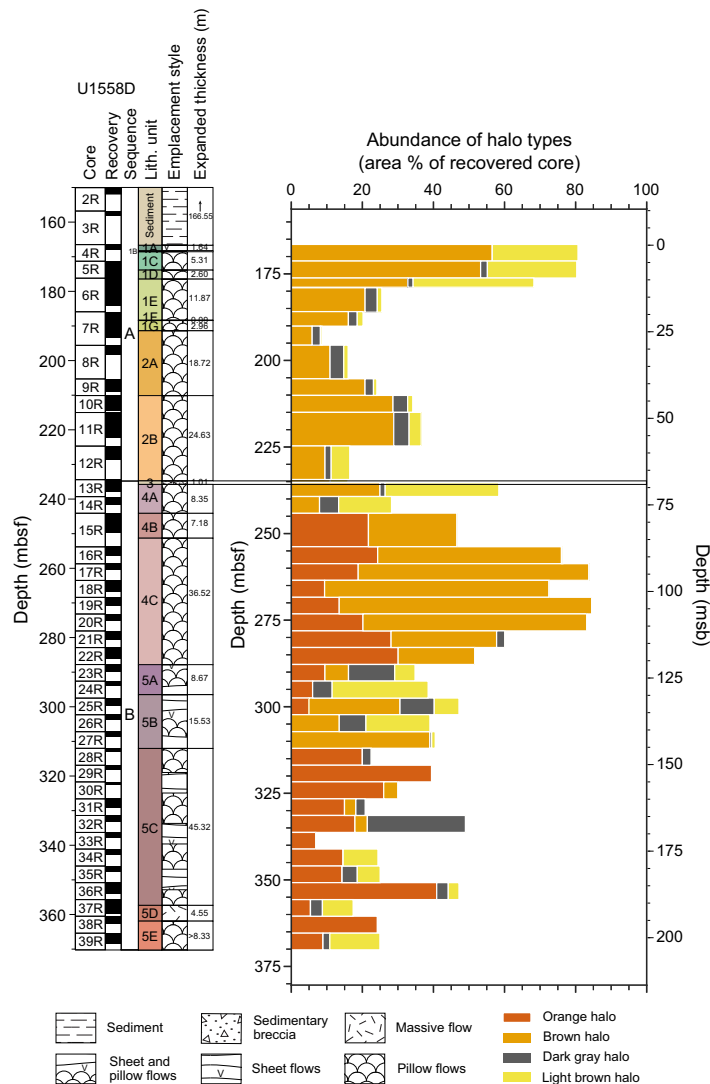
**Figure F41.** Mottled gray chilled margin alteration showing narrow (3–4 mm) band of gray alteration between glassy margin and pillow interior that is altered to orange halo.

most common colors displayed. In some occurrences, these brown halos blend continuously with the orange halos.

In thin section, brown halos are 25%–69% secondary minerals and show heterogeneity in alteration intensity on the scale of a single thin section. Secondary minerals are dominated by brown to yellow clays ± Fe oxyhydroxides that replace olivine and the groundmass (Figure F45).

### 6.3.4. Orange halos

Orange halos are the most distinctive halo type in Hole U1558D with a reddish yellow (5YR 6/6 reddish yellow) color, and they are present from 244.55 mbsf (Section 393-U1558D-15R-1, 45 cm) to the base of the hole. Once this halo type appears downhole, it displays a reasonably consistent abundance within each core (range of 5%–40% of the area of the core, average = 18.3% of the area of the core). The strong coloration of this halo is a result of the formation of Fe oxyhydroxide and clay minerals that pervasively replace the groundmass and phenocrysts (Figure F46). The orange halos are commonly associated with the chilled margins of pillow lavas, but in some rare cases they occur around veins. Most commonly they consume small core pieces that preserve no vein or margin. As described in the alteration of the glass, this halo type commonly occurs with pillow lavas that preserve thick (~10–20 mm) rims of fresh glass (Figure F34). In Unit 5, the orange halos



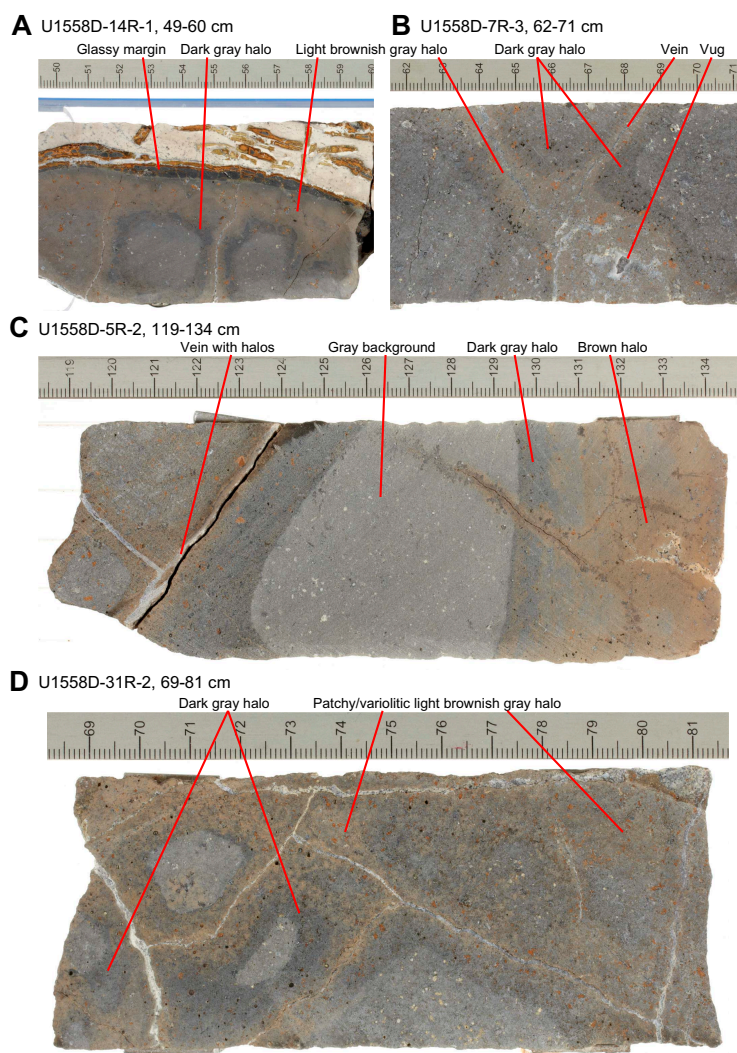
**Figure F42.** Downhole variation in area abundance of alteration halo types calculated on section unit basis, Hole U1558D. There are clear peaks in brown halo abundance around 175 and 270 mbsf. Orange halos are absent from above ~250 mbsf and then present throughout rest of hole.

are present both along chilled margins and locally overprint whole pieces. In Unit 5, these halos show the patchy to variolitic texture that is also present in the background and light brownish gray halos (Figure F46).

In thin section, the orange halos have secondary mineral abundances of 60%–70%. The groundmass is extensively replaced by orange-brown clay minerals and Fe oxyhydroxides, giving the strong orange color to the rocks (Figure F46). Plagioclase (micro)phenocrysts are also variably altered to orange-brown clays or show staining to orange colors. Although the extent of replacement is high, this is pseudomorphic in texture and there is little evidence for extensive recrystallization and loss of igneous texture.

#### 6.4. Breccia

Breccias are commonly the most altered rocks recovered from the seafloor because their high porosity and abundance of reactive fresh surface area encourages fluid/rock reaction. Breccias occur throughout Hole U1558D and range from small pieces of interpillow breccia (e.g., Unit 3) to larger intervals of brecciation (239.3–248.8 mbsf). Based on the alteration characteristics of the component parts (clasts, matrix, and cement), two groups of breccias are present in Hole U1558D.



**Figure F43.** Dark gray and light brownish gray halos, Hole U1558D. A. Dark gray and light brownish gray halos extending from glassy margin and veins. B. Extension of dark gray halo around vugs and along veins; light brownish gray halo overprints dark gray halo. C. Pronounced dark gray halos extending into gray background. Dark gray halos are irregularly overprinted by light brownish gray halos. D. Overprinting of dark gray halo by light brownish gray halo with patchy to variolitic texture.



### 6.4.1. Type 1: sediment matrix with carbonate cement

The interpillow breccia present in Units 1 and 2 all contain a mixture of sediment matrix (Figure F20, F22, F24) and carbonate cement with clasts of volcanic glass and basalt. The sediment matrix is described in Unit 3. The extent of clast alteration is moderate to complete, with smaller clasts more strongly altered. Larger clasts show the least alteration, which is focused around the margins of the clasts, to orange clays (Figure F47). Clasts <10 mm are generally completely altered, predominantly to pale olive-green (5Y 6/4) clays. Some small clasts show concentric zonation from green to brown or orange clays with black residual cores of only moderately altered glass.

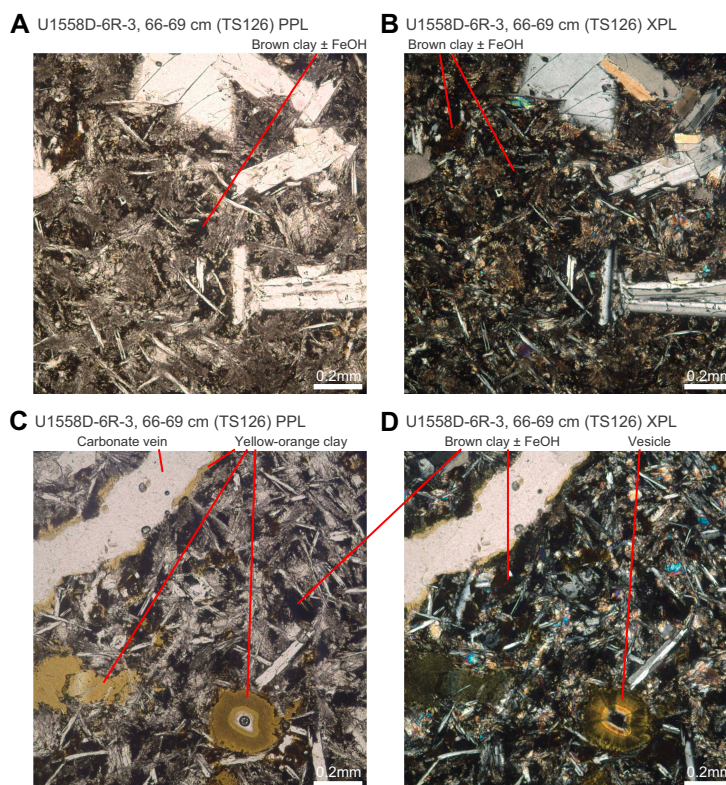
Calcite cements that have precipitated from fluids are a small proportion of these breccias (<5%), but locally on the scale of a single piece the cement may occupy up to 30%. The distribution of cement is highly variable, with patches that are cement free to areas dominated by calcite cement that locally retains open space. Another common feature are veins of calcium carbonate along clast edges that then continue into the interstitial space.

### 6.4.2. Type 2: clast dominated with clay + zeolite cement

In Unit 5, the interpillow breccias are clast dominated and the sediment-derived matrix common in the overlying units is absent (Figure F47D). These breccias comprise variable sizes of altered glass cemented by varying proportions of clay and zeolites. The clast alteration is highly variable with the interiors of centimeter-sized clasts still glassy, whereas small clasts are strongly to completely altered to clays (Figure F48). Cement volumes are low (1%–9%) and are predominantly phillipsite-Na with minor clay (montmorillonite; Table T8).

## 6.5. Veins

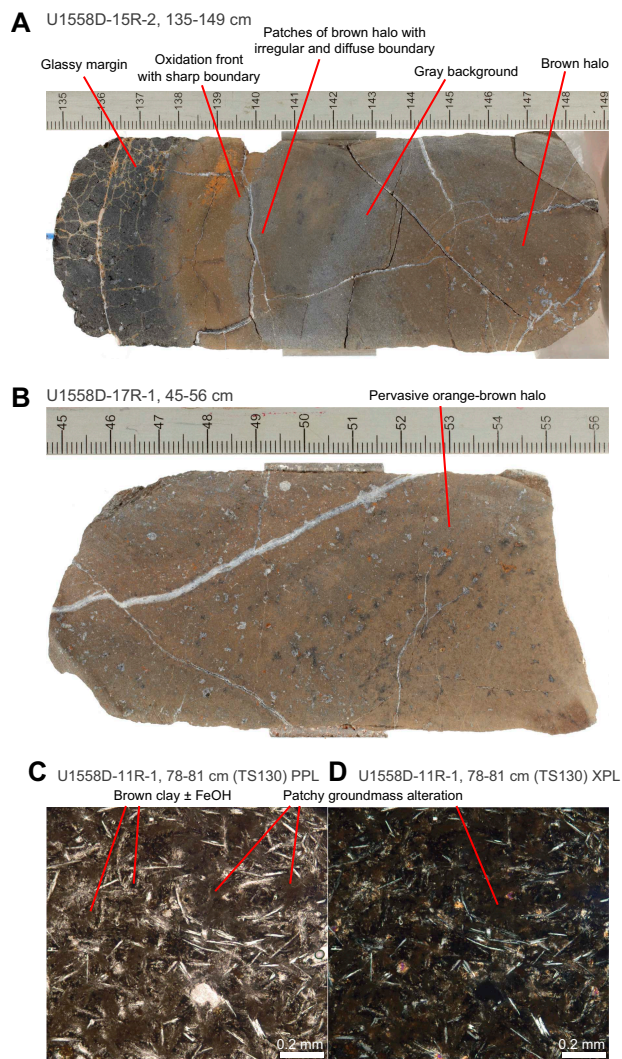
Hydrothermal veins are present throughout Hole U1558D and provide a record of the secondary minerals precipitated from seawater-derived hydrothermal fluids. The mineralogy and physical



**Figure F44.** Alteration in dark gray and light brownish gray halos, Hole U1558D. A, B. Low alteration intensity in dark gray halo; chiefly mesostasis is replaced by brown clay ± Fe oxyhydroxides. C, D. In light brownish gray halo, yellow-orange clay is observed replacing groundmass, filling vesicles, and as lining of carbonate-filled vein. Mesostasis is altered to brown clay ± Fe oxyhydroxides as in A and B.



characteristics of 2963 veins were logged, including structural orientations for 903 veins. A total of 489 veins have associated alteration halos, of which 57% have a single halo type with others exhibiting multiple halos where several halo colors occur together. Vein widths range <math><0.1\text{--}9\text{ mm}</math> (median =



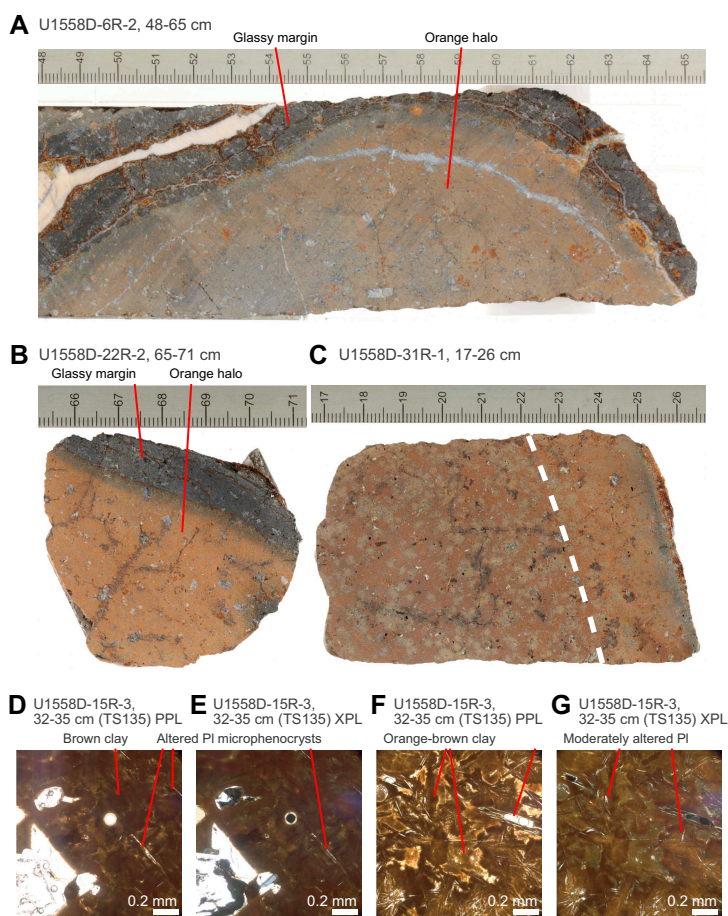
**Figure F45.** Brown halos, Hole U1558D. A. Glassy pillow margin with orange oxidation region and pervasive brown halo; bands of gray background are locally preserved. B. Core piece pervasively altered to brown halo. C, D. Groundmass in brown halo irregularly replaced by brown clay ± Fe oxyhydroxides.

**Table T9.** Halo types with average percent abundance per section unit and average half-width when found bordering veins, Site U1558. Note that orange halos rarely occur with veins. [Download table in CSV format.](#)

Halo type	Average abundance per section unit (%)	Average half-width around veins (mm)
Dark gray	4.4	4.1
Light brownish gray	10.1	4.1
Brown	28.0	8.7
Orange	18.3	—

30% of all veins are filled with only one mineral, 56% of veins are filled with two minerals, and the remaining veins are filled with three or four minerals.

The most common vein assemblage is clay + carbonate, where clay forms the lining of the vein. The downhole distribution of secondary mineral abundances (volume%) shows several interesting trends (Figure F51). First, the volume of calcium carbonate veins decreases overall downhole. Superimposed within this overall decrease, carbonate abundance increases from 160 to 270 mbsf and then shows a marked decrease in Unit 5. A small amount of zeolite is present at the top of the hole, but zeolite occurs most commonly below 275 mbsf. Zeolites (confirmed by XRD to be mostly phillipsite-Na; Table T8) are absent from Unit 2 and parts of Unit 3. The volume of clay minerals remains fairly uniform downhole, although clay vein density increases slightly downhole. The volume of clay does not show the same decrease deeper than 110 msb as calcium carbonate, even though these minerals commonly occur together. The volume of clay does not decrease because the drop in calcium carbonate veins is accompanied by an increase in the thickness of clay veins and the appearance of slightly greener and commonly powdery clay veins that appear to offset the decrease in calcium carbonate. Zeolite veins are predominantly associated with chilled margins and occur as thin <0.5 mm coatings on either fresh or altered glass. Some zeolite ± clay ± sediment-bearing veins penetrate through the glassy margin into the host rock, but they abruptly change to calcium carbonate veins within a few centimeters of the margin. These transitions in vein composition along the length of a vein are also observed in Hole U1556B (see [Alteration petrology](#) in the Site U1556 chapter [Coggon et al., 2024a]).

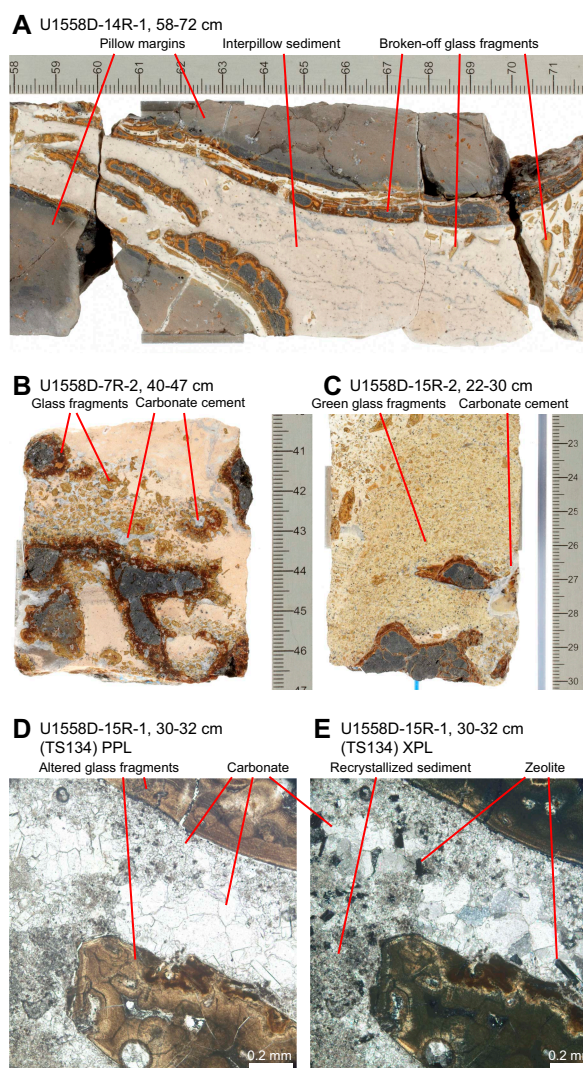


**Figure F46.** Chilled margin-related orange halos, Hole U1558D. A. Orange alteration zone at pillow margin; note variable and irregular extent of alteration, with gray background locally preserved. B. Pronounced orange alteration zone. C. Variable orange halos extending from glassy margin into flow interior. Dashed line = approximate extent of chilled margin-related oxidation zone. D, E. Orange halo close to chilled margin. Groundmass, including plagioclase microphenocrysts, is strongly altered to brown clay ± Fe oxyhydroxides. F, G. Orange halo further away from chilled margin, relative to D and E. Groundmass is less intensely altered, and microphenocrysts of plagioclase (PI) and clinopyroxene are partially retained.

Calcium carbonate veins also host sediment infill, particularly where veins are close to pillow or flow margins. The abundance of sediment in veins decreases downhole, and sediment is rare below 275 mbsf (~110 msb). Sediment veins are common in Unit 4. An increase in sediment in veins is seen in Subunit 4A where sediment also occurs as matrix fill in breccias. Similar to the relationship with clay, the textural relationship between calcium carbonate and sediment is variable. The most common association is patches or zones within a vein that are sediment dominated, but examples of crack-seal morphology are also observed (Figure F53).

Vein textures indicate that 67% of all veins display evidence of multiple episodes of fracturing and precipitation as multiple minerals occur within a single discrete vein such as calcium carbonate (the most abundant vein filling material) occurring in the same vein assemblage with clay (Figure F54A). The incorporation of wall rock fragments into the vein fillings indicates repeated episodes of fracturing and precipitation within veins (Figure F54B).

Occurrences of veins that display clear crosscutting relationships are rare, and there is no systematic relationship between calcium carbonate and clay veins or fillings. In some calcite veins, clay lines vein margins, indicating that clays filled the initial fracture before subsequent opening and



**Figure F47.** Breccias, Hole U1558D. A. Two glassy margins with interpillow sediment. Fragments of volcanic glass are broken off pillow margins with mostly limited transport of fragments. Glass clasts show alteration to orange-brown clays along edges. B. Breccia with variably altered glass fragments, cemented by carbonate. C. Clast-supported breccia with highly altered glass fragments, cemented by carbonate. D, E. Breccia matrix (recrystallized sediment) and cement (mostly carbonate, some zeolites) between altered glass fragments in interpillow breccia.



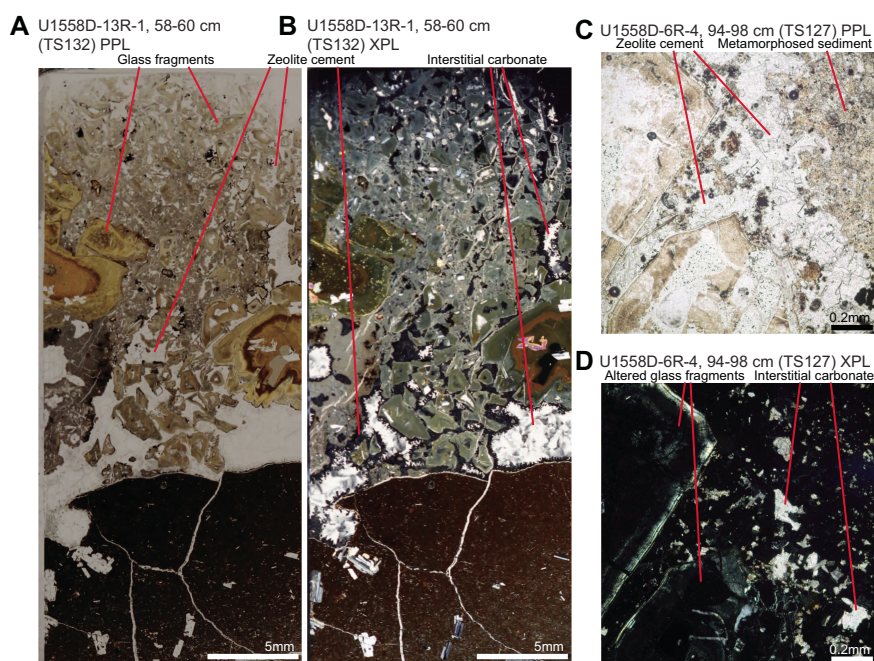
precipitation of calcium carbonate in the center of the vein (Figure F54C). However, in other examples, calcium carbonate lines the vein wall and clay occurs in the core, suggesting a contrasting fracture-precipitation sequence (Figure F54D). Crack-seal stretching veins occur and are differentiated by multiple successive episodes of fracturing and precipitation along differing arbitrary fracture planes, resulting in a heterogeneously stretched crystal morphology and the incorporation of wall rock into the vein assemblage (e.g., Figure F54B–F54D; Bons et al., 2012). Calcium carbonate veins preserve a range of internal microstructures from primary crack-seal syntaxial growth to crack-seal stretching veins (Figure F54B–F54D) including fibrous calcium carbonate antitaxial veins (Figure F54A). Some calcium carbonate veins display variable extents of recrystallization and preservation of original microstructures (Figure F54A–F54D).

## 6.6. Structural data

The dip direction and dip angle of 30% of logged veins were measured with true dip angles ranging between 2° and 90° (Figure F55). The median vein true dip angle of measured veins is 50°, and the mean vein true dip angle is 48° (Figure F55). The distribution of all measured vein true dip angles generally yields a weakly bimodal distribution (Figure F55B) with 31% of veins ranging 45°–67.5° and 26% of veins ranging 7.5°–30°. No systematic relationship between true vein dip angle and depth occurs (Figure F55). Single event veins generally yield a uniform distribution, whereas multiple event veins dominate the orientated logged vein budget and show a bimodal distribution, with a first mode between 20° and 30° and a second mode occurring between 50° and 70° (Figure F56). The lack of subvertical and subhorizontal veins is mostly an artifact of recovery and the inherently low likelihood of intersecting steeply dipping features during coring and core breaks with grinding along gently dipping veins.

## 6.7. X-ray diffraction

To refine macroscopic observations of secondary mineralogy, XRD spectra were generated for powdered materials from veins, vugs, and fracture surfaces and for bulk rock powders. The spectra evaluation reveals dominantly (magnesian) calcite and/or phillipsite-Na and other zeolite minerals in vein, vug, and fracture surface fillings both within the interior of basaltic pillows/flows as well as in veins in glassy margins (Table T8). Spectra from interpillow sediments and breccia matrix and cement are chiefly representative of (magnesian) calcite and phillipsite-Na, but addi-



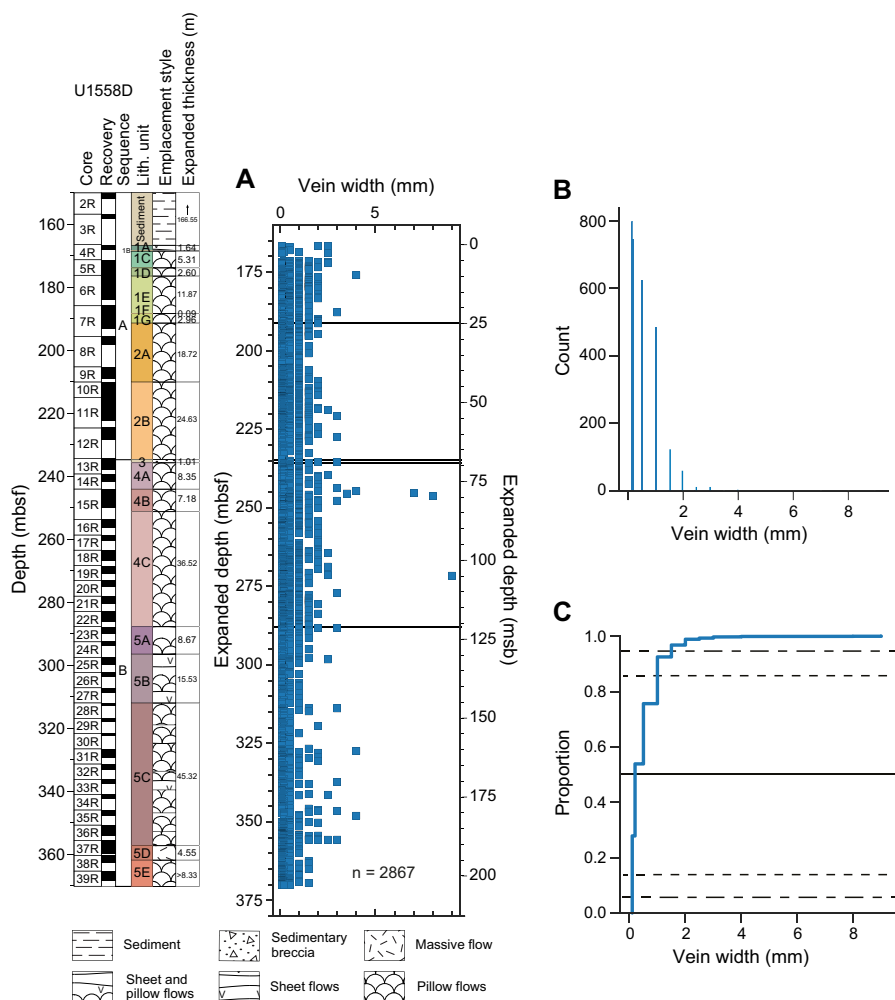
**Figure F48.** Zeolite-cemented breccias, Hole U1558D. A, B. Altered glass fragments cemented by zeolites; euhedral carbonate has formed in larger interstices. C, D. Altered glass fragments and recrystallized sediment cemented by mostly zeolites.



tional peaks suggest the presence of clays such as the smectite montmorillonite. Altered clasts within interpillow breccias further suggest an anorthite component. The results from XRD analyses of bulk rock powders (see U1558D\_XRD.xlsx in ALTPET in **Supplementary material**) reveal mostly sodic feldspars and clinopyroxene as well as minor olivine, oxides, and additional spectral peaks that indicate the variable presence of clays, presumably montmorillonite.

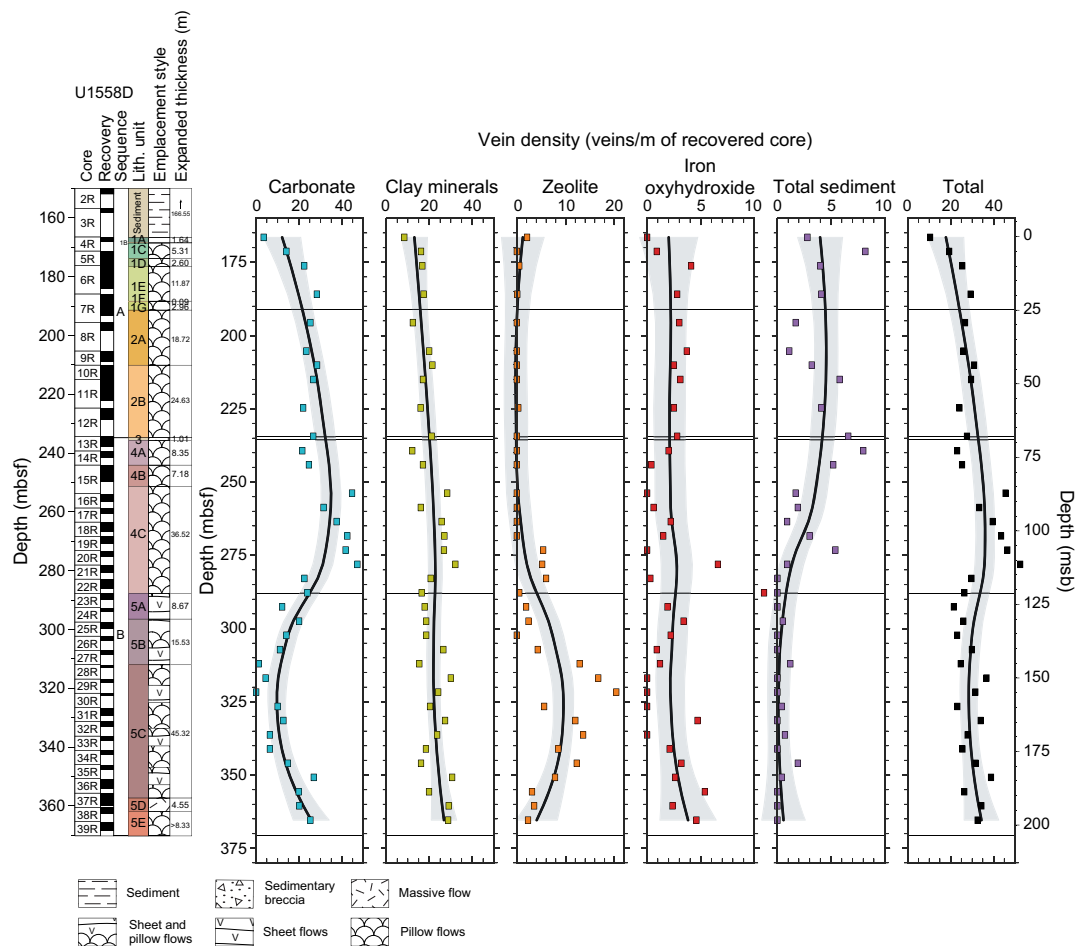
### 6.8. Summary

Alteration in Hole U1558D can be distinguished into four zones (Figure F57). From the top of the hole to 179 mbsf in Unit 1, dominant brown halo alteration is associated with the chilled margins of pillow lavas. Between 179 and 234 mbsf (partway through Subunit 1E to the base of Subunit 2B), the second zone sees the abundance of all halo types drop and gray background alteration and orange speckled background alteration of the pillow lavas dominate the alteration. This shift from brown halo dominated to background alteration dominated is interpreted to represent a seafloor weathering overprint and suggests that the pillow lavas were exposed to open circulation of seawater for some period of time before becoming covered with sediment. The third zone (234–286 mbsf) is broadly associated with Units 3 and 4 and is marked by the first appearance of orange alteration within pillow lavas. This alteration represents the strongest color change in Hole U1558D and is generally associated with alteration fronts developing from the glassy margins of

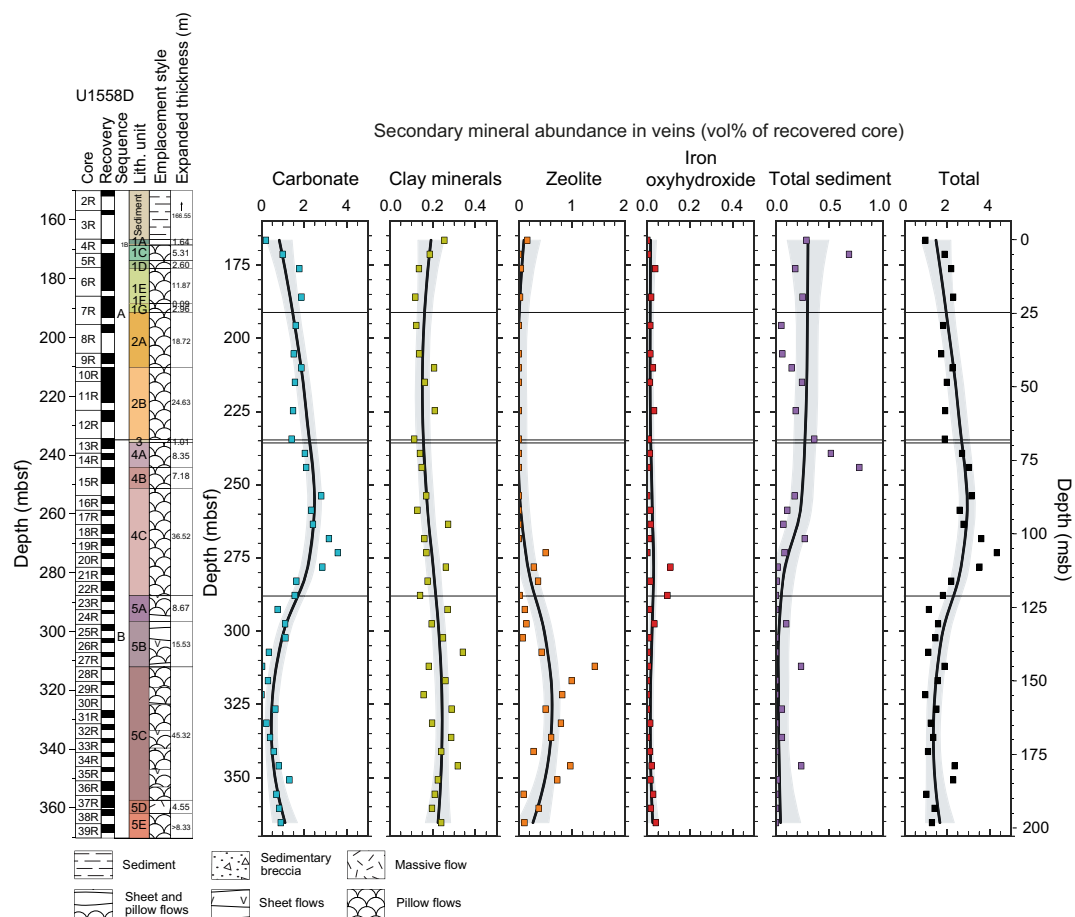


**Figure F49.** A–C. Vein width characteristics, Hole U1558D. C: solid line = median value (0.5 proportion), dashed lines = 1σ equivalent range of median, dot-dashed lines = 2σ equivalent range of median. Expanded depth scale stretches curated depths within each core advance to compensate for incomplete recovery (see Expedition 390/393 methods chapter [Coggon et al., 2024b]).

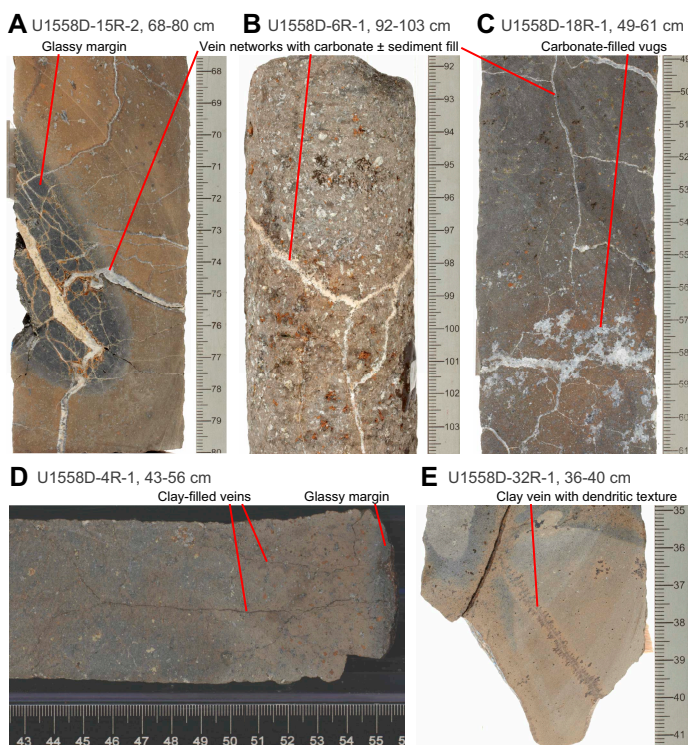
individual pillows. Macroscopically, several centimeters away from chilled margins, these orange alteration fronts transition into the more ubiquitous brown halos seen throughout Hole U1558D, suggesting this oxidative alteration exists along a spectrum of intensity. Some of the freshest volcanic glass is preserved where groundmass alteration of the pillow lavas is strongest, as previously documented (e.g., Honnorez, 1981). The abundance of breccia and sediment at the top of this interval suggests that these rocks were also exposed to seawater for a significant duration before becoming covered by the overlying lava sequences. The fourth alteration zone is defined by the onset of mixed gray-brown background alteration that has a common but not unique association with variolitic textures. The orange halos persist through this change in background alteration with orange examples of variolitic textures recovered. Although there are some associations between the igneous units and the different alteration zones, the onset of the key alteration features defining the zones do not generally follow igneous boundaries. The downhole changes in secondary minerals filling veins also do not follow the alteration zones, in particular with the dominance of zeolites toward the base of the hole occurring above the onset of the fourth (mixed gray-brown background alteration) zone.



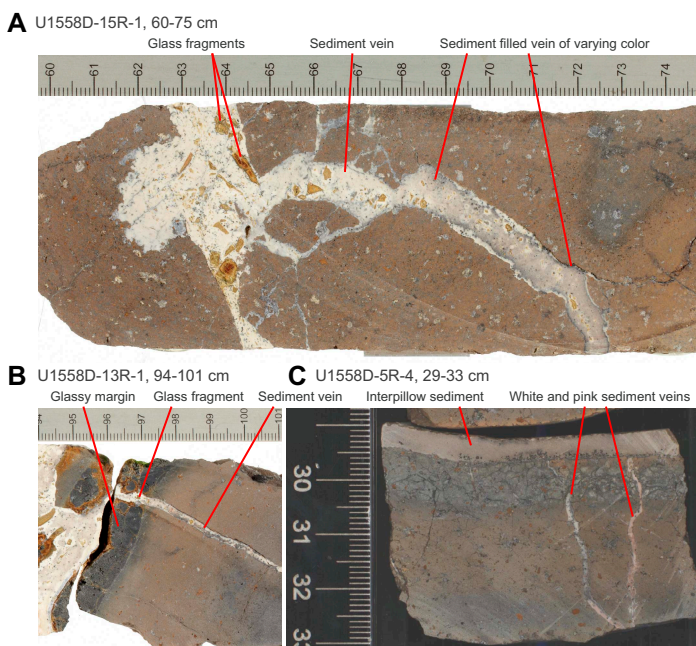
**Figure F50.** Vein density per meter normalized to core recovery, Hole U1558D. Total veins are separated by secondary mineral fill. Data plotted at top depth of each core. Black trend lines = locally weighted scatter plot smoothing (LOWESS) non-parametric regression, gray shading =  $2\sigma$  of mean.



**Figure F51.** Secondary mineral abundance in veins normalized to core recovery, Hole U1558D. Data plotted at top depth of each core. Black trend lines = locally weighted scatter plot smoothing (LOWESS) nonparametric regression, gray shading =  $2\sigma$  of mean.

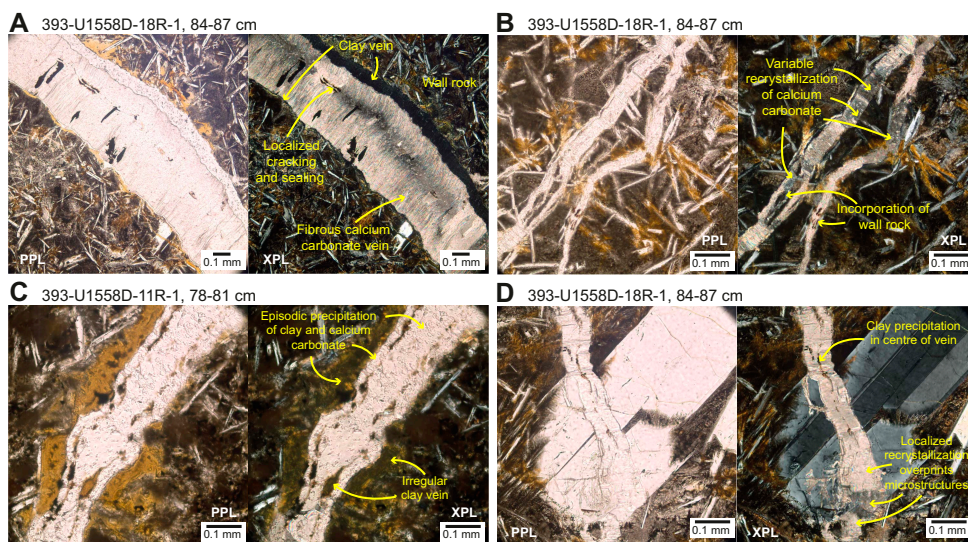


**Figure F52.** Characteristics of carbonate, sediment, and clay fillings in hydrothermal veins, Hole U1558D. A. Several veins crosscut glassy chilled margin and run perpendicular into pillow. In pillow lavas, veins are dominantly filled with carbonate, but in glassy chilled margins this transitions into indurated calcareous sediment. B. Network of veins filled with carbonate  $\pm$  indurated calcareous sediment on outer core surface. C. Branched carbonate-filled veins. Vuggy space in the interior is also filled with carbonate. D. Several narrow veins filled with brown clay perpendicular to chilled margin. E. Clay vein with dendritic halo texture.

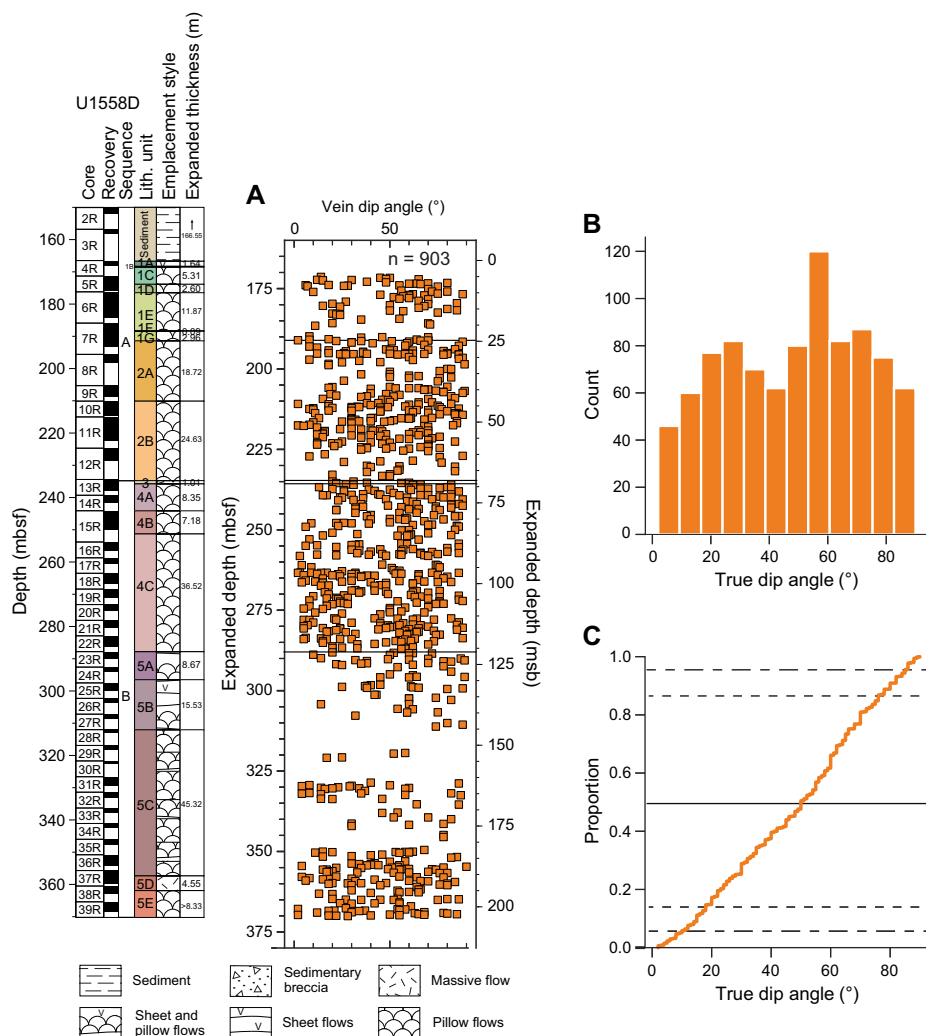


**Figure F53.** Sediment-filled veins, Hole U1558D. A. Centimeter-wide fractures are filled with white-beige sediment with fragments of altered glass and small opaque grains, presumably oxides, irregularly distributed throughout. B. Sediment-filled vein cutting across glassy margin into pillow. Vein is clearly connected to interpillow sediment and contains glass fragments and opaques, similar to A. C. White and pink sediment in veins extending from interpillow sediment into chilled margin. Note compositional changes in veins.

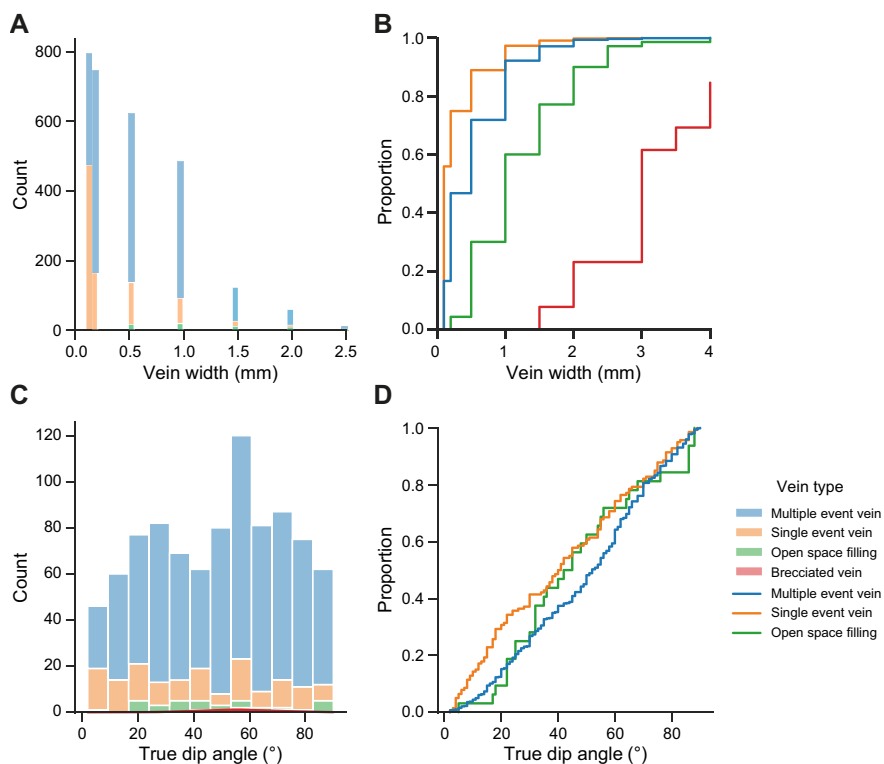




**Figure F54.** Vein microstructures, Hole U1558D. A. Typical vein assemblage with multiple generations of precipitation of vein material. Vein edge is lined with clay; subsequent precipitation of antitaxial fibrous calcium carbonate occurred closer to vein center. Localized cracking and sealing occurred along median line of fibrous calcium carbonate vein with formation of syntaxial calcium carbonate in center of vein assemblage. B. Typical crack-seal stretching calcium carbonate vein assemblage with localized incorporation of wall rock with variable recrystallization of calcium carbonate. C. Typical crack-seal clay–calcium carbonate vein assemblage with distinct episodic events of cracking and clay and calcium carbonate precipitation and partial preservation of vein microstructures. D. Multigeneration vein composed of calcium carbonate with local formation of clay in partially crack-sealed vein center. Localized calcium carbonate recrystallization overprints vein microstructure resulting in variable preservation of original textures.



**Figure F55.** A. Vein dip angles, Hole U1558B. B. Histogram is binned into 12 distinct groups (spaced 7.5° each) with probability density function showing bimodal distribution. C. Dip angle proportions. Solid line = median value (0.5 proportion), dashed lines = 1σ equivalent range of median, dot-dashed lines = 2σ equivalent range of median. Expanded depth scale stretches curated depths within each core advance to compensate for incomplete recovery (see Expedition 390/393 methods chapter [Coggon et al., 2024b]).



**Figure F56.** Vein width and dip angle statistics, Hole U1558D. A. Vein width histogram of vein types: single-event veins (massive veins; see Alteration petrology in the Expedition 390/393 methods chapter [Coggon et al., 2024b]), multiple event veins (polycrystalline and crack-seal veins), and open space fillings with respective probability density. B. Vein width cumulative frequency of differing vein types. C. Vein dip angle histogram of vein types. D. Vein dip angle cumulative frequency of differing vein types.

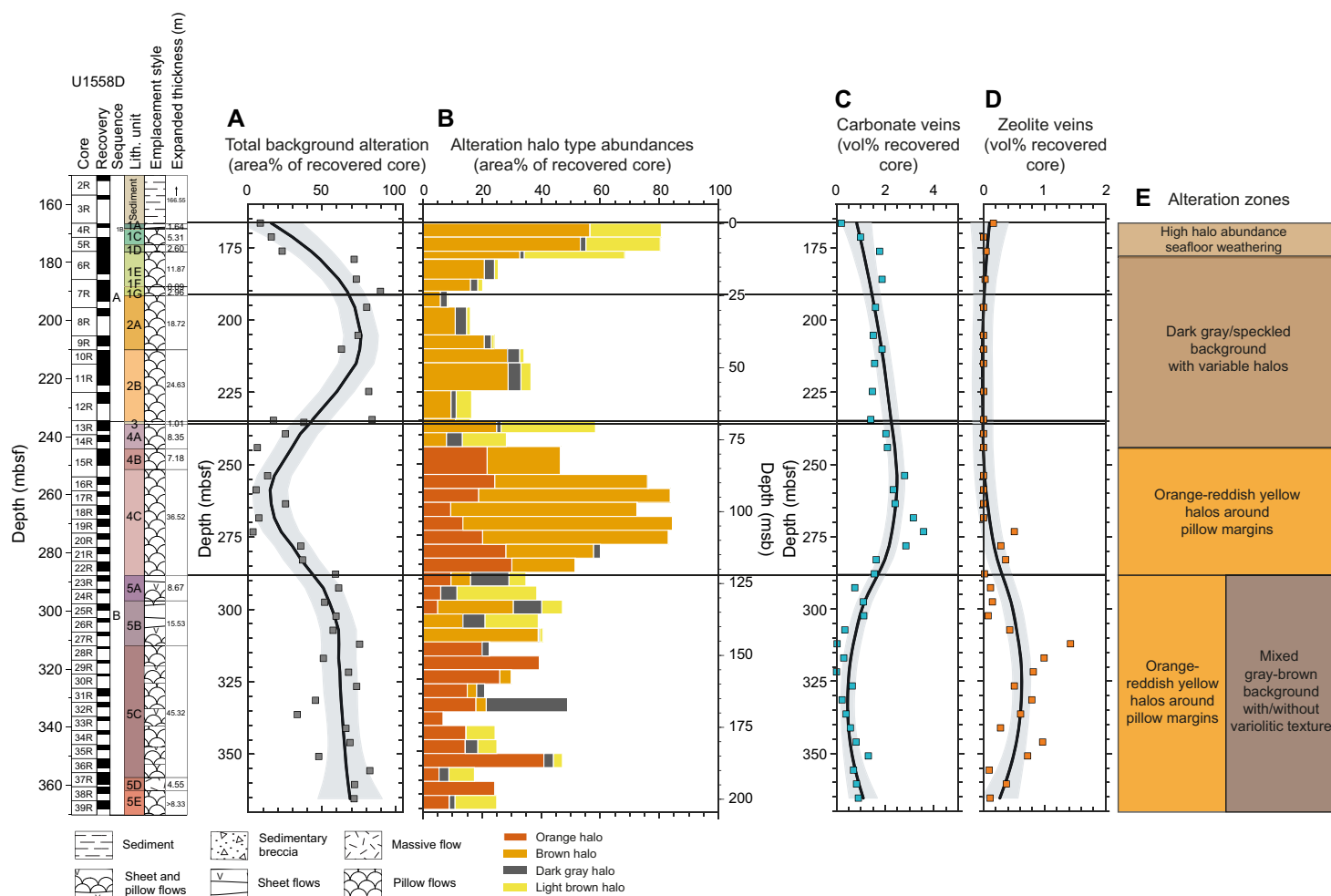


Figure F57. A–E. Overview of alteration zones, Hole U1558D.

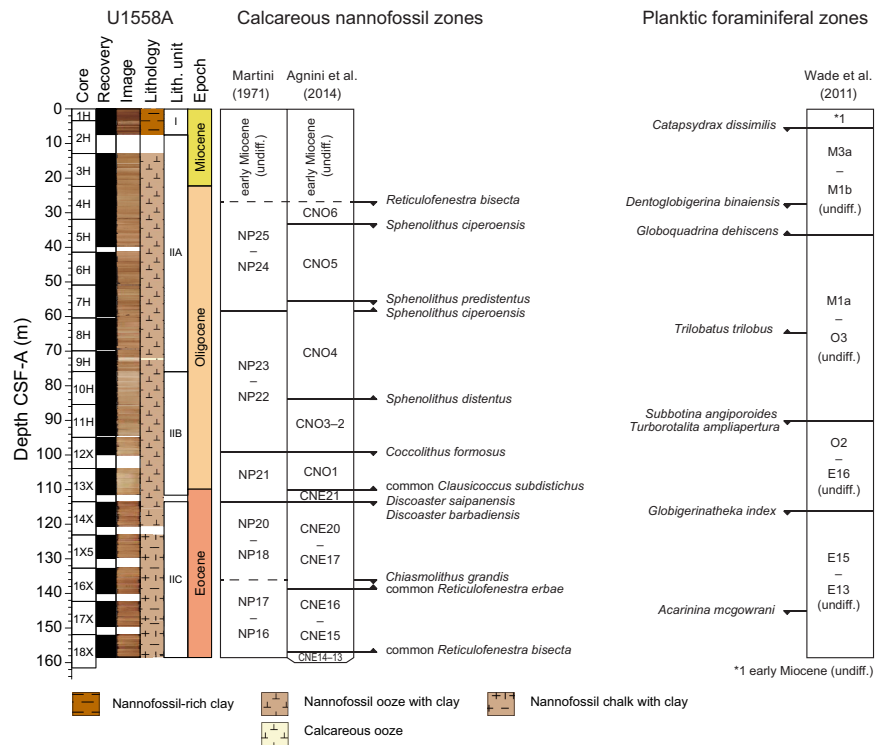
## 7. Biostratigraphy

The 158.5–175.4 m thick sedimentary succession of pelagic nannofossil oozes/chalks and nannofossil-rich clays at Site U1558 ranges in age from the Early Miocene to late Eocene (see [Sedimentology](#)). The integrated calcareous nannoplankton and planktic foraminiferal biozonation for Site U1558 is summarized in Figures [F58](#) and [F59](#) and Tables [T10](#) and [T11](#). The list of biostratigraphic datums and paleomagnetic reversals used to construct the age model for Holes U1558A and U1558F can be found in [Age model and mass accumulation rates](#) (Tables [T23](#), [T24](#); Figures [F79](#), [F80](#)).

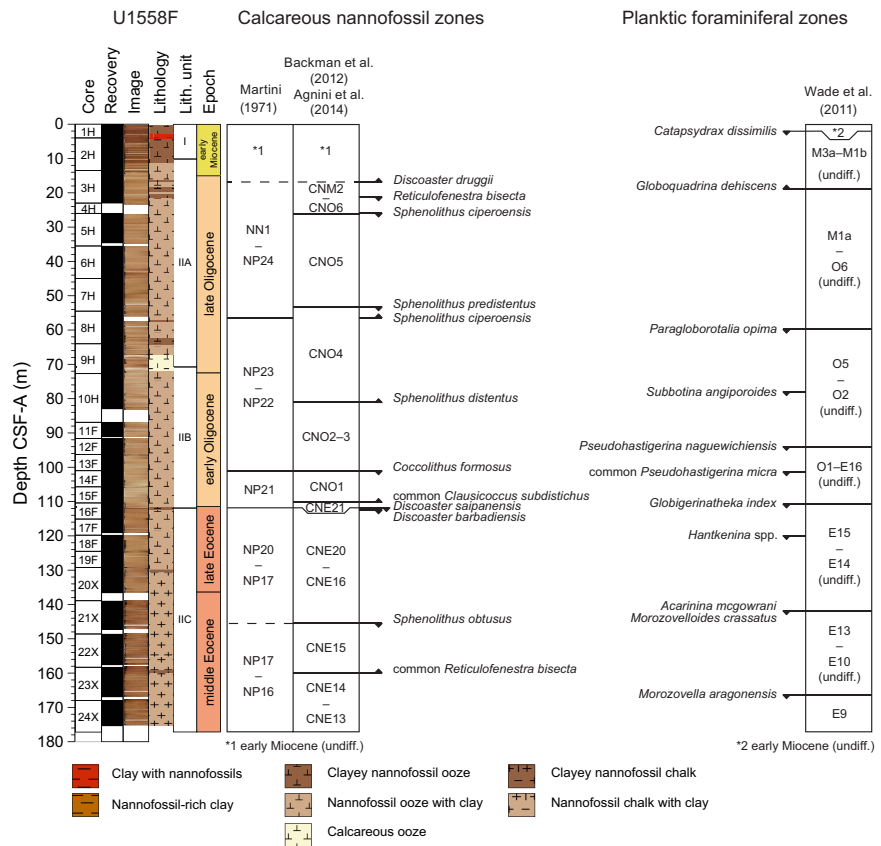
Samples analyzed from Hole U1558A were primarily core catcher samples studied onshore following Expedition 390C (see [Background and objectives](#)). These samples were supplemented by nannoplankton smear slides taken on the ship during Expedition 393 from the archive halves of Hole U1558A. Samples analyzed from Hole U1558F, cored during Expedition 393, came from core catcher samples (some of which were only ~5 m apart because of half-length coring operations), and two additional smear slide samples for each full-length core (or one sample per half-length core) were taken from the working halves. These additional samples were taken at evenly spaced intervals, avoiding clay-rich intervals where possible.

The Hole U1558A mudline sample is barren; however, given the presence of microfossils in the Hole U1558F mudline sample, this is likely the result of some sort of sampling bias during Expedition 390C. The Pleistocene and Pliocene epochs are completely missing from Hole U1558A; Sam-





**Figure F58.** Calcareous nannofossil and planktic foraminiferal biostratigraphic zones and datums, Hole U1558A. Upward arrows = bioevent base (first occurrence), downward arrows = bioevent top (last occurrence).



**Figure F59.** Calcareous nannofossil and planktic foraminiferal biostratigraphic zones and datums, Hole U1558F. Upward arrows = bioevent base (first occurrence), downward arrows = bioevent top (last occurrence).

ple 390C-U1558A-1H-CC contains microfossils indicative of a Middle to Early Miocene age. In contrast, the Hole U1558F mudline sample contains Pleistocene planktic foraminifera, whereas calcareous nannoplankton assemblages comprise a predominantly modern assemblage mixed with some reworked Miocene and Paleogene taxa.

**Table T10.** Integrated calcareous nannofossil and planktic foraminiferal datums, Hole U1558A. T = top, B = bottom, Bc = base common. Nannofossil biozonation follows Martini (1971), Backman et al. (2012), and Agnini et al. (2014), and planktic foraminiferal biozonation is based on Wade et al. (2011). [Download table in CSV format.](#)

Datum type/Taxon	Biozone	Age (Ma)	Core, section, interval above (cm)	Sample above depth CSF-A (m)	Sample above depth CSF-B (m)	Core, section, interval below (cm)	Sample below depth CSF-A (m)	Sample below depth CSF-B (m)	Midpoint depth CSF-A (m)	Midpoint depth CSF-B (m)	Depth error (±) CSF-A (m)	Depth error (±) CSF-B (m)
			390C-U1558A-			390C-U1558A-						
<i>T Reticulofenestra bisecta</i>	in CNO6/in NP25	23.13	4H-3, 20	25.60	25.44	4H-5, 35	28.76	28.45	27.18	26.95	1.58	1.51
<i>T Sphenolithus ciperoensis</i>	T CNO5/in NP25	24.36	4H-CC	32.34	31.85	5H-2, 107	34.48	34.48	33.41	33.17	1.07	1.31
<i>T Sphenolithus predistentus</i>	T CNO4/in NP24	26.93	7H-3, 4	53.94	53.94	7H-5, 6	56.97	56.97	55.46	55.46	1.52	1.52
<i>B Sphenolithus ciperoensis</i>	in CNO4/T NP23	27.13	7H-5, 6	56.97	56.97	7H-CC	60.09	60.09	58.53	58.53	1.56	1.56
<i>B Sphenolithus distentus</i>	T CNO3/in NP23	30	10H-5, 40	82.31	82.11	10H-CC	85.71	85.40	84.01	83.76	1.70	1.65
<i>T Coccolithus formosus</i>	T CNO1/T NP21	32.92	12X-3, 37	98.20	98.20	12X-CC	100.10	100.10	99.15	99.15	0.95	0.95
<i>Bc Clausiococcus subdistichus</i>	T CNE21/in NP21	33.88	13X-4, 51	108.90	108.90	13X-CC	111.61	111.61	110.26	110.26	1.36	1.36
<i>T Discoaster saipanensis</i>	T CNE20/T NP20	34.44	13X-CC	111.56	111.56	14X-2, 81	115.81	115.81	113.69	113.69	2.13	2.13
<i>T Discoaster barbadiensis</i>	in CNE20/in NP20	34.77	13X-CC	111.56	111.56	14X-2, 81	115.81	115.81	113.69	113.69	2.13	2.13
<i>T Chiasmolithus grandis</i>	in CNE16/in NP17-18	37.77	16X-2, 94	135.14	135.14	16X-4, 36	137.55	137.55	136.35	136.35	1.21	1.21
<i>Bc Reticulofenestra erbae</i>	T CNE16/T NP17	37.88	16X-4, 36	137.55	137.55	16X-CC	140.19	140.19	138.87	138.87	1.32	1.32
<i>Bc Reticulofenestra bisecta</i>	T CNE14/in NP16	40.25	18X-3, 130	156.20	156.20	18X-CC	158.41	158.41	157.31	157.31	1.10	1.10
<i>T Catapsydrax dissimilis</i>	M3	17.51	1H-CC, 9-14	3.42	3.35	2H-CC, 21-26	7.48	7.48	5.45	5.42	2.03	2.06
<i>T Dentoglobigerina binaiensis</i>	in M3	19.26	3H-CC, 0-5	22.22	22.22	4H-CC, 34-39	32.39	31.90	27.31	27.06	5.09	4.84
<i>B Globoquadrina dehiscens</i>	M1b	22.5	4H-CC, 34-39	32.34	31.85	5H-CC, 17-22	39.88	39.88	36.11	35.87	3.77	4.01
<i>B Trilobatus trilobus</i>	in M1a	22.88	7H-CC, 10-15	60.05	60.05	8H-CC, 10-15	69.51	69.51	64.78	64.78	4.73	4.73
<i>T Subbotina angiporoides</i>	in O3	30.1	10H-CC, 16-21	85.66	85.35	11H-CC, 31-36	94.50	94.50	90.08	89.93	4.42	4.57
<i>T Turborotalia ampliapertura</i>	O2	30.4	10H-CC, 16-21	85.66	85.35	11H-CC, 31-36	94.50	94.50	90.08	89.93	4.42	4.57
<i>T Globigerinatheka index</i>	E15	34.5	13X-CC, 9-14	111.56	111.56	14X-CC, 21-26	120.66	120.66	116.11	116.11	4.55	4.55
<i>T Acarinina mcgowrani</i>	in E13	37.7	16X-CC, 15-20	140.14	140.14	17X-CC, 15-20	149.58	149.58	144.86	144.86	4.72	4.72

**Table T11.** Integrated calcareous nannofossil and planktic foraminiferal datums, Hole U1558F. T = top, B = bottom, HCO = highest common occurrence, Bc = bottom common. ML = mudline core. Nannofossil biozonation follows Martini (1971), Backman et al. (2012), and Agnini et al. (2014). Planktonic foraminiferal biozonation is based on Wade et al. (2011). [Download table in CSV format.](#)

Datum type/Taxon	Biozone	Age (Ma)	Core, section, interval above (cm)	Sample above depth CSF-A (m)	Sample above depth CSF-B (m)	Core, section, interval below (cm)	Sample below depth CSF-A (m)	Sample below depth CSF-B (m)	Midpoint depth CSF-A (m)	Midpoint depth CSF-B (m)	Depth error (±) CSF-A (m)	Depth error (±) CSF-B (m)
			393-U1558F-			393-U1558F-						
<i>B Discoaster druggii</i>	in CNM2/T NN1	22.68	2H-CC	13.99	13.45	3H-3, 1-3	19.61	19.54	16.80	16.50	2.81	3.05
<i>T Reticulofenestra bisecta</i>	in CNO6/in NP25	23.13	3H-5, 7-9	19.59	19.52	3H-CC, 41-46	23.11	23.00	21.35	21.26	1.76	1.74
<i>T Sphenolithus ciperoensis</i>	T CNO5/in NP25	24.36	3H-CC, 41-46	23.06	22.95	5H-2, 136-138	28.85	28.85	25.96	25.90	2.89	2.95
<i>T Sphenolithus predistentus</i>	T CNO4/in NP24	26.93	7H-5, 88-90	51.91	51.59	7H-CC, 34-39	54.96	54.50	53.44	53.05	1.52	1.45
<i>B Sphenolithus ciperoensis</i>	in CNO4/T NP23	27.13	7H-CC, 34-39	54.91	54.45	8H-3, 25-27	57.79	57.61	56.35	56.03	1.44	1.58
<i>B Sphenolithus distentus</i>	T CNO3/in NP23	30	10H-5, 58-60	79.31	79.31	10H-CC, 34-39	83.05	83.05	81.18	81.18	1.87	1.87
<i>T Coccolithus formosus</i>	T CNO1/T NP21	32.92	13F-2, 80-82	98.60	98.58	14F-2, 78-80	103.30	103.19	100.95	100.89	2.35	2.31
<i>Bc Clausiococcus subdistichus</i>	T CNE21/in NP21	33.88	15F-3, 84-85	109.55	109.45	15F-CC, 13-14	110.53	110.40	110.04	109.93	0.49	0.47
<i>T Discoaster saipanensis</i>	T CNE20/T NP20	34.44	16F-1, 130-135	111.74	111.69	16F-2, 1-2	111.92	111.86	111.83	111.78	0.09	0.08
<i>T Discoaster barbadiensis</i>	in CNE20/in NP20	34.77	16F-2, 1-2	111.91	111.85	16F-2, 118-120	113.10	113.00	112.51	112.43	0.59	0.58
<i>T Sphenolithus obtusus</i>	T CNE15/in NP17	38.42	21X-4, 87-89	144.27	144.27	21X-CC, 28-33	147.29	147.29	145.78	145.78	1.51	1.51
<i>Bc Reticulofenestra bisecta</i>	T CNE14/in NP16	40.25	22X-CC, 15-20	157.58	157.58	23X-3, 81-83	162.12	162.12	159.85	159.85	2.27	2.27
<i>T Catapsydrax dissimilis</i>	M3	17.51	1H-1, 0-0 (ML)	0.00	0.00	1H-CC, 10-15	4.03	4.00	2.02	2.00	2.02	2.00
<i>B Globoquadrina dehiscens</i>	M1b	22.5	2H-CC, 15-20	13.99	13.45	3H-CC, 41-46	23.11	23.00	18.55	18.23	4.56	4.77
<i>T Paragloborotalia opima</i>	O5	27.3	7H-CC, 34-39	54.91	54.45	8H-CC, 16-21	64.56	64.00	59.74	59.23	4.83	4.77
<i>T Subbotina angiporoides</i>	in O3	30.1	9H-CC, 14-19	72.65	72.65	10H-CC, 34-39	83.05	83.05	77.85	77.85	5.20	5.20
<i>T Pseudohastigerina naguiewichiensis</i>	O1	32.2	11F-CC, 15-20	91.08	91.08	12F-CC, 16-21	96.57	96.30	93.83	93.69	2.75	2.61
<i>HCO Pseudohastigerina micra</i>	in O1	33.9	12F-CC, 16-21	96.52	96.25	14F-CC, 9-14	105.93	105.70	101.23	100.98	4.71	4.72
<i>T Globigerinatheka index</i>	E15	34.5	14F-CC, 9-14	105.88	105.65	16F-CC, 15-20	115.29	115.10	110.59	110.38	4.70	4.72
<i>T Acarinina mcgowrani</i>	in E13	37.7	20X-CC, 20-25	136.62	136.62	22X-CC, 15-20	147.29	147.29	141.96	141.96	5.34	5.34
<i>T Morozovelloides crassatus</i>	E13	37.7	20X-CC, 20-25	136.62	136.62	22X-CC, 15-20	147.29	147.29	141.96	141.96	5.34	5.34
<i>T Morozovella aragonensis</i>	E9	42.6	22X-CC, 15-20	157.58	157.58	24X-CC, 15-17	175.31	175.31	166.45	166.45	8.87	8.87

Biostratigraphic analyses indicate that Miocene sediments are recorded above 22.27 m core depth below seafloor, Method B (CSF-B), in Hole U1558A and above 13.50 m CSF-B in Hole U1558F. This corresponds to Lithostratigraphic Unit I and the uppermost part of Subunit IIA in both holes (Figures F58, F59). Oligocene-aged sediments are recorded from 31.85–108.90 m CSF-B in Hole U1558A and 28.83–110.40 m CSF-B in Hole U1558F. This generally overlaps with Subunits IIA and IIB (Figures F58, F59). The Eocene/Oligocene boundary is inferred in the lowermost part of Subunit IIB (at 108.90 m CSF-B in Hole U1558A and 109.45 m CSF-B in Hole U1558F).

Benthic foraminifera were analyzed onshore using core catcher samples from Hole U1558A. The data collected suggest that Site U1558 lay at upper abyssal depths (~2000–3000 m) during the Eocene and subsided to lower abyssal depths (>3000 m) by the early Oligocene.

## 7.1. Age of basement

The top of the sediment/basement interface in both Holes U1558A and U1558F contained *Reticulofenestra umbilicus*, suggesting these sediments are younger than 42.72 Ma. The planktic foraminifera *Globigerinatheka index*, which has a first occurrence at 42.9 Ma, is also present directly above basement in both holes. Together, these taxa indicate that the sediment/basement interface is between 42.72 and 42.9 Ma, substantially younger than the estimated crustal age of 49.2. A single limestone sample from the sediment/basement interface in Hole U1558D was analyzed for calcareous nannoplankton, but preservation was very poor and nannofossils did not yield any reliable age estimates. Thin section Sample 393-U1558D-4R-1, 62–65 cm (167.12 m CSF-B), taken from interpillow limestone, was analyzed for the presence of age-diagnostic planktic foraminifera. The sample largely contains fragments of planktic foraminiferal tests as well as a few whole specimens belonging to the common late Eocene genera *Subbotina* and *Acarinina*. Unfortunately, identification to the species level was not possible and no tighter age constraints are provided.

## 7.2. Calcareous nannofossils

Core catcher samples and additional smear slide samples from Holes U1558A and U1558F were analyzed to establish the calcareous nannofossil biostratigraphy at this site. Calcareous nannofossil preservation and abundance are presented in Figure F60. Nannofossil occurrence data are shown in Tables T12 and T13; note that the distribution chart is biased toward age-diagnostic and other notable taxa. Light photomicrographs of selected calcareous nannofossil specimens from Site U1558 are shown in Figure F61.

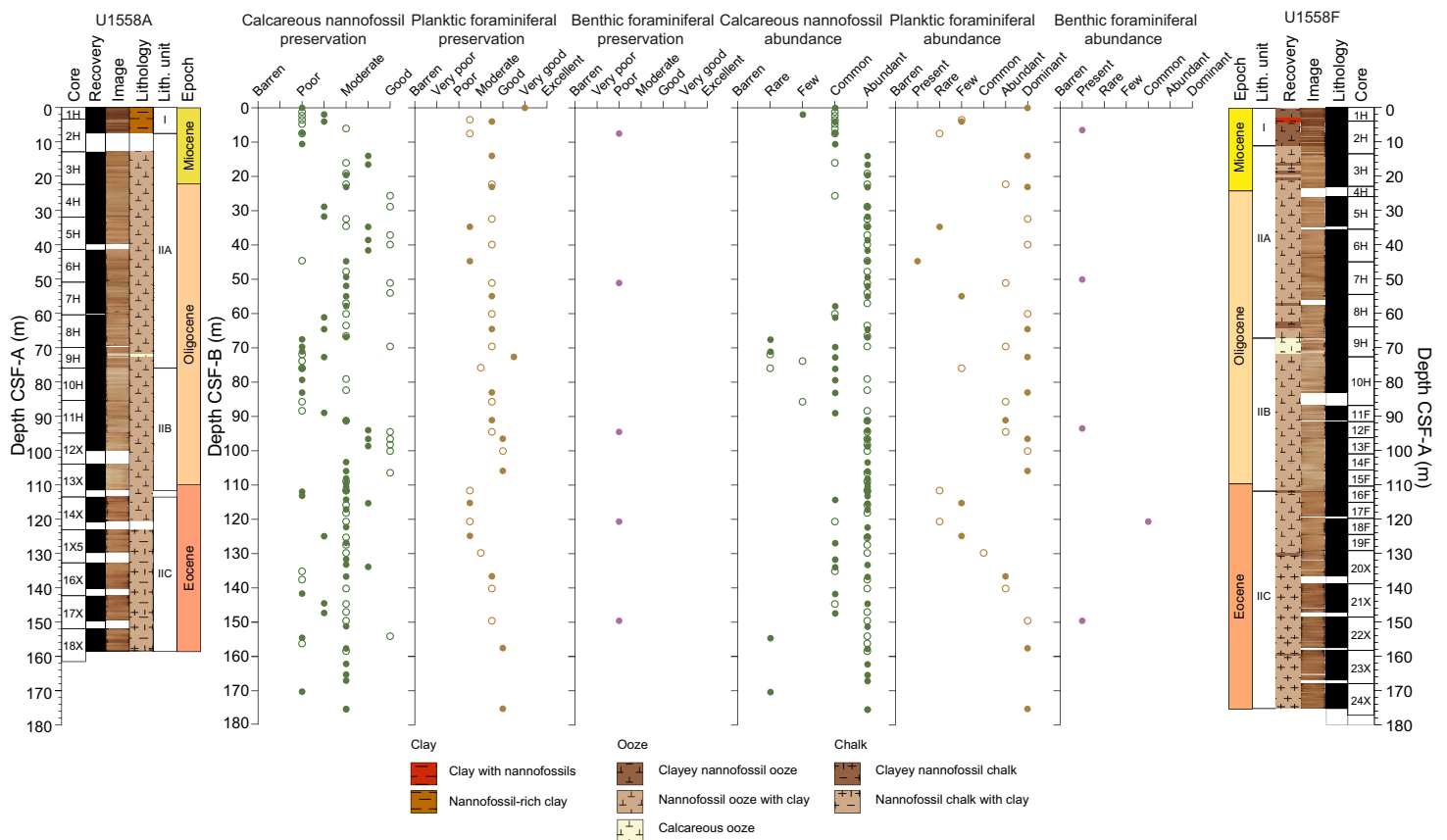
Nannofossil preservation at Site U1558 varies from poor to good, and nannofossils are generally abundant (Figure F60). In nannofossil-rich clay samples (Lithostratigraphic Unit I; see **Sedimentology**), nannofossils are common to abundant with poor preservation. In contrast, nannofossils are abundant with varying degrees of preservation (poor to good) in the carbonate-rich samples (Lithostratigraphic Unit II). At this site, reworked specimens of Eocene and early Oligocene nannofossils, such as *Discoaster barbadiensis*, *Discoaster saipanensis*, and *R. umbilicus* are present in middle Oligocene–Neogene samples overlying Cores 390C-U1558A-11H and 393-U1558F-16F (~88 and ~111 m CSF-B).

Taxa that evolved after the Middle Miocene, such as *Gephyrocapsa*, *Florisphaera*, and *Pseudoemiliana*, are present above Sample 393-U1558F-1H-2, 43–45 cm (1.92 m CSF-B), but are mixed with reworked older taxa (i.e., *Cyclicargolithus floridanus* and *Discoaster deflandrei*). Above Samples 390C-U1558A-3H-CC, 0–5 cm (22.22 m CSF-B), and 393-U1558F-2H-CC, 15–20 cm (13.46 m CSF-B), the sediments are assigned to the Early Miocene because of the presence of *C. floridanus* and absence of Oligocene *Sphenolithus* specimens. No zonation could be assigned to these samples, as there are no age-diagnostic species in the assemblage, which also includes many reworked taxa.

Samples 390C-U1558A-4H-CC, 34–39 cm, through 13X-4, 51 cm (31.85–108.90 m CSF-B), and 393-U1558F-3H-CC, 41–46 cm, through 15F-CC (22.96–110.52 m CSF-B) are placed in the Oligocene. The youngest biohorizon in this interval is the top of *Sphenolithus ciperoensis* (top of Zone CNO5), identified in Samples 390C-U1558A-5H-2, 107 cm (34.48 m CSF-B), and 393-U1558F-5H-2, 136–138 cm (28.83 m CSF-B). The top of *Sphenolithus predistentus* defines the top of Zone

CNO4 and is identified in Samples 390C-U1558A-7H-5, 6 cm (56.97 m CSF-B), and 393-U1558F-7H-CC, 34–39 cm (54.47 m CSF-B). The base of Zone CNO4 is defined by the base of *Sphenolithus distentus* located in Samples 390C-U1558A-10H-5, 40 cm (82.11 m CSF-B), and 393-U1558F-10H-5, 58–60 cm (79.31 m CSF-B). The top of *Coccolithus formosus* (top of Zone CNO1) is recorded within Samples 390C-U1558A-12X-CC, 21–26 cm (100.05 m CSF-B), and 393-U1558F-14F-2, 78–80 cm (103.21 m CSF-B).

The base common of *Clausicoccus subdistichus* (33.88 Ma) is the closest nannofossil datum to the Eocene/Oligocene boundary and is identified in Samples 390C-U1558A-13X-4, 51 cm (108.90 m CSF-B), and 393-U1558F-15F-3, 84–85 cm (109.47 m CSF-B). Samples 390C-U1558A-14X-2, 81 cm (115.81 m CSF-B), and 393-U1558F-16F-2, 1–2 cm (111.85 m CSF-B), through the bottom of the holes comprise an Eocene sequence with a diverse nannofossil assemblage. Two biohorizons close in age, the top of *D. saipanensis* (top of Zone CNE20; 34.44 Ma) and top of *D. barbadiensis* (34.77 Ma), are both recorded in Sample 390C-U1558A-14X-2, 81 cm (115.81 m CSF-B). However, in Hole U1558F, these biohorizons occur more than a meter apart with the top of *D. saipanensis* identified in Sample 393-U1558F-16F-2, 1–2 cm (111.85 m CSF-B), and the top of *D. barbadiensis* in Sample 393-U1558F-16F-2, 118–120 cm (113.02 m CSF-B). The top of *Chiasmolithus grandis* and base common of *Reticulofenestra erbae* (top of Zone CNE16) were identified in Sample 390C-U1558A-16X-4, 36 cm (137.55 m CSF-B). In Hole U1558F, the top of *Sphenolithus obtusus* was identified in Sample 393-U1558F-21X-CC, 28–33 cm (147.24 m CSF-B), and marks the top of Zone CNE15. The base common of *Reticulofenestra bisecta* was recorded in both holes in Samples



**Figure F60.** Downhole variations in group abundance and preservation of calcareous nannofossils and foraminifera, Holes U1558A and U1558F.

**Table T12.** Occurrences of important calcareous nannofossils, Hole U1558A. [Download table in CSV format.](#)

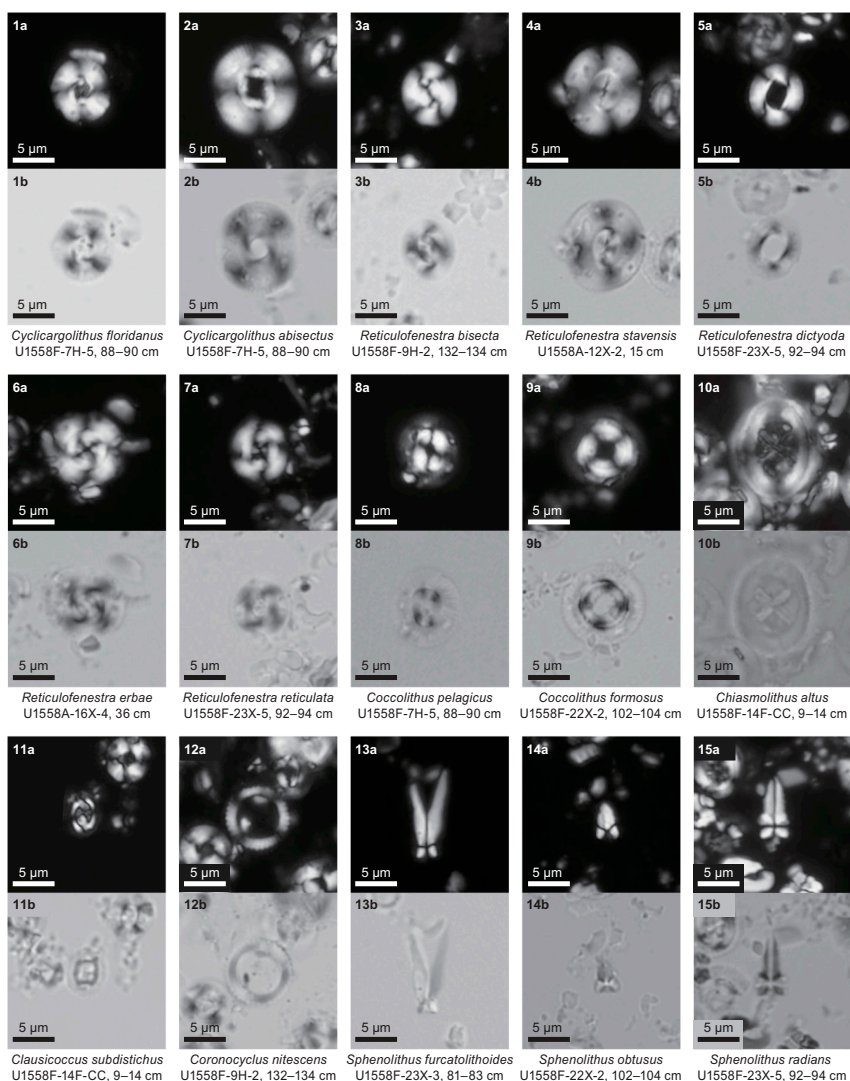
**Table T13.** Occurrences of important calcareous nannofossils, Hole U1558F. [Download table in CSV format.](#)



390C-U1558A-18X-3, 130 cm (156.20 m CSF-B), and 393-U1558F-22X-CC, 15–20 cm (157.58 m CSF-B). The deepest sample analyzed from each hole at Site U1558 contains common *R. umbilicus*, suggesting the sediment is younger than 42.72 Ma (above the base common of *R. umbilicus*). This age agrees with the planktic foraminiferal biostratigraphy as well as the magnetostratigraphy (see **Sediment** in Paleomagnetism; refer to Figures **F79**, **F80**). However, the basal sedimentary age of <42.72 Ma suggests that the overlying sediment is ~6.5 Myr younger than the estimated crustal age for Site U1558 of ~49.2 Ma.

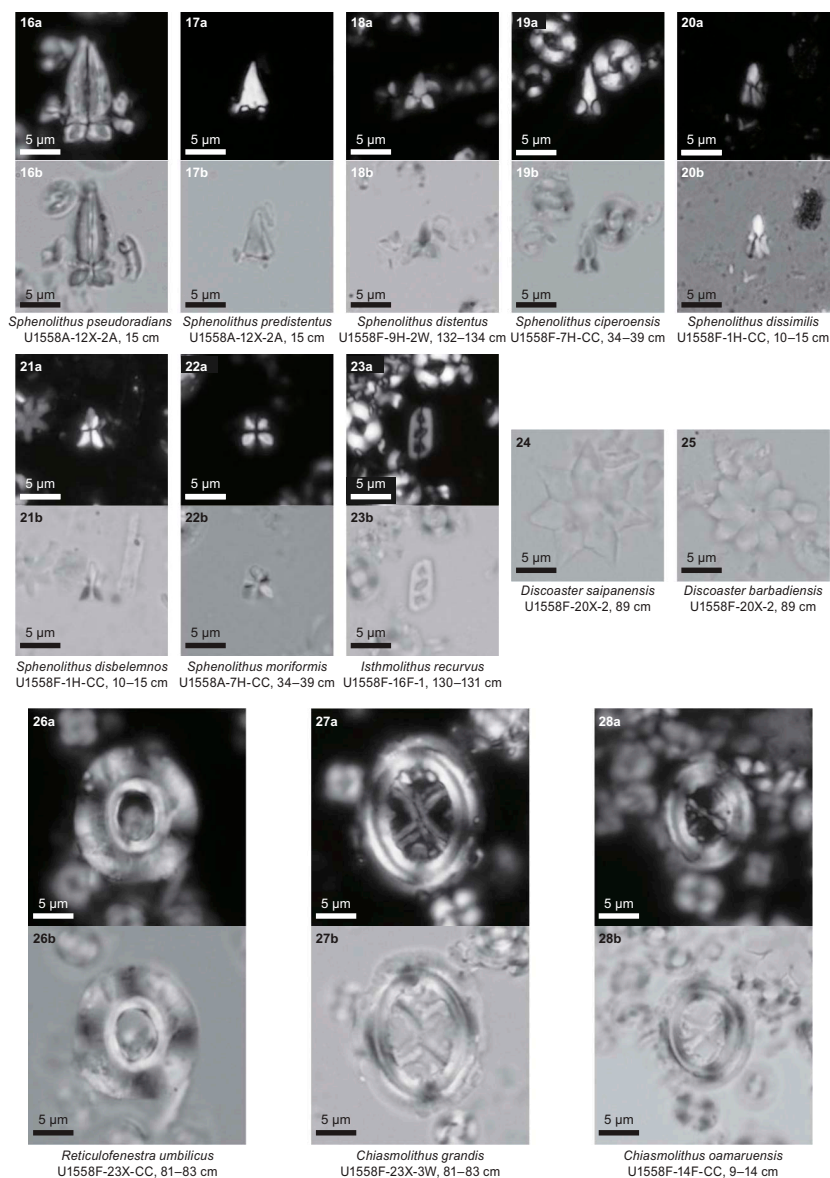
### 7.3. Planktic foraminifera

Occurrences of biostratigraphically significant planktic foraminifera from Holes U1558A and U1558F are summarized in Tables **T14** and **T15**. Planktic foraminiferal abundance and preservation at U1558 varies throughout the sedimentary sequence; preservation ranges from poor to very good and is typically good to moderate (Figure **F60**). Assemblages are often characterized by fragmented specimens and are dominated by robust taxa indicating corrosive conditions at the seafloor. Some samples are nearly barren of planktic foraminifera, in contrast to high numbers of benthic foraminifera, fish teeth, and planktic and benthic foraminiferal fragments, which is indicative of high-dissolution intervals. In most samples, a few robust species dominate the assemblage, including *Catapsydrax* spp., *Subbotina senni*, and *Globigerinatheka* spp. (Figure **F62**).



**Figure F61.** Biostratigraphically important and other notable calcareous nannofossil taxa, Site U1558 ([a] XPL and [b] PPL at 1000× magnification). (Continued on next page.)

The Hole U1558A mudline sample had no particles larger than 63  $\mu\text{m}$ , and as such, the age of the uppermost sediments could not be determined. In contrast, the Hole U1558F mudline sample contained Pleistocene assemblages including *Globorotalia crassaformis*, *Globorotalia truncatulinoides*, *Globorotalia hirsuta*, and *Globorotalia tosaensis*. The presence of *G. hirsuta* (0–0.45 Ma; King et al., 2020) and *G. tosaensis* (0.61–3.35 Ma; King et al., 2020) in the same sample indicates some degree of mixing. However, these species are noted to overlap in the midlatitudes of the Pacific Ocean (Lam and Leckie, 2020; Lam et al., 2022).



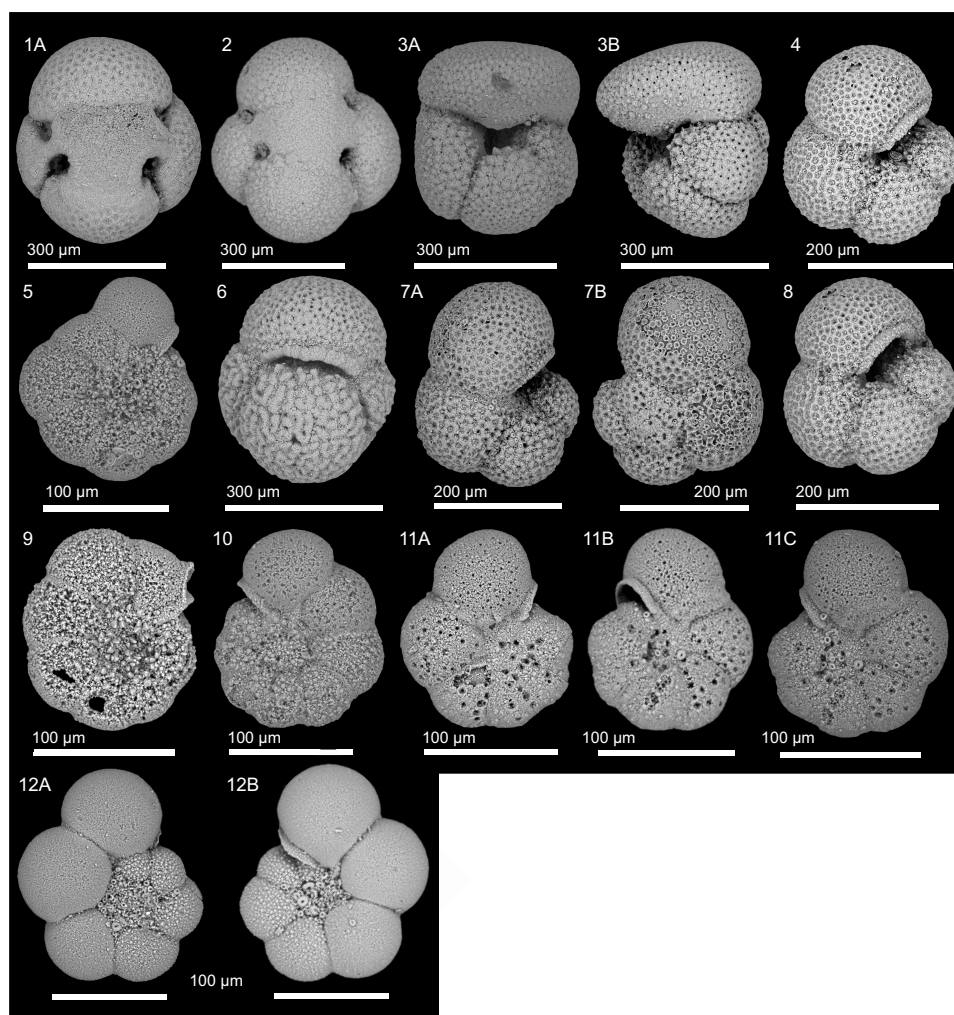
**Figure F61 (continued).** 24 and 25 = PPL.

**Table T14.** Occurrences of biostratigraphically significant planktic foraminifera, Hole U1558A. [Download table in CSV format.](#)

**Table T15.** Occurrences of biostratigraphically significant planktic foraminifera, Hole U1558F. [Download table in CSV format.](#)

Sample 390C-U1558A-1H-CC, 9–14 cm (3.35 m CSF-B), is tentatively placed in Middle Miocene because of the presence of *Globoconella miozea*, a species that ranges from Zones M9a to M5b (13.2–15.9 Ma) in the midlatitudes of the South Pacific Ocean (Site 593; Lam et al., 2022) and has been previously recorded from the Middle Miocene of southwest Atlantic sites (e.g., Site 516; Berggren et al., 1983).

Samples 390C-U1558A-2H-CC, 21–26 cm (7.43 m CSF-B), and 393-U1558F-1H-CC, 10–15 cm (3.95 m CSF-B), both contain *Catapsydrax dissimilis*; the highest occurrence of this taxon marks the top of Zone M3. Samples 390C-U1558A-3H-CC, 0–5 cm, and 4H-CC, 34–39 cm, are unzoned, but Sample 4H-CC, 34–39 cm (31.85 m CSF-B), is likely younger than the base of Zone M1b (22.50 Ma) because of the presence of *Globoquadrina dehiscens*, a basal marker for that zone (King et al., 2020). The same bioevent occurs higher in the sedimentary sequence in Hole U1558F, where *G. dehiscens* is not found below Sample 393-U1558F-2H-CC, 15–20 cm (13.46 m CSF-B). In Hole U1558A, the base of *G. dehiscens* is located between Samples 390C-U1558A-4H-CC, 34–39 cm, and 5H-CC, 17–22 cm (31.85 and 39.83 m CSF-B, respectively). The next three consecutive core catcher samples in Hole U1558A (39.83–60.01 m CSF-B) are assigned to Zone M1a (22.50–22.88 Ma) based on the occurrence of *Trilobatus trilobus*, which has a base within that zone. No *T. trilobus* specimens were observed in Hole U1558F, but Sample 393-U1558F-8H-CC, 16–21 cm



**Figure F62.** Scanning electron microscope images of biostratigraphically important and other notable planktic foraminiferal taxa, Hole U1558F. Each number represents a specimen; differing views of same specimen are denoted by the addition of letters. 1, 2. *Catapsydrax dissimilis* (1: 1H-CC, 10–15 cm; 2: 2H-CC, 21–26 cm). 3. *Globoquadrina dehiscens* (2H-CC, 15–20 cm). 4, 7, 8. *Paragloborotalia opima* (8H-CC, 16–21 cm). 5, 9–11. *Pseudohastigerina nagewichiensis* (5, 9: 12H-CC, 16–21 cm; 10, 11: 14H-CC, 9–14 cm). 6. *Subbotina angiporoides* (10H-CC, 34–39 cm). 12. *Tenuitella gemma* (12H-CC, 16–21 cm).

(63.96 m CSF-B), contains the top of *Paragloborotalia opima*, a late Oligocene taxon whose highest occurrence marks the top of Zone O5 (26.9 Ma). This means that five consecutive core catcher samples from above this bioevent in Hole U1558F (22.96–54.47 m CSF-B) are assigned to Zones M1a–O6 undifferentiated, representing a time span of 4.4 My (22.5–26.9 Ma).

In Hole U1558A, Sample 390C-U1558A-8H-CC, 10–15 cm (69.54 m CSF-B), does not contain *T. trilobus* and is thus no younger than the lower part of Zone M1a. Because this sample does not contain any other age-indicative species aside from long-ranging planktic taxa (e.g., *Catapsydrax unicavus*, *C. dissimilis*, and *Dentoglobigerina tripartita*), it is possible this sample could be Oligocene. Samples 9H-CC, 8–13 cm, and 10H-CC, 16–21 cm (75.85 and 85.35 m CSF-B), also lack age-diagnostic taxa and remain unzoned. The next biostratigraphically useful sample in Hole U1558A is Sample 11H-CC, 31–36 cm (94.45 m CSF-B), which contains the highest occurrences of Oligocene taxa *Turborotalia ampliapertura* (which defines the top of Zone O2) and *Subbotina angiporoides* (which ranges from Zone O3 to E11). Therefore, the Oligocene/Miocene boundary must occur somewhere between Cores 8H and 11H. The boundary likely falls closer to the top of this interval based on the occurrence of the late Oligocene species *P. opima* identified in Hole U1558F (Sample 393-U1558F-8H-CC, 16–21 cm; 63.96 m CSF-B). The top of *S. angiporoides* was also observed in adjacent Hole U1558F in Sample 10H-CC, 34–39 cm (83.00 m CSF-B), placing this sample in Zone O3. The calibrated age for this bioevent is 30.1 Ma (Wade et al., 2011), so the absence of *S. angiporoides* in Sample 9H-CC, 14–19 cm (72.65 m CSF-B), combined with the presence of *P. opima* suggests that this sample's age is between 26.9 and 30.1 Ma. *T. ampliapertura* was not observed in Hole U1558F.

Sample 390C-U1558A-12X-CC, 21–26 cm (100.05 m CSF-B), only contains *T. ampliapertura* and *S. angiporoides*; thus, this sample is also placed within Zone O2. Sample 393-U1558F-11F-CC, 15–20 cm (91.08 m CSF-B), is dominated by long-ranging taxa (e.g., *Dentoglobigerina venezuelana* and *C. unicavus*) and lacks any age-diagnostic taxa, precluding zonal assignments. Sample 393-U1558F-12F-CC, 16–21 cm (96.26 m CSF-B), contains the top of *Pseudohastigerina naguewichiensis*, which marks the top of Zone O1. This bioevent is followed by identification of the highest common occurrence of *Pseudohastigerina micra* in Sample 393-U1558F-14F-CC, 9–14 cm (105.66 m CSF-B). This bioevent is typically placed at the top of Zone E16, alongside the top of *Hantkenina alabamensis* with the same age calibration at 33.9 Ma. The top of *Hantkenina* spp. (often only represented in samples by a few broken tubulospines) is found deeper in the sedimentary sequence (Sample 393-U1558F-18F-CC, 19–24 cm; 124.47 m CSF-B), which may be an artifact of taxon rarity in the upper part of its range.

No bioevents of *Pseudohastigerina* or *Hantkenina* specimens are identified in Hole U1558A, which might be a result of the coarser sampling interval (core catcher samples from half-length piston cores in Hole U1558F versus full-length piston cores in Hole U1558A). Sample 390C-U1558A-13X-CC, 9–14 cm (111.56 m CSF-B), is unzoned because of the dissolution of planktic foraminifera and lack of primary and secondary marker species. This sample contains dominantly benthic foraminifera, fish teeth, and skeletal fragments and only rare whole planktic foraminifera. Sample 14X-CC, 21–26 cm (120.61 m CSF-B), contains rare specimens of *G. index*, placing this sample in the late Eocene Zone E15. Because Sample 13X-CC was devoid of marker species, we suspect the Eocene/Oligocene boundary is located between Samples 13X-CC and 14X-CC in Hole U1558A. However, because both *T. ampliapertura* and *S. angiporoides* occur in the late Eocene, we cannot rule out the possibility that Sample 12X-CC, 21–26 cm (100.05 m CSF-B), could potentially be Eocene in age. The lack of primary and secondary marker species and the presence of long-ranging taxa in this sample (e.g., *C. dissimilis* and *C. unicavus*) prohibits a more precise placement of the Eocene/Oligocene boundary in Hole U1558A.

In parallel Hole U1558F, the top of *G. index* is present in Sample 393-U1558F-16F-CC, 15–20 cm (115.06 m CSF-B), and marks the top of Zone E15. The top of *Acarinina mcgowrani* (calibrated at 37.7 Ma) is identified in Sample 22X-CC, 15–20 cm (157.58 m CSF-B), with the former marking the top of Zone E13. Samples 18F-CC, 19–24 cm, and 20X-CC, 20–25 cm (124.47 and 136.62 m CSF-B, respectively), contain *G. index* but lack additional marker species, so this interval is assigned to Zones E15–E14.



Similarly, in Hole U1558A Samples 390C-U1558A-15X-CC, 20–25 cm, and 16X-CC, 15–20 cm (129.77 and 140.14 m CSF-B), contain *G. index* with no additional marker species present in the sample. Thus, these samples occur in Zones E15–E14, undifferentiated. Sample 17X-CC, 15–20 cm (149.53 m CSF-B), contains two marker species: *G. index* and *A. mcgowrani*. The top of *A. mcgowrani* and co-occurrence of *G. index* places this sample in Zones E13–E10, undifferentiated. As *G. index* is still present in Sample 17X-CC and the base of this species occurs at 42.9 Ma, the bottom of the sediment sequence in Hole U1558A must be younger than 42.9 Ma.

#### 7.4. Benthic foraminifera

Onshore analysis of benthic foraminifera was conducted on core catcher samples from Hole U1558A collected during Expedition 390C. The composition of the benthic foraminiferal assemblage, as well as the benthic foraminiferal abundance and preservation, is biased toward the qualitative analysis of depth-diagnostic calcareous species and other notable calcareous taxa. Agglutinated species are reported if identified. The occurrence of important benthic foraminiferal species is reported in Table T16.

Benthic foraminifera are present in all the samples analyzed, with highest abundance in Sample 390C-U1558A-14X-CC, 21–26 cm (120.61 m CSF-B), where benthic foraminifera are common (Figure F60). Overall, specimen preservation is poor, although it ranges from moderate to very poor depending on the species (Figure F60).

According to the site age model (see Figure F79), Sample 390C-U1558A-1H-CC, 9–14 cm (3.35 m CSF-B), is Early Miocene in age. In this sample, the benthic foraminiferal assemblage is dominated by *Cibicidoides mundulus* and *Oridorsalis umbonatus*. Other species include *Cibicidoides bradyi*, *Cibicidoides havanensis*, *Globocassidulina subglobosa*, *Nuttallides umbonifera*, *Pullenia bulloides*, and *Stilostomella subspinosa*.

The late Oligocene Sample 390C-U1558A-6H-CC, 10–15 cm (50.85 m CSF-B), and the early Oligocene Sample 11H-CC, 31–36 cm (94.45 m CSF-B), are dominated by *Cibicidoides mundulus/praemundulus* and *O. umbonatus*, similar to Sample 1H-CC. In addition, *G. subglobosa*, *N. umbonifera*, and *P. bulloides* are present in both samples. *Anomalinoidea pseudogrosserugosus*, *Cibicidoides laurissae*, *Epistominella exigua*, and *S. subspinosa* characterize Sample 6H-CC, whereas *Cibicidoides cf. dickersoni*, *Cibicidoides eoceanus*, and *Nonion havanense* are observed in Sample 11H-CC.

Late Eocene Sample 390C-U1558A-14X-CC, 21–26 cm (120.61 m CSF-B), and late middle Eocene Sample 17X-CC, 15–20 cm (149.53 m CSF-B), contain Eocene assemblages, with *Cibicidoides grimsdalei*, *Cibicidoides praemundulus*, *G. subglobosa*, *Nuttallides truempyi*, and *O. umbonatus* being the most common species. *Anomalinoidea semicribratus* and *C. havanensis* are present in both samples, but *Plectofrondicularia cf. kerni*, *Plectofrondicularia lirata*, and *Pullenia eoceanica* characterize only Sample 14X-CC. *Anomalina spissiformis* is present only in Sample 17X-CC.

Finally, we note the presence of Gyroidinoidids and Stilostomellids, as well as the presence of the agglutinated species *Vulvulina spinosa* in many of the analyzed samples.

The benthic foraminiferal assemblage in Samples 390C-U1558A-14X-CC and 17X-CC, in particular the presence of *C. grimsdalei*, suggests that Site U1558 was lying at lower upper abyssal depths (close to ~3000 m) during the Eocene. The presence of *N. umbonifera* in Sample 11H-CC constrains the timing of the transition of Site U1558 to lower abyssal depths (>3000 m) (Katz et al., 2003) in the early Oligocene.

**Table T16.** Occurrences of notable benthic foraminiferal species, Hole U1558A. [Download table in CSV format.](#)

## 8. Paleomagnetism

### 8.1. Sediment

Remanent magnetization was measured at 2 cm spacing using the superconducting rock magnetometer (SRM) on the archive half of the sedimentary core sections from Hole U1558F and the sediment/basement interface from Hole U1558D (Cores 393-U1558D-2R and 3R). Archive-half sections were also subjected to progressive alternating field (AF) demagnetization at three different steps up to a maximum peak field of 20 mT (see [Paleomagnetism](#) in the Expedition 390/393 methods chapter [Coggon et al., 2024b]). Strongly disturbed intervals of the XCB cores (a total of 105 cm) were excluded from the measurements to avoid generating spurious data. Discrete samples were taken from working halves as 7 cm<sup>3</sup> J-cubes (see [Paleomagnetism](#) in the Expedition 390/393 methods chapter [Coggon et al., 2024b]) at a frequency of 2 samples per core. Only 1 sample per core was taken from HLAPC cores. Remanence before and after AF demagnetization and anisotropy of magnetic susceptibility (AMS) were measured on a total of 38 discrete samples. Acquisition of isothermal remanent magnetization (IRM) was performed on 8 selected samples, 2 from each lithostratigraphic unit/subunit. To establish the magnetostratigraphy at Site U1558, magnetic polarities were analyzed using the results from both Holes U1558F and U1558A.

#### 8.1.1. Results

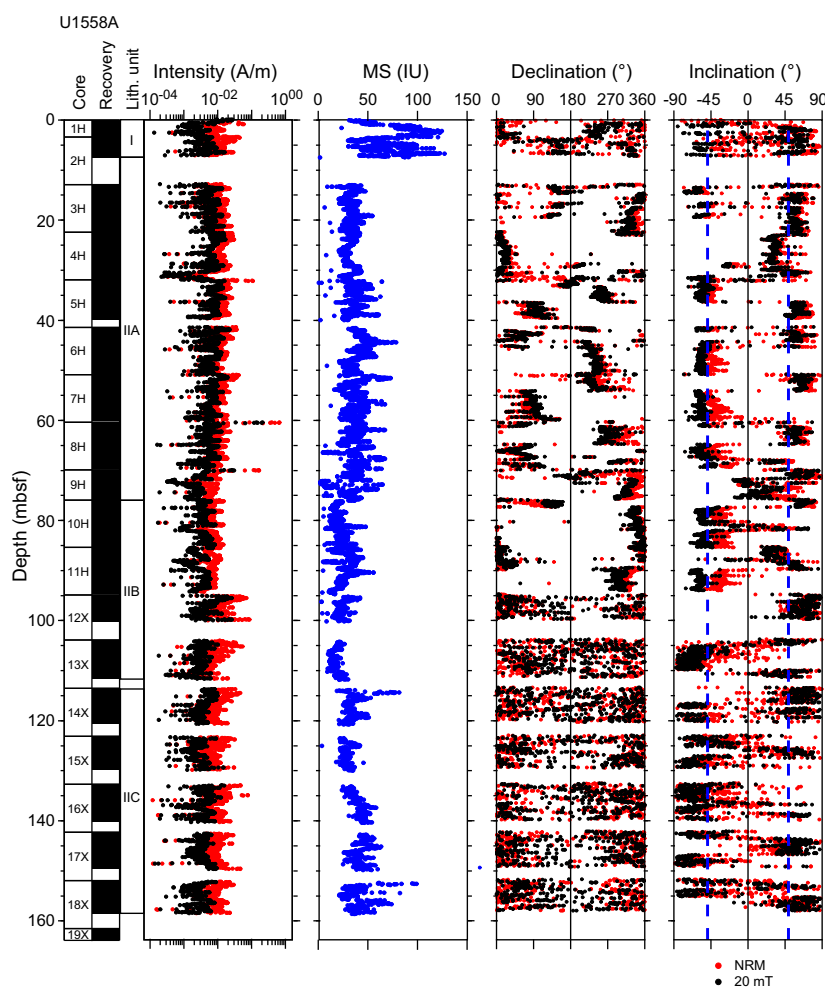
Measurement of the natural remanent magnetization (NRM) and remanence after in-line AF demagnetization of APC cores (Cores 390C-U1558A-1H through 11H and Cores 393-U1558F-1H through 19F) and XCB cores (Cores 390C-U1558A-12X through 19X and Cores 393-U1558F-20X through 24X) were carried out to define the magnetostratigraphy for the entire sediment section at Site U1558. AF demagnetization up to 20 mT was applied to remove any viscous remanent magnetization and isolate the characteristic remanent magnetization (ChRM). Remanence and inclination after 20 mT AF demagnetization will be referred to as 20 mT remanence and 20 mT inclination, respectively, hereafter. The NRM and 20 mT remanence intensities of the sediments at Site U1558 are relatively strong for pelagic sediments. Values are on the order of 10<sup>-2</sup> A/m for NRM and 10<sup>-3</sup> to 10<sup>-2</sup> A/m for 20 mT intensity in both Holes U1558A and U1558F. Recurrent oscillations in remanence intensity can be observed throughout Holes U1558A and U1558F (Figures [F63](#), [F64](#)). At the sediment/basement interface in Hole U1558D, only a small number of intervals could be measured and the variation in the remanence behavior was not clearly observed (Figure [F65](#)). Variations in the remanence intensity are more pronounced in Hole U1558F, as the 20 mT intensity is an order of magnitude lower than the NRM intensity (Figure [F64](#)). The presence of high NRM intensity is associated with an almost constant positive NRM inclination throughout Hole U1558F, pointing to a drilling overprint that was removed after the 5 mT demagnetization step. Moreover, there are differences in average values of 20 mT intensity between Holes U1558A and U1558F, which are about 1.6 × 10<sup>-2</sup> and 5.0 × 10<sup>-3</sup> A/m, respectively. Overall, no specific variations in the remanence intensity are associated with differences between the lithostratigraphic units or depths at Site U1558. Clear variations in both NRM and 20 mT inclination are visible in both Holes U1558A and U1558F (Figures [F63](#), [F64](#)), allowing for a good definition of polarity reversals (see [Age model and sedimentation rates](#)). The distribution of the 20 mT inclination is bimodal in both holes, with values clustered around ±56° in Hole U1558A and +60° and -51° in Hole U1558F (Figure [F66](#)). This is slightly steeper than the expected inclination based on the geocentric axial dipole (GAD; ±49.1° at 30°S).

##### 8.1.1.1. Discrete samples

We collected about 2 discrete cubes per core from Hole U1558F (38 in total), targeting the visible variations in color associated with changes in modal abundance of clay minerals (see [Sedimentology](#)). All lithostratigraphic units/subunits were sampled (Table [T17](#)). AF demagnetization up to a maximum of 100 mT was conducted on all discrete samples to identify the ChRM and provide constraints on the SRM data. Most of the samples reveal a single component after the 5 mT AF demagnetization step with maximum angular deviation angles spanning 1.9°–13.9° (Figure [F67](#); Table [T17](#)). This indicates that ChRM components are generally well defined in Hole U1558F, as the values are less than the maximum uppermost cutoff, which is defined at 15° (Butler, 1992). In contrast, most of the discrete sediment samples from Unit I display noisy orthogonal vector plots

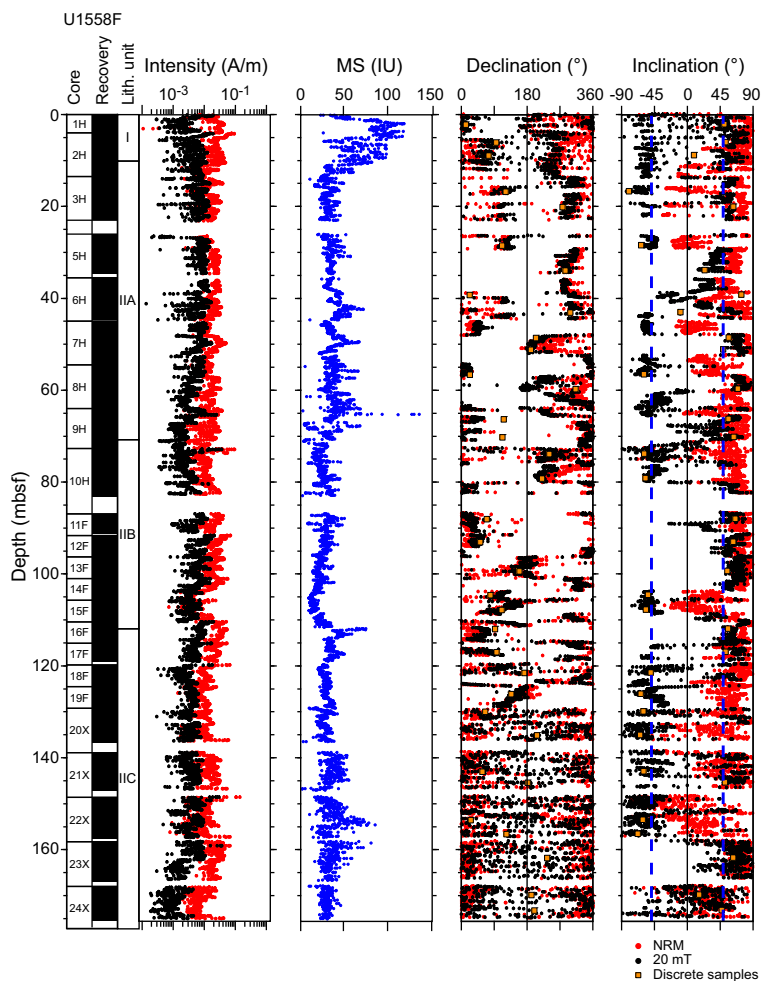
(OVPs) or maximum angular deviation higher than  $15^\circ$ , suggesting that lithologic variation (see **Sedimentology**) may affect the efficiency of retaining a stable remanent magnetization. Overall, the ChRM directions derived from discrete measurements show both inclination and declination values similar to the SRM data (Figure F64), contributing to the robustness of the Site U1558 magnetostratigraphy.

Acquisition of IRM and backfield experiments were conducted on 8 discrete samples, 2 from each lithostratigraphic unit/subunit, to characterize the magnetic mineral assemblages. Samples saturate at fields of 300–400 mT (Figure F68A), which implies the dominance of low-coercivity minerals. The intensity of saturation IRM (SIRM) is significantly higher in Unit I (Table T18). The trend of backfield curves generally shows a coercivity of remanence ( $B_{cr}$ ) around 30 mT with no variations among lithostratigraphic units. Deconvolution of the IRM acquisition curves (Figure F68B) shows a best-fit model characterized by 2 components. A dominant low-coercivity component with a mean remanence coercivity ( $B_h$ ) of  $\sim 1.57 \log_{10}$  units and a minor (5%–10%) second component showing  $B_h$  values  $\sim 2.50$ – $2.70 \log_{10}$  units. Both  $IRM_{100}/SIRM$  ratio ( $S_{0.1}$ ) and S ratio ( $S_{0.3}$ ) display values close to 1 on all measured samples with no variations with depth (Figure F69; Table T18), which supports the dominance of low-coercivity components such as magnetite (Bloemen et al., 1992), typical of pelagic sediments. No specific trend is defined in the variation of the median destructive field (MDF) and the frequency-dependent magnetic susceptibility ( $K_{fd\%}$ ) (Figure F69). Only few samples show  $K_{fd\%}$  values  $\sim 15\%$  (Table T18), indicating the local dominance of superparamagnetic (SP) particles (Dearing et al., 1996).

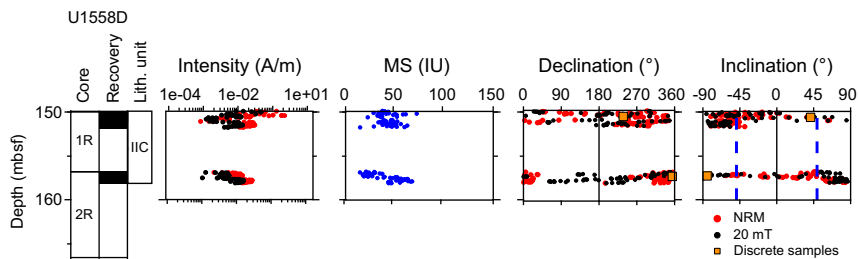


**Figure F63.** Archive-half MSP (MS; from SHMSL) and SRM measurements in sediments, Hole U1558A. Dashed lines on inclination = inclination ( $\pm 49.1^\circ$ ) expected based on the GAD for this latitude ( $\sim 30^\circ\text{S}$ ).

AMS measurements display slight dispersion of the AMS axes in Hole U1558F. The pole of the magnetic foliation ( $K_{\min}$  axis) shows a bimodal distribution (Figure F70A). In particular, 70% of the samples show subhorizontal magnetic foliation characteristic of a primary depositional sedimentary fabric (Tarling and Hrouda, 1993). In contrast, the remaining samples display inclined magnetic foliation with the  $K_{\min}$  axis clustered around the north–south direction (in the core coordinate system). In addition, the magnetic lineation ( $K_{\max}$  axis) is well defined for these samples, which might represent a registration of incipient deformation rather than drilling/reworking. In fact, some of these samples are located in Cores 393-U1558F-6H through 8H, where evidence of soft-sediment deformation was detected (see [Sedimentology](#)).



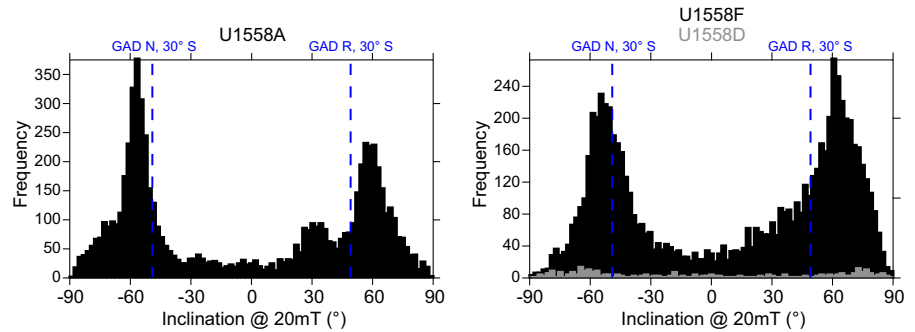
**Figure F64.** Archive-half MSP (MS; from SHMSL) and SRM measurements in sediments, Hole U1558F. Dashed lines on inclination = inclination ( $\pm 49.1^\circ$ ) expected based on the GAD for this latitude ( $\sim 30^\circ\text{S}$ ).



**Figure F65.** Archive-half MSP (MS; from SHMSL) and SRM measurements in sediments, Hole U1558D. Dashed lines on inclination = inclination ( $\pm 49.1^\circ$ ) expected based on the GAD for this latitude ( $\sim 30^\circ\text{S}$ ).

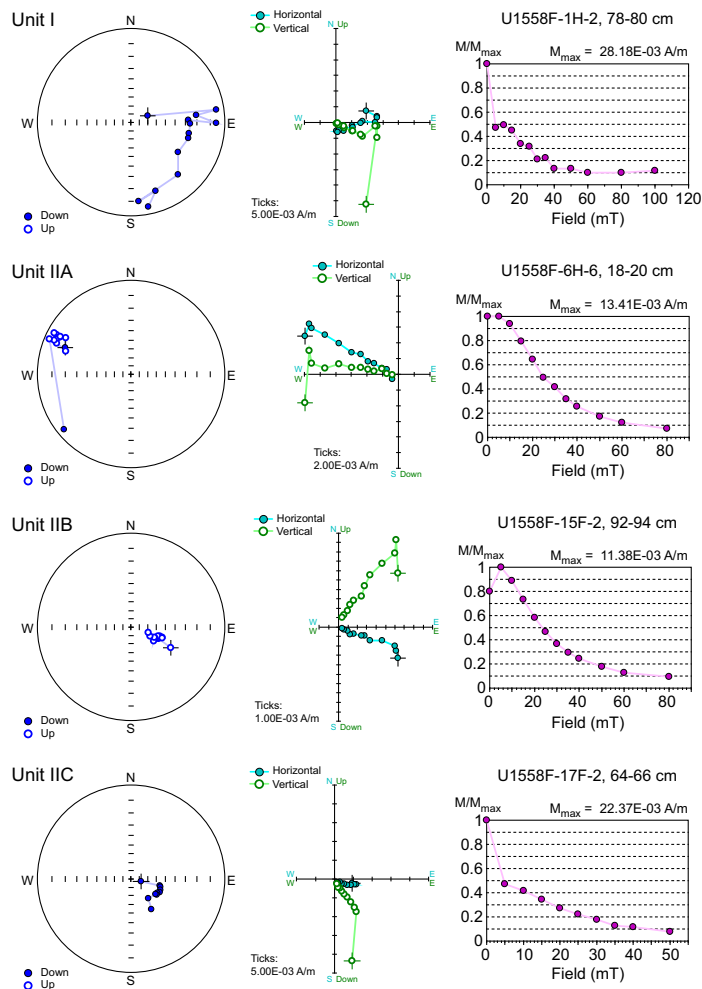


The degree of anisotropy ( $P$ ) is low to moderate (1.002–1.042), and the shape parameter ( $T$ ) spans from prolate to oblate (Figure F70B; Table T19). In addition, the bulk susceptibility ( $K_m$ ) is higher in Unit I (Figure F71), which is in agreement with the higher clay mineral content. Similar values



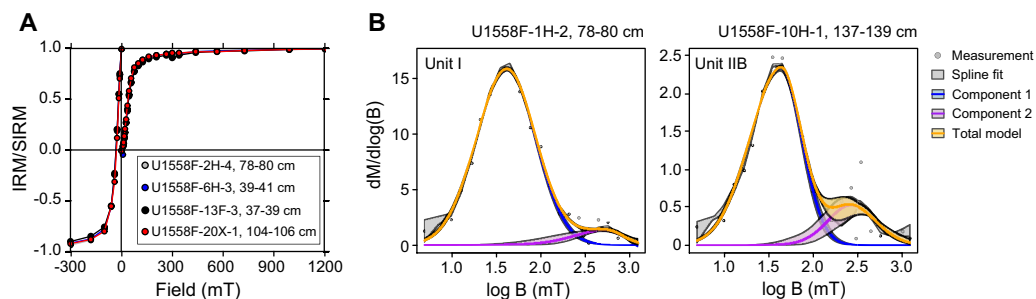
**Figure F66.** Histogram of SRM inclination data after 20 mT AF demagnetization for sediment, Holes U1558A, U1558F, and U1558D. Dashed lines = inclination ( $\pm 49.1^\circ$ ) of GAD at this latitude ( $\sim 30^\circ S$ ) for normal (N) and reversed (R) chrons.

**Table T17.** Discrete sample directional remanent magnetization components, declination, and inclination of ChRM and their maximum angular deviation, Hole U1558F. [Download table in CSV format.](#)



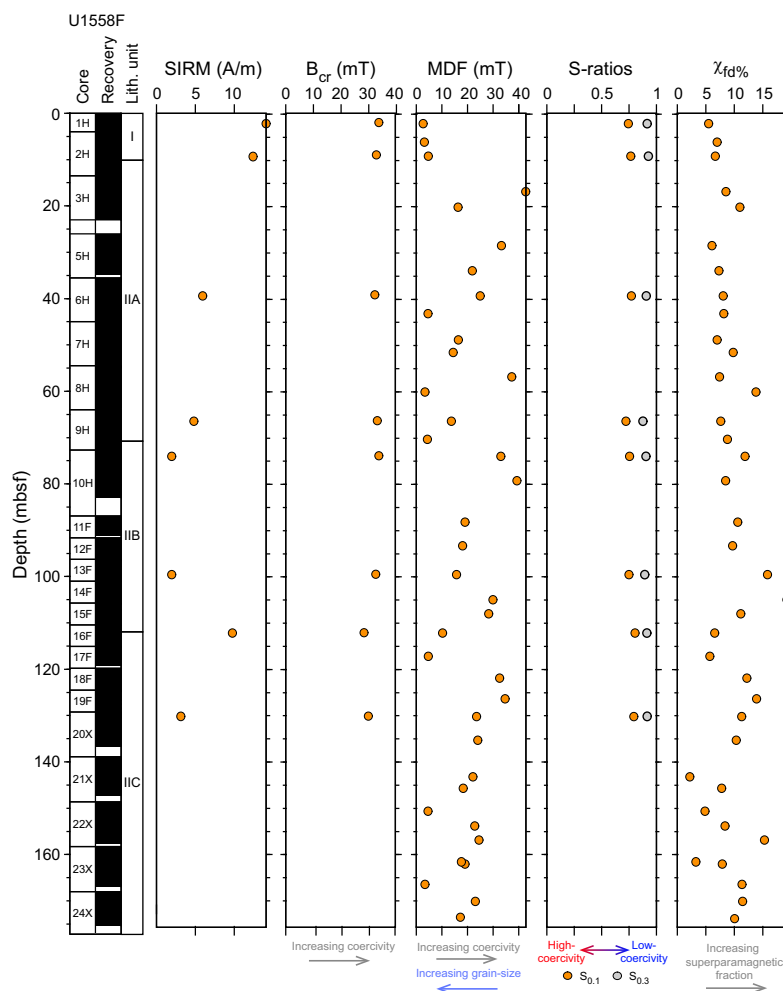
**Figure F67.** Representative AF demagnetization results for each lithostratigraphic unit, with equal-angle projections, OVPs (Zijderveld, 1967), and demagnetization trends of normalized intensity, Hole U1558F.

were observed at the top of Subunit IIC in discrete samples taken from Cores 393-U1558F-16F and 17F. Moreover,  $P$  and  $T$  show highest values within Lithostratigraphic Subunit IIC (below 110 m), where higher values can be related to increasing compaction with depth.



**Figure F68.** A. SIRM acquisition curves up to 1200 mT and backfield IRM truncated at -300 mT for representative samples from each sedimentary lithostratigraphic unit, Hole U1558F. B. Coercivity distribution and unmixing of IRM acquisition curves (Maxbauer et al., 2016) for samples from Unit I and Subunit IIB.

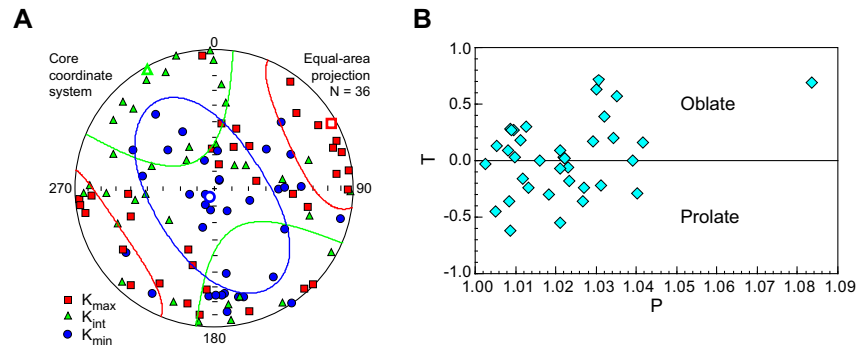
**Table T18.** Frequency-dependent magnetic susceptibility ( $K_{fd\%}$ ), IRM acquisition, and MDF, Hole U1558F. [Download table in CSV format.](#)



**Figure F69.** Magnetic mineralogy data, Hole U1558F.

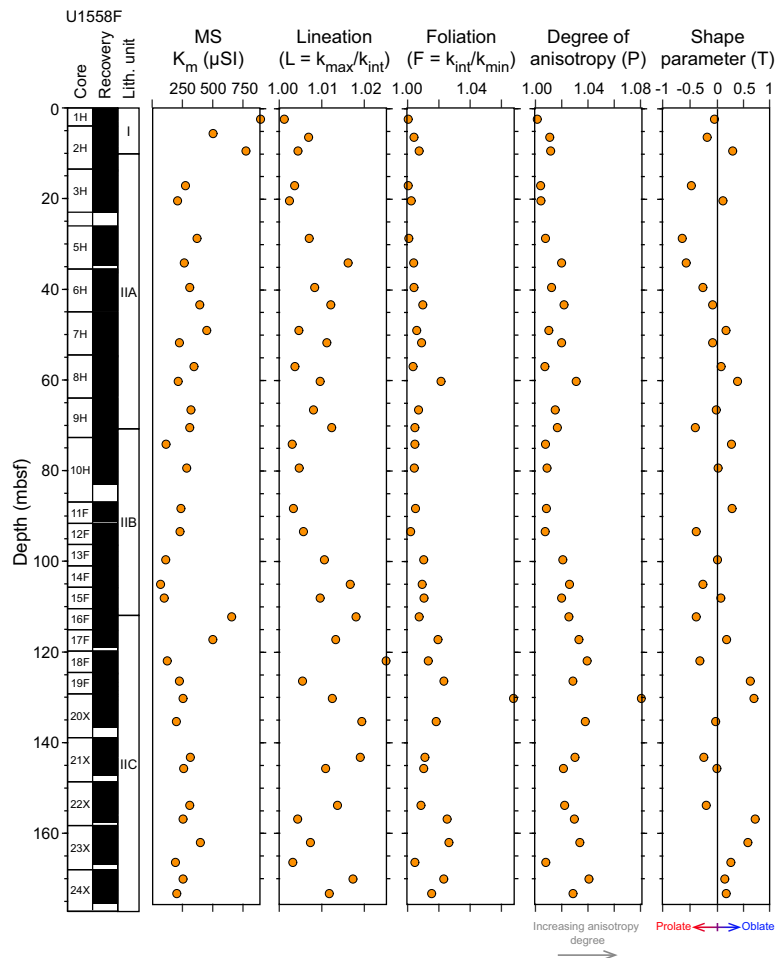
### 8.1.1.2. Magnetostratigraphy

SRM data from the archive halves of sediment cores from Holes U1558A and U1558F after AF demagnetization at 20 mT were used to define a partial polarity sequence for Site U1558. The interpretation of the polarity sequence was based on relative length of polarity intervals and the



**Figure F70.** A. Equal-area projection (in core coordinate system) showing orientation of principal magnetic susceptibility axes for measured discrete sediment samples, Site U1558. Mean tensors (open symbols) and 95% confidence ellipsoids are also shown. B. Shape parameter ( $T$ ) vs. degree of anisotropy ( $P$ ).

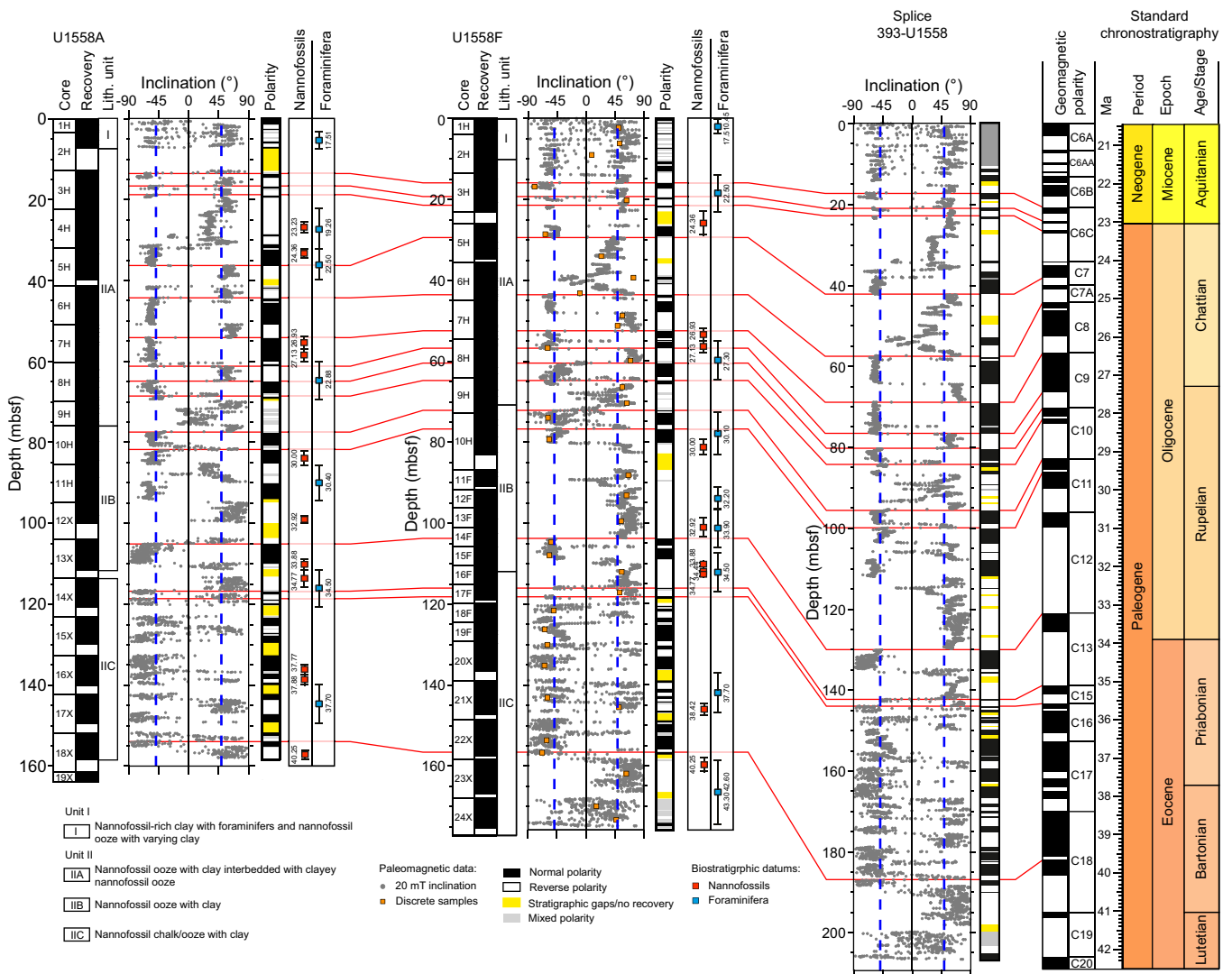
**Table T19.** AMS, Hole U1558F. [Download table in CSV format.](#)



**Figure F71.** Bulk susceptibility ( $K_m$ ) and AMS parameters (Jelinek, 1981), Hole U1558F.

biostratigraphic datums from both nannofossils and foraminifera (see **Biostratigraphy** and **Age model and sedimentation rates**) (Figure F72). Inclinations of the calculated ChRM directions from discrete samples were used to verify the inclinations measured from SRM in Hole U1558F and support the polarity interpretations (Figure F64). Correlation of polarity reversals between sites was performed using the CSF-A depth scale. The spliced inclination reversal stratigraphy (see **Physical properties and downhole measurements**) was used to complete the remanence data, helping in the correlation of the magnetostratigraphy between Holes U1558A and U1558F. A preliminary correlation with the current geomagnetic polarity timescale (Gradstein et al., 2020) is reported in Figure F72.

At the top of the sedimentary sequence, between 2 and 10 m CSF-A, the presence of gaps in core recovery makes the correlation in polarity reversals between Holes U1558A and U1558F difficult. Remanence data are less clear in Unit I, as confirmed by the elevated maximum angular deviation values in the discrete sample OVPs (Figure F67; Table T17). From 10 to ~120 m CSF-A, both holes predominantly show clear polarity reversals that can be unambiguously correlated. Preliminary correlation with the geomagnetic polarity timescale (GPTS) was executed starting from ~15 m CSF-A. Despite the presence of gaps in Core 390C-U1558A-2H and the missing Core 393-U1558F-4H, the reversal pattern observed between 15 and 20 m CSF-A was tentatively correlated



**Figure F72.** Archive-half SRM inclination measurements after 20 mT demagnetization for Hole U1558A and U1558F sediment cores, plotted with inclination splice (CCSF-393-U1558-AF scale). Red lines = intervals where reversal patterns were associated with GPTS (Gradstein et al., 2020). Biostratigraphic ages based on nannofossils and planktic foraminifera used to constrain magnetic polarity ties are also shown.



with the GPTS at the Neogene–Paleogene transition based on the reversal pattern and nannofossils (Figure F72). The well-defined polarity sequences allow detection of the Chattian/Rupelian boundary (28.1 Ma) (Gradstein et al., 2020) within Subunit IIB and the Oligocene/Eocene boundary at the transition between Subunits IIB and IIC.

Below 120 m CSF-A, due to the presence of stratigraphic gaps and uncertainties, correlations cannot be confidently made with the exception of the reversals at ~150 m CSF-A, where the biostratigraphic datums provide additional confidence in constraining the reversal pattern.

## 8.2. Basement

Measurements of the remanent magnetization of basement cores from Hole U1558D were made with the SRM on archive-half core pieces longer than 9 cm (see **Paleomagnetism** in the Expedition 390/393 methods chapter [Coggon et al., 2024b]). Remanent magnetization was measured at 2 cm intervals before and after AF demagnetization at three different steps (5, 10, and 20 mT). The amount of data collected with the SRM varies with recovery rate (11%–90%) in Hole U1558D. High resolution was achieved in Cores 393-U1558D-5R through 12R but was lower in Cores 24R–30R. Cores 22R, 28R–31R, and 35R were not subjected to SRM measurements, as no pieces were longer than 9 cm.

One to two 8 cm<sup>3</sup> cubes per core were taken from the working halves of Hole U1558D basement cores for discrete measurements, making a total of 38 cubes. The cubes consisted of basalts with various degrees of alteration and include 1 sample of sedimentary breccia as well as 2 samples of sediments at the sediment/basement interface (Cores 393-U1558D-2R and 3R). Paleomagnetic studies on discrete samples were principally undertaken to better constrain the SRM data and to characterize the magnetic mineralogy. Both AF demagnetization and IRM experiments were conducted. In addition, AMS measurements were performed to clarify the dominant magnetic fabric.

### 8.2.1. Results

NRM and in-line AF demagnetization of cores from Hole U1558D were measured to characterize the remanent records of ~49.2 Ma basalts, whose age was calculated from magnetic data acquired during the CREST cruise (Kardell et al., 2019). AF demagnetization up to 20 mT removed most of the viscous remanent magnetization that generally comprises a small portion of the total remanence. This viscous overprint is presumably induced during RCB drilling. Remanence after 20 mT AF demagnetization will be referred to as 20 mT remanence hereafter. The intensities of NRM and 20 mT remanence of the igneous rocks show mean values of ~0.92 and 0.68 A/m, respectively (Figure F73). Significantly higher NRM intensity was detected in 4 of the measured cores (Cores 393-U1558D-12R, 14R, 31R, and 37R), which coincides with the highest MS values (see **Physical properties and downhole measurements**). The 20 mT remanence values predominantly show negative inclination (normal geomagnetic polarity at these latitude, 30°S) in measured intervals of Hole U1558D, in agreement with the expected polarity for a 49.2 Ma (Gradstein et al., 2020) basement. However, Cores 7R–12R and 31R–39R locally recorded positive (reversed) inclination values. Overall, the inclination values are densely clustered around –55° and display a Gaussian distribution skewed to the negative end (Figure F74). This inclination is ~6° steeper than the inclination expected based on the GAD ( $\pm 49.1^\circ$  at 30°S).

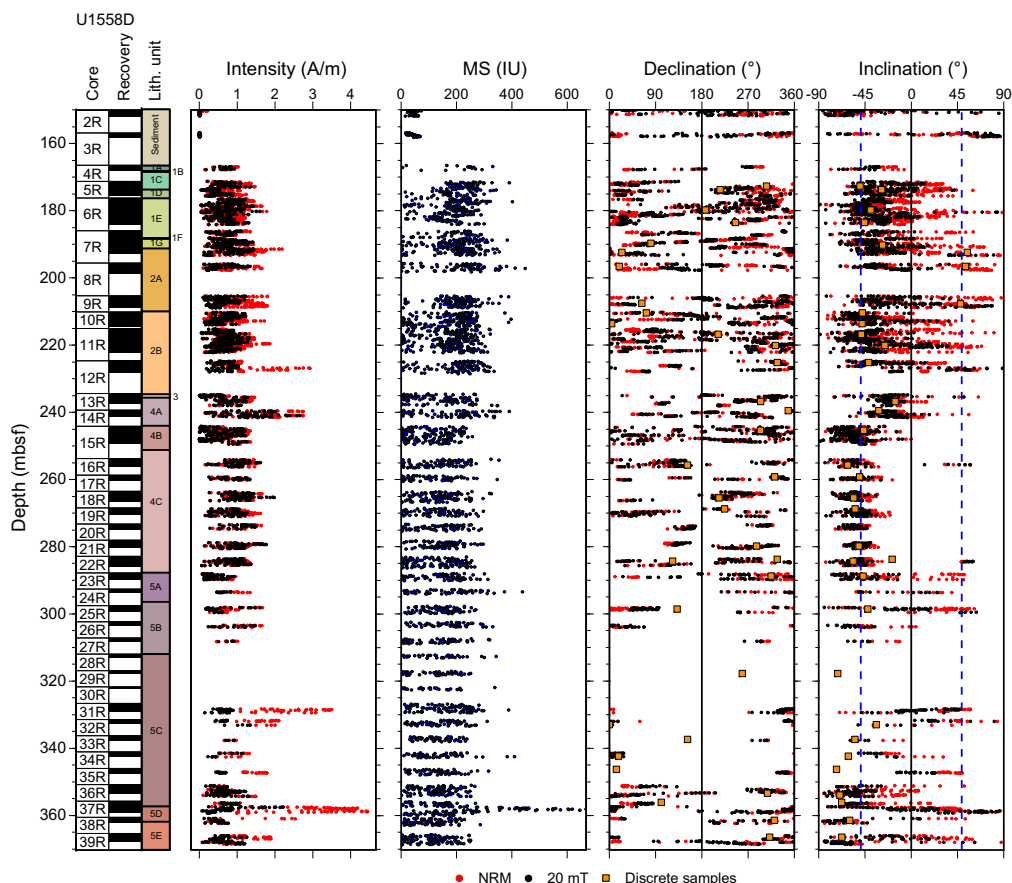
#### 8.2.1.1. Discrete samples

The discrete samples from basement cores of Site U1558 were selected from basalts with varying degrees of alteration, ranging from intervals of slightly altered gray basalts to strongly altered orange-brown basalts, totaling 38 samples (Tables T20, T21). We have also included a single sedimentary breccia sample to test for a possible chemically induced remanence due to alteration. AF demagnetization up to a maximum of 130 mT was conducted on 32 of the discrete samples to isolate the ChRM and constrain the SRM data.

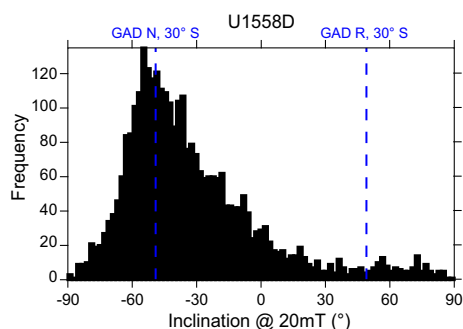
After removing a low-coercivity (<20 mT) viscous remanent magnetization component, a single stable component was detected on the orthogonal vector projection (Zijderveld diagram), which should represent the ChRM. However, this component does not converge to the origin in most

samples analyzed (Figure F75A), suggesting the presence of an overlapping high-coercivity component that cannot be completely separated using AF demagnetization.

Most of the samples display MDFs around or higher than 50 mT and require strong fields of more than 100 mT to be fully demagnetized (Figures F75, F76; Table T21). Two samples collected from



**Figure F73.** Archive-half MSP (MS; from SHMSL) and SRM measurements, Hole U1558D. Dashed lines on inclination = inclination ( $\pm 49.1^\circ$ ) expected based on the GAD for this latitude ( $\sim 30^\circ\text{S}$ ).



**Figure F74.** Histogram of SRM inclination data after 20 mT AF demagnetization for basement, Hole U1558D. Dashed lines = inclination ( $\pm 49.1^\circ$ ) of GAD at this latitude ( $\sim 30^\circ\text{S}$ ) for normal (N) and reversed (R) chrons.

**Table T20.** Directional remanent magnetization components, Hole U1558D. [Download table in CSV format.](#)

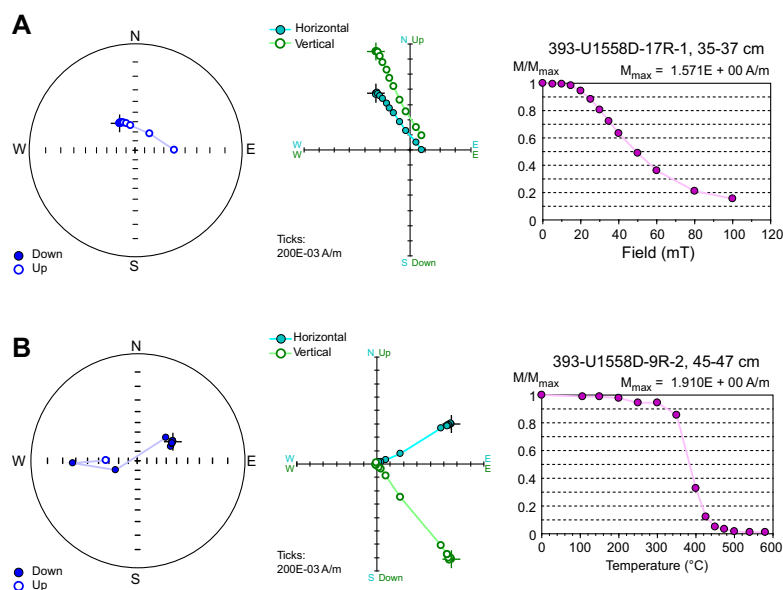
**Table T21.** IRM acquisition and MDF, Hole U1558D. [Download table in CSV format.](#)

cores at the sediment/basement interface (Samples 393-U1558D-2R-1, 67–69 cm, and 3R-1, 48–50 cm) and the sedimentary sample collected from Core 13R show significantly lower MDF, <20 mT, indicating the dominance of coarser grained low-coercivity phases (Table T21).

A subset of 6 samples, 3 of which retained >20% of the natural remanence after AF demagnetization of <100 mT field, were subjected to thermal demagnetization up to 580°C. Compared to AF demagnetization, thermal demagnetization trends reveal a clear single component that converges to the origin (Figure F75B). The derived components displayed maximum angular deviation angles between 0.4° and 5.9°, which indicates that ChRM directions are well defined in the measured samples (Table T20) (Butler, 1992). Inclinations of the ChRM, calculated with principal component analysis (PCA; Kirschvink, 1980), are consistent with the inclination measured on the SRM (Figure F73).

Acquisition of IRM and backfield experiments was conducted on 24 discrete samples to further distinguish their mineralogy. IRM acquisition results show saturation at fields of 150–300 mT, implying that magnetic minerals of different coercivity coexist within the cores (Figure F76A). Deconvolution of the IRM acquisition curves (Figure F76B) shows a best-fit model characterized by 2 components for most of the samples. A dominant low-coercivity component is characterized by a mean remanence coercivity ( $B_h$ ) of 1.50–1.70  $\log_{10}$  units with a variable contribution (5%–15%) of a second component showing higher  $B_h$  values of  $\sim 2.3 \log_{10}$  units (Figure F76B). In addition, Sample 393-U1558D-10R-1, 38–40 cm, shows the presence of a third component with high coercivity (>3  $\log_{10}$  units).

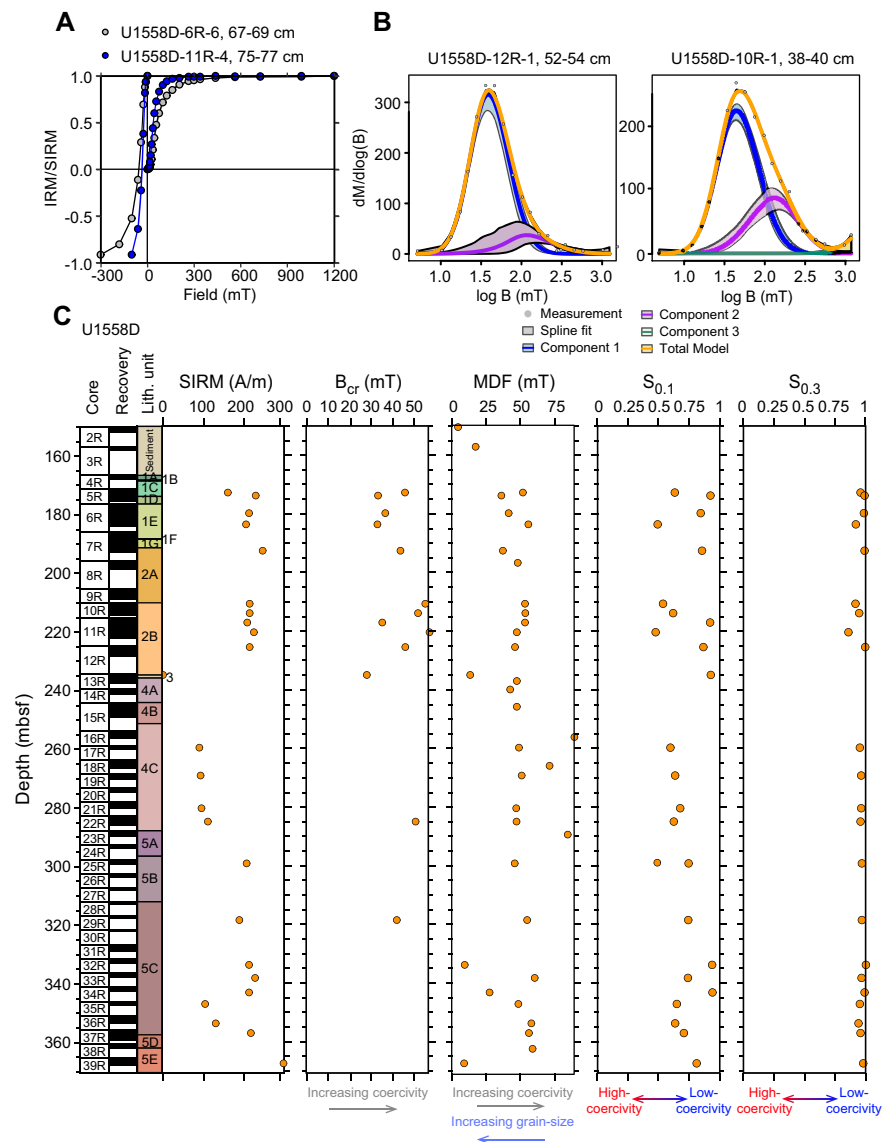
Variations in intermediate- to high-coercivity mineral content is indicated by the variability of the  $IRM_{100}/SIRM$  ( $S_{0.1}$ ) ratio of 0.5–1 (Figure F76C; Table T21). The intensity of SIRM varies among igneous units, suggesting different content in ferromagnetic minerals, with lower values in the pillow lavas of Subunit 4C, at the base of Subunit 5C, and in the breccia sample (Sample 393-U1558D-13R-1, 29–31 cm). In particular, the lowest SIRM values were observed in the most altered samples, which display brown and orange-reddish halos of various intensities (alteration degrees 4 and 6; Figure F77A; Table T21). However, MDF and mass magnetic susceptibility ( $\chi_m$ ) display similar values among all samples, independent of the extent or style of alteration (Figure F77B, F77C). The intensity of the remanence after the 5 mT demagnetization step is the only parameter that varies depending on the alteration degree, with higher values in the light brownish gray halo samples (Figure F77D). We used the remanence at the 5 mT step instead of the NRM to



**Figure F75.** Representative demagnetization results for discrete samples, Hole U1558D. A. AF demagnetization (17R-1, 35–37 cm). B. Thermal demagnetization (9R-2, 45–47 cm). Equal-angle projections, orthogonal projection diagrams (Zijderveld, 1967), and demagnetization trends of normalized intensity.

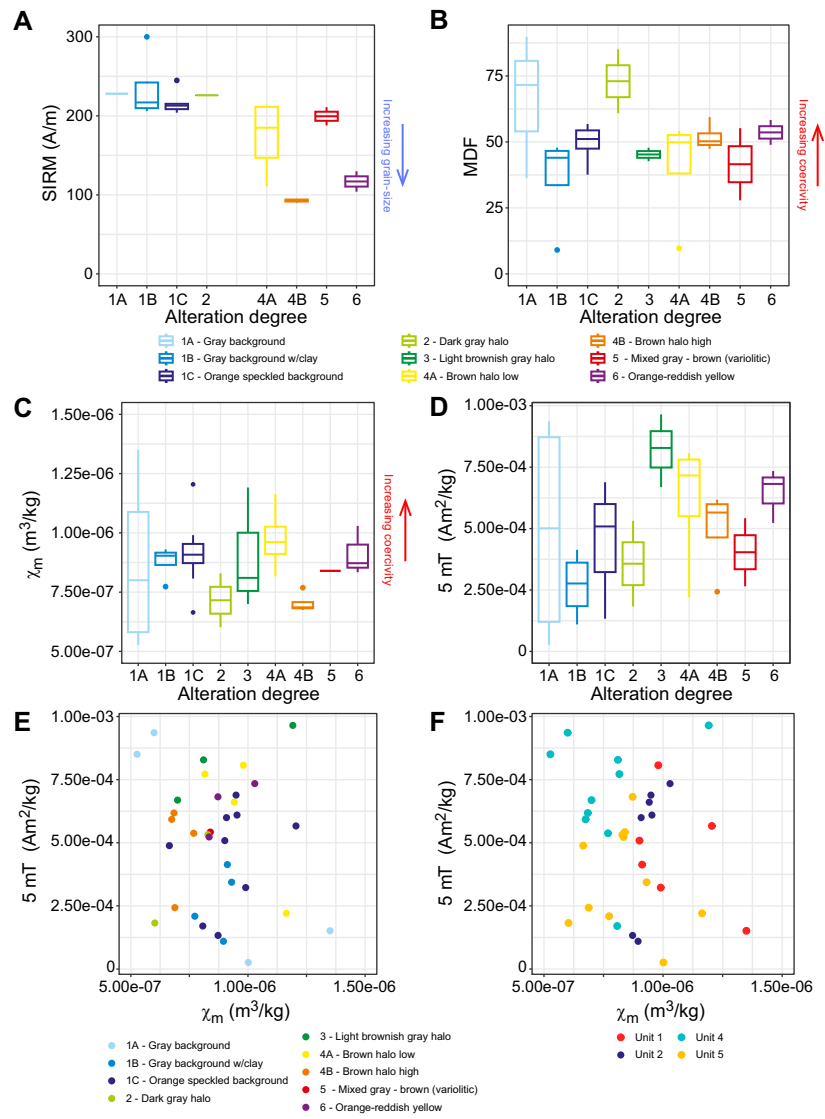
avoid spurious data related to drilling overprint. Variations of remanence intensity and  $\chi_m$  show no significant correlation with alteration degree (Figure F77E) but do appear to be linked to the different igneous units (Figure F77F; Table T21).

AMS was measured on all of the discrete samples collected. The resultant magnetic fabric is generally well defined with subhorizontal magnetic foliation and predominantly prolate shape of the anisotropy ellipsoid ( $-1 < T < 0$ ) (Figure F78). Only 8 of the total 38 samples indicate an oblate magnetic fabric (Figure F78B; Table T22). The oblate fabric for the sediment samples at the sediment/basement interface indicates elevated vertical compaction compared to the overlying sedimentary package. However, no correlation between the shape of the magnetic fabric and the different igneous units was observed. Sample 393-U1558D-13R-1, 129–131 cm, which is the only sample taken from the sedimentary breccia unit, shows a bulk susceptibility ( $K_m$ ) value around  $1.7 \times 10^{-4}$ , similar to the susceptibility of the sediments at the sediment/basement interface collected in Cores 2R and 3R (Figure F78C).

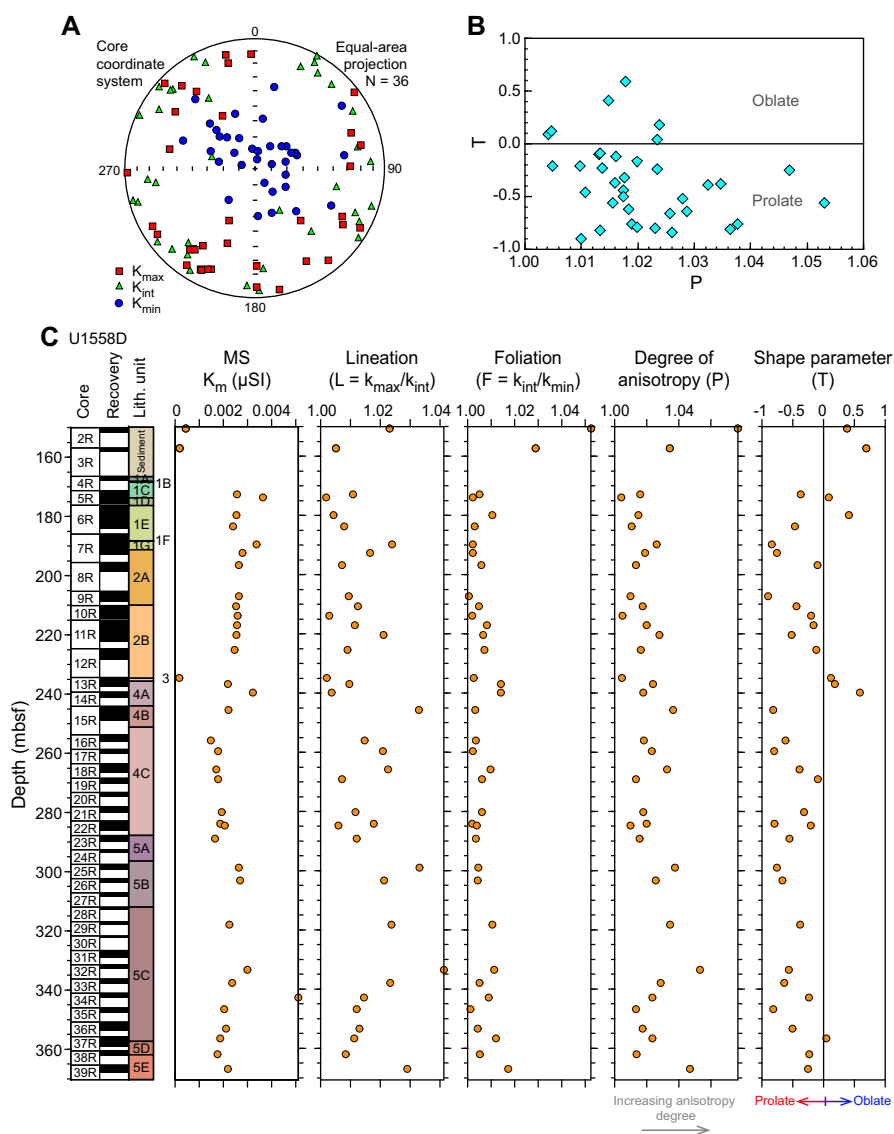


**Figure F76.** A. SIRM acquisition curves up to 1200 mT and backfield IRM truncated at  $-300$  mT for 2 basement rock samples, Hole U1558D. B. Coercivity distribution and unmixing of IRM acquisition curves (Maxbauer et al., 2016). C. IRM acquisition data.





**Figure F77.** Box-and-whisker plots of (A) SIRM at 1200 mT, (B) MDF, (C) mass magnetic susceptibility ( $\chi_m$ ), (D) remanence intensity after 5 mT step, divided by alteration degree, Hole U1558D. Remanence intensity after 5 mT step vs.  $\chi_m$ , divided by (E) alteration degree and (F) igneous units.



**Figure F78.** A. Equal-area projection showing shape of magnetic susceptibility axes, Hole U1558D. B. Shape parameter ( $T$ ) vs. degree of anisotropy ( $P$ ). C. Bulk susceptibility ( $K_m$ ) and AMS parameters (Jelinek, 1981).

**Table T22.** AMS data for basalt samples, Hole U1558D. [Download table in CSV format.](#)

## 9. Age model and mass accumulation rates

### 9.1. Age model and linear sedimentation rates

The age model for Site U1558 is based on calcareous nannoplankton and planktic foraminiferal lowest (base) and highest (top) occurrence datums and paleomagnetic reversal datums from Holes U1558A and U1558F (Tables T23, T24; Figures F79, F80).

Planktic foraminifera and calcareous nannoplankton occur throughout the cored sediment sequence. Foraminifera tend to be largely absent in the upper portion of Holes U1558A and U1558F, corresponding to nannofossil-rich clays in Lithostratigraphic Unit I (see [Sedimentology](#) and [Biostratigraphy](#)). In Lithostratigraphic Subunit IIA (nannofossil ooze with clay) and much of Subunit IIB (nannofossil chalk with clay), foraminifera are present in greater numbers, but are sparse again in upper Subunit IIC across the Eocene–Oligocene transition (see [Biostratigraphy](#)).

Calcareous nannofossils are common to abundant in nannofossil-rich clay samples but are poorly preserved (Lithostratigraphic Unit I), however, in the carbonate-rich intervals, such as Lithostratigraphic Unit II, nannofossils are more abundant with variable preservation.

Overall, we identified 7 planktic foraminifera and 12 calcareous nannoplankton bioevents in Hole U1558A and 18 planktic foraminifera and 13 calcareous nannoplankton bioevents in Hole U1558E. Magnetic reversals were recorded throughout the sedimentary sections, except for the early Neogene (Early to Middle Miocene) in Hole U1558A. Five magnetic reversal boundaries were identified in Hole U1558A between 14.77 and 19.52 m CSF-A, possibly corresponding to the late Oligocene to Early Miocene. However, we have refrained from interpreting these reversals because this interval contains short and frequent polarity reversals, and Hole U1558A contains few microfossil datums to constrain paleomagnetic interpretations. There is also a void in Core 390C-U1558A-2H, and significant drilling disturbances occur at the tops of Cores 2H and 3H, so the reversals lack sufficient support. In total, 14 and 22 magnetic reversal boundaries were identified from Holes U1558A and U1558E, respectively (Figures F79, F80).

There is good agreement between the fossil datums and paleomagnetic reversals in both holes, with the best agreement between microfossil datums and magnetic reversals occurring in Hole U1558E. In Hole U1558A, all planktic foraminiferal datums lie away from the calcareous nannofossil and magnetic reversal boundaries, which could be attributed to species' diachroneity in the midlatitudes. Planktic foraminiferal species used in biostratigraphy have been demonstrated to

**Table T23.** All biostratigraphic and paleomagnetic datums in stratigraphic order, Hole U1558A. \* = datums used to plot the age model curve in Figure F79 and calculate LSRs using CSF-A depths. T = top, B = base, Bc = base common, B reversal = base of a paleomagnetic reversal event. CN = calcareous nannofossils, PF = planktic foraminifera. Pmag = paleomagnetism. [Download table in CSV format.](#)

Datum	Taxon/Chron (base)	Age (Ma)	Sample	Sample depth CSF-A (m)	Sample depth CSF-B (m)	Sample above/below	Sample above/below depth CSF-A (m)	Sample above/below depth CSF-B (m)	Midpoint depth CSF-A (m)	Midpoint depth CSF-B (m)	Depth error (±) CSF-A (m)	Depth error (±) CSF-B (m)	LSR (cm/ky)
			390C-U1558A-			390C-U1558A-							
PF	<i>T Catapsydrax dissimilis</i> *	17.51	1H-CC, 9–14	3.42	3.35	2H-CC, 21–26	7.48	7.48	5.45	5.42	2.03	1.38	0.45
PF	<i>T Dentoglobigerina binaiensis</i>	19.26	3H-CC, 0–5	22.22	22.22	4H-CC, 34–39	32.39	31.90	27.31	27.06	5.09	3.06	
CN	<i>T Reticulofenestra bisecta</i>	23.13	4H-3, 20	25.60	25.44	4H-5, 35	28.76	28.45	27.18	26.95	1.58	1.51	
CN	<i>T Sphenolithus ciperoensis</i>	24.36	4H-CC	32.34	31.85	5H-2, 107	34.48	34.48	33.41	33.17	1.07	1.31	
Pmag	B C7n.2n*	24.459	5H-3, 148	36.40	36.40	5H-4, 0	36.41	36.41	36.41	36.41	0.01	0.00	0.95
PF	<i>B Globoquadrina dehiscens</i>	22.5	4H-CC, 34–39	32.34	31.85	5H-CC, 17–22	39.88	39.88	36.11	35.87	3.77	2.68	
Pmag	B C8n.2n*	25.987	6H-7, 70	50.90	50.90	7H-1, 0	50.90	50.90	50.90	50.90	0.01	0.08	0.76
Pmag	B C8r*	26.42	7H-3, 28	54.18	54.18	7H-3, 30	54.20	54.20	54.19	54.19	0.01	0.01	0.7
CN	<i>T Sphenolithus predistentus</i>	26.93	7H-3, 4	53.94	53.94	7H-5, 6	56.97	56.97	55.46	55.46	1.52	1.52	
CN	<i>B Sphenolithus ciperoensis</i>	27.13	7H-5, 6	56.97	56.97	7H-CC	60.09	60.09	58.53	58.53	1.56	1.56	
Pmag	B C9n*	27.439	8H-1, 96	61.36	61.36	8H-1, 92	61.32	61.32	61.34	61.34	0.01	0.01	0.84
PF	<i>B Trilobatus trilobus</i>	22.88	7H-CC, 0–8	60.05	60.05	8H-CC, 10–15	69.51	69.51	64.78	64.78	4.73	3.15	
Pmag	B C9r*	27.859	8H-3, 150	64.90	64.90	8H-4, 0	64.91	64.91	64.91	64.91	0.01	0.00	1.03
Pmag	B C11n.1r*	29.527	10H-5, 10	82.01	81.82	10H-5, 12	82.03	81.84	82.02	81.83	0.01	0.01	0.79
CN	<i>B Sphenolithus distentus</i>	30	10H-5, 40	82.31	82.11	10H-CC	85.71	85.40	84.01	83.75	1.70	0.99	
Pmag	B C11n.2n*	29.97	10H-7, 88	85.50	85.20	11H-1, 12	85.52	85.40	85.51	85.30	0.01	0.10	0.71
Pmag	B C11r*	30.591	11H-4, 18	89.92	89.92	11H-4, 20	89.94	89.94	89.93	89.93	0.01	0.01	1.09
PF	<i>T Subbotina angiporoides</i>	30.1	10H-CC, 16–21	85.66	85.35	11H-CC, 31–36	94.50	94.50	90.08	89.93	4.42	3.05	
PF	<i>T Turborotalita ampliapertura</i>	30.4	10H-CC, 16–21	85.66	85.35	11H-CC, 31–36	94.50	94.50	90.08	89.93	4.42	3.05	
Pmag	B reversal C12n*	30.977	11H-6, 138	94.13	94.13	12X-1, 0	94.90	94.90	94.52	94.52	0.01	0.39	0.49
CN	<i>T Coccolithus formosus</i>	32.92	12X-3, 37	98.20	98.20	12X-CC	100.10	100.10	99.15	99.15	0.95	0.63	
Pmag	B C12r*	33.214	13X-1, 112	105.02	105.02	13X-1, 114	105.04	105.04	105.03	105.03	0.01	0.01	0.98
Pmag	B C13n*	33.726	13X-5, 16	110.04	110.04	13X-5, 18	110.06	110.06	110.05	110.05	0.01	0.01	0.48
CN	<i>Bc Clausiococcus subdistichus</i>	33.88	13X-4, 51	108.90	108.90	13X-CC	111.61	111.61	110.26	110.26	1.36	1.36	
CN	<i>T Discoaster saipanensis</i>	34.44	13X-CC	111.56	111.56	14X-2, 81	115.81	115.81	113.69	113.69	2.13	1.42	
CN	<i>T Discoaster barbadiensis</i>	34.77	13X-CC	111.56	111.56	14X-2, 81	115.81	115.81	113.69	113.69	2.13	1.42	
Pmag	B C13r*	35.102	14X-3, 14	116.64	116.64	14X-3, 16	116.66	116.66	116.65	116.65	0.01	0.01	0.82
PF	<i>T Globigerinatheka index</i>	34.5	13X-CC, 9–14	111.56	111.56	14X-CC, 21–26	120.66	120.66	116.11	116.11	4.55	3.03	
CN	<i>T Chiasmolithus grandis</i>	37.77	16X-2, 94	135.14	135.14	16X-4, 36	137.55	137.55	136.35	136.35	1.21	0.80	
CN	<i>Bc Reticulofenestra erbae</i>	37.88	16X-4, 36	137.55	137.55	16X-CC	140.19	140.19	138.87	138.87	1.32	0.88	
PF	<i>T Acarinina mcgowrani</i>	37.7	16X-CC, 15–20	140.14	140.14	17X-CC, 15–20	149.58	149.58	144.86	144.86	4.72	3.15	
Pmag	B C18n.1r*	39.666	18X-2, 44	153.84	153.84	18X-2, 46	153.86	153.86	153.85	153.85	0.01	0.01	0.38
Pmag	B C18n.2n*	40.073	18X-3, 50	155.40	155.40	18X-3, 52	155.42	155.42	155.41	155.41	0.01	0.01	1.07
CN	<i>Bc Reticulofenestra bisecta</i> *	40.25	18X-3, 130	156.20	156.20	18X-CC	158.41	158.41	157.31	157.31	1.10	1.10	

have different first and last occurrence dates in the midlatitudes of the Pacific compared to the ages of these datums reported in the tropical–subtropical zonation schemes (Wade et al., 2011; King et al., 2020), with ages differing by more than 3 My (Lam et al., 2022). Two of the planktic foraminiferal datums that lie outside of the calcareous nannofossil and magnetic reversal boundaries are bases (*G. dehiscens* and *T. trilobus*; Tables T23, T24) and therefore cannot be explained by reworking nor are the events artificially lower in the section because of poor preservation.

**Table T24.** All biostratigraphic and paleomagnetic datums in stratigraphic order, Hole U1558F. \* = datums used to plot the age model curve in Figure F80 and calculate LSRs using CSF-A depths. B = base, T = top, Bc = base common, B reversal = base of a paleomagnetic reversal event. CN = calcareous nannofossils, PF = planktic foraminifera. Pmag = paleomagnetism. ML = mudline core. [Download table in CSV format.](#)

Datum	Taxon/Chron (base)	Age (Ma)	Sample	Sample depth CSF-A (m)	Sample depth CSF-B (m)	Sample above/below	Sample above/below depth CSF-A (m)	Sample above/below depth CSF-B (m)	Midpoint depth CSF-A (m)	Midpoint depth CSF-B (m)	Depth error (±) CSF-A (m)	Depth error (±) CSF-B (m)	LSR (cm/ky)
			393-U1558F-			393-U1558F-							
PF	<i>B Globorotalia hirsuta*</i>	0.45	1H-1, 0 (ML)	0.00	0.00	1H-CC, 10–15	4.03	4.00	2.02	2.00	2.02	2.00	0
PF	<i>B Globorotalia truncatulinoides</i>	1.92	1H-1, 0 (ML)	0.00	0.00	1H-CC, 10–15	4.03	4.00	2.02	2.00	2.02	2.00	
PF	<i>B Globorotalia tosaensis</i>	3.35	1H-1, 0 (ML)	0.00	0.00	1H-CC, 10–16	4.03	4.00	2.02	2.00	2.02	2.00	
PF	<i>B Globorotalia crassaformis</i> s.l.	4.3	1H-1, 0 (ML)	0.00	0.00	1H-CC, 10–15	4.03	4.00	2.02	2.00	2.02	2.00	
PF	<i>B Sphaeroidinella dehiscens</i> s.l.	5.54	1H-1, 0 (ML)	0.00	0.00	1H-CC, 10–15	4.03	4.00	2.02	2.00	2.02	2.00	
PF	<i>B Globorotalia tumida</i>	5.82	1H-1, 0 (ML)	0.00	0.00	1H-CC, 10–15	4.03	4.00	2.02	2.00	2.02	2.00	
PF	<i>B Globigerinoides conglobatus*</i>	6.21	1H-1, 0 (ML)	0.00	0.00	1H-CC, 10–15	4.03	4.00	2.02	2.00	2.02	2.00	0
PF	<i>T Catapsydrax dissimilis*</i>	17.51	1H-1, 0 (ML)	0.00	0.00	1H-CC, 10–15	4.03	4.00	2.02	2.00	2.02	2.00	0.27
PF	<i>B Globoquadrina dehiscens</i>	22.5	2H-CC, 15–20	13.99	13.45	3H-CC, 41–46	23.11	23.00	18.55	18.23	4.56	4.77	
Pmag	<i>B C6Br*</i>	22.621	3H-2, 82	15.83	15.80	3H-2, 84	15.82	15.82	15.81	15.81	0.01	0.01	0.91
CN	<i>B Discoaster druggii</i>	22.68	2H-CC	13.99	13.45	3H-3, 1–3	19.61	19.54	16.80	16.50	2.81	3.05	
Pmag	<i>B C6Cn.1n*</i>	22.792	3H-3, 88	17.40	17.36	3H-3, 90	17.38	17.38	17.37	17.37	0.01	0.01	1.1
Pmag	<i>B C6Cn.1r*</i>	22.973	3H-4, 140	19.42	19.35	3H-4, 142	19.37	19.37	19.36	19.36	0.01	0.01	1.24
Pmag	<i>B C6Cn.2n*</i>	23.04	3H-5, 74	20.26	20.18	3H-5, 76	20.20	20.20	20.19	20.19	0.01	0.01	0.84
CN	<i>T Reticulofenestra bisecta</i>	23.13	3H-5, 7–9	19.59	19.52	3H-CC, 41–46	23.11	23.00	21.35	21.26	1.76	1.74	
Pmag	<i>B C6Cn.2r*</i>	23.212	3H-6, 58	21.61	21.52	3H-7, 0	21.76	21.76	21.64	21.64	0.12	0.12	0.49
Pmag	<i>B C6Cn.3n*</i>	23.318	3H-7, 40	22.25	22.15	3H-7, 42	22.17	22.17	22.16	22.16	0.01	0.01	0.63
Pmag	<i>B C6Cr*</i>	24.025	5H-1, 62	26.62	26.62	5H-1, 64	26.64	26.64	26.63	26.63	0.01	0.01	0.63
CN	<i>T Sphenolithus cipoensis</i>	24.36	3H-CC, 41–46	23.06	22.95	5H-2, 136–138	28.85	28.85	25.96	25.90	2.90	1.97	
Pmag	<i>B C7n.2n*</i>	24.459	5H-3, 40	29.37	29.37	5H-3, 42	29.39	29.39	29.38	29.38	0.01	0.01	1.23
Pmag	<i>B C8n.2n*</i>	25.987	7H-3, 10	48.12	47.98	7H-3, 12	48.18	47.99	48.15	47.98	0.03	0.01	1.03
Pmag	<i>B C8r*</i>	26.42	7H-6, 8	52.61	52.26	7H-6, 10	52.63	52.28	52.62	52.27	0.01	0.01	0.44
CN	<i>T Sphenolithus predistentus</i>	26.93	7H-5, 88–90	51.91	51.59	7H-CC, 34–39	54.96	54.50	53.44	53.05	1.53	0.82	
Pmag	<i>B C9n*</i>	27.439	8H-2, 106	57.07	56.93	8H-2, 108	57.09	56.95	57.08	56.94	0.01	0.01	0.76
CN	<i>B Sphenolithus cipoensis</i>	27.13	7H-CC, 34–39	54.91	54.45	8H-3, 25–27	57.79	57.61	56.35	56.03	1.44	0.99	
PF	<i>T Paragloborotalia opima</i>	26.9	7H-CC, 34–39	54.91	54.45	8H-CC, 16–21	64.56	64.00	59.74	59.23	4.83	4.77	
Pmag	<i>B C9r*</i>	27.859	8H-4, 124	60.25	59.93	8H-4, 126	60.27	59.95	60.26	59.94	0.01	0.01	2.45
Pmag	<i>B C10n.1n*</i>	28.087	8H-7, 82	65.84	65.84	9H-1, 0	65.86	65.86	65.85	65.85	0.01	0.01	0.71
Pmag	<i>B C11n.1n*</i>	29.477	10H-3, 4	75.75	75.75	10H-3, 6	75.77	75.77	75.76	75.76	0.01	0.01	1.8
Pmag	<i>B C11n.1r*</i>	29.527	10H-3, 94	76.65	76.65	10H-3, 96	76.67	76.67	76.66	76.66	0.01	0.01	0.85
PF	<i>T Subbotina angiporoides</i>	30	9H-CC, 14–19	72.65	72.65	10H-CC, 34–39	83.05	83.05	77.85	77.85	5.20	5.20	
Pmag	<i>B C11n.2n*</i>	29.97	10H-6, 18	80.42	80.42	10H-6, 20	80.44	80.44	80.43	80.43	0.01	0.01	0.72
CN	<i>B Sphenolithus distentus</i>	30	10H-5, 58–60	79.31	79.31	10H-CC, 34–39	83.05	83.05	81.18	81.18	1.87	1.25	
PF	<i>T Pseudohastigerina nagewichiensis</i>	32	11H-CC, 15–20	91.08	91.08	12H-CC, 16–21	96.57	96.30	93.83	93.69	2.75	2.61	
CN	<i>T Coccolithus formosus</i>	32.92	13F-2, 80–82	98.60	98.58	14F-2, 78–80	103.30	103.19	100.95	100.88	2.35	1.50	
PF	<i>HCO Pseudohastigerina micra</i>	33.9	12F-CC, 16–21	96.52	96.25	14F-CC, 9–14	105.93	105.70	101.23	100.98	4.71	3.07	
Pmag	<i>B C12r*</i>	33.214	14F-2, 124	103.74	103.61	14F-3, 0	104.00	103.86	103.87	103.74	0.13	0.12	1.01
Pmag	<i>B C13n*</i>	33.726	15F-3, 30	109.01	108.92	15F-3, 32	109.03	108.94	109.02	108.93	0.01	0.01	0.49
CN	<i>Bc Clausiococcus subdistichus</i>	33.88	15F-3, 84–85	109.55	109.45	15F-CC, 13–14	110.53	110.40	110.04	109.92	0.49	0.27	
PF	<i>T Globigerinatheka index</i>	34.5	14F-CC, 9–14	105.88	105.65	16F-CC, 15–20	115.29	115.10	110.59	110.38	4.71	3.09	
CN	<i>T Discoaster saipanensis</i>	34.44	16F-1, 130–135	111.74	111.69	16F-2W 1–2	111.92	111.86	111.83	111.77	0.09	0.04	
CN	<i>T Discoaster barbadiensis</i>	34.77	16F-2, 1–2	111.91	111.85	16F-2, 118–120	113.10	113.00	112.51	112.42	0.59	0.35	
Pmag	<i>B C13r*</i>	35.102	17F-1, 68	115.78	115.78	17F-1, 70	115.80	115.80	115.79	115.79	0.01	0.01	0.90
PF	<i>T Hantkenina</i> spp.	33.9	16F-CC, 15–20	115.24	115.05	18F-CC, 19–24	124.90	124.50	120.07	119.78	4.83	3.02	
PF	<i>T Acarinina mcgowrani</i>	37.7	20X-CC, 20–25	136.62	136.62	22X-CC, 15–20	147.29	147.29	141.96	141.96	5.34	3.56	
PF	<i>T Morozovelloides crassatus</i>	37.7	20X-CC, 20–25	136.62	136.62	22X-CC, 15–20	147.29	147.29	141.96	141.96	5.34	3.56	
CN	<i>T Sphenolithus obtusus</i>	38.42	21X-4, 87–89	144.27	144.27	21X-CC, 28–33	147.29	147.29	145.78	145.78	1.51	1.01	
Pmag	<i>B C18n.1n*</i>	39.582	22X-2, 132	155.70	155.70	22X-3, 0	156.12	156.12	155.91	155.91	0.21	0.21	0.43
Pmag	<i>B C18n.1r*</i>	39.666	22X-3, 60	156.26	156.26	22X-3, 62	156.28	156.28	156.27	156.27	0.01	0.01	0.39
Pmag	<i>B C18n.2n*</i>	40.073	23X-1, 12	157.42	157.42	23X-1, 14	158.30	158.30	157.86	157.86	0.44	0.44	0.34
CN	<i>Bc Reticulofenestra bisecta</i>	40.25	22X-CC, 15–20	157.58	157.58	23X-3, 81–83	162.12	162.12	159.85	159.85	2.27	1.51	
PF	<i>T Morozovella aragonensis*</i>	42.6	22X-CC, 15–20	157.58	157.58	24X-CC, 15–17	175.31	175.31	166.45	166.45	8.87	5.91	



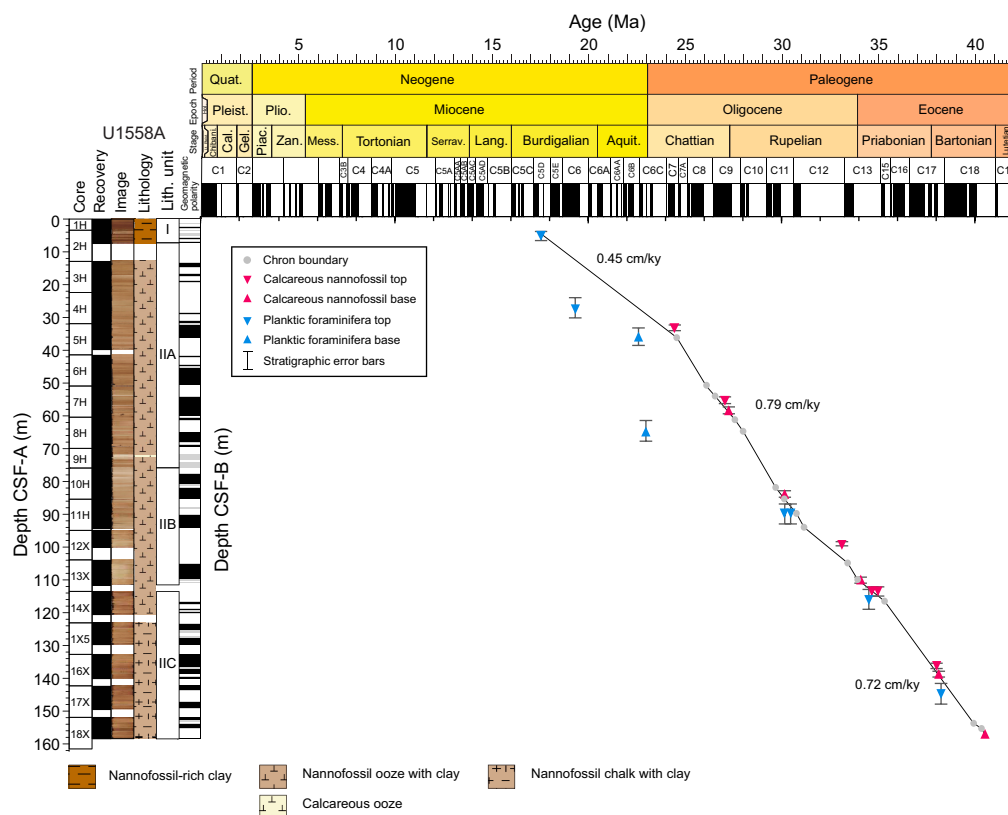
Therefore, shore-based analyses and further refinement and calibration of planktic foraminiferal datums is required to fully understand the magnitude of such potential offsets in age. Hole U1558F may have recorded better fossil datum agreement with the age model because of different species used (e.g., *P. opima*) that may have less diachroneity than species used in Hole U1558A (e.g., *T. trilobus*).

Linear sedimentation rates (LSRs) were calculated using paleomagnetic reversal boundaries and microfossil datums. Datums used in LSR calculations are given in Tables T23 and T24. Average LSRs are fairly similar in both holes, with values in the Early Miocene of around 0.3–0.4 cm/ky, and values in the Oligocene and Eocene around 0.7–0.8 cm/ky (Figures F79, F80).

## 9.2. Mass accumulation rates

Mass accumulation rates (MARs) were calculated for Holes U1558A and U1558F using the LSRs and bulk density from gamma ray attenuation (GRA) measurements collected during Whole-Round Multisensor Logger (WRMSL) scans (see [Age model and mass accumulation rates](#) in the Expedition 390/393 methods chapter [Coggon et al., 2024b]; see also AGEMODEL in [Supplementary material](#)). The data presented in Figure F81 are binned into 1 My intervals. Gaps represent bins with no data.

MARs vary throughout the sedimentary succession in Holes U1558A and U1558F (Figure F81; see AGEMODEL in [Supplementary material](#)). Generally, MARs are highest in the mid-late Oligocene, with values peaking around 2.8 g/cm<sup>2</sup>/ky in Hole U1558F. This peak is not observed in Hole U1558A, where late Oligocene values generally hover between 0.9 and 1.4 g/cm<sup>2</sup>/ky. Interestingly, this relationship is reversed in the Eocene, with Hole U1558A MAR values higher (around 1.0 g/cm<sup>2</sup>/ky) than Hole U1558F values (around 0.65 g/cm<sup>2</sup>/ky). Values are lowest at both holes in the Early Miocene with values around 0.4 g/cm<sup>2</sup>/ky.



**Figure F79.** Age-depth model showing biostratigraphic and magnetostratigraphic datums, Hole U1558A. LSRs calculated based on indicated datums in Table T23 and averaged for Miocene, Oligocene, and Eocene.

### 9.3. Carbonate and organic carbon accumulation rates

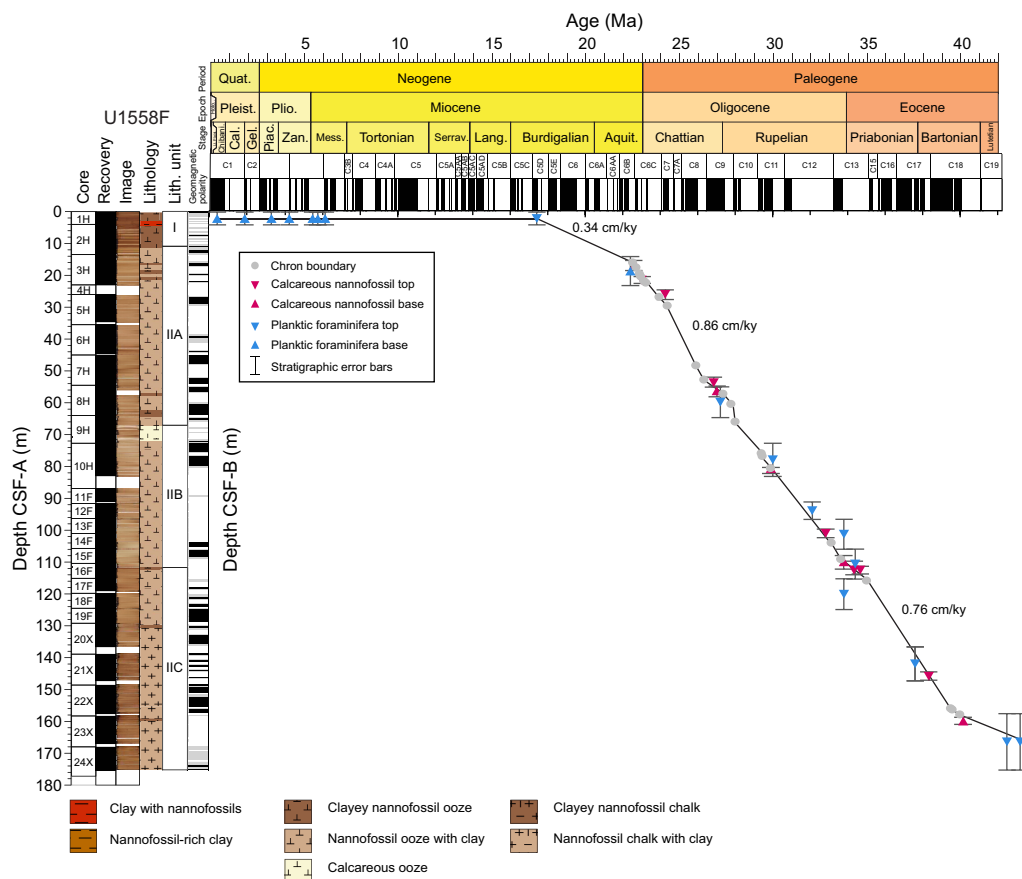
Carbonate accumulation rates (CARs) and organic carbon accumulation rates (OCARs) were calculated by multiplying the MAR by the weight percent of carbonate and total organic carbon (TOC), respectively (see AGEMODEL in [Supplementary material](#)). In Hole U1558A, carbonate analysis was performed on interstitial water (IW) squeeze cakes, which were taken at a resolution of one per core. One additional discrete sample per core for carbonate and organic carbon analysis was taken from the working halves of Cores 390C-U1558A-13X-17X. In Hole U1558F, three additional discrete carbonate and organic carbon samples were taken from Core 393-U1558F-1H, two from Core 2H, and one per core were taken from most cores (3H-10H, 13E, 15E, 16E, and 20X-24X).

#### 9.3.1. Carbonate accumulation rates

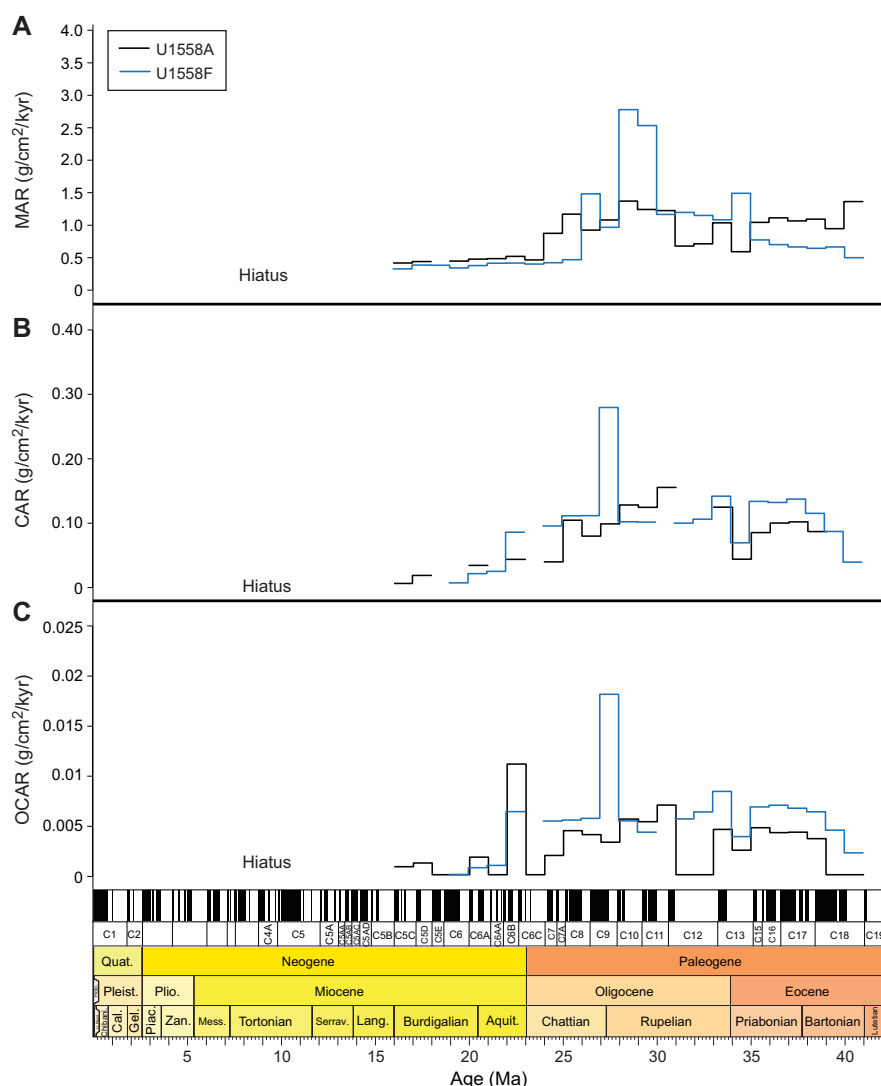
CARs are variable throughout the sedimentary successions in Holes U1558A and U1558F (Figure [F81](#); see AGEMODEL in [Supplementary material](#)). In both Holes U1558A and U1558F, CARs are highest for the Eocene and Oligocene, with values ranging 0.04–0.16 g/cm<sup>2</sup>/ky in Hole U1558A and 0.03–0.35 g/cm<sup>2</sup>/ky in Hole U1558F. Neogene CARs are slightly lower and variable throughout the sections, with values ranging 0.01–0.05 g/cm<sup>2</sup>/ky in Hole U1558A and 0.008–0.04 g/cm<sup>2</sup>/ky in Hole U1558F.

#### 9.3.2. Organic carbon accumulation rates

OCARs are extremely low and variable throughout the sedimentary successions in Holes U1558A and U1558F (Figure [F81](#); see AGEMODEL in [Supplementary material](#)). Through the Eocene and Oligocene, OCARs range 0.002–0.007 g/cm<sup>2</sup>/ky in Hole U1558A and 0.002–0.02 g/cm<sup>2</sup>/ky in Hole U1558F. Neogene OCARs are in general slightly lower, except for a peak in OCAR in Hole U1558A



**Figure F80.** Age-depth model showing biostratigraphic and magnetostratigraphic datums, Hole U1558F. LSRs calculated based on indicated datums in Table T24 and averaged for Miocene, Oligocene, and Eocene.



**Figure F81.** (A) MAR, (B) CAR, and (C) OCAR calculated at 1 My intervals, Holes U1558A and U1558F. Gaps in MAR, CAR, and OCAR values = 1 My time intervals with no data available.

at 22 Ma (0.01 g/cm<sup>2</sup>/ky), and range 0.009–0.01 g/cm<sup>2</sup>/ky in Hole U1558A and 0.0005–0.002 g/cm<sup>2</sup>/ky in Hole U1558F.

## 10. Physical properties and downhole measurements

### 10.1. Sediment

Physical properties characterization of the sediment sequence at Site U1558 was primarily based on cores from Holes U1558A (recovered during Expedition 390C) and U1558F (Expedition 393). Hole U1558E (Expedition 393) missed the mudline, so the physical properties data from this single core, although measured, are not part of the interpretation. Unless specified otherwise, all depths given are in meters below seafloor (mbsf) on the CSF-A scale. Holes U1558A and U1558F encountered basement rocks at 158.9 and 176.0 mbsf, respectively. Basement reentry Hole U1558D recovered the sediment/basement interface at 166.8 mbsf as well as ~3 m of sediment above the basement.

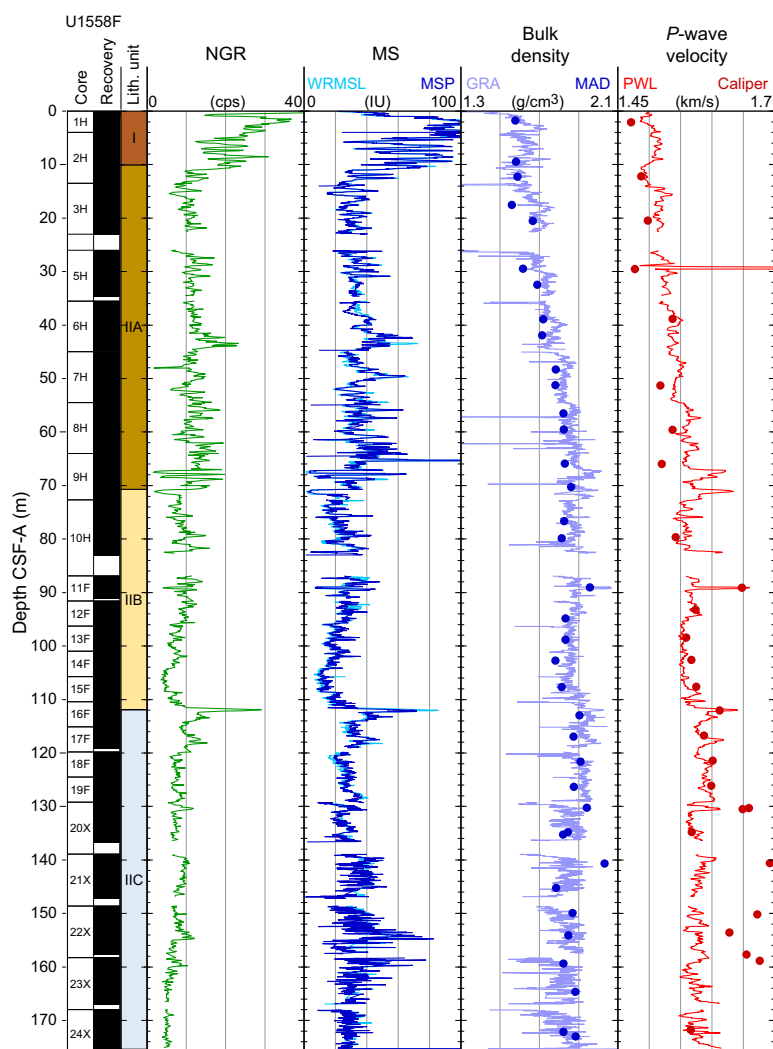
Whole-round core section measurements from Hole U1558F included NGR, GRA bulk density, MS, and compressional wave (*P*-wave) velocity (Figure F82). Split-core section measurements

included discrete measurements of point magnetic susceptibility (MSP), *P*-wave velocity, thermal conductivity, and sediment shear and compressional strength (Table T25). Discrete sediment samples were taken from the working halves for moisture and density (MAD) analysis (Table T26; Figure F83). Only core logging (track) physical properties measurements were made on cores from Hole U1558A (Figure F84). Because coring with the APC system continued to greater depths in Hole U1558F than in Hole U1558A before switching to XCB and because data from both holes display similar features (see **Stratigraphic correlation**), the interpretation of Site U1558 sediment physical properties is predominantly based on Hole U1558F. Unless specified otherwise, mean values of all physical properties are represented as arithmetic means with  $\pm 1$  standard deviation.

### 10.1.1. Physical properties

#### 10.1.1.1. Natural gamma radiation

NGR ranges 2–50 counts/s through the sedimentary section in Hole U1558F (Figure F82). The upper ~10 m shows the highest NGR values (range = 12–50 counts/s; mean =  $24 \pm 7$  counts/s)



**Figure F82.** Summary of core physical properties data, Hole U1558F. Solid circles = discrete bulk density and *P*-wave velocity measurements. cps = counts per seconds.

**Table T25.** Physical properties, Hole U1558F. [Download table in CSV format.](#)

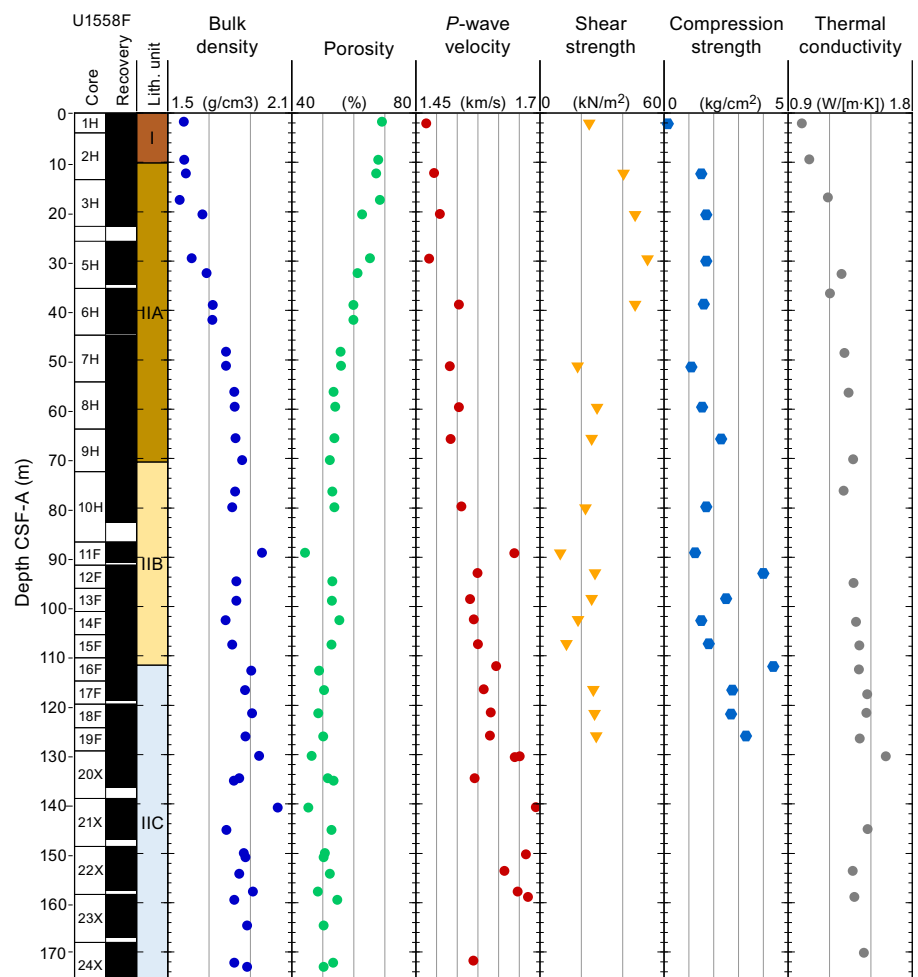
**Table T26.** Discrete MAD, Site U1558. [Download table in CSV format.](#)



compared to other depth intervals (mean =  $9 \pm 3$  counts/s) (Table T27) and corresponds to nanofossil-rich clay and nanofossil ooze present in Lithostratigraphic Unit I (see **Sedimentology**). NGR ranges 2–24 counts/s in Subunit IIA (10.1–70.75 mbsf; mean =  $12 \pm 3$  counts/s) and stays uniformly low in Subunits IIB and IIC (70.75–111.90 and 111.90–175.43 mbsf, respectively; mean [both subunits] =  $8 \pm 3$  counts/s) (Table T27). These low NGR values (<15 counts/s) are typical of carbonate ooze (Dunlea et al., 2013). NGR shows an abrupt spike to 29 counts/s at 112 mbsf at the boundary between Lithostratigraphic Subunits IIB and IIC, nanofossil ooze with clay to nanofossil ooze/chalk with clay, respectively (Figure F82; see **Sedimentology**). A similar NGR spike is also found in Hole U1558A (114 mbsf; 20 counts/s) (Figure F84) and provides a key tie point for stratigraphic correlation (see **Stratigraphic correlation**). Intervals with elevated NGR are associated with separate peaks in U, Th, and K when the concentrations are examined separately (Figures F85, F86) (see **Physical properties and downhole measurements** in the Expedition 390/393 methods chapter [Coggon et al., 2024b]).

### 10.1.1.2. Magnetic susceptibility

Despite differences in frequency and resolution between the two magnetic susceptibility systems (see **Physical properties and downhole measurements** in the Expedition 390/393 methods chapter [Coggon et al., 2024b]), both MS measured on the WRMSL and MSP data show similar downhole trends and magnitude of susceptibility throughout the sedimentary sections. Similar to the NGR record, magnetic susceptibility shows highest values in the upper ~10 m in Unit I (range = 18–118 instrument units [IU]; mean =  $70 \pm 22$  IU) compared to other units, reflecting the characteristics of the clayey nanofossil ooze layers (Figure F82). Magnetic susceptibility decreases throughout Subunit IIA between ~10 and ~70 mbsf (mean =  $34 \pm 12$  IU), and there are further



**Figure F83.** Summary of discrete physical properties data, Hole U1558F.

reductions throughout Subunit IIB between 70 and 112 mbsf (mean =  $19 \pm 8$  IU). This is followed by an increase in magnetic susceptibility in Subunit IIC to mean values of  $31 \pm 10$  IU (Figure F82; Table T27). An abrupt spike (85 IU) marks the boundary between Subunits IIB and IIC (112 mbsf), and it is used as a tie point for stratigraphic correlation. The lower magnetic susceptibility values in all subunits of Unit II compared to Unit I are indicative of clay-poor carbonate oozes in these intervals.

### 10.1.1.3. Gamma ray attenuation bulk density

Bulk density measured from both GRA and MAD methods shows generally consistent results, ranging 1.0–2.4 g/cm<sup>3</sup> throughout the sedimentary sections (mean =  $1.8 \pm 0.1$  g/cm<sup>3</sup>), although MAD bulk densities are consistently around 2% lower than GRA (Figure F82). This may be due to sediment drying after exposure to air when the cores were split. The mean bulk density is lowest in Unit I ( $1.6 \pm 0.1$  g/cm<sup>3</sup>) compared to the other three subunits ( $1.8 \pm 0.1$  g/cm<sup>3</sup>). Bulk density shows an overall gradual increase from the seafloor to the basement (Figure F82) reflecting the increasing compaction of sediments with depth.

### 10.1.1.4. Moisture and density

A total of 37 discrete samples were taken for MAD analysis. Generally, two samples were chosen per core in representative lithologies (mostly nannofossil-rich clay and ooze) from Hole U1558F. Porosity of the sedimentary section shows a decreasing trend from ~70% at the seafloor to ~50% at 173 mbsf at the sediment/basement interface (Figure F87), mirroring the trend observed in bulk

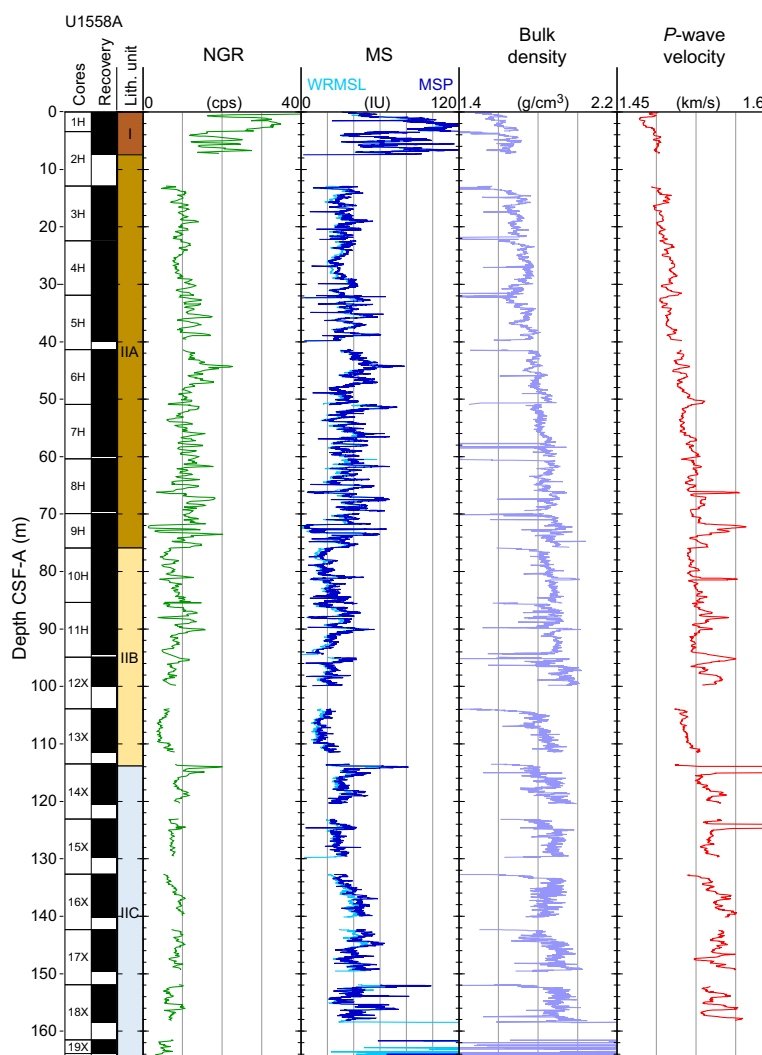


Figure F84. Summary of core physical properties data, Hole U1558A. cps = counts per seconds.

density (Figure F83). The mean values of porosity in Unit I and Subunit IIA ( $68 \pm 1\%$  and  $59 \pm 5\%$ , respectively) are higher than those in Subunits IIB and IIC ( $52 \pm 4\%$  and  $51 \pm 3\%$ , respectively).

In Figure F87 we compare the porosities measured downhole by MAD with sediment porosity profiles for common seafloor sediment types (see Spinelli et al., 2004). Although the sediments recovered in Hole U1558F are predominantly nannofossil ooze (83–94 wt%  $\text{CaCO}_3$ ; see **Sedimentology**), their porosities have lower values and show a slightly steeper porosity profile with depth than calcareous ooze reported in published compilations (e.g., Spinelli et al., 2004) (Figure F87). This difference can likely be attributed to the limited amount of data the calcareous ooze curve in Spinelli et al. (2004) is based on (Hamilton, 1976) and to the nannofossil ooze having a lower porosity than other calcareous ooze such as foraminiferal ooze, due to its smaller grain size and reduced amount of intraparticle void space. For example, reported porosities in seafloor coccolith ooze (54%–67%) (Bennett et al., 1989) are significantly lower than suggested seafloor porosity of the calcareous ooze ( $\sim 72\%$ ) in Spinelli et al. (2004). If sediments at Site U1558 entirely comprised nannofossil ooze, the projected seafloor porosity would fall within the Bennett et al. (1989) observed range. However, in Hole U1558F the uppermost 15 m includes Unit I sediments with up to 43% unconsolidated clay minerals that increase the porosity at the shallowest levels (see Figure F87).

#### 10.1.1.5. P-wave velocity

Discrete measurements were chosen to target intact pieces and avoid the drilling mud from XCB coring, which is significantly softer (Figure F82, F83). Given the instrument uncertainties, we always consider the higher discrete *P*-wave values likely to be the better representation of the *P*-wave velocity ( $V_p$ ) of the formation (see **Physical properties and downhole measurements** in the Expedition 390/393 methods chapter [Coggon et al., 2024b]).

After filtering out unrealistic spikes  $>1.8$  km/s (outside the typical range of pelagic sediments shallower than 200 mbsf and anomalous in the trends recorded here) and  $<1.45$  km/s (below the velocity of water) from the WRMSL data, the *P*-wave velocity throughout the section ranges 1.45–1.74 km/s (Figure F82; Table T25) (mean =  $1.56 \pm 0.03$  km/s; Table T27). *P*-wave velocity in Hole U1558F generally increases with depth, from a mean of  $1.51 \pm 0.02$  km/s in Unit I to mean values of  $1.54 \pm 0.03$  km/s,  $1.56 \pm 0.02$  km/s, and  $1.58 \pm 0.02$  km/s in Subunits IIA, IIB, and IIC, respectively; this is also in agreement with data from Hole U1558A (Figure F84; Table T27). The overall

**Table T27.** Physical properties statistics, Site U1558.  $1\sigma$  = one standard deviation. MAD = moisture and density. No discrete measurements were made in Hole U1558A. Groups with only one sample do not have a standard deviation (NA). Empty cells = no measurements were made. [Download table in CSV format.](#)

Group	Core logging measurements									
	NGR mean	NGR $1\sigma$	WRMSL MS mean	WRMSL MS $1\sigma$	WRMSL <i>P</i> -wave velocity mean	WRMSL <i>P</i> -wave velocity $1\sigma$	MSP mean	MSP $1\sigma$	GRA bulk density mean	GRA bulk density $1\sigma$
	(counts/s)	(counts/s)	(IU)	(IU)	(km/s)	(km/s)	(IU)	(IU)	(g/cm <sup>3</sup> )	(g/cm <sup>3</sup> )
Unit I	24.10	7.44	69.50	22.10	1.51	0.02	73.20	22.30	1.62	0.07
Unit IIA	11.80	3.04	33.50	11.50	1.54	0.03	35.20	11.10	1.77	0.11
Unit IIB	8.03	2.60	19.30	7.88	1.56	0.02	22.00	7.39	1.87	0.04
Unit IIC	7.79	2.50	31.20	9.90	1.58	0.02	32.10	12.40	1.86	0.08
Hole U1558F	14.24	8.17	73.24	24.14	1.51	0.08	NA	NA	1.60	0.07
Hole U1558A	12.27	7.96	69.85	24.63	1.51	0.12	NA	NA	1.67	0.09

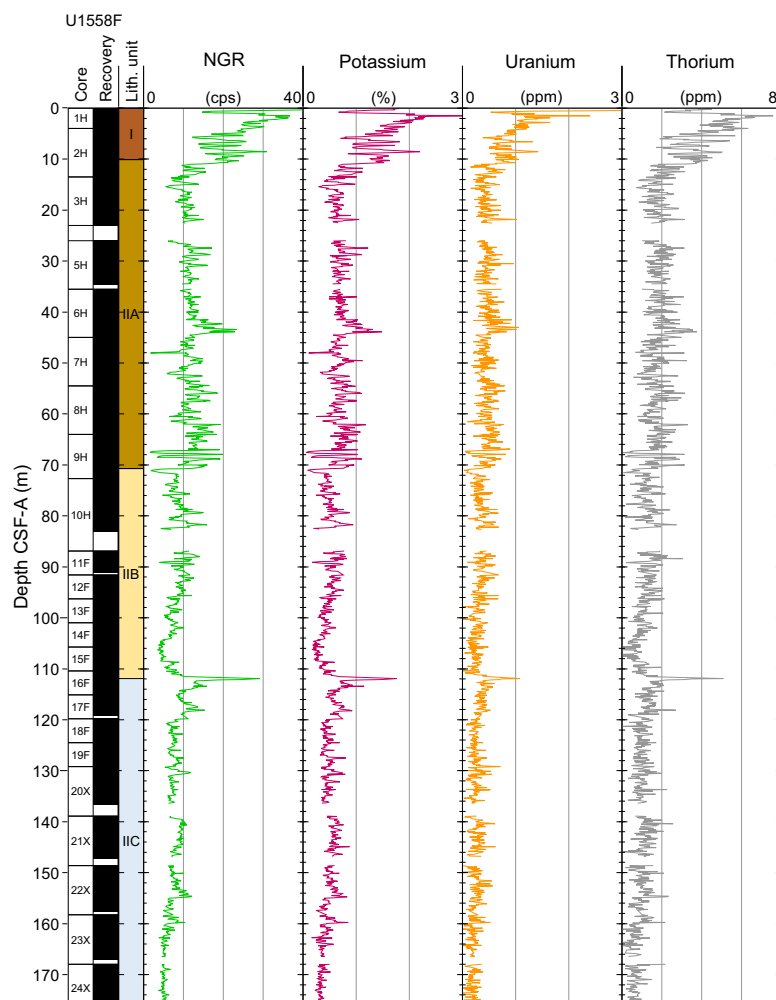
Group	Discrete sample measurements													
	Thermal conductivity mean	Thermal conductivity $1\sigma$	Caliper <i>P</i> -wave velocity mean	Caliper <i>P</i> -wave velocity $1\sigma$	Porosity mean	Porosity $1\sigma$	MAD bulk density mean	MAD bulk density $1\sigma$	Grain density mean	Grain density $1\sigma$	Compressional strength mean	Compressional strength $1\sigma$	Vane shear strength mean	Vane shear strength $1\sigma$
	(W/[m·K])	(W/[m·K])	(km/s)	(km/s)	(%)	(%)	(g/cm <sup>3</sup> )	(g/cm <sup>3</sup> )	(g/cm <sup>3</sup> )	(g/cm <sup>3</sup> )	(kg/cm <sup>2</sup> )	(kg/cm <sup>2</sup> )	(KN/m <sup>2</sup> )	(KN/m <sup>2</sup> )
Unit I	1.03	0.03	1.47	NA	68.40	0.92	1.58	0.00	1.62	0.07	0.20	NA	23.8	NA
Unit IIA	1.28	0.07	1.52	0.02	59.20	5.49	1.73	0.10	1.77	0.11	1.63	0.36	36.4	12.8
Unit IIB	1.37	0.05	1.58	0.04	52.20	3.58	1.84	0.06	1.87	0.04	2.12	1.01	19.1	6.7
Unit IIC	1.44	0.06	1.62	0.04	50.60	2.60	1.87	0.06	1.86	0.08	3.29	0.79	26.5	0.71
Hole U1558F	1.31	0.01	1.55	0.05	56.51	6.78	1.77	0.11	2.74	0.02	2.20	0.96	27.8	11.73
Hole U1558A	1.27	0.03												

increasing trend is likely a result of an increasing degree of sediment consolidation with depth. The WRMSL method measures *P*-wave velocities that are generally consistent with results from the caliper method in Cores 393-U1558F-1H through 19F but shows much lower velocity values in Cores 20X–22X (Figure F82). This is likely due to the change to XCB coring from Core 20X. In XCB cores (20X–24X), the WRMSL cannot distinguish the intact “biscuits” of sediment from the surrounding ground-up “gravy” sediment material and measures values that are significantly lower than the discrete *P*-wave velocity measurements from the caliper system (see **Physical properties and downhole measurements** in the Expedition 390/393 methods chapter [Coggon et al., 2024b]). Conversely, shallower than ~80 mbsf, most of the WRMSL data are higher than the caliper measurements (Figure F82). In fact, in APC cores with good contact with the liner, the pinching of the sensors onto the liner may even introduce some amount of compression and increase these readings.

#### 10.1.1.6. Sediment strength

Compressional strength and shear strength were only measured on Cores 393-U1558F-1H through 19F, where either the APC or half-length APC coring systems were used. These measurements could not be performed on sediments cored with the XCB system (Cores 20X–24X) because they were either too consolidated or too brittle for the automated vane or the penetrometer, reflecting the same lithologic changes that required the switch from APC to XCB coring.

The compressional strength is lowest in Unit I ( $0.2 \text{ kg/cm}^2$ ) and increases with depth through Sub-units IIA ( $1.6 \pm 0.4 \text{ kg/cm}^2$ ), IIB ( $2.1 \pm 1.0 \text{ kg/cm}^2$ ), and IIC ( $3.3 \pm 0.8 \text{ kg/cm}^2$ ) (Figure F83; Table T27). Shear strength is highest in the uppermost 30 m in Hole U1558F, increasing progressively



**Figure F85.** NGR spectrometry data showing potassium, uranium, and thorium, Hole U1558F. cps = counts per seconds.



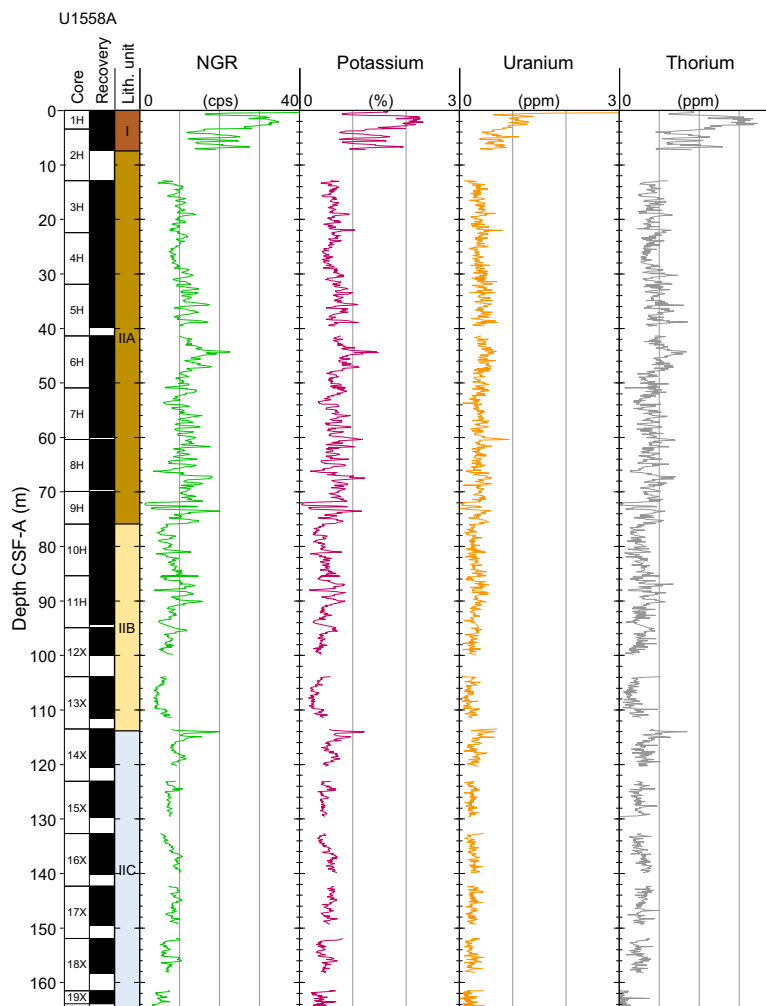
from the top of the hole (Core 393-U1558F-1H; Unit I) to the maximum measurement of 52 kN/m<sup>2</sup> at 30 mbsf (Core 5H; Subunit IIA). Below 30 mbsf, values decrease progressively until ~50 mbsf (lower Subunit IIA) then varies irregularly between ~10–30 kN/m<sup>2</sup> through the rest of the APC cored record to ~125 mbsf (lower Subunits IIA–IIC) (Table T25). Based on sedimentologic descriptions (see [Sedimentology](#)), higher shear strength corresponds to intervals with higher clay content (Figure F83).

#### 10.1.1.7. Thermal conductivity

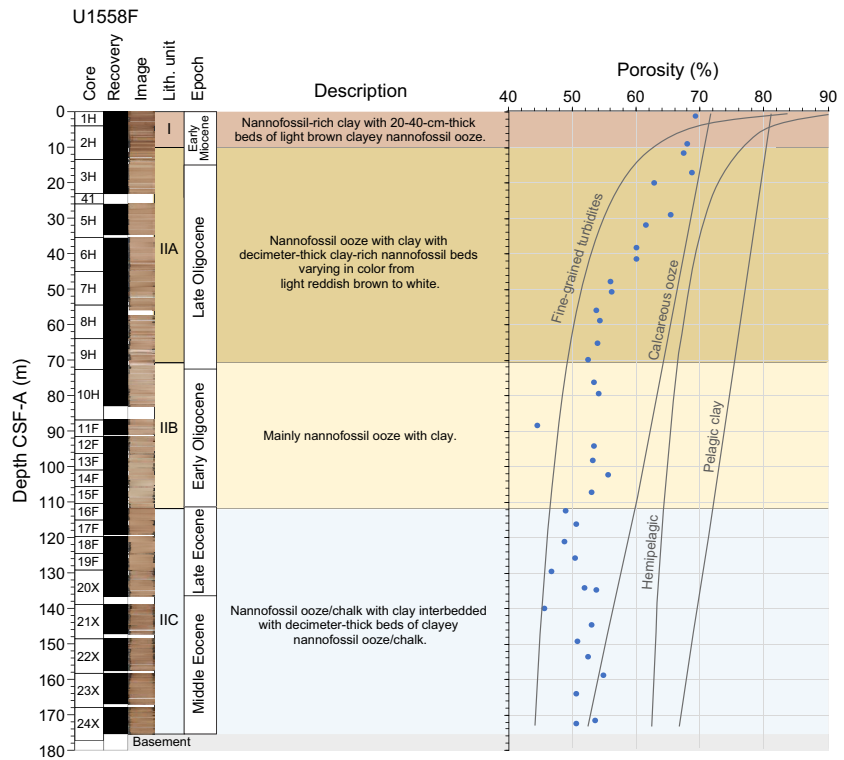
A total of 21 discrete thermal conductivity measurements, approximately one per core, were conducted on representative lithologies from Hole U1558F using the half-space puck on split section halves. Thermal conductivity ranges 1–1.61 W/(m·K) (Table T25) throughout all sections (mean =  $1.34 \pm 0.14$  W/[m·K]). Thermal conductivity gradually increases downhole with a similar trend to bulk density but with an inverse trend compared to porosity (Figure F83). Mean thermal conductivity for lithostratigraphic units ranges  $1.03 \pm 0.03$  W/(m·K) in Unit I to  $1.28 \pm 0.07$  W/(m·K) in Subunit IIA,  $1.37 \pm 0.05$  W/(m·K) in Subunit IIB, and  $1.44 \pm 0.06$  W/(m·K) in Subunit IIC (Table T27).

#### 10.1.2. Lithostratigraphic unit comparison

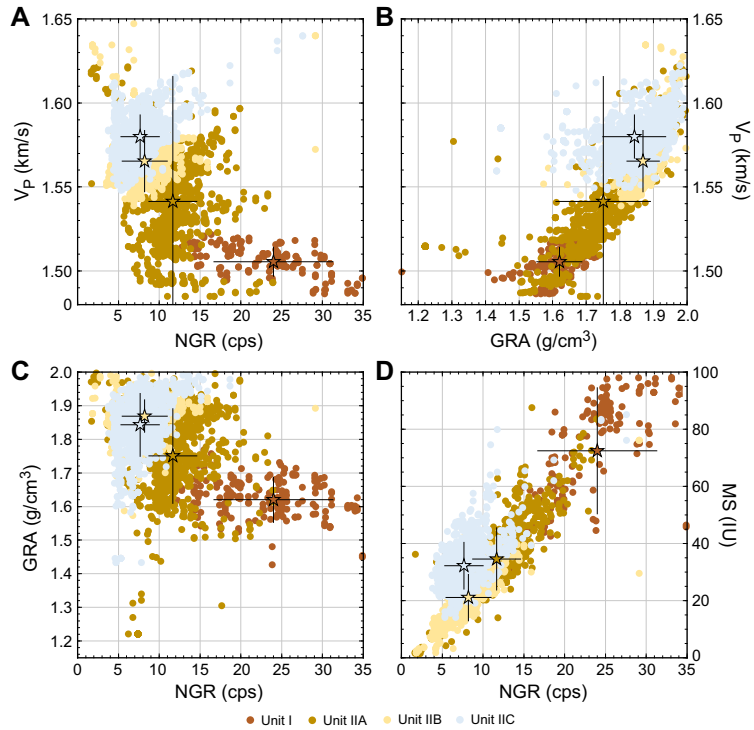
Crossplot analyses of core logging (track) physical properties data from Hole U1558F show comparisons between *P*-wave velocity, GRA bulk density, MS, and NGR, sorted by lithostratigraphic units (Figure F88). Figure F88B shows an overall positive correlation between *P*-wave velocity and bulk density, consistent with compaction of sediments with depth; the deeper units correspond to



**Figure F86.** NGR spectrometry data showing potassium, uranium, and thorium, Hole U1558A. cps = counts per seconds.



**Figure F87.** Comparison of porosity from Hole U1558F (blue dots) with typical sediment porosity profiles for common oceanic deepwater sediment types (Spinelli et al., 2004).



**Figure F88.** Crossplots of sediment sample by lithology, Hole U1558F. A. NGR vs.  $V_p$ . B. GRA bulk density vs.  $V_p$ . C. NGR vs. GRA bulk density. D. NGR vs. MS. Unit I is nannofossil-rich clay, Subunit IIA is nannofossil ooze with clay, Subunit IIB is nannofossil ooze, and Subunit IIC is nannofossil ooze/chalk with clay. Mean (stars) and standard deviation (error bars) for each unit are also shown. cps = counts per seconds.

higher values. Unit I clusters in a narrow range of low velocity and low density, whereas density data from Subunit IIA increase almost linearly with increasing *P*-wave velocity. Data from Subunit IIB plot in agreement with the Subunit IIA trend, albeit clustering only within higher ranges of *P*-wave velocity and density. Unlike the others, Subunit IIC (the deepest unit) is characterized by a widespread data set with high velocities but a large range of bulk density. This different physical behavior could be biased by the XCB coring system.

Figure **F88A and F88C** shows the relationships between NGR and *P*-wave velocity and between NGR and GRA density, respectively. Although there are no clear trends between units, the figures illustrate the overall decrease in NGR in the deeper units, combined with higher velocity and density with depth. Plotting MS against NGR (Figure **F88D**) shows an almost linear relationship, where Unit I stands out with higher values and a wider range in both data sets, reflecting the influence of its higher clay content.

### 10.1.3. Downhole measurements

#### 10.1.3.1. Downhole temperature

During APC coring in both Holes U1558A and U1558F, the APCT-3 temperature probe was deployed while coring Cores 390C-U1558A-4H, 7H, and 10H, as well as Cores 393-U1558F-3H, 7H, and 10H (Table **T28**). Figure **F89** shows the intervals in the temperature records for each deployment that were used to estimate formation temperature by finding a best fit for a theoretical model to the temperature decay as a function of time (see **Physical properties and downhole measurements** in the Expedition 390/393 methods chapter [Coggon et al., 2024b]), as it recovers from the frictional heating generated when entering the formation with the APCT-3 temperature probe.

#### 10.1.3.2. Heat flow

Although the temperature records show that some of the temperature stations were stable for only a few minutes (Core 393-U1558F-3H in particular; Figure **F89**), the resulting temperatures define a steadily increasing temperature profile with a least-squares linear fit gradient of 23°C/km (Figure **F90C**; Table **T29**).

A simple estimate of the vertical conductive heat flow can be made by the product of this gradient with the mean thermal conductivity ( $1.23 \pm 0.12$  W/[m·K]) (Figure **F90A**) measured on the cores recovered over this interval, yielding an estimate of 28 mW/m<sup>2</sup>. The heat flow estimate defined by the Bullard plot method (see **Physical properties and downhole measurements** in the Expedition 390/393 methods chapter [Coggon et al., 2024b]), using the slope of the least-squares linear fit to the Site U1558 temperature data, is 30 mW/m<sup>2</sup> (Figure **F90D**; Bullard, 1939), close to the estimate from the simpler approach above.

Table **T29** summarizes these results as well as the results of the same calculation for each hole. It confirms that both holes display very similar temperature gradients and heat flow values, all lower than the 50 mW/m<sup>2</sup> estimated for 50 Ma Southern Atlantic crust (Sclater et al., 1980) and results of heat flow modeling along the South Atlantic Profile (Kardell et al., 2021) but similar to the closest values (25 and 38 mW/m<sup>2</sup>) listed in the Fuchs et al. (2021) global heat flow compilation. The

**Table T28.** Formation temperature measurements, Site U1558. [Download table in CSV format.](#)

Core, section	Measurement depth (mbsf)	Equilibrium temperature (°C)
390C-U1558A-		
4H	31.9	2.38
7H	60.4	3.1
10H	85.4	3.38
393-U1558F-		
3H	23	2.05
7H	54.5	3.12
10H	82.2	3.5

significant differences between the measurements and the predictions could be an indication of extensive hydrothermal advection at this site (Kardell et al., 2021).

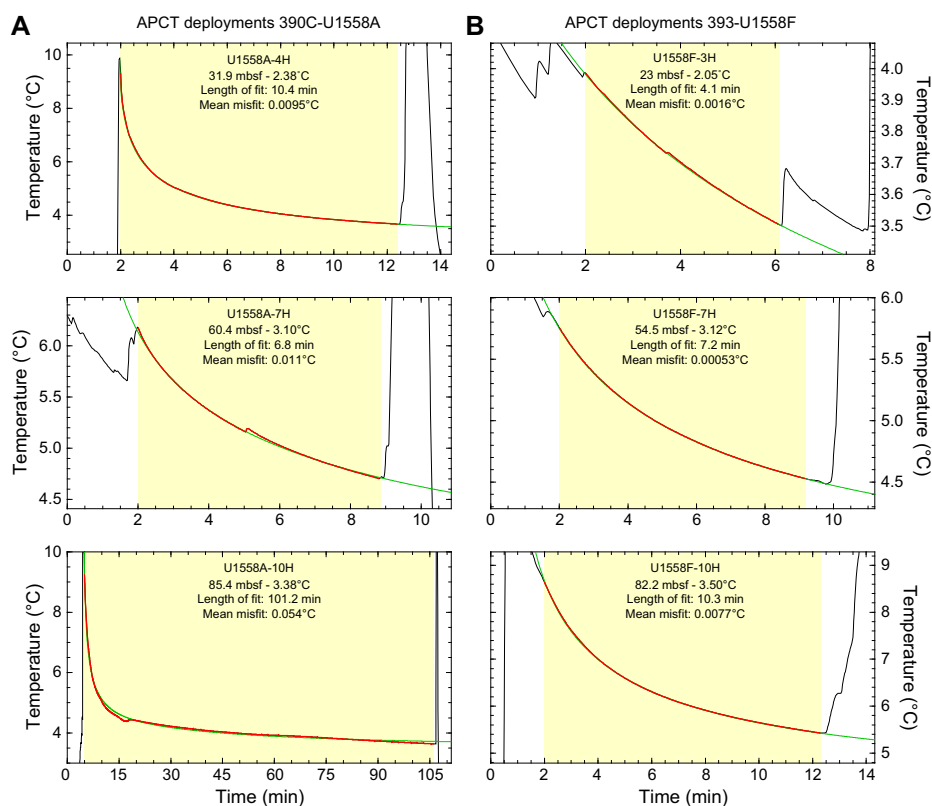
#### 10.1.4. X-ray imaging

X-ray imaging of sediment can be used to identify primary sedimentologic features, such as bedding, laminations, volcanic ash layers or glass fragments, and ichnofossils, based on density differences between lithology types. X-ray images can also help identify regions of slumping or drilling disturbance such as expansion cracks and fall-in at the top of cores. Archive halves of sediment cores from Hole U1558F were scanned using the X-ray Logger (XMAN), and the images were used to assist visual core description. Despite some irregularities in the grayscale within individual cores, sedimentologic features, including bioturbation and bedding, are visible in some of the images and highlight features (Figure F91) that are not readily apparent in the photographs from the Section Half Imaging Logger (SHIL) (see [Sedimentology](#)).

#### 10.1.5. Seismic integration

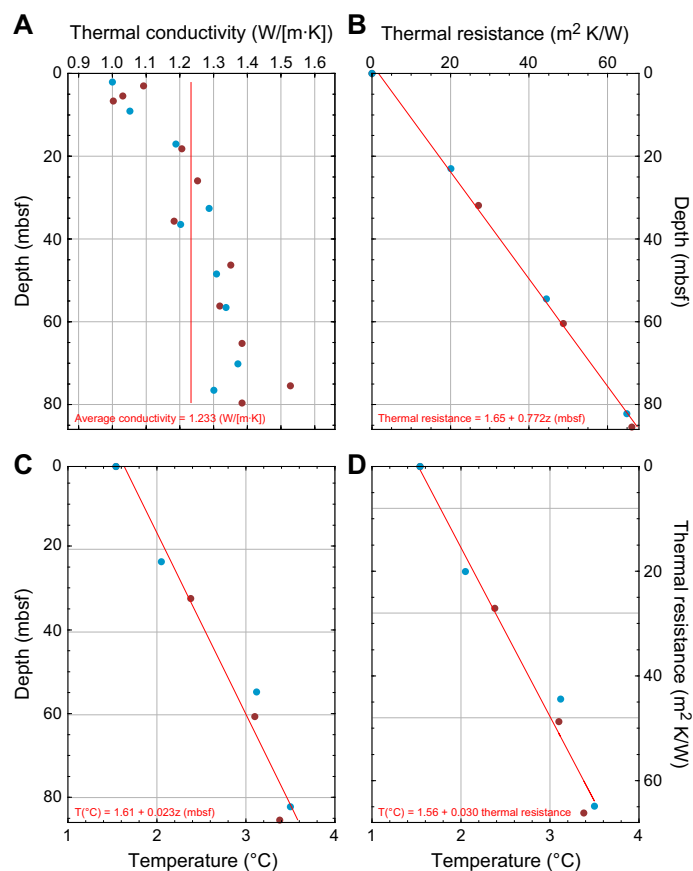
One of the most basic applications of physical properties is to help relate some of the observations and descriptions made on the recovered core to the data and surveys that were used to identify and select the drilling sites. A synthetic seismogram can be generated from some of the most routine physical property data (*P*-wave velocity and density) to reproduce the signal that would be generated by a theoretical seismic wave going across Site U1558 and compare it with the seismic survey data that were used to select the drilling targets.

Figure F92 shows preliminary results of such an interpretation using the *P*-wave velocity data from the WRMSL and the GRA density data. The product of these two properties, the seismic impedance, was converted into a reflection coefficient series that was convolved with a 40 Hz Ricker wavelet, simulating the source used during the acquisition of CREST Line 1, to create the synthetic trace displayed at the location of the site. Disregarding the likely underestimation of in



**Figure F89.** APCT-3 temperature records. A. Hole U1558A. B. Hole U1558F. Highlighted time intervals in each record show where curve-fitting algorithm was applied to derive equilibrium temperature for each deployment. In situ formation temperature value for each record is extrapolated from best-fit model.

situ velocity in WRMSL velocity data (see [Physical properties and downhole measurements](#) in the Expedition 390/393 methods chapter [Coggon et al., 2024b]), this simulation suggests that the dipping reflector at  $\sim 5.9$  s two-way traveltimes coincides with the boundary between Lithostratigraphic Subunits IIB and IIC at  $\sim 112$  mbsf, which corresponds to a marked change in the density and velocity trends downhole (Figure F82) that generates the reflector. The lack of a stronger reflector for the basement below is puzzling for now, but if, as originally interpreted, this reflector was the basement, encountered at 166.5 mbsf, it would require a mean velocity of  $>2$  km/s in the sediments, much higher than the measured velocity. Possible factors to explain a shallower-than-expected basement reflection include a side reflection from the shallower basement to the east; a rugged basement surface topography where Site U1558 happens to be located in a relatively deep area; and/or an underestimate of the in situ velocity in laboratory measurements.



**Figure F90.** Thermal properties of sediments and calculated conductive heat flow, Site U1558. A. Thermal conductivity measured on cores, Holes U1558A (red) and U1558F (blue). B. Mean thermal conductivity for site with calculated thermal resistance. C. Temperature measured in Holes U1558A and U1558F with linear regression for all measurements. D. Bullard plot of measured temperature vs. calculated thermal resistance, Holes U1558A and U1558F. Slope of regression line is conductive heat flow for Site U1558.

**Table T29.** Derived temperature gradient and heat flow, Holes U1558A and U1558F. Values for Site U1558 are derived from the linear fits (as a function of depth or thermal resistance) for all measurements in Figure F90. [Download table in CSV format.](#)

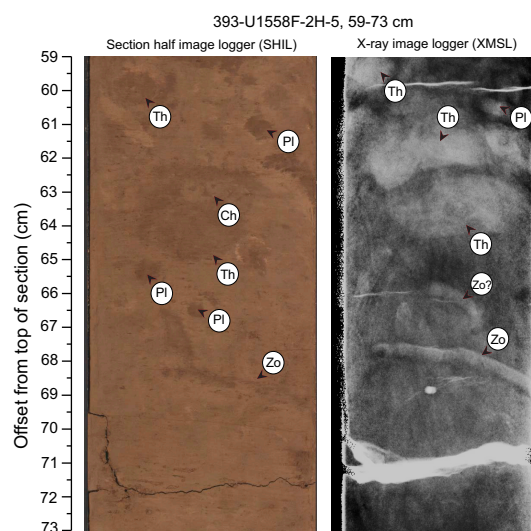
Site/hole	Gradient (°C/km)	Correlation coefficient	Average thermal conductivity (W/[m·K])	Heat flow from gradient (mW/m <sup>2</sup> )	Heat flow from Bullard plot (mW/m <sup>2</sup> )	Correlation coefficient
U1558A	22	0.99	1.34	30	29	0.99
U1558F	25	0.99	1.23	31	32	0.99
Site U1558	23	0.98	1.23	28	30	0.98



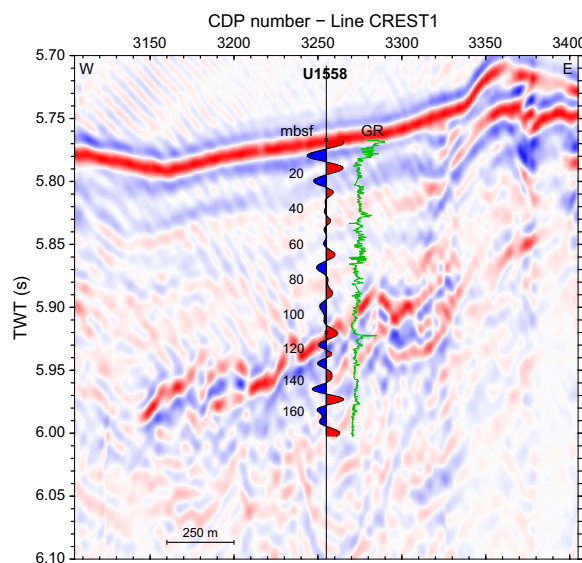
### 10.1.6. Stratigraphic correlation

Recovery of sediments during ocean drilling is generally high; however, gaps in recovery between individual cores are inevitable. To compensate for this loss, at least two sediment holes were cored per site. Hole U1558A was cored during engineering Expedition 390C (Estes et al., 2021) (see [Background and objectives](#)) to 163.9 m and Hole U1558F was cored ~50 m to the southeast to 177.2 m DSE. The sediment/basement contact is recorded at 158.9 m DSE in Hole U1558A and at 176 m DSE in Hole U1558F, ~18 m deeper than in Hole U1558A. Equivalent stratigraphic layers in the lower part of the two holes were found to be thicker in Hole U1558F.

Before coring Hole U1558F, the bit was positioned 2 m above the predicted seafloor depth to attempt to recover the mudline and recovery gaps present within Hole U1558A. During drilling, the relative position of coring gaps in the two holes was monitored by correlating features in MS



**Figure F91.** Left: true-color image from SHIL, Hole U1558F. Right: X-ray image from XMAN. This interval shows heavy bioturbation. Zo = *Zoophycos*, Pl = *Planolites*, Th = *Thalassinoides*, Ch = *Chondrites*.



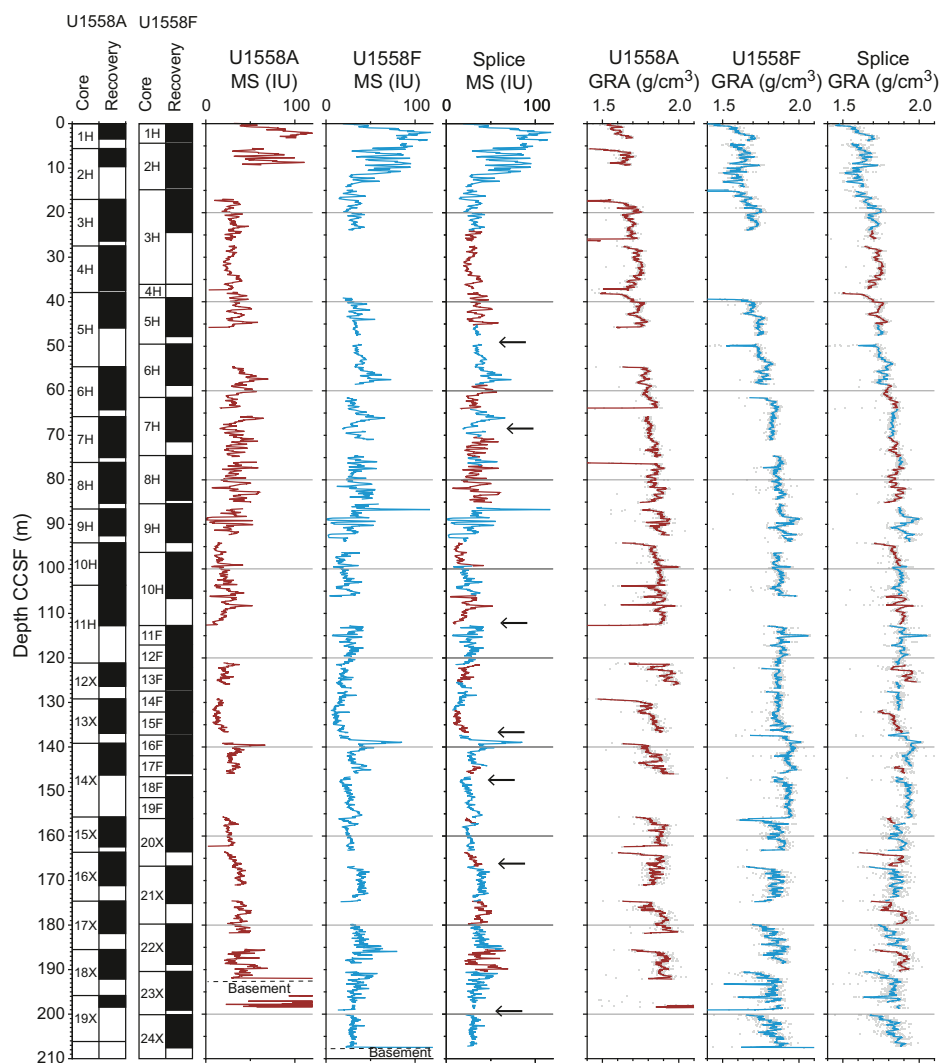
**Figure F92.** Preliminary synthetic seismogram generated from WRMSL *P*-wave velocity and GRA density data. Overlain on CREST Seismic Line 1B/1C that crosses Hole U1558B, seismogram defines a local time-depth relationship that allows display of core data as a function of time on seismic line, allowing preliminary seismic/well correlations. CDP = common depth point, TWT = two-way traveltime.

and GRA bulk density data obtained using the Special Task Multisensor Logger (STMSL; see **Physical properties and downhole measurements** in the Expedition 390/393 methods chapter [Coggon et al., 2024b]). To improve the offset of core gaps, after Core 393-U1558F-3H we drilled ahead by 3 m (drilled interval 393-U1558F-41).

#### 10.1.6.1. Correlation and splice

Physical property data such as MS, GRA, NGR, and magnetic inclination (see **Paleomagnetism**) from Holes U1558A and U1558F were correlated to establish a composite depth scale (CCSF) at Site U1558 (see Figures F93, F94) that includes the core recovery summary and vertical core offsets (e.g., affine and splice tables; Tables T30, T31).

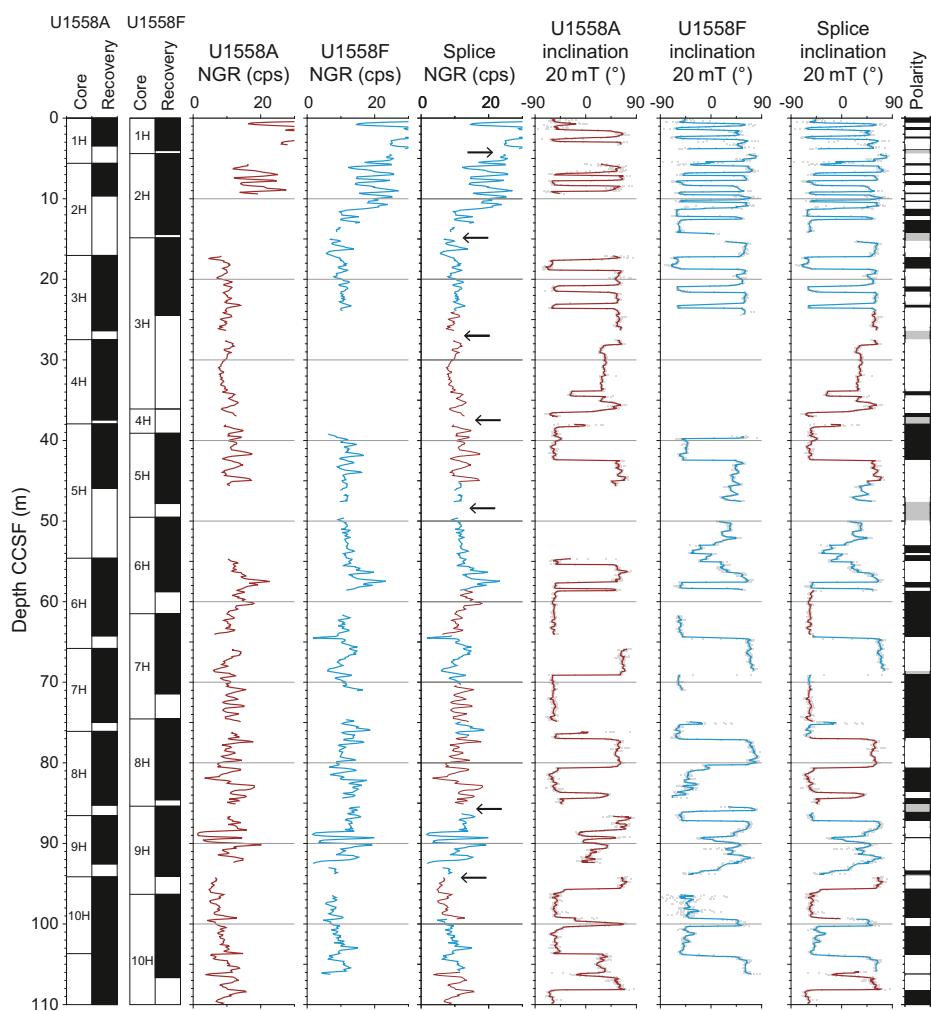
Correlation of records from Holes U1558A and U1558F produced an almost continuous spliced record to 207 m CCSF. The records from each individual hole are characterized by major core gaps, the largest of which is ~15 m (located at 24–39 m CCSF) in Hole U1558F in Lithostratigraphic Subunit IIA (see **Sedimentology**). This gap results from half recovery of Core 393-U1558F-3H followed by ~3 m of core barrel advancement (drilled interval 393-U1558F-41) requested to improve the stratigraphic overlap between the holes. In both holes, larger missing intervals coincide where coring operations changed from APC to half-length APC (e.g., ~50% recovery in Cores 393-U1558F-10H and 390C-U1558A-11H) in Subunit IIB, and from half-length APC to the XCB system (Core 393-U1558F-20X), in Subunit IIC. However, during the correlation



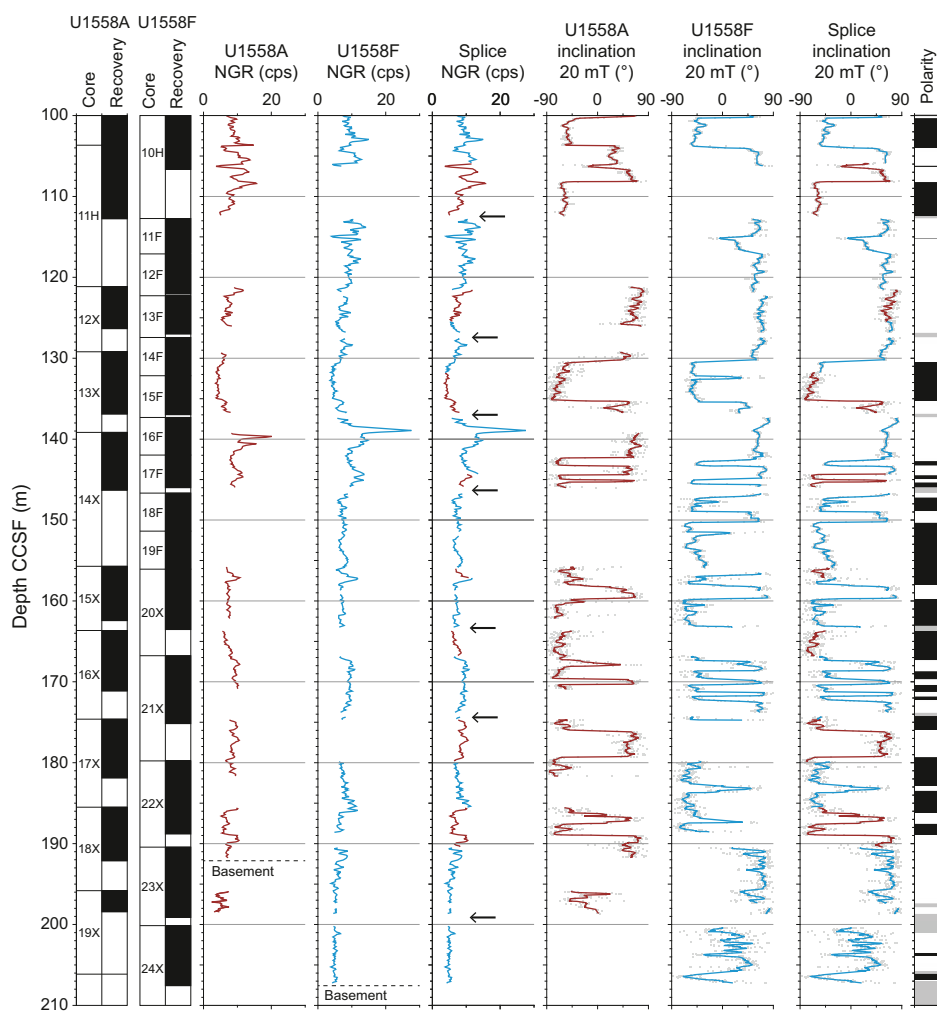
**Figure F93.** Construction of Site U1558 composite depth scale (CCSF) and splice, using MS and GRA bulk density from Holes U1558A (red) and U1558F (blue). Spliced record indicates which hole contributes to each interval of splice.

it was possible to fill the majority of those gaps, and the two holes are almost continuously tied to ~120 m CCSF with only ~12 m of total core gap in the splice (Figures F93, F94).

From ~140 to ~190 m CCSF in Hole U1558F, Subunit IIC (nannofossil ooze/chalk with clay; see **Sedimentology**) contains a few expanded intervals with respect to the equivalent intervals in Hole U1558A. Thickness variation (estimated to be ~2 m) is recognizable by physical properties data, especially NGR and MS, at 138–146 m CCSF where Core 390C-U1558A-14X is tied to Cores 393-U1558F-16F and 17F (Figures F93, F94). Sedimentologic characterization of Subunit IIC (see **Sedimentology**) supports the lateral correlation between the “condensed” Subunit IIC in Hole U1558A and the “expanded” counterpart in Hole U1558F. It was not possible to acknowledge this stratigraphic variation and correlate both the top and bottom of equivalent layers with different thickness because the Correlator software does not stretch or squeeze within individual cores. Despite being only ~50 m apart, due to basement topography Holes U1558A and U1558F show substantial differences in layer thickness. In the rugged ocean crust on the flanks of slow-spreading ridges, accommodation space and consequently sediment accumulation are also controlled by the local-scale bathymetry of the seafloor (e.g., Christeson et al., 2020). For these reasons (higher recovery, thicker units), the splice section preferentially consists of intervals from Hole U1558F (Table T31).



**Figure F94.** Construction of Site U1558 composite depth scale (CCSF) and splice, using NGR and paleomagnetic inclination from Holes U1558A (red) and U1558F (blue). Spliced record indicates which hole contributes to each interval of splice. Black arrows = recovery gaps in splice section. Magnetic polarity column: black = negative inclination (normal polarity for sites in Southern Hemisphere), white = positive inclination (reversed polarity), gray = no data. cps = counts per second. (Continued on next page.)



**Figure F94 (continued).**

**Table T30.** Affine table, Holes U1558A and U1558F. [Download table in CSV format.](#)

**Table T31.** Splice table, Site U1558. [Download table in CSV format.](#)

## 10.2. Basement

Petrophysical characterization of the 49.2 Ma ocean crustal section at Site U1558 is primarily based on cores from Hole U1558D that were recovered during Expedition 393. The uppermost basement was also recovered from Hole U1558A during Expedition 390C (Estes et al., 2021) and Hole U1558F during Expedition 393. Because of difficulties with the reentry system (see [Operations](#)), it was not possible to reenter Hole U1558D following the completion of coring. Consequently, the planned wireline logging at Site U1558 could not be undertaken.

### 10.2.1. Physical properties

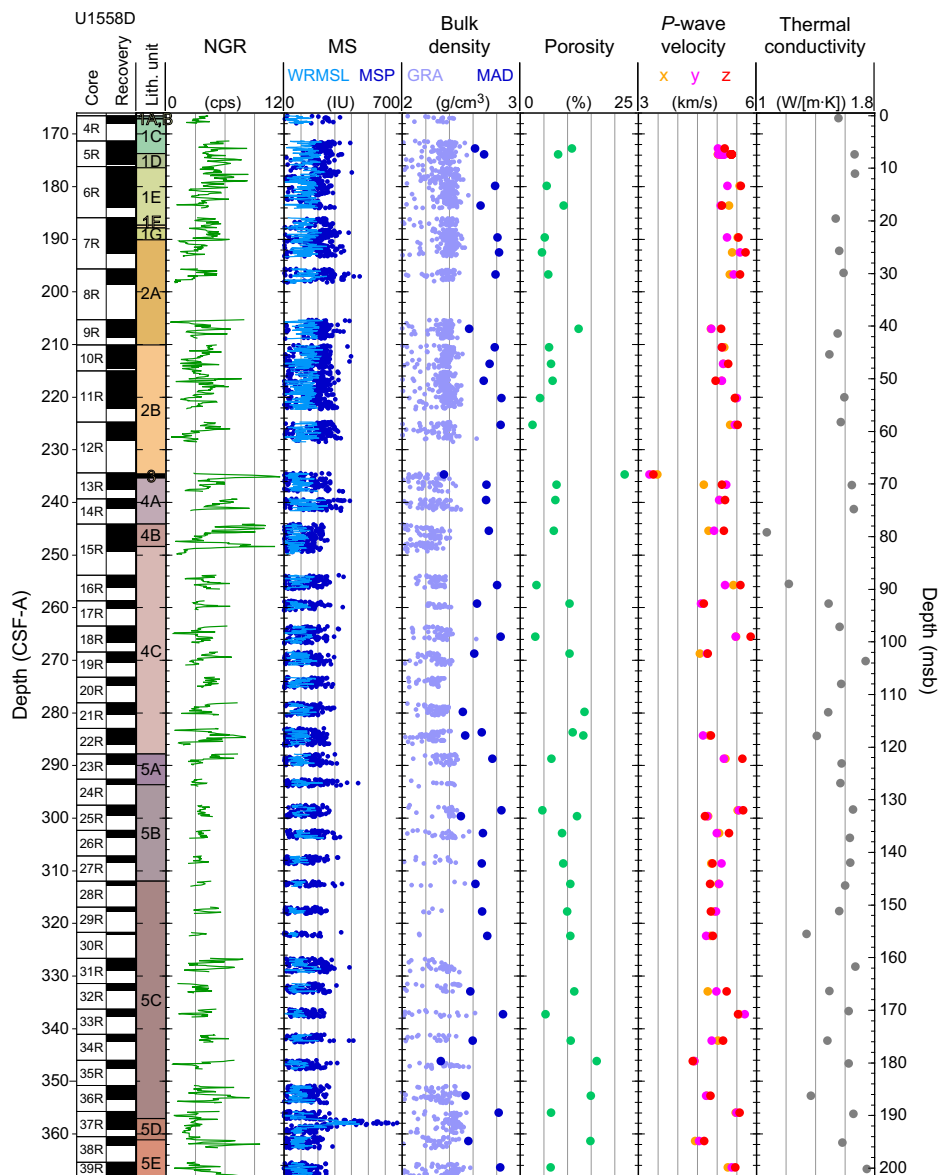
Whole-round core section measurements included NGR, GRA bulk density, MS, and X-ray imaging. Archive halves of all split-core sections were measured for MSP. A total of 40 discrete sample cubes were taken for *P*-wave velocity and MAD measurements, including one sample of breccia matrix composed of sediment and altered glass (Table T32). All discrete samples were also used for paleomagnetic measurements (see [Paleomagnetism](#)). Thermal conductivity measurements were made on 39 individual pieces from working halves of split cores. Full circumference, true

color images of whole-round core exteriors were recorded with the DMT CoreScan3 system. Approximately 72% of the basement material from Site U1558 could be scanned on the DMT system, including 100% of the basement material from Hole U1558E, 93% of the material from Hole U1558A, and 72% of the material from Hole U1558D. An additional ~3 m (total) of cylindrical, oriented pieces was used for microbiological sampling in Hole U1558D and removed from the core before scanning took place (see [Microbiology](#)). A summary of core section and discrete physical properties data from Hole U1558D is shown in Figure F95 and Tables T32 and T33. All depths in the tables and figures are in meters below seafloor (mbsf) on the CSF-A scale, and the means of all physical properties are arithmetic means presented with uncertainty ranges of  $\pm 1$  standard deviation ( $1\sigma$ ).

**10.2.1.1. Natural gamma radiation**

In Hole U1558D, mean NGR is 4.0 counts/s (range = 0.15–11.60 counts/s) (Figure F95; Table T32). In the uppermost part of the sequence (Unit 1 and Subunit 2A) NGR decreases from ~8

**Table T32.** Discrete physical properties, Hole U1558D. [Download table in CSV format.](#)



**Figure F95.** Summary of physical properties, Hole U1558D. cps = counts per second.



**Table T33.** Physical properties statistical results, Site U1558.  $1\sigma$  = one standard deviation. Emplacement style, groundmass grain size, and alteration level for discrete measurements follow Table T32. Emplacement styles for the continuous track measurements are based on the typical emplacement style for each lithostratigraphic unit or subunit (see Igneous petrology). Alteration level and groundmass grain size were not assigned for the track measurements. Groups with only one sample do not have a standard deviation (NA), and empty cells indicate no measurements. [Download table in CSV format.](#)

Groups/subgroup	Core logging measurements							
	GRA bulk density mean (g/cm <sup>3</sup> )	GRA bulk density 1 $\sigma$ (g/cm <sup>3</sup> )	NGR mean (counts/s)	NGR 1 $\sigma$ (counts/s)	MS WRMSL mean (IU)	MS WRMSL 1 $\sigma$ (IU)	MSP mean (IU)	MSP 1 $\sigma$ (IU)
Igneous unit								
1	2.36	0.09	4.49	1.22	130	54	192	71
2	2.35	0.09	3.36	1.26	131	55	188	82
3	2.13	0.06	9.09	1.92	47	26	47	43
4	2.26	0.10	4.32	1.76	88	50	136	80
5	2.34	0.13	3.80	1.35	98	61	144	94
Emplacement style								
Massive flow	2.30	0.12	3.79	0.38	107	32	243	45
Pillow flow	2.32	0.10	4.11	1.57	109	56	160	82
Large pillow flow	2.36	0.09	3.12	1.34	136	56	200	83
Breccia matrix	2.13	0.06	9.09	1.92	47	26	47	43
Sheet flow	2.34	0.12	3.80	1.35	98	61	144	94
Groundmass grain size								
Cryptocrystalline								
Microcrystalline								
Fine-grained								
Alteration level								
1: Gray/orange speckled background								
2: Dark gray halo								
3: Light brownish-gray halo								
4: Brown halo								
5: Mixed gray-brown (variolithic)								
6: Orange-reddish yellow								
Hole U1558D	2.33	0.11	3.98	1.55	109	59	159	88

Groups/subgroup	Discrete sample measurements									
	Thermal conductivity mean (W/[m-K])	Thermal conductivity 1 $\sigma$ (W/[m-K])	Max P-wave velocity mean (km/s)	Max P-wave velocity 1 $\sigma$ (km/s)	Porosity mean (%)	Porosity 1 $\sigma$ (%)	MAD bulk density mean (g/cm <sup>3</sup> )	MAD bulk density 1 $\sigma$ (g/cm <sup>3</sup> )	Grain density mean (g/cm <sup>3</sup> )	Grain density 1 $\sigma$ (g/cm <sup>3</sup> )
Igneous unit										
1	1.61	0.07	5.40	0.17	7.78	2.41	2.72	0.08	2.85	0.04
2	1.56	0.04	5.38	0.24	6.13	2.86	2.76	0.09	2.87	0.05
3	NA	NA	3.48	NA	22.10	NA	2.35	NA	2.73	NA
4	1.49	0.21	5.16	0.41	8.76	3.66	2.68	0.11	2.84	0.05
5	1.58	0.11	5.15	0.38	9.91	3.48	2.66	0.14	2.84	0.10
Emplacement style										
Massive flow										
Pillow flow	1.54	0.15	5.22	0.35	8.64	3.58	2.69	0.12	2.85	0.07
Large pillow flow	1.57	0.02	5.47	0.33	7.60	4.12	2.73	0.14	2.86	0.07
Breccia matrix			3.38	NA	22.10	NA	2.35	NA	2.73	NA
Sheet flow	1.61	0.05	5.21	0.37	8.65	3.00	2.68	0.14	2.83	0.10
Groundmass grain size										
Cryptocrystalline	1.53	0.15	5.41	0.22	7.33	0.70	2.72	0.03	2.86	0.02
Microcrystalline	1.56	0.12	5.22	0.35	8.67	3.61	2.69	0.13	2.84	0.08
Fine-grained	1.67	NA								
Alteration level										
1: Gray/orange speckled background			5.48	0.20	6.72	4.27	2.75	0.12	2.88	0.05
2: Dark gray halo			5.67	0.04	5.95	0.92	2.81	0.06	2.92	0.05
3: Light brownish-gray halo			5.19	0.02	8.53	2.23	2.70	0.03	2.86	0.02
4: Brown halo			4.93	0.27	11.48	2.41	2.59	0.07	2.79	0.05
5: Mixed gray-brown (variolithic)			5.04	0.10	10.18	0.68	2.66	0.05	2.84	0.05
6: Orange-reddish yellow			4.79	0.34	14.47	1.99	2.48	0.13	2.72	0.13
Hole U1558D	1.54	0.14	5.19	0.42	8.90	4.05	2.68	0.13	2.84	0.08

counts/s at ~175–180 mbsf (Subunits 1D and 1E) to 2 counts/s at ~200 mbsf (Figure F95). NGR remains low (mean ~3 counts/s) in the lower half of eruptive Sequence A (Subunits 2A and 2B; mean =  $3.4 \pm 1.3$  counts/s). NGR increases 4-fold (to 11.60 counts/s) in the sedimentary breccia (Unit 3) at 235.1 mbsf, which shows the highest mean values of  $9.1 \pm 1.9$  counts/s (Table T33). Although highly variable, there are also prominent spikes in NGR in the underlying Subunits 4A and 4B.

NGR is lower in Subunit 4C (from ~248 to ~353 mbsf) and decreases downhole to <6 counts/s in Subunit 5B. Unit 5 is the thickest unit (expanded thickness of 73.33 m, see **Igneous petrology**) and has a low mean value of  $3.8 \pm 1.4$  counts/s. The NGR has moderately low values in Subunit 5B and upper Subunit 5C, but there is low core recovery, especially in Cores 393-U1558D-24R through 30R, so it is possible that unrecovered rocks have higher NGR values (see **Curatorial core procedures and sampling depth calculations** in the Expedition 390/393 methods chapter [Coggon et al., 2024b]).

#### 10.2.1.2. Magnetic susceptibility

MS at Site U1558 was measured on whole-round core sections using a pass-through sensor on the WRMSL and on split core sections using a MSP sensor on the Section Half Multisensor Logger (SHMSL). The pass-through and point-contact data show similar trends, though the MSP data tend to cover a wider range and reach higher values over the same depth interval compared to the WRMSL data (Figure F95). The lower WRMSL values may result from gaps and irregular shaped/small core pieces (heavily influencing the continuous measurements), and/or from the different frequency and resolution between the two magnetic susceptibility systems (see **Physical properties and downhole measurements** in the Expedition 390/393 methods chapter [Coggon et al., 2024b]). Thus, absolute differences between the two measurement systems should be interpreted with caution. As a whole, both the WRMSL and MSP measurements suggest that Units 1 and 2 have a higher mean magnetic susceptibility than Units 4 and 5, with the lowest magnetic susceptibility observed in sedimentary Unit 3 (Table T33).

MSP values from Hole U1558D range 1–669 IU (mean =  $159 \pm 88$  IU). Although most magnetic susceptibility values fall below 300 IU, a small peak in magnetic susceptibility occurs at ~294 mbsf (near the Subunit 5A/5B boundary) and the highest magnetic susceptibility values (669 IU) were measured in Subunit 5D at 357.9 mbsf (Figure F95).

#### 10.2.1.3. Gamma ray attenuation bulk density

Bulk density values  $<2$  g/cm<sup>3</sup> were culled from all figures and interpretations, as these values likely represent gaps due to incomplete filling of the core liner and are not representative of the recovered material. GRA bulk density from Hole U1558D ranges 2–2.6 g/cm<sup>3</sup> (mean =  $2.3 \pm 0.1$  g/cm<sup>3</sup>) (Figure F95; Tables T32, T33) and is relatively consistent across the different igneous units. It is noticeable though that GRA bulk density is slightly lower in Unit 4 and slightly higher deeper than ~300 mbsf in Subunits 5C–5E. GRA bulk density values are consistently lower than the discrete sample bulk densities (MAD). This is due in large part to calibration of the GRA instrument, which assumes that the core liner is completely filled. The narrower RCB core diameters leave an air-filled gap between core and liner that reduces the apparent GRA bulk density.

#### 10.2.1.4. Moisture and density

Samples for MAD analysis were taken once per core or once per distinct lithology. These samples were selected to be representative of various levels of alteration of the basalts recovered at Site U1558. A total of 40 discrete samples from the basement sections of Hole U1558D were investigated (Table T32). MAD samples are typically taken from pieces appearing cohesive enough to withstand being cut into cubes, which may bias the data toward higher density rocks than the surrounding more heterogeneous intervals (see **Physical properties and downhole measurements** in the Expedition 390/393 methods chapter [Coggon et al., 2024b]).

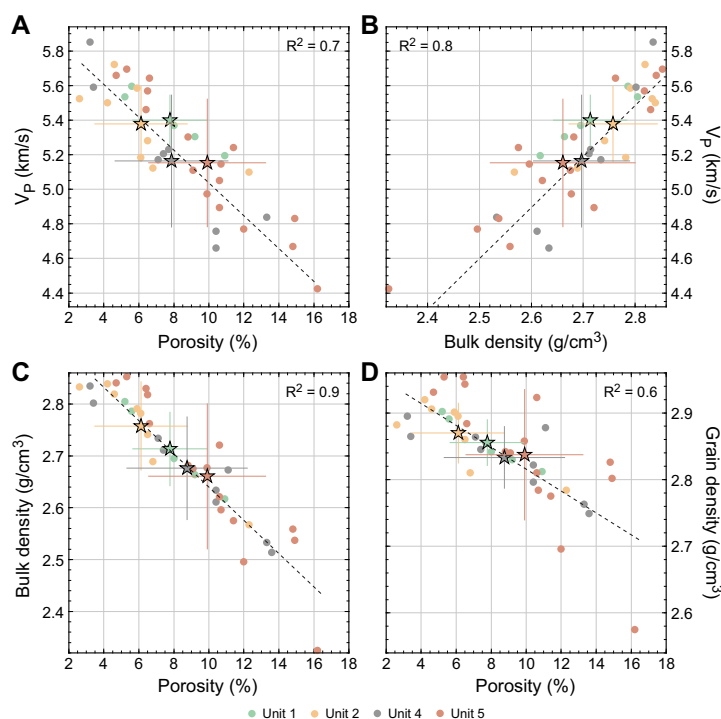
The mean porosity for each lithostratigraphic unit from Hole U1558D ranges from 6.1% (Unit 2) to 9.9% (Unit 5) (Table T32) with an overall mean of  $8.9\% \pm 4.1\%$  (Table T33). The highest porosity is seen in the single sedimentary sample from Unit 3 (22.1%; 393-U1558D-13-1, 29–31 cm). Bulk density and grain density from Hole U1558D range 2.3–2.85 and 2.58–2.95 g/cm<sup>3</sup>, respectively (Table T32), with the lowest bulk and grain densities in the sedimentary sample from Unit 3,

reflecting the high porosity in this sample. Among the igneous units, Units 1 and 2 have higher mean bulk and grain densities compared to Units 4 and 5, though these differences are subtle (Table T33; Figure F96). In summary, when MAD results from basalt sequences are correlated against each other and  $P$ -wave velocity (Figure F96), mean values from Units 1 and 2 always plot in the regions with low porosity and high bulk/grain density, and therefore also high  $P$ -wave velocity as well. In contrast, Units 4 and 5 plot in regions with higher mean porosity and higher bulk/grain density, and therefore lower  $P$ -wave velocity.

The physical properties of these igneous rocks may also be influenced by primary lithologic features of the basalts such as their magmatic emplacement (pillow, sheet, or massive flows) or groundmass crystal size (see **Igneous petrology**) (Figure F97; Table T32). For example, throughout Hole U1558D the mean porosity for basalts described as “large pillows” (with microcrystalline groundmass crystal size) is  $7.6\% \pm 4.1\%$ . These large pillows also have the highest mean bulk density of the different emplacement types ( $2.73 \pm 0.14 \text{ g/cm}^3$ ). Basalts emplaced as “pillow flows” (mostly microcrystalline) show high variability in physical properties, with data defining a linear trend. They also show the highest mean porosity ( $8.6\% \pm 3.6\%$ ) and a slightly lower mean bulk density ( $2.69 \pm 0.12 \text{ g/cm}^3$ ) compared to the “large pillows.” Sheet flows have variable groundmass grain size (from cryptocrystalline to fine-grained), but they are very similar to pillow flows in terms of porosity and density (Table T33; Figure F97).

#### 10.2.1.5. $P$ -wave velocity

$P$ -wave velocity was measured on the  $x$ -,  $y$ -, and  $z$ -axes of the discrete sample cubes. The standard deviation of the  $x$ ,  $y$ , and  $z$  measurements for each sample varies by one order of magnitude (0.03–0.30 km/s) (Table T32). However, the standard deviations of repeated measurements on each axis (among different samples) are relatively consistent (0.42, 0.41, and 0.45 km/s for  $x$ -,  $y$ -, and  $z$ -axes, respectively). Without orientation of the core, the  $x$ - and  $y$ -directions are arbitrarily defined by the splitting plane and are likely to change from section to section. The  $z$ -axis, in contrast, is always oriented parallel to the coring direction. All three velocities measured for each sample are shown in Figure F95 and Table T32; however, only the highest value measured for each sample is used in



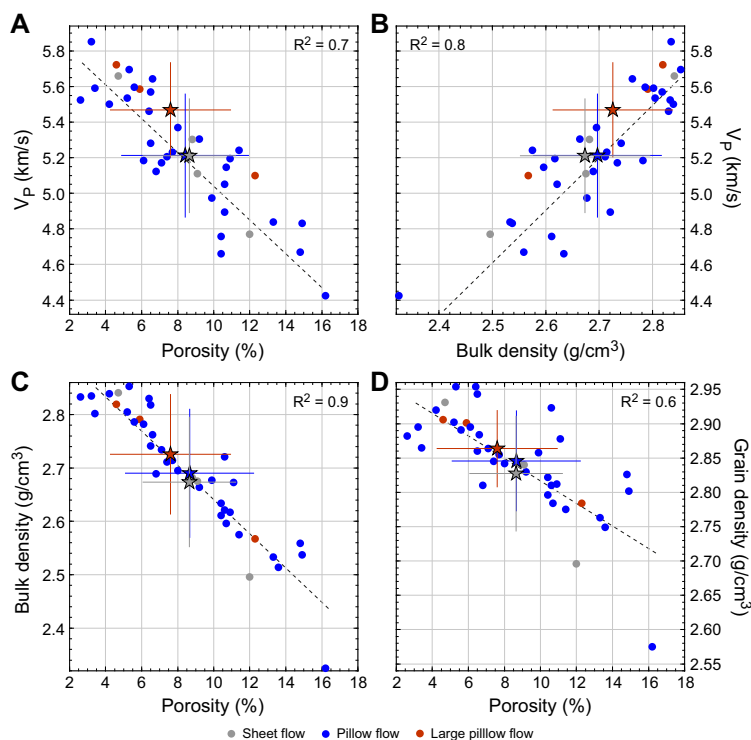
**Figure F96.** Hole U1558D discrete sample physical properties by lithostratigraphic unit (see Igneous petrology). A.  $V_p$  vs. porosity. B.  $V_p$  vs. bulk density. C. Bulk density vs. porosity. D. Grain density vs. porosity.  $V_p$  shown is maximum velocity measured for each sample. Mean (stars) and standard deviation (error bars) for each unit are also shown.

the crossplots (see **Physical properties and downhole measurements** in the Expedition 390/393 methods chapter [Coggon et al., 2024b]).

*P*-wave velocity ranges 3.48–5.56 km/s on the *x*-axis, 3.28–5.70 km/s on the *y*-axis, and 3.38–5.85 km/s on the *z*-axis. *P*-wave velocity along the *z*-axis is generally greater than the *x*- and *y*-directions in 26 of the 40 discrete samples. The highest measured *P*-wave velocity (5.85 km/s) was recorded in a pillow flow from Subunit 4C at 265 mbsf (Sample 393-U1558D-18R-2, 70–72 cm) (Table T32; Figures F95, F96, F97). The lowest velocity was measured on a single sample from Unit 3, the sedimentary breccia made up of clasts of broken pillows and altered glass in an indurated calcareous sediment matrix (Sample 13R-1, 29–31 cm; see also **Igneous petrology**). The velocities along the *x*-, *y*-, and *z*-axes for this sample are all significantly lower (mean =  $3.48 \pm 0.10$  km/s) than the lowest velocities measured in the basalt samples through the rest of the sequence (Tables T32, T33). Basalt samples from microcrystalline large pillows yield the highest mean velocity ( $5.47 \pm 0.33$  km/s), followed by pillow and sheet flows ( $5.22 \pm 0.35$  km/s and  $5.20 \pm 0.36$  km/s, respectively) (Table T33; Figure F97). Postexpedition research could focus on further refining the relationship between emplacement style and *P*-wave velocity, particularly with respect to the observed differences in the *x*-, *y*-, and *z*-axes.

#### 10.2.1.6. Thermal conductivity

Thermal conductivity in Hole U1558D ranges from 1.07 W/(m·K) (observed in Subunit 4B) to a maximum of 1.75 W/(m·K) (observed in Subunits 4C and 5E) (Table T32; Figure F95). The mean thermal conductivity of the entire data set is  $1.54 \pm 0.14$  W/(m·K). Thermal conductivity remains relatively constant around 1.6 W/(m·K) from Unit 1 through Subunit 4A. A noticeable drop in thermal conductivity occurs between Subunits 4A and 4B, where the lowest value of 1.07 W/(m·K) is observed at ~245 mbsf (Sample 393-U1558D-15R-2, 25 cm). Below this, there are two broad peaks in thermal conductivity between ~260 and 320 mbsf, separated by a relative minimum very close to the boundary between Units 4 and 5. The upper broad peak has a maximum thermal conductivity of  $1.74 \pm 0.01$  W/(m·K) in the middle of Subunit 4C (~270 mbsf; Sample 19R-2, 44 cm)



**Figure F97.** Hole U1558D discrete sample physical properties by magmatic emplacement style (see **Igneous petrology**). A.  $V_p$  vs. porosity. B.  $V_p$  vs. bulk density. C. Bulk density vs. porosity. D. Grain density vs. porosity.  $V_p$  shown is maximum velocity measured for each sample. Mean (stars) and standard deviation (error bars) are calculated from data plotted for each emplacement style.

below which values decrease gradually through the lower part of Unit 4 (Figure F95). The second broad peak is recorded from the top of Subunit 5A to the upper part of Subunit 5C, with a maximum of  $1.65 \pm 0.01$  W/(m·K) at ~300 mbsf (Sample 25R-1, 85 cm). Further downhole, the deeper portions of Subunits 5C and 5D do not show any clear pattern in thermal conductivity with depth, and measurements are scattered around the Unit 5 mean of  $1.6 \pm 0.1$  W/(m·K). Close to the bottom of Hole U1558D in Subunit 5E, the thermal conductivity is relatively high, with the deepest sample showing the highest value of the entire data set, along with Sample 19R-2, 44 cm, in Subunit 4C.

The mean thermal conductivity of large pillow and pillow flows ( $1.57 \pm 0.02$  and  $1.54 \pm 0.15$  W/[m·K], respectively) falls within  $1\sigma$  of the mean for the entire basement sequence ( $1.54 \pm 0.14$  W/[m·K]). In contrast, basalts emplaced as sheet flows show higher mean thermal conductivities ( $1.61 \pm 0.05$  and  $1.66$  W/[m·K], respectively) (Table T33).

### 10.2.2. Data integration

Discrete samples used for both MAD and *P*-wave analyses were classified into nine alteration levels based on color, texture, and presence of alteration halos following the scheme used in Hole U1558D macroscopic core descriptions (see **Igneous petrology** and **Alteration petrology**) (Tables T32, T33). From freshest to most altered basalt recovered at the site, the samples are ordered as follows:

- Group 1A: gray background.
- Group 1B: gray background with clay.
- Group 1C: orange speckled background.
- Group 2: dark gray halo.
- Group 3: light brownish gray halo.
- Group 4A: brown halo (weak).
- Group 4B: brown halo (strong).
- Group 5: mixed gray-brown (variolitic).
- Group 6: orange-reddish yellow.

The single interpillow sedimentary sample from Unit 3 was not included in this classification. This classification provides a way to compare independently measured physical properties attributes with alteration style for basalts recovered from Site U1558.

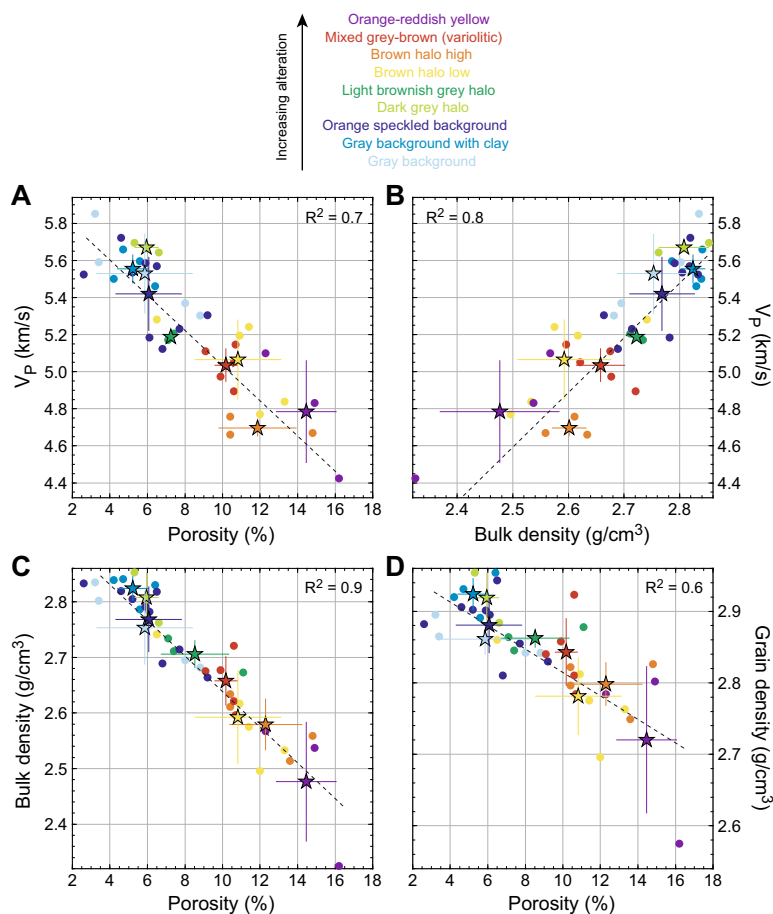
An inverse linear regression ( $R^2 = 0.8$ ) is seen between porosity and *P*-wave velocity, with “fresher” samples displaying higher *P*-wave velocity compared to more altered samples (Figure F98A). A positive linear relationship ( $R^2 = 0.7$ ) is seen when comparing *P*-wave velocity and bulk density, as expected (Figure F98B), with the more altered samples (Groups 4A–6) showing lower density and lower *P*-wave velocity. Similar to other sites along the transect, bulk and grain densities show inverse linear relationships with porosity ( $R^2 = 0.9$  and  $0.6$ , respectively) in samples from Site U1558 (Figure F98C, F98D). Samples from fresh basalts (Groups 1A–1C) tend to show higher values of bulk density and lower porosity compared to the most altered basalt samples (Groups 4A–6), with alteration Levels 2 and 3 occupying a range of intermediate bulk density and porosity values, although there is considerable overlap among groups. This result is somewhat counterintuitive, as secondary minerals might be expected to decrease porosity in the samples (see **Basement** in Physical properties and downhole measurements in the Site U1556 chapter [Coggon et al., 2024a]). Postexpedition work will be necessary to fully characterize what is being captured by the shipboard porosity measurements.

### 10.2.3. Comparison to ODP Hole 896A

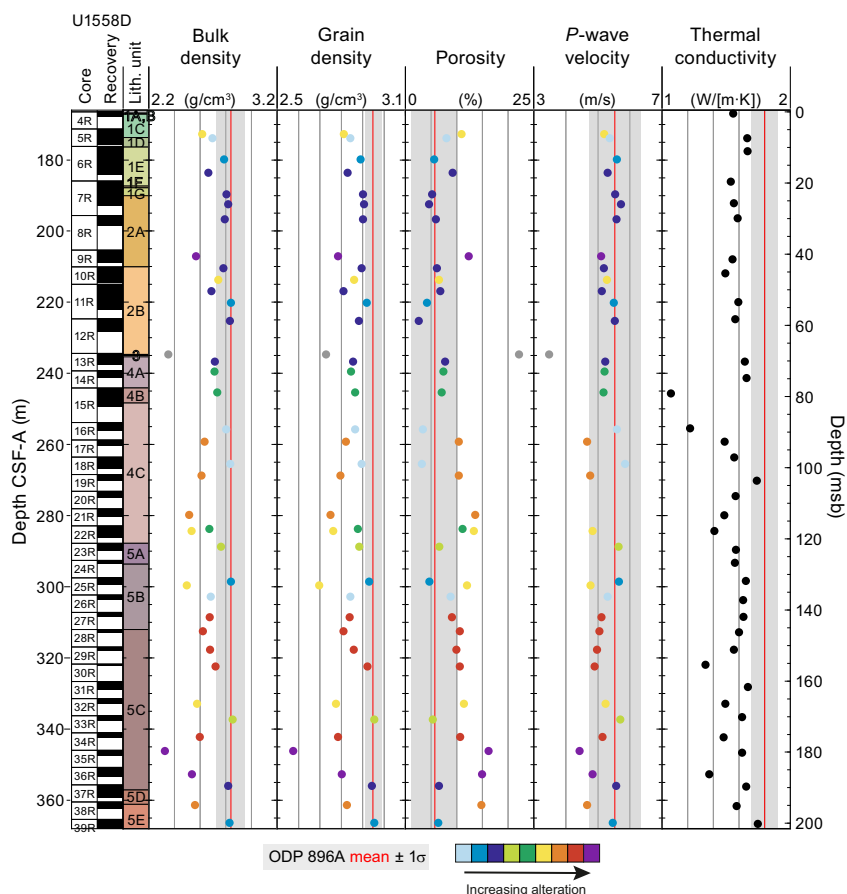
We compare the discrete physical properties measurements made in Hole U1558D (MAD, *P*-wave velocity, and thermal conductivity) with the full data set of equivalent measurements from Ocean Drilling Program (ODP) Hole 896A in ~7 Ma ocean crust as a benchmark to evaluate changes in physical properties with crustal age across the SAT (Shipboard Scientific Party, 1993; see **Physical properties and downhole measurements** in the Expedition 390/393 methods chapter [Coggon et al., 2024b]). The basement in Hole 896A is ~42 My younger than that in Hole U1558D. Despite the age difference, there is not a wide offset in most of the physical properties trends from the two



holes, except for the thermal conductivity (Figure F99). Bulk density in Hole U1558D is, on average, lower than in Hole 896A. Porosity at the two sites is similar in the upper  $\sim 100$  m of basement; below this depth, porosity in Hole U1558D increases slightly beyond  $1\sigma$  of the mean in Hole 896A. The  $P$ -wave velocities at the two sites are very similar, although the velocities measured in Hole U1558D decrease slightly below  $1\sigma$  of the mean in Hole 896A from Subunit 5B to the bottom of



**Figure F98.** Hole U1558D discrete sample physical properties by level of alteration (see Alteration petrology). A.  $V_p$  vs. porosity. B.  $V_p$  vs. bulk density. C. Bulk density vs. porosity. D. Grain density vs. porosity.  $V_p$  shown is maximum velocity measured for each sample. Mean (stars) and standard deviation (error bars) are calculated from data plotted for each alteration level.



**Figure F99.** Comparison of discrete sample properties, Hole U1558D and ODP Hole 896A. Discrete measurements from Hole U1558D are colored by level of alteration (see Alteration petrology). Mean values for Hole 896A, calculated from the entire data set for each parameter, are shown (red lines = mean value of each data type, shaded boxes =  $\pm 1\sigma$ ). *P*-wave velocity shown for Hole U1558D is maximum velocity measured for each sample. Thermal conductivity measurements lack alteration level description.

**Table T34.** Geochemical analyses of interstitial water samples, Site U1558. [Download table in CSV format.](#)

the hole. Thermal conductivity in Hole U1558D is noticeably lower than  $1\sigma$  of the mean in Hole 896A and covers a considerably wider range (Figure F99).

## 11. Geochemistry

### 11.1. Sediment

#### 11.1.1. Interstitial water and mudline sampling

From sediment cored in Holes U1558A, U1558D, and U1558E, IW was extracted via squeezing whole-round sediment cores under laboratory atmosphere (see [Geochemistry](#) in the Expedition 390/393 methods chapter [Coggon et al., 2024b]). Mudline water samples were collected from both Holes U1558A and U1558F. During Expedition 390C, squeezed IW was collected once per core from Cores 390C-U1558A-1H through 11H and 18X and twice per core from Cores 13X–17X; no IW was extracted from Core 12X. During Expedition 393, IW samples were collected once per core from Cores 393-U1558F-11F through 19F and 1H and twice per core from Cores 2H–10H and Cores 20X–24X. One IW sample was collected in Hole U1558D (Core 393-U1558D-2R). A total of 23, 1, and 37 IW samples were taken from Holes U1558A, U1558D, and U1558E, respectively (Table T34). Splits of squeezed IW and solid residue (squeeze cake) samples were saved for shipboard analyses and postexpedition research.

During Expedition 393, Rhizon samplers were also used to collect in situ interstitial waters from Hole U1558F prior to core splitting (see **Geochemistry** in the Expedition 390/393 methods chapter [Coggon et al., 2024b]). Fluid sampling was performed from Sections 1–6 (full cores) or 1–3 (half cores) in both APC and XCB cores. Volume yields ranged from 0 to ~21 mL, with particularly high volumes recovered for a number of XCB core sections (393-U1558F-20X-3, 20X-4, 21X-4, 22X-3, 22X-5, 23X-4, 23X-5, 24X-2, 24X-3, and 24X-4), likely resulting from drill fluid contamination. A total of 90 Rhizon IW samples were collected from Sections 1H-1 through 24X-5 and subsampled for postexpedition work (Table **T34**). A total of 17 Rhizon samples from Cores 1H–10H were analyzed shipboard during Expedition 393 to supplement and compare with IW pore water measurements. A small split (~0.5 mL) was allocated for these shipboard analyses, which included measurements of major cations (Na, Mg, K, and Ca) and anions (Cl, Br, and SO<sub>4</sub>) by ion chromatography (IC). No Rhizon samples were collected during engineering Expedition 390C. For Hole U1558F, oxygen was measured after the cores were run through the STMSL roughly within 30 min of the core arriving on the catwalk (see **Geochemistry** in the Expedition 390/393 methods chapter [Coggon et al., 2024b]). No in situ analyses of oxygen were performed during Expedition 390C.

Tables **T34**, **T35**, and **T36** present all shipboard pore water and sediment analyses from Site U1558 collected during Expeditions 390C and 393, with selected concentration profiles illustrated in Figures **F100**, **F101**, **F102**, **F103**, **F104**, and **F105**. Although major cations (Na, Mg, K, and Ca) are measured by both IC and ICP-AES techniques, all plotted data correspond to IC values (see **Geochemistry** in the Expedition 390/393 methods chapter [Coggon et al., 2024b]). Reported errors are based on replicate measurements of the International Association for the Physical Sciences of the Oceans (IAPSO) seawater (for IC and ICP-AES) and IODP in-house (for ICP-AES and UV-Vis) standards. Instrumental detection limits are estimated as three times the standard deviation of blanks (Table **T9** in the Expedition 390/393 methods chapter [Coggon et al., 2024b]).

The composition of the mudline sample (i.e., bottom seawater, 0 m CSF-A) from Hole U1558A was offset from the expected values (based on the IAPSO standard) for a number of analytes that are known to be homogeneous in the ocean (Na, Mg, Sr, Cl, and SO<sub>4</sub>). To resolve this discrepancy, a mudline correction factor was applied to the Expedition 390C data. For each analyte, this correction factor was calculated from the ratio between the expected bottom seawater concentration and the measured mudline value from Expedition 390C. These corrections resulted in changes ( $\Delta$ , reported here in percent) beyond analytical precision for elements measured by IC ( $\Delta$ SO<sub>4</sub> = +3.4%,  $\Delta$ Cl = +2.1%,  $\Delta$ Na = +1.8%, and  $\Delta$ Mg = +1.7%) and ICP ( $\Delta$ Sr = -6.4%). The corrected values show overall excellent agreement with data from Expedition 393. For the analytes that yield significant offsets between raw and corrected values, both data sets are plotted in Figures **F100**, **F101**, **F102**, **F103**, and **F104** (light blue = raw values; dark blue = “mudline corrected” values) and reported in Table **T34**. No bromide data are plotted or reported from Hole U1558A because of poor IC recovery rates during Expedition 390C (as low as 86% for Br).

## 11.1.2. Measurement results of water samples

### 11.1.2.1. Salinity, sodium, chloride, and bromide

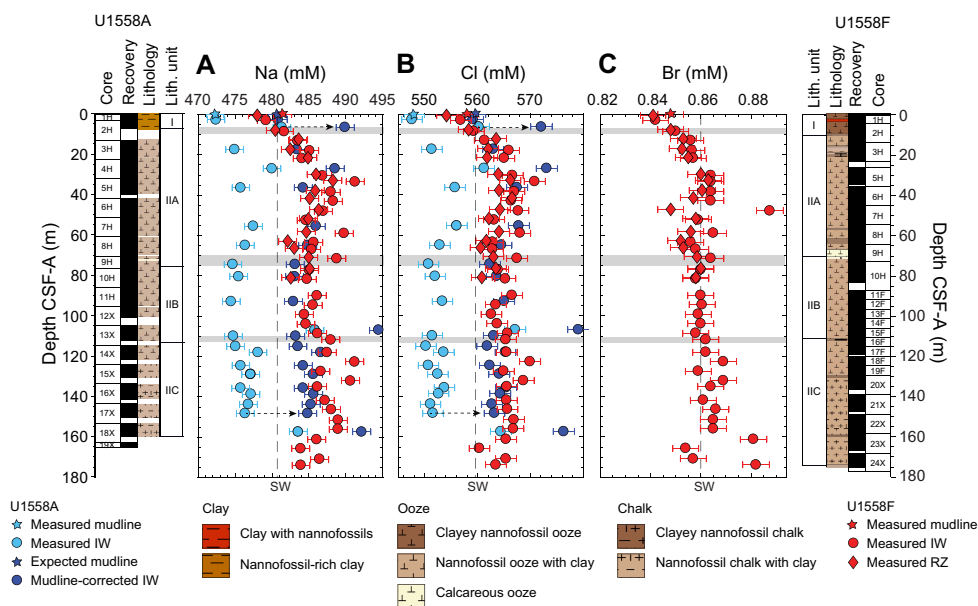
Mudline (i.e., bottom seawater, 0 m CSF-A) and pore water salinity in Holes U1558A and U1558F are largely uniform at the seawater value (35), with a few outliers both below (34,  $n = 2$ ) and above (36,  $n = 3$ ) this baseline (Table **T34**). The uppermost ~30 m of sediment in Hole U1558F shows a sharp increase (2.3%–2.5%) in pore water Na (479 to 491 mM), Cl (557 to 571 mM), and Br (0.84 to 0.86 mM) concentrations (Figure **F100**), although Na/Cl and Br/Cl ratios remain indistinguishable from those in seawater (0.86 and  $1.5 \times 10^{-3}$ , respectively). Similar patterns are observed for Na (481 to 490 mM) and Cl (559 to 573 mM) in Hole U1558A. There is excellent agreement between shipboard analyses of squeezed IW and Rhizon-collected fluid samples for Na, Cl, and Br concentrations, and there appears to be no significant sampling bias for these elements (Figure **F100**; cf. Miller et al., 2014).

### 11.1.2.2. pH and alkalinity

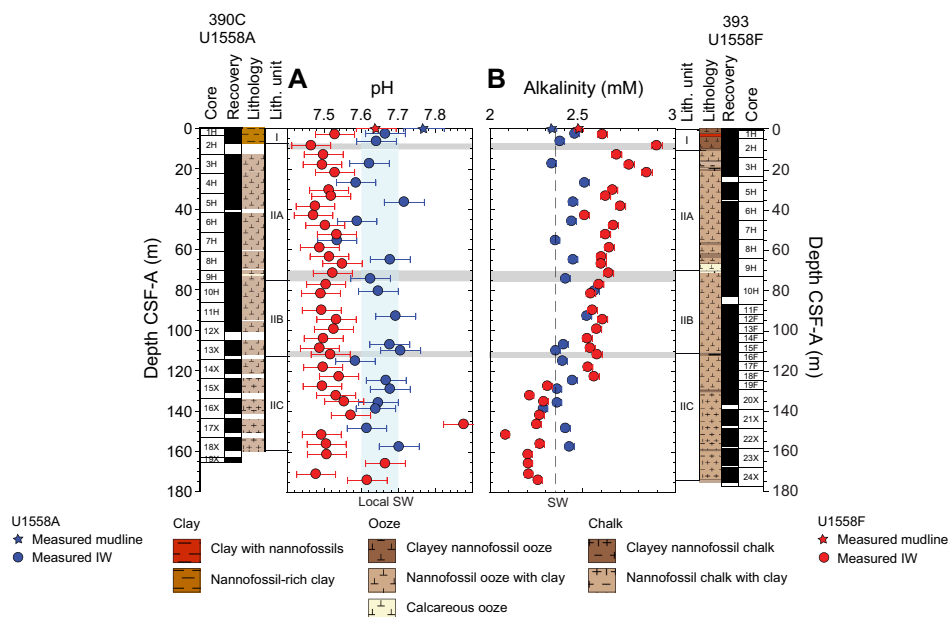
Mudline (0 m CSF-A) pH values in Holes U1558A (7.8) and U1558F (7.6) are offset by 0.2 pH units but are mostly within error of the pH range (7.6–7.7) observed for the deep South Atlantic Ocean waters (~31°S; Ríos et al., 2015) (Figure **F101A**). Measured pH values tend to be higher in Hole

U1558A (7.5–7.8) than in Hole U1558F (7.5–7.7) for any given depth. In both holes, pH decreases in Unit I (nannofossil-rich clay), and deeper values remain roughly constant throughout most of the sediment column, with the exception of a potential outlier in Hole U1558F (pH = 7.9 at 146.25 m CSF-A). The deepest sample in Hole U1558F (173.86 m CSF-A) increases back to the bottom seawater pH values reported for this latitude (7.6–7.7; Ríos et al., 2015).

Mudline values for alkalinity are distinct between Holes U1558A (2.3 mM) and U1558F (2.5 mM). In Hole U1558A, alkalinity varies by ~12% with a minimum of 2.3 mM (138.6 m CSF-A; Subunit IIC, nannofossil chalk with clay and volcanoclastics) and a maximum value of 2.6 mM (80.36 m



**Figure F100.** IW profiles of (A) sodium, (B) chloride, and (C) bromide concentrations, Holes U1558A and U1558F. RZ = Rhizon sampler. Hole U1558A Na and Cl data include raw and mudline-corrected values (see text for details). Seawater (SW) reference values correspond to IAPSO standard composition. Shaded gray areas = unit boundaries.



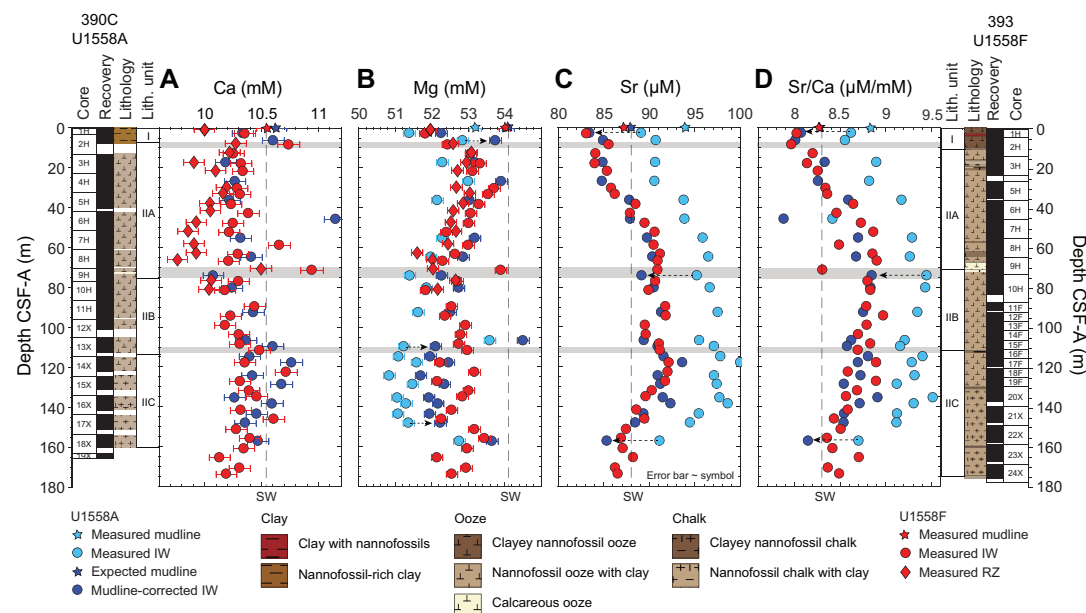
**Figure F101.** IW profiles of (A) pH and (B) alkalinity, Holes U1558A and U1558F. Seawater (SW) reference values are given for pH (7.6–7.7 at ~31°S; Ríos et al., 2015) and alkalinity (IAPSO standard). Shaded gray areas = unit boundaries.

CSF-A; Subunit IIB, nanfossil chalk with clay), but there is no discernible pattern with depth (Figure F101B). In contrast, alkalinity in Hole U1558F increases from 2.5 to 2.9 mM (~17%) in the uppermost ~10 m (Unit I, nanfossil-rich clay), and remains high (2.7–2.8 mM) at the top of Unit IIA (nanfossil ooze with clay; 10–20 m CSF-A) before gradually decreasing to 2.6 mM at 122.66 m CSF-A (Subunits IIA, nanfossil ooze with clay, and IIB). The increase in alkalinity in Unit I coincides with overall decreases in Ca, Mg, Sr concentrations, and Sr/Ca ratios below their respective seawater values (Figure F102), suggesting possible precipitation of authigenic carbonate (e.g., Kastner, 1999; Turchyn et al., 2021). Within Subunit IIC in Hole U1558F, pore water alkalinity decreases sharply from 2.6 mM (122.66 m CSF-A) to 2.3 mM (127.35 m CSF-A), and again gradually below ~127 m CSF-A (values range between 2.1 and 2.3 mM; Figure F101B). Alkalinity values in Hole U1558A are generally lower than those observed in Hole U1558F, with the exception of the interval below ~125 m CSF-A. Below that interval, measured values in Hole U1558F drop below seawater and remain lower than those measured in Hole U1558A.

### 11.1.2.3. Calcium, magnesium, strontium, and Sr/Ca

Pore fluid Ca concentrations in Holes U1558A (10.1–11.2 mM) and U1558F (10.1–10.9 mM) follow similar trends (Figure F102A). Between 0 and ~20 m CSF-A in both holes (Unit I, nanfossil-rich clay, and the top of Subunit IIA, nanfossil ooze with clay), measured Ca concentrations in IW samples gradually decrease from the mudline value (10.6 mM in Hole U1558A and 10.5 mM in Hole U1558F, 0 m CSF-A) to 10.2 mM in Hole U1558A (17.36 m CSF-A) and 10.3 mM in Hole U1558F (17.96 m CSF-A). In Subunits IIA (nanfossil ooze with clay) and IIB (nanfossil chalk with clay), Ca concentrations in Holes U1558A (10.1–11.2 mM) and U1558F (10.2–10.9 mM) remain mostly below the seawater value ( $10.6 \pm 0.4$  mM,  $2\sigma$ ,  $n = 55$ ) and do not vary systematically. In Hole U1558A, Subunit IIC (nanfossil chalk with clay and volcanoclastics) shows an overall increase in Ca concentrations with an average value ( $10.5 \pm 0.3$  mM,  $2\sigma$ ,  $n = 9$ ) that is indistinguishable from the seawater Ca content. Although pore fluids from Hole U1558F also move toward seawater-like compositions in Subunit IIC (10.3–10.7 mM), values drop slightly (10.1–10.3 mM) below ~160 m CSF-A.

Mg concentrations decrease from 54.1 ( $2\sigma = 0.6$ ,  $n = 2$ ) to 52.3 mM (Hole U1558A; mudline corrected values) and from 54.0 to 51.8 mM (Hole U1558F) within the uppermost ~5 m of sediment in both holes (Figure F102B). Between 5 and ~30 m CSF-A, values increase to 53.9 mM in Hole U1558A and 53.7 mM in Hole U1558F. Below ~30 m CSF-A, concentration trends vary between



**Figure F102.** IW profiles of (A) calcium, (B) magnesium, (C) strontium, and (D) Sr/Ca ratios, Holes U1558A and U1558F. RZ = Rhizon sampler. Hole U1558A Mg, Sr, and Sr/Ca data include raw and mudline-corrected values (see text for details). Seawater (SW) reference values correspond to IAPSO standard composition. Shaded gray areas = unit boundaries.



the two holes. In Hole U1558A, pore fluid Mg concentrations show a broad decrease from 54.0 to 52.2 mM between ~30 and 150 m CSF-A. The Mg content of the lowermost sampled pore fluid from Hole U1558A is measurably higher at 53.7 mM ( $2\sigma = 0.6$ ,  $n = 2$ ). In Hole U1558F, Mg concentrations smoothly decrease from 53.7 to 53.0 mM between ~30 and 50 m CSF-A. Below ~50 m CSF-A, values remain lower than in seawater ( $[\text{Mg}]_{\text{SW}} = 53.9 \text{ mM} \pm 0.7$ ,  $2\sigma$ ,  $n = 55$ ), ranging between 51.8 and 53.9 mM and showing no strong trend with depth.

Pore fluid Sr concentrations decrease at the top of Unit I (nannofossil-rich clay) from 88.0 to 83.2  $\mu\text{M}$  in Hole U1558A (0–2.66 m CSF-A; mudline corrected) and from 87.2 to 83.1  $\mu\text{M}$  in Hole U1558F (0–2.95 m CSF-A) (Figure F102C). Following this initial drop, Sr values broadly increase to 93.6  $\mu\text{M}$  (117.95 m CSF-A; Hole U1558A) and 92.2  $\mu\text{M}$  (117.97 m CSF-A; Hole U1558F) across Subunits IIA (nannofossil ooze with clay) and IIB (nannofossil chalk with clay). In Subunit IIC (nannofossil chalk with clay and volcanoclastics), Sr values again decrease, reaching  $85.4 \pm 1.6 \mu\text{M}$  in Hole U1558A ( $2\sigma$ ,  $n = 2$ ; 157.35 m CSF-A) and 86.6  $\mu\text{M}$  in Hole U1558F (173.86 m CSF-A). Sr/Ca ratios broadly reproduce the trends observed in Sr concentrations in both holes (Figure F102D). In the uppermost ~20 m of sediment, pore water Sr/Ca ratios drop below the seawater value (8.3  $\mu\text{M}/\text{mM}$ ) and the lowest measured ratios (8.0  $\mu\text{M}/\text{mM}$ ; 6.35 m CSF-A in Hole U1558A; 8.46 m CSF-A in Hole U1558F) correspond to local minima in Ca, Mg, and Sr concentrations in both holes. Sr/Ca ratios increase across Subunit IIA, reaching local maxima (8.9  $\mu\text{M}/\text{mM}$ ) at the boundary between Subunits IIA and IIB (74.30 m CSF-A in Hole U1558A; 66.91 m CSF-A in Hole U1558F). Values remain above the seawater Sr/Ca ratio in Subunit IIB before decreasing again at the top of Subunit IIC.

Despite the lack of strong correlations between the Ca, Mg, and Sr profiles at Site U1558, the changes observed here are consistent with diagenetic reactions involving carbonate formation and recrystallization. In Hole U1558A, concomitant decreases in Ca, Mg, and Sr concentrations in Unit I (nannofossil-rich clay) may indicate the formation of authigenic carbonates. In Hole U1558F, the lower Ca, Mg, and Sr concentrations also coincide with higher pore water alkalinity, which favors in situ carbonate precipitation (e.g., Hein et al., 1979; Schrag et al., 2013; Turchyn et al., 2021). Throughout Subunits IIA and IIB in both holes, recrystallization from a low-Mg biogenic carbonate, typical of nannofossil ooze, to higher-Mg diagenetic calcite (e.g., Baker et al., 1982; Higgins and Schrag, 2012) may explain some of the observed profile changes. First, Mg substitution into diagenetic carbonates would lead to a decrease in pore fluid Mg contents, which is in line with Mg concentrations that are persistently lower than the seawater value in Subunits IIA and IIB in both holes (Figure F102B). Second, the lower Sr content of diagenetic calcite relative to its biogenic precursor (e.g., Baker et al., 1982) would result in increased pore water Sr/Ca ratios following carbonate recrystallization. Indeed, Sr/Ca ratios are overall higher than the seawater value (8.3  $\mu\text{M}/\text{mM}$ ) throughout Subunits IIA, IIB, and part of IIC in both holes (Figure F102D).

#### 11.1.2.4. Boron, lithium, silica, and potassium

Very high to moderate concentration increases (relative to the mudline) are observed for B (67%), Li (18%–25%), Si (153%), and K (25%) in Unit I (nannofossil-rich clay) of Holes U1558A and U1558F (Figure F103). Following this initial increase, the pore fluid concentrations of these elements continue to change as a function of depth and sediment composition.

B concentrations decrease between the nannofossil-rich clay in Unit I (669–687  $\mu\text{M}$  in Hole U1558A; 665–670  $\mu\text{M}$  in Hole U1558F) and the nannofossil ooze with clay in Subunit IIA (580–637  $\mu\text{M}$  in Hole U1558A; 571–651  $\mu\text{M}$  in Hole U1558F) and become more scattered in the nannofossil chalk with clay in Subunit IIB (547–659  $\mu\text{M}$  in Hole U1558A; 458–700  $\mu\text{M}$  in Hole U1558F) (Figure F103A). At the boundary between Subunits IIB and IIC (nannofossil chalk with clay and volcanoclastics), B values increase from 640 to 742  $\mu\text{M}$  in Hole U1558A and from 541 to 615  $\mu\text{M}$  in Hole U1558F, remaining high throughout Subunit IIC. In Hole U1558F, B concentrations decrease below 150 m CSF-A, ranging 551–593  $\mu\text{M}$  (Figure F103A).

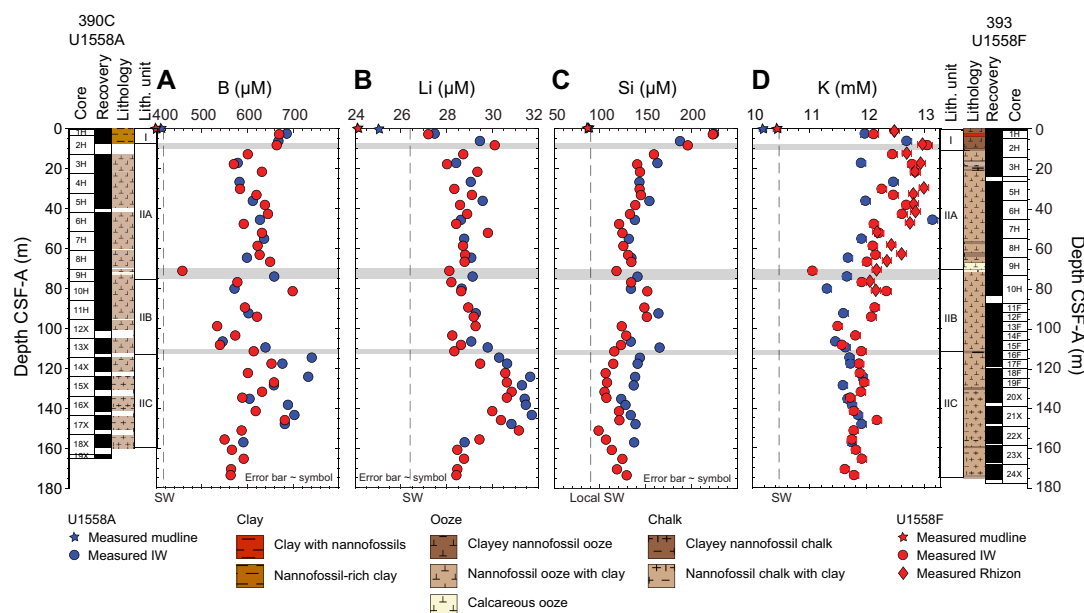
Pore-fluid Li concentrations also decrease between Unit I and Subunit IIA, but values remain fairly uniform (~28.0–30.0  $\mu\text{M}$ ) across Subunits IIA (nannofossil ooze with clay) and IIB (nannofossil chalk with clay) in both holes (Figure F103B). A smooth increase in Li concentrations is observed within the uppermost 40 m (~110–150 m CSF-A) of Subunit IIC (nannofossil chalk with

clay and volcanoclastics; 29.8–31.8  $\mu\text{M}$  in Hole U1558A; 28.4–31.2  $\mu\text{M}$  in Hole U1558F) before concentrations decrease again below 150 m CSF-A (28.8  $\mu\text{M}$  in Hole U1558A; 28.5  $\mu\text{M}$  in Hole U1558F).

Following the sharp increase in Unit I (nannofossil-rich clay), Si concentrations decrease uniformly from ~10 to 70 m CSF-A (Subunit IIA, nannofossil ooze with clay), varying from 163.5 to 135.0  $\mu\text{M}$  in Hole U1558A and from 159.7 to 135.0  $\mu\text{M}$  in Hole U1558F (Figure F103C). The transition from Subunit IIA into IIB (nannofossil chalk with clay; ~65–90 m CSF-A) is marked by an increase in Si concentrations (135.0 to 164.6  $\mu\text{M}$  in Hole U1558A; 135.0 to 151.9  $\mu\text{M}$  in Hole U1558F). In Hole U1558A, measured Si values decrease throughout Subunit IIC (nannofossil chalk with clay and volcanoclastics) between 144 and 138  $\mu\text{M}$ . In Hole U1558F, Si concentrations decrease from ~95 to 140 m CSF-A (151.9 to 107.6  $\mu\text{M}$ ) before increasing again toward the bottom of Subunit IIC (from 98.1 to 129.8  $\mu\text{M}$  between 146 and 174 m CSF-A) (Figure F103C).

Pore-fluid K concentrations show a much simpler profile than those observed for B, Li, and Si. Measured K values decrease from 12.7 to 11.6 mM (Hole U1558A) and from 13.1 to 11.6 mM (Hole U1558F) between Unit I (nannofossil-rich clay; ~10 m CSF-A) and the bottom of Subunit IIB (nannofossil chalk with clay; ~110 m CSF-A) (Figure F103D). Throughout Subunit IIC (nannofossil chalk with clay and volcanoclastics), K concentrations are roughly uniform with depth and show great agreement between Holes U1558A ( $11.8 \pm 0.2$  mM,  $2\sigma$ ,  $n = 9$ ) and U1558F ( $11.8 \pm 0.3$  mM,  $2\sigma$ ,  $n = 14$ ) (Figure F103D).

The most significant changes observed in the concentration profiles of B, Li, Si, and K at Site U1558 correspond to the Unit I interval (0–7.48 m CSF-A in Hole U1558A; 0–9.98 m CSF-A in Hole U1558F) and the transition from Subunit IIB to IIC (~110–150 m CSF-A). Based on calcium carbonate measurements of sediments from Hole U1558F (Table T35), Unit I is characterized by relatively low calcite abundance (18–65 wt%) in comparison to Unit II (52–97 wt%) and occurs together with considerable amounts of total clays (27–43 wt%), quartz (4–10 wt%), and K-feldspar (6–9 wt%) (Table T3). Smear slide photomicrographs of Site U1558 sediments also indicate the presence of sponge spicules (i.e., biogenic silica) in Unit I (Figure F14), and gamma ray readings



**Figure F103.** IW profiles of (A) boron, (B) lithium, (C) silicon, and (D) potassium concentrations, Holes U1558A and U1558F. RZ = Rhizon sampler. Seawater (SW) reference values for B, Li, and K correspond to IAPSO standard composition; local Si concentration is from Sarmiento et al. (2007). Shaded gray areas = unit boundaries.

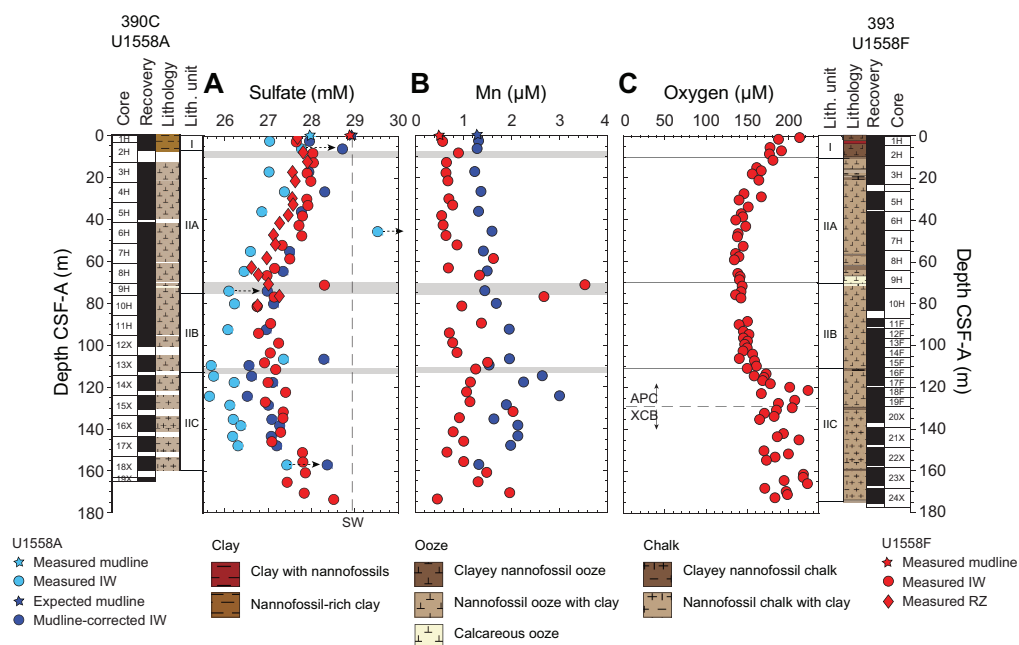
**Table T35.** Geochemical analyses of sediments, Site U1558. [Download table in CSV format.](#)

above 40 counts/s are also recorded in this interval (Figure F82). Together, these observations suggest that the concomitant increases in B, Li, Si, and K concentrations in Unit I could result from the combined effects of biogenic silica dissolution, weathering of detrital silicates, and/or ion exchange between clays and pore fluids. Diagenetic reactions involving silicates and/or biogenic silica may also explain the observed increases in B and Li concentrations at the boundary between Subunits IIB and IIC, which coincide with sharply elevated NGR counts (Figure F82) and an increase in the modal proportion of total clays (Figure F16). The observation that Si and K concentrations do not increase at the Subunit IIA/IIB boundary may suggest that this interval may act as a sink, rather than a source, of those elements. Other processes with potential to affect these cation concentration profiles at Site U1558 include the transformation of smectite to illite during burial, weathering of underlying oceanic crust (e.g., Gieskes, 1975), and advection of water masses with variable compositions.

#### 11.1.2.5. Sulfate, manganese, ammonium, and phosphate

Depth profiles of  $\text{SO}_4$  and Mn show some variation between Holes U1558A and U1558F. In particular, the sulfate minimum happens at much shallower depths in Hole U1558F (62.73 m CSF-A; Subunit IIA, nannofossil ooze with clay) compared to Hole U1558A (124.54 m CSF-A; Subunit IIC, nannofossil chalk with clay and volcanoclastics) (Figure F104A), consistent with the overall higher TOC content in U1558F (Figure F105B). In both holes,  $\text{SO}_4$  contents increase toward the seawater value at depth.

Mn concentrations vary between 1.25 and 3.02  $\mu\text{M}$  in Hole U1558A and from 0.47 to 3.55  $\mu\text{M}$  in Hole U1558F (Figure F104B). In Hole U1558A, measured Mn values generally increase from the mudline (1.31  $\mu\text{M}$ ; 0 CSF-A) to the top of Subunit IIC (3.02  $\mu\text{M}$ ; 124.54 m CSF-A) and then decrease toward the bottom of the hole (1.34  $\mu\text{M}$ ; 157.35 m CSF-A). In Hole U1558F, the Mn profile shows intervals where concentrations both increase and decrease, with some local maxima at 58.91 m CSF-A (1.64  $\mu\text{M}$ ; Subunit IIA), 71.44 m CSF-A (3.55  $\mu\text{M}$ ; top of Subunit IIB), 108.56 m CSF-A (1.52  $\mu\text{M}$ ; bottom of Subunit IIB), and 170.85 m CSF-A (1.98  $\mu\text{M}$ ; bottom of Subunit IIC). Although no strong correlation is observed between  $\text{SO}_4$  and Mn, the highest Mn concentrations in Holes U1558A and U1558F coincide with their respective intervals of low  $\text{SO}_4$  (Figure F104). The sample from Section 393-U1558F-9H-5 (71.44 m CSF-A; Subunit IIB), with visibly higher  $\text{SO}_4$  and Mn contents, is likely an outlier.  $\text{NH}_4$  and  $\text{PO}_4$  concentrations in these pore fluids are close to or at the level of instrumental detection limits, an observation consistent with the low organic



**Figure F104.** IW profiles of (A) sulfate, (B) manganese, and (C) oxygen, Holes U1558A and U1558F. RZ = Rhizon sampler. Dashed horizontal line in C denotes where APC coring stopped and XCB coring started. Reference value for seawater (SW) sulfate corresponds to IAPSO standard composition. Shaded gray areas/lines = unit boundaries.

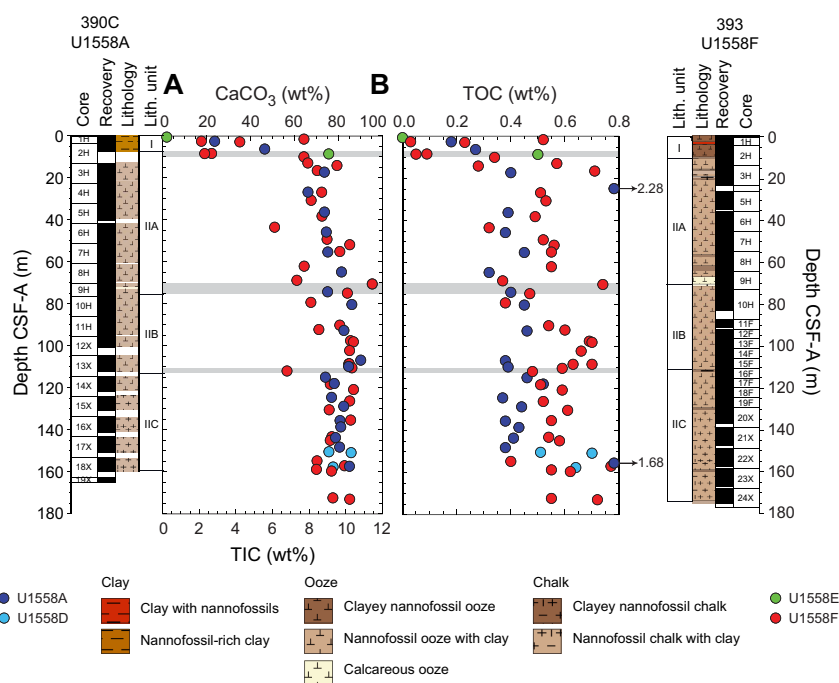
carbon content and the persistently oxic conditions at this site (see next section). For that reason, we report the data in Table T34 but do not discuss it any further here.

### 11.1.2.6. Oxygen

Oxygen is the pore water constituent measured with the highest reduction potential and is the first molecule reduced during microbial degradation of organic matter. Its profile provides insight into subseafloor biogeochemical and microbial processes. Oxygen concentrations in Hole U1558F decrease from a mudline concentration of ~210 to ~135  $\mu\text{M}$  in Subunit IIA at ~60 m CSF-A (Table T36; Figure F104C). Oxygen concentrations remain nearly constant for most of Subunits IIA (nanfossil ooze with clay) and IIB (nanfossil chalk with clay) before increasing in Subunit IIC (nanfossil chalk with clay and volcanoclastics). Concentrations return to surface values (~200  $\mu\text{M}$ ) in Subunit IIC at the end of APC coring. The points below ~130 m CSF-A were collected during XCB coring, and the trend in the concentration data becomes more scattered, with measurements ranging 165–223  $\mu\text{M}$  to basement (Figure F104C).

### 11.1.3. Sediment sampling

Sediment from Holes U1558A, U1558D, U1558E, and U1558F was analyzed for carbon and nitrogen concentrations from a combination of squeeze cake residues and samples selected by the sedimentologists from the core working halves (see **Geochemistry** in the Expedition 390/393 methods chapter [Coggon et al., 2024b]). During Expedition 390C, all sediment samples were taken from IW squeeze cake residues, totaling 22 samples. During Expedition 393, one sample was taken from the IW squeeze cake in Section 393-U1558D-2R-1, in addition to samples selected by sedimentologists from Cores 2R ( $n = 1$ ), 3R ( $n = 1$ ), and 393-U1558E-1H ( $n = 2$ ). Although our samples from Holes U1558D and U1558E were only from single sediment cores, they were included in sample analyses to provide additional data at critical intervals such as the mudline and sediment/basement interface. In Hole U1558F, sediment was sampled once from the working halves in Cores 393-U1558F-11F, 12F, 14F, and 17F–19F and twice in Cores 3H–10H, 13F, 16F, and 20X–24X. Sediments from IW squeeze cake residues were analyzed once in Core 1H and twice in Cores 2H and 15F. During Expedition 393, a total of 48 samples were taken at Site U1558, 6 from



**Figure F105.** Sediment (A) calcium carbonate and TIC and (B) TOC, Site U1558. Two TOC outliers are plotted at their respective depths. Shaded gray areas = unit boundaries.

**Table T36.** Oxygen concentrations, Hole U1558F. [Download table in CSV format.](#)

IW squeeze cake residues and 42 from sediment working halves. In total, 70 sediment samples were analyzed at Site U1558 during Expeditions 390C and 393 (Table T35).

During Expedition 390C, sediment was sampled from whole-round sediment cores for hydrocarbon analyses (see **Geochemistry** in the Expedition 390/393 methods chapter [Coggon et al., 2024b]). Samples were taken at the top of Section 2 in Cores 390C-U1558A-14X, 15X, and 17X, Section 3 in Cores 1H, 2H, 13X, and 16X, Section 4 in Cores 3H–10H and 12X, Section 5 in Core 18X, and Section 6 in Core 11H. In total, 18 sediment samples were analyzed at Site U1558 (Table T35).

#### 11.1.4. Sediment bulk geochemistry

##### 11.1.4.1. Calcium carbonate

The carbonate content of the sediment in all holes at Site U1558 increases with depth in Unit I (0–10 m CSF-A; nannofossil-rich clay; 2–77 wt%,  $n = 9$ ; Figure F105) and shows an invariant trend downhole in Unit II in all holes (>10 m CSF-A; nannofossil ooze/chalk with clay;  $79 \pm 17$  wt%,  $2\sigma$ ,  $n = 60$ ). Carbonate content from Hole U1558F ( $78 \pm 20$  wt%,  $\pm 2\sigma$ ,  $n = 48$ ) displays greater scatter compared to analyses from Hole U1558A ( $80 \pm 11$  wt%,  $\pm 2\sigma$ ,  $n = 22$ ).

##### 11.1.4.2. Total organic carbon and nitrogen

TOC was calculated for all samples measured for  $\text{CaCO}_3$  as the difference between total carbon (TC) and total inorganic carbon (TIC) (see **Geochemistry** in the Expedition 390/393 methods chapter [Coggon et al., 2024b]). TOC concentrations (Figure F105) show a large range with depth in Unit I (0–10 m CSF-A, nannofossil-rich clay), varying between ~0 and 0.52 wt% across Holes U1558A, U1558E, and U1558F. In Unit II (>10 m CSF-A; nannofossil ooze/chalk with clay), TOC concentrations in Hole U1558F are more scattered and generally higher ( $0.56 \pm 0.23$  wt%,  $2\sigma$ ,  $n = 37$ ) than those in Hole U1558A ( $0.41 \pm 0.09$  wt%,  $2\sigma$ ,  $n = 18$ , outliers excluded), aside from two data points that are greater than 1.5 wt% in Hole U1558A (Sections 390C-U1558A-4H-3 and 18X-4; TOC = 2.28 and 1.68 wt%, respectively).

Total nitrogen (TN) concentrations were measured on all samples analyzed for  $\text{CaCO}_3$  ( $n = 70$ ). Total nitrogen concentrations throughout all holes at Site U1558 are close to or below detection levels and are not discussed further. Total sulfur (TS) and total hydrogen (TH) were not measured.

##### 11.1.4.3. Headspace analysis of hydrocarbons

Sediment headspace was sampled once per core in Hole U1558A for hydrocarbon analysis. Concentrations of all hydrocarbons are below detection limit (1 ppmv) in all 18 sampled intervals (Table T35).

## 11.2. Basement

During Expedition 393, ~220 m of moderately to highly altered ~49.2 Ma basalts were drilled in Hole U1558D, recovering 98 m of volcanic rocks representing five major igneous units, including several zones of variably cemented volcano-sedimentary breccias (see **Igneous petrology**). A total of 29 basement samples were selected for shipboard geochemical study, which included 25 basalts and 4 breccias. These breccia samples are physically and hydrothermally perturbed, originally sedimentary mixtures of now-indurated calcareous sediments with abundant fragments of fresh to completely altered volcanic glass, and biogenic and clastic phases. Analyses included both solution analysis using ICP-AES and direct measurements of sample powders and sample surfaces using pXRF. In addition to data from Hole U1558D, Sample 390C-U1558A-19X-2, 45–40 cm, from the basalt/sediment interface in Hole U1558A was also analyzed.

### 11.2.1. Basement rock sampling and geochemical analysis

The geochemical samples selected included typical materials from each of the magmatic units identified (see **Igneous petrology**). Geochemical samples were taken adjacent to other sampling (thin sections, PMAG, XRD, etc.) to generate integrated data on these materials. In some cases, samples of more altered materials were selected to try and assay the geochemical range of down-hole alteration effects. A powder mount of each freshly made sample powder was prepared for pXRF analysis (see **Geochemistry** in the Expedition 390/393 methods chapter [Coggon et al.,



2024b]). ICP-AES measurements were completed on oxidized samples that had undergone loss on ignition (LOI) determinations, so ICP-AES data are reported on a volatile-free basis.

### 11.2.2. Bulk chemical compositions and trace element abundances of basalts

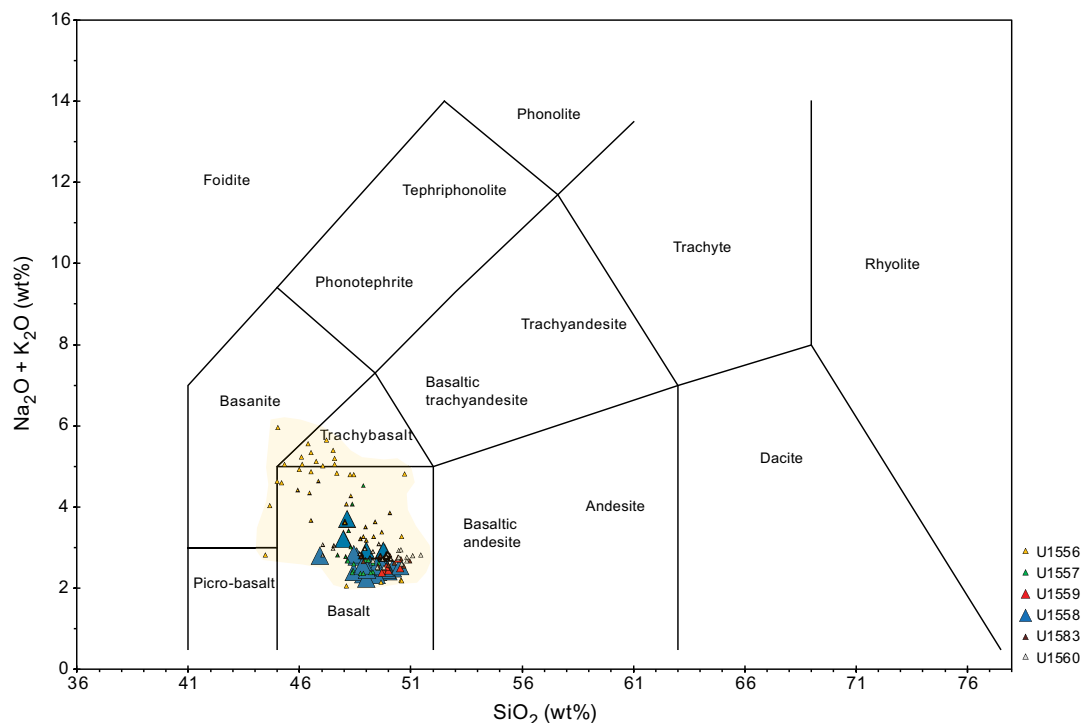
Table T37 lists the shipboard geochemical data collected on Site U1558 samples using ICP-AES analysis, and Table T38 presents pXRF data collected for the same samples from unignited powder mounts.

On the total alkalis versus silica diagram of Le Bas et al. (1986) (Figure F106), the Site U1558 samples all fall in the basalt field. The samples with the lowest LOI contents from this site are olivine tholeiites per the Yoder and Tilley (1962) basalt classification scheme, but some of the more altered samples, due to seawater-basalt exchange and other processes, now include normative nepheline, which in the Yoder and Tilley scheme categorizes them as alkali basalts (Table T37).

Figure F107 compares our Site U1558 basalt data to results for basalt glasses from the southern Atlantic compiled from the EarthChem Portal and MORBs from other SAT sites on a plot of Sr versus  $\text{TiO}_2$ . Both Ti and Sr behave as incompatible elements in MORB systems, although Ti is generally immobile during low-temperature hydrothermal alteration and most other fluid-mediated chemical exchanges. Although Sr is sensitive to alteration, as documented by  $^{87}\text{Sr}/^{86}\text{Sr}$  variations in ocean crustal lithologies (e.g., Teagle et al., 1996, 1998; Harris et al., 2015), Sr abundances are commonly not strongly modified in basalts except through carbonate precipitation. In Figure F107, the Site U1558 basalts plot largely within the field for South Atlantic MORBs, at broadly similar Sr and Ti abundances to basalts from Site U1559 but at higher abundances than the Site U1557 basalts or the basalts from the deepest section of Site U1556, Stratigraphic Sequence C.

**Table T37.** ICP-AES major and trace element compositions and CIPW norms, Site U1558. [Download table in CSV format.](#)

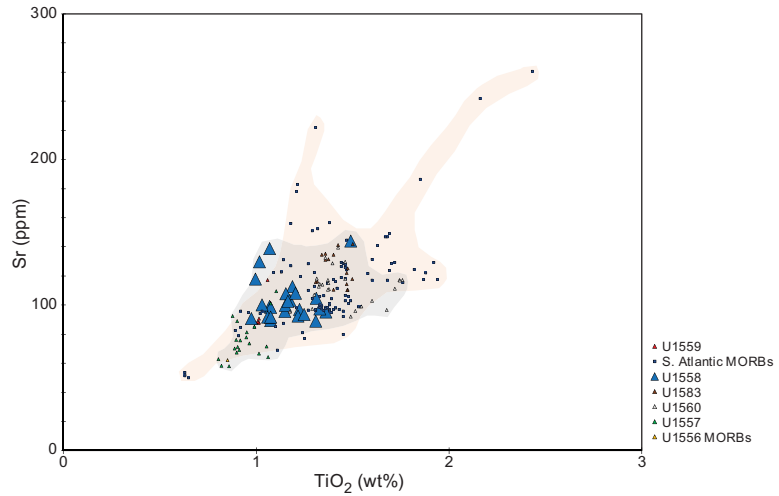
**Table T38.** Powder pXRF elemental data, Site U1558. [Download table in CSV format.](#)



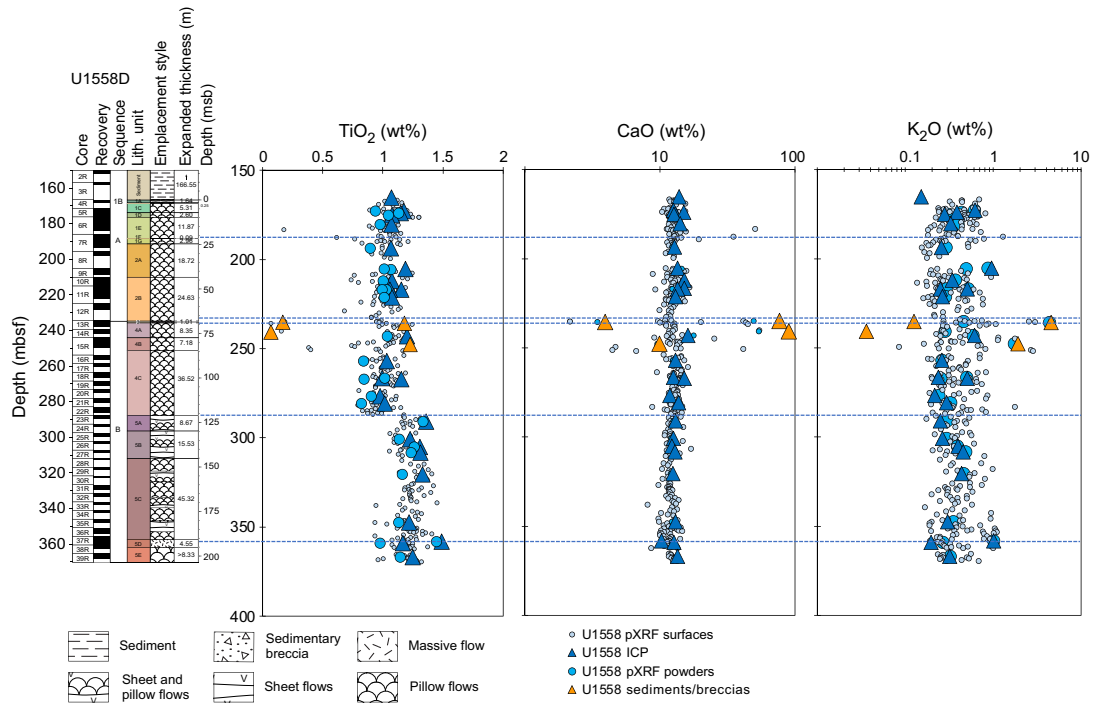
**Figure F106.** Total alkalis vs. silica diagram (Le Bas et al., 1986), plotting ICP-AES data for the Site U1558 basalts compared to basalts from Sites U1556, U1557, and U1559.

### 11.2.3. Downhole geochemical variations

Figure F108 presents downhole plots for several major elements analyzed by ICP-AES and pXRF analysis of both sample powders and sample surfaces. A clear downhole change in magmatic composition is evident at 288 mbsf (Subunit 4C/5A boundary), where the lavas become higher in  $\text{TiO}_2$ . Also evident on these plots are the positions of basalt-sediment breccia zones and/or zones with thick interpillow sediments (Unit 3 and Subunits 4A and 4B), which presumably reflect breaks in magmatic activity, as they are associated with highly variable  $\text{CaO}$  and  $\text{K}_2\text{O}$  contents and decreases



**Figure F107.** Sr vs.  $\text{TiO}_2$  contents comparing samples from Site U1558 and other SAT sites (gray field) with data for zero-age South Atlantic MORBs compiled from EarthChem Portal (<http://portal.earthchem.org/>) on 10 July 2022 via map polygon function for MORB glasses <100,000 y old from South Atlantic Ocean (specific sources: Kelley et al., 2013; Kendrick et al., 2017; Le Roux, 2000; Michael and Graham, 2015; Paulick et al., 2010; Reekie et al., 2019; van der Zwan et al., 2017; Yang et al., 2018).



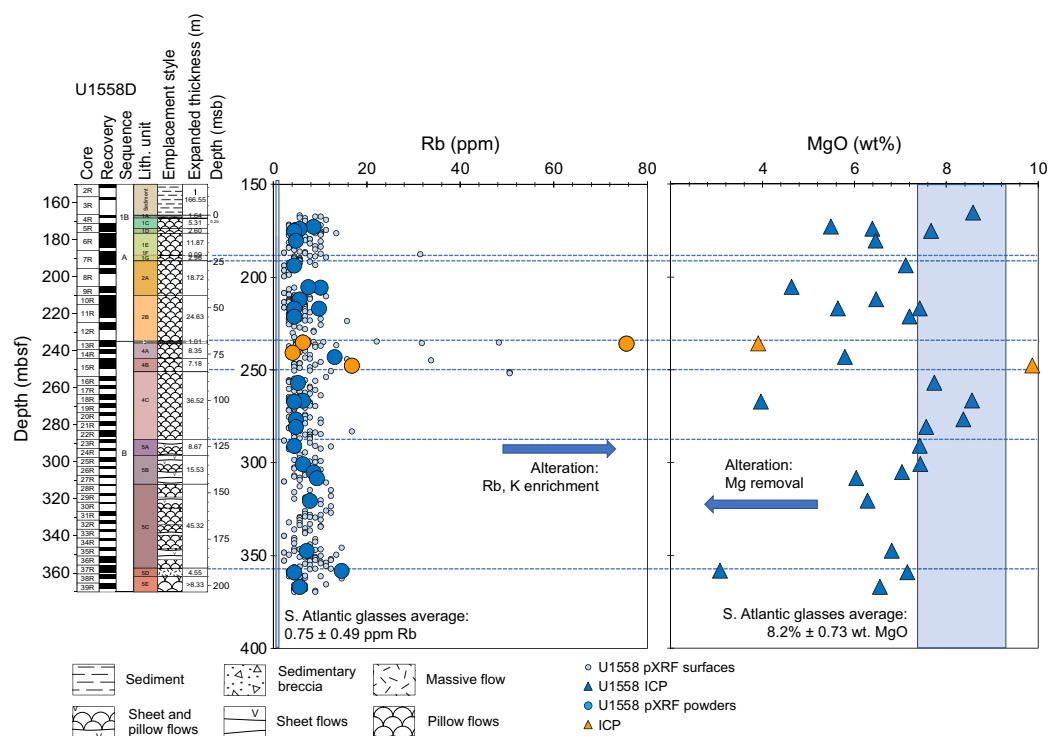
**Figure F108.** Key major elements ( $\text{TiO}_2$ ,  $\text{CaO}$ , and  $\text{K}_2\text{O}$ ), Hole U1558B. Horizontal dotted lines = lithostratigraphic boundary depths evident in combined geochemical results, mapped to Site U1558 lithology column developed by Igneous petrology team.

in  $\text{TiO}_2$ . These chemostratigraphic breaks match unit boundaries identified (**Igneous petrology**), though the finer-scale subunit boundaries are often not reflected in the downhole chemistry, partly due to the coarser resolution of our whole-rock sampling and partly because physical distinctions observable in the core may not relate to changes in chemical signature.

#### 11.2.4. Effects of alteration

As indicated by the downhole variations of both  $\text{CaO}$  and  $\text{K}_2\text{O}$  in Figure F108, the Site U1558 basalts have been extensively altered through exchanges with seawater-derived fluids. This pervasive alteration is partly reflected in LOI values, which range 1.0–4.5 wt% in most of our samples. In plots of Rb and MgO versus depth (Figure F109), Rb concentrations are markedly high as compared to typical MORB values, presumably due to seafloor basalt alteration processes. In contrast, Mg concentrations are variably lower, presumably due to these same seafloor alteration processes. Alteration-related Mg losses are at odds with the observed Mg systematics in seafloor hydrothermal systems, where Mg is removed from the fluids and sequestered in the rock (e.g., Von Damm and Bischoff, 1987). However, similarly lowered MgO contents are observed in altered basaltic rocks from Deep Sea Drilling Project (DSDP) Holes 417A and 417D (Donnelly et al., 1980). Seafloor weathering processes have been suggested as a cause for variable Mg leaching from basalts in other oceanic settings (e.g., Hart et al., 1974; Pichler et al., 1999). The evidence for alteration at Site U1558 (age ~49.2 Ma) is far more substantial than that observed at Site U1559 (age ~6.6 Ma), where both MgO and Rb were found to have concentrations similar to those of fresh South Atlantic MORBs.

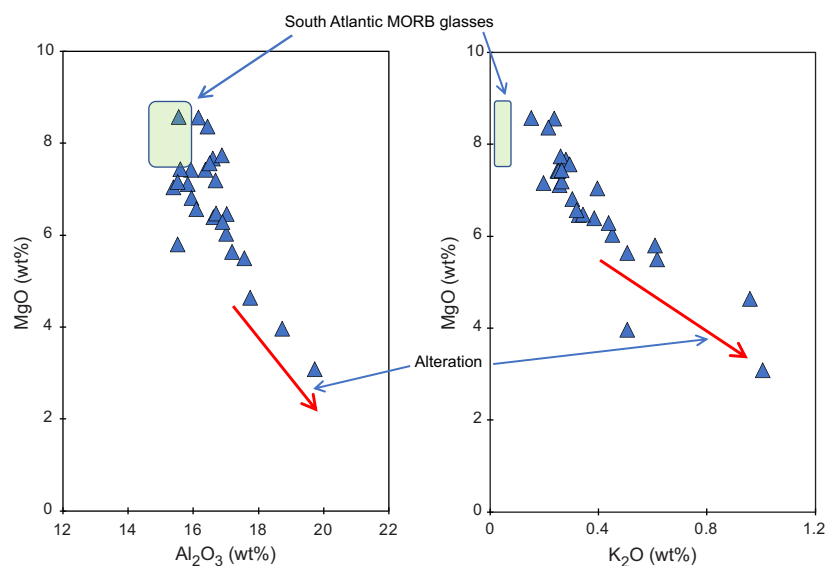
Figure F110 reports these effects further through plots of MgO versus  $\text{Al}_2\text{O}_3$  and  $\text{K}_2\text{O}$  for the Site U1558 sample suite.  $\text{Al}_2\text{O}_3$  is effectively immobile during fluid-rock exchanges, whereas  $\text{K}_2\text{O}$  is high in seawater and partitions into low-temperature seafloor alteration phases. MgO forms clear inverse correlations with both  $\text{Al}_2\text{O}_3$  and  $\text{K}_2\text{O}$ , suggesting that the seafloor processes that remove MgO from these rocks enrich them in  $\text{Al}_2\text{O}_3$  as well as  $\text{K}_2\text{O}$ , particularly at the highest degrees of alteration (i.e., lowest MgO). These patterns are suggestive of the formation of K-rich, Mg-poor alteration phases during seafloor alteration at Site U1558 as opposed to the formation of abundant



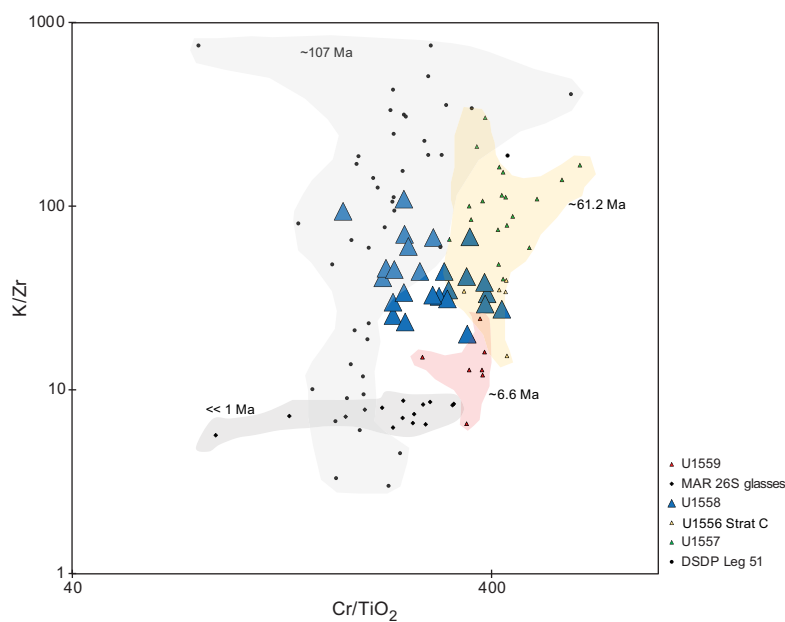
**Figure F109.** Rb and MgO highlighting alteration effects, Hole U1558D. Rb data collected by pXRF; MgO data collected by ICP-AES. Shaded fields = mean Rb and MgO concentrations of South Atlantic D-MORB glasses, compiled via <http://portal.earthchem.org/>.

saponite and/or other Mg-rich alteration minerals, as has been observed in altered basalts at several different sites in the Pacific Ocean (Alt et al., 1986; Alt and Teagle, 2003; Teagle et al., 1996).

In Figure F111, K/Zr ratios, as a proxy for alteration effects, are plotted versus Cr/TiO<sub>2</sub> ratios, as an indicator of magmatic source and differentiation effects. Our Site U1558 basalts are distinctively higher in K/Zr than D-MORB glasses from 26°N on the Mid-Atlantic Ridge and the much younger lavas (~6.6 Ma) recovered at Site U1559. However, Site U1558 samples are overall somewhat lower in K/Zr than the older (~61.2 Ma) MORB-like basalts recovered at Sites U1556 and U1557 during Expedition 390 and lower than the most altered ~107 Ma basalts recovered at Sites 417A and 417D during DSDP Leg 51 (Donnelly et al., 1980). Thus, although our ~49.2 Ma suite of



**Figure F110.** Al<sub>2</sub>O<sub>3</sub> and K<sub>2</sub>O vs. MgO from Site U1558 basalts with fields for fresh South Atlantic MORB glasses from mean and standard deviations of data compiled through <http://portal.earthchem.org/>.



**Figure F111.** K/Zr vs. Cr/TiO<sub>2</sub> comparing ICP-AES data from Site U1558 with depleted MORB-like samples from Sites U1556 (Stratigraphic Sequence C; 61.2 Ma), U1557 (61.2 Ma), and U1559 (6.6 Ma), with data for Mid-Atlantic Ridge 26°S N-MORB basalt glasses (Marschall et al., 2017) and ~107 Ma altered basalts from DSDP Leg 51 (Donnelly et al., 1980).

Site U1558 samples shows extensive geochemical evidence for alteration, overall they appear to be not as modified as those from older Atlantic MORB crust.

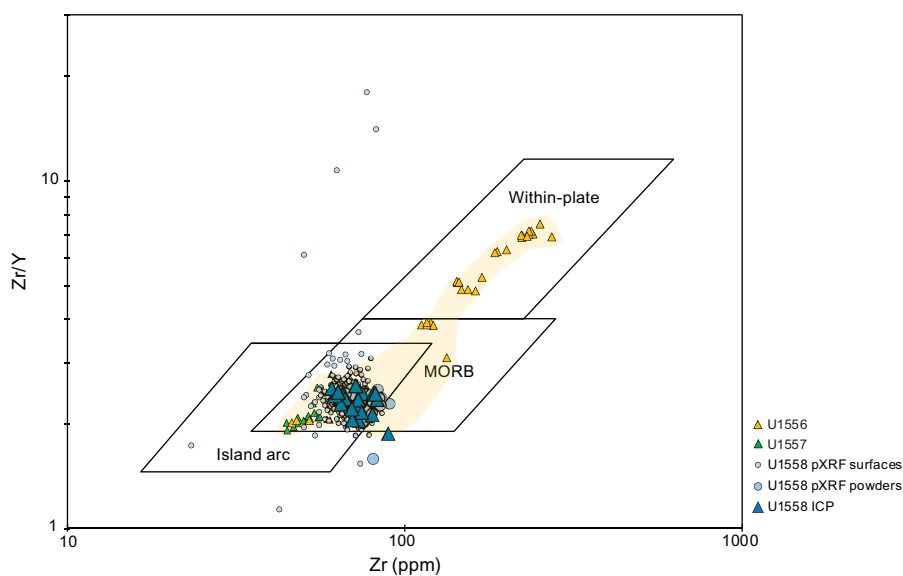
### 11.2.5. Breccia/sediment fill compositions

Unit 3 (Core 393-U1558D-13R) comprises a volcano-sedimentary breccia unit, and comparably modified interpillow sedimentary materials are encountered in Cores 14R and 15R in Subunits 4A and 4B. Several breccia and sedimentary fill samples were selected to better understand the compositional range of these materials. The breccia fill compositions are highly variable, ranging from very CaO rich for samples with large proportions of sediment-derived calcium carbonate (e.g., Samples 13R-1, 29–31 cm, and 14R-1, 42–48 cm) to compositions that are distinctively low in CaO and TiO<sub>2</sub> but markedly high in SiO<sub>2</sub>, K<sub>2</sub>O, and Rb (up to 56.6 wt% SiO<sub>2</sub>, 4.5 wt% K<sub>2</sub>O, and 73 ppm Rb; Sample 13R-1, 55–58 cm) (Figures F108, F109; Tables T34, T35). Visually, the breccia zones in the Site U1558 suite appear to be mixtures of calcareous sediment and variably altered volcanic glass. However, their bulk elemental compositions, in particular their elevated SiO<sub>2</sub> and K<sub>2</sub>O contents, indicate substantial postdepositional modification of these materials through seawater and hydrothermal exchanges.

### 11.2.6. Discriminator diagram systematics and anomalies

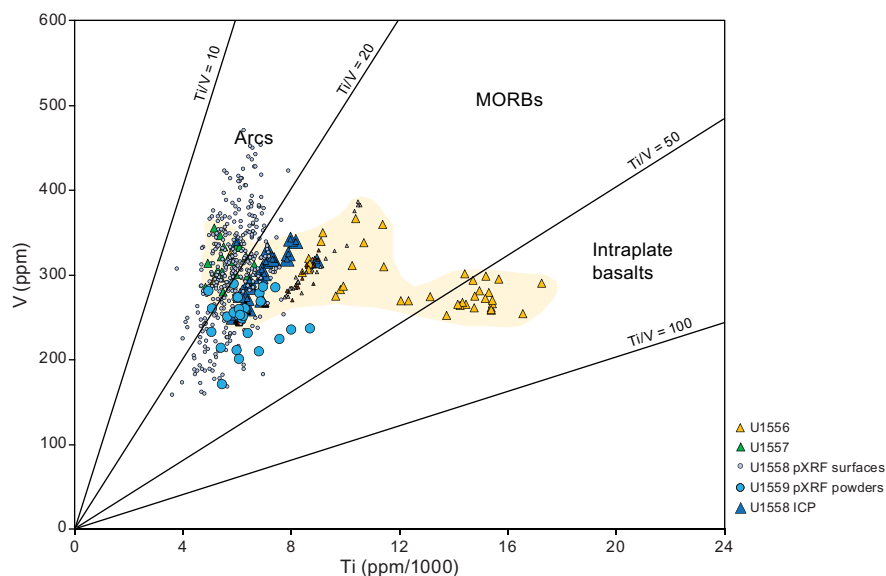
Pearce and others (Pearce and Cann, 1973; Pearce and Norry, 1979; Shervais, 1982) pioneered the use of tectonic discriminant diagrams utilizing immobile trace elements as a way of inferring protoliths and modes of origin for altered and/or metamorphosed units in the geologic record. Although the broader tectonic origins of the SAT lavas are largely agreed upon, such diagrams can also be used to spot anomalous trace element systematics among rock suites that may offer additional tectonic insights.

The Pearce and Norry (1979) Zr/Y vs. Zr discriminant diagram shows that basalts from Site U1558 consistently plot as MORBs irrespective of the data set examined (solution analyses, powders, rock surfaces), and solution, powder, and rock surface analyses show no offset relative to one another (Figure F112). Stratigraphic Sequences A and B from Site U1556, by contrast, show clear intraplate affinities, forming a trend into the within-plate basalt field, whereas basalts from Site U1556, Stratigraphic Sequence C, and Site U1557 plot largely in the MORB field but are offset from the Site U1558 and U1559 suites toward the island arc field. On the V vs. Ti/1000 diagram (Figure F113) (Shervais, 1982), the offset of the Site U1557 data is even more apparent, as these rocks, along with the MORB-like samples from the bottom of Hole U1556B (Stratigraphic Sequence C), fall within the arc field, even though they are clearly not arc related. Data for Site



**Figure F112.** Zr/Y vs. Zr tectonic discrimination diagram from Pearce and Norry (1979) showing combined pXRF and ICP-AES data for Site U1558 basalts compared to Sites U1556 and U1557 and other SAT sites (shaded field).





**Figure F113.** V vs. Ti/1000 tectonic discrimination diagram of Shervais (1982) showing combined pXRF and ICP-AES data for Site U1558 compared to Sites U1556 and U1557 and other SAT sites (shaded field).

**Table T39.** Microbiology whole-round samples, Hole U1558F. [Download table in CSV format.](#)

U1558 basalts, as best demonstrated by the higher-precision ICP-AES results, straddle the boundary between the MORB and arc fields. The lower Zr/Y and higher V/Ti ratios seen in the Site U1557 suite and in some Site U1558 samples suggest comparatively lower incompatible element concentrations in the protoliths of these older (~61.2–49.2 Ma) lavas.

## 12. Microbiology

### 12.1. Sediment

Microbiology sampling in Hole U1558F during Expedition 393 focused on exploring evidence for life in the sediments and at the sediment/basement interface using culture-based and culture-independent approaches. In Hole U1558F, one standard microbiology whole-round sample (5–10 cm long) was collected from each 9.5 m core and subsampled for different shipboard and shore-based scientists, as described below (Table T39). Additional personal whole-round cores for specialized shore-based analyses were also taken (Table T39). In summary, 18 standard microbiology and 38 personal whole-round samples were taken from Hole U1558F.

#### 12.1.1. Microbiological sample processing and experiments

##### 12.1.1.1. Cell and viral counts

Subsamples for cell enumeration were taken in duplicate from every standard microbiology whole round. An additional subsample was taken for viral counts from each of the 10 cores that were sampled for viral metagenomic analysis. Conducting cell and virus counting is difficult on the R/V *JOIDES Resolution* because of the time required for microscopy sample preparation and counting. Therefore, shipboard cell counts were not attempted during the SAT expeditions; instead, samples were preserved for postexpedition analyses by diluting 1 cm<sup>3</sup> of sample in 4 mL of 4% paraformaldehyde in 100 mM phosphate-buffered saline (PBS). Duplicate samples were collected to enable cross-calibration of cell count results between different laboratories, and a third sample was collected for virus counts from samples where viral metagenomes were also collected.

### 12.1.1.2. Microbial community structure

From the standard microbiology whole rounds, 38 samples were preserved for shore-based polymerase chain reaction [PCR] amplicon-based analysis (from DNA and RNA), 18 samples were preserved for single-cell genomics, 10 samples were preserved for viral production experiments, and 9 samples were preserved for high-throughput culturing. The following additional personal whole-round (5–10 cm long) samples were collected and preserved: 10 samples for viral metagenomics, 9 samples for sediment metagenomics, 7 samples for anaerobic enrichments, and 6 samples for the anaerobic enrichment of Archaea (Table T39). All samples were preserved as described in **Microbiology** in the Expedition 390/393 methods chapter (Coggon et al., 2024b) for postexpedition research.

### 12.1.1.3. Microbial incubation experiments

To determine the extent of viral activity, experiments were performed (see **Microbiology** in the Expedition 390/393 methods chapter [Coggon et al., 2024b]) in duplicate using 10 cm<sup>3</sup> from the standard microbiology whole-round sample from Cores 393-U1558F-1H, 3H, 8H, 16F, 21X, and 24X (see Table T39 for specific sections and depths). Virus-induced microbial mortality and prophage induction experiments were initiated in a Coy anaerobic chamber (see **Microbiology** in the Expedition 390/393 methods chapter [Coggon et al., 2024b]). These samples were chosen to represent a range of oxygen and nutrient concentrations throughout the hole. The samples were incubated at room temperature (~18°C), and duplicate 1 mL subsamples were collected after 0, 3, 6, 12, 24, and 48 h and then at 7 and 14 days. The seawater that was used to dilute 1 cm<sup>3</sup> sediment for samples from Cores 16F, 21X, and 24X (see Table T39 for specific sections and depths) was collected shortly after arrival at Site U1559 on 19 June 2022 using a field-rinsed bucket attached to a rope. This surface seawater was filtered through a 0.22 µm polyethersulfone (PES) membrane twice and autoclaved. The pH was 7.99 after autoclaving, and the salinity was 37. For samples from Cores 1H, 3H, and 8H, 0.22 µm filtered and autoclaved deep seawater (4333 m depth) was collected on 28 June at Site U1558 using a Niskin bottle attached to the subsea camera system frame. The pH of the deep water was 7.54, and the temperature was 13°C.

### 12.1.2. Microbiological contamination monitoring

To determine the number of microorganisms present in drilling fluid and also generate a database of potential contaminants, we collected drilling fluid from the standpipe on the rig floor two times during coring operations in Hole U1558F: (1) while drilling Core 4H (~126 mbsf) and (2) at the end of drilling Core 24X (~174 mbsf). Drilling fluid samples were collected for cell counts, and 500 mL was filtered onto a 0.20 µm pore size 47 mm diameter filter and frozen at –80°C for shore-based molecular biology analysis.

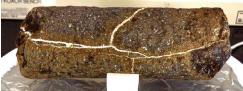





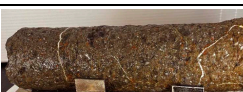
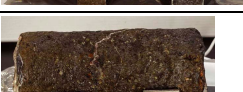

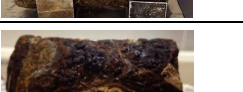
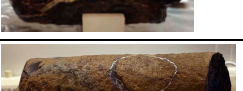
## 12.2. Basement

Microbiology sampling from volcanic rocks in Hole U1558D during Expedition 393 focused on culture-based and culture-independent approaches to characterize microbial communities and their activity near the sediment/basement interface and in underlying basement. Sampling efforts focused on collecting one whole-round core sample from each 9.5 m advance that would be processed and subsampled for different analyses. In total, 25 whole-round samples (12–23 cm long) were collected for microbiological analyses (Figure F114). The rock types collected were as follows (Figure F114) (see **Igneous petrology**):

- Moderately plagioclase-olivine-pyroxene-phyric, cryptocrystalline basalt pillow lava (1 sample);
- Highly plagioclase-olivine-pyroxene phyric, cryptocrystalline basalt pillow lava with glassy margin (1 sample);
- Moderately plagioclase-olivine-pyroxene phyric, cryptocrystalline basalt pillow lava with glassy margin (4 samples);
- Highly plagioclase-olivine-pyroxene phyric, cryptocrystalline basalt pillow lava with glassy margin (2 samples);
- Moderately plagioclase-olivine-pyroxene phyric, microcrystalline to locally cryptocrystalline basalt (1 sample);

- Sparsely olivine-plagioclase phyric, cryptocrystalline basalt pillow lava and interpillow sediment (1 sample);
- Fractured pillow lavas, pillow breccias, and hyaloclastite breccias (1 sample);
- Sparsely plagioclase-olivine-phyric, microcrystalline basalt pillow lava with cryptocrystalline to glassy margin (3 samples);
- Moderately plagioclase-olivine-phyric, microcrystalline basalt (1 sample);
- Sparsely plagioclase-olivine-phyric, microcrystalline basalt (1 sample);
- Moderately olivine-plagioclase-phyric, cryptocrystalline basalt (1 sample);
- Moderately olivine-plagioclase-phyric, variolitic basalt (3 samples); and
- Moderately plagioclase-olivine-phyric basalt (1 sample).

After the exteriors of whole-round pieces were removed to avoid material contaminated during coring (see **Microbiology** in the Expedition 390/393 methods chapter [Coggon et al., 2024b]), the remaining material was split into subsamples that were prepared for different microbiological analyses. The number of subsamples depended on the amount of material available from each whole round (Table T40).

Sample	Top depth (mbsf)	Lithology	Veins	Foldio turntable photo
393-U1558D-5R-1 123-126 cm	172.56	Moderately plagioclase-olivine-pyroxene-phyric, cryptocrystalline basalt pillow lava	Veins up to 2.5 mm composed of smectite and carbonate	
393-U1558D-6R-6 42-60 cm	183.35	Highly plagioclase-olivine-pyroxene phyric, cryptocrystalline basalt pillow lava with glassy margin	Veins up to 1.5 mm composed of smectite and carbonate	
393-U1558D-7R-2 49-63 cm	187.84	Moderately plagioclase-olivine-pyroxene phyric, cryptocrystalline basalt pillow lava with glassy margin	Veins up to 1 mm composed of smectite and carbonate	
393-U1558D-9R-2 68-82 cm	197.72	Moderately plagioclase-olivine-pyroxene phyric, microcrystalline basalt sheet flow with glassy margin	Veins up to 0.5 mm composed of carbonate and FeOH	
393-U1558D-9R-1 30.5-51 cm	205.61	Moderately plagioclase-olivine-pyroxene phyric, microcrystalline basalt pillow flow with glassy margin	Veins up to 0.5 mm composed of smectite, carbonate and FeOH	
393-U1558D-10R-3 62-78 cm	213.49	Highly plagioclase-olivine-pyroxene phyric, cryptocrystalline basalt pillow lava with glassy margin	Veins up to 1 mm composed of smectite, carbonate and green clay	
393-U1558D-11R-2 42-65 cm	216.93	Moderately plagioclase-olivine-pyroxene phyric, cryptocrystalline basalt pillow lava with glassy margin	Veins up to 1.5 mm composed of smectite, carbonate, FeOH, and green clay	
393-U1558D-12R-3 0-17 cm	227.47	Moderately plagioclase-olivine-pyroxene phyric, microcrystalline to locally cryptocrystalline basalt	Veins up to 1 mm composed of smectite and carbonate	
393-U1558D-13R-2 120-133 cm	237.10	Sparsely olivine-plagioclase phyric, cryptocrystalline basalt pillow lava and interpillow sediment	Veins up to 1.5 mm composed of smectite and carbonate	
393-U1558D-15R-3 48-60 cm	247.41	Fractured pillow lava, pillow breccia, and hyaloclastite breccia. Sparsely plagioclase-olivine-phyric pillow basalt with locally intense oxidation	Veins up to 1 mm composed of smectite and carbonate	
393-U1558D-16R-1 58-73 cm	254.38	Sparsely plagioclase-olivine-phyric, cryptocrystalline basalt pillow lava with glassy margin	Veins up to 1 mm composed of smectite and carbonate	

**Figure F114.** Samples collected for shore-based microbiology research, Hole U1558D. (Continued on next page.)

## 12.2.1. Microbiological sample processing and experiments

### 12.2.1.1. Cell and viral counts

A total of 22 samples were processed for cell counts. Performing shipboard enumeration from rock samples is difficult and time consuming; therefore, shipboard cell counts were not attempted during the SAT expeditions. Samples were broken into small chips and/or powder and preserved for postexpedition analyses (1 cm<sup>3</sup> in 4 mL of 4% paraformaldehyde in 100 mM PBS). Duplicate cell count samples were prepared for all samples so that the measurements can be performed independently in two different laboratories. When samples were taken for viral metagenomics, a third replicate was added to allow for viral counts.

### 12.2.1.2. Microbial community structure

A total of 21 samples were processed for shore-based DNA (PCR amplicon based and metagenomes) and/or RNA (PCR amplicon based and/or metatranscriptomes) analysis, 22 samples were preserved for single-cell genomics, and 21 samples were collected for lipid analysis (Table T40). Material for DNA, RNA, and lipid-based analyses of microbial community composition, which will be performed as part of the postexpedition research, was collected and preserved following


Sample	Top depth (mbsf)	Lithology	Veins	Folio turntable photo
393-U1558D-18R-2 0-16 cm	264.77	Sparsely plagioclase-olivine-phyric, microcrystalline basalt pillow lava with cryptocrystalline to glassy margin	Veins up to 1 mm composed of smectite and carbonate	
393-U1558D-21R-2 44-57 cm	280.04	Sparsely plagioclase-olivine-phyric, microcrystalline basalt pillow lava with cryptocrystalline to glassy margin	Veins up to 1 mm composed of smectite and carbonate	
393-U1558D-22R-1 32-47 cm	283.22	Sparsely plagioclase-olivine-phyric, microcrystalline basalt pillow lava with cryptocrystalline to glassy margin	Veins up to 1 mm composed of smectite and carbonate	
393-U1558D-25R-1 21-36 cm	297.71	Moderately plagioclase-olivine-phyric, microcrystalline basalt	Veins up to 1 mm composed of smectite and carbonate	
393-U1558D-31R-2 83-96 cm	328.82	Sparsely plagioclase-olivine-phyric, fine-grained basalt	Veins up to 1 mm composed of smectite and carbonate	
393-U1558D-33R-1 78-96 cm	337.08	Moderately olivine-plagioclase-phyric, cryptocrystalline basalt	Veins up to 0.2 mm composed of smectite and zeolite	
393-U1558D-35R-2 0-14 cm	346.68	Moderately olivine-plagioclase-phyric, strongly variolitic basalt	Veins up to 1 mm composed of smectite and carbonate	
393-U1558D-36R-3 45-61 cm	353.75	Moderately plagioclase-olivine-phyric, slightly variolitic basalt	Veins up to 1 mm composed of smectite, carbonate, and zeolite	
393-U1558D-37R-1 75-92 cm	356.45	Moderately plagioclase-olivine-phyric basalt	Veins up to 1 mm composed of smectite and carbonate	
393-U1558D-39R-1 106-120 cm	366.46	Moderately plagioclase-olivine-phyric, variolitic basalt	Veins up to 1 mm composed of smectite	

Figure F114 (continued).

Table T40. Microbiology whole-round samples, Hole U1558D. [Download table in CSV format.](#)

the procedures described in **Microbiology** in the Expedition 390/393 methods chapter (Coggon et al., 2024b).

### 12.2.1.3. Microbial incubation experiments

To determine the extent of viral activity in basement, incubation experiments were performed (see **Microbiology** in the Expedition 390/393 methods chapter [Coggon et al., 2024b]). The sample from Section 393-U1558D-5R-1 was used to initiate viral production and prophage induction experiments. Duplicates of approximately 4 g of pulverized rock (crushed with a sterile hammer inside a rock box) were resuspended in 40 mL of autoclaved deep seawater and sampled (duplicates of 1 mL) after 0, 3, 6, 12, 24, and 48 h and then 7 and 14 days. The deep seawater used was collected on 4 July 2022 at Site U1558 using a Niskin bottle attached to the subsea camera system frame. It was filtered through a 0.22  $\mu\text{m}$  polyether sulfone (PES) membrane and autoclaved. The pH was 7.6, the temperature at collection was 1.3°C, and the salinity was 35.

To better understand nitrogen cycling across the sediment/basement interface, basement samples from Sections 393-U1558D-2R-1 and 5R-1 were used in ammonium enrichment incubation experiments (see **Microbiology** in the Expedition 390/393 methods chapter [Coggon et al., 2024b]). A total of 9 g of rocks was crushed with a sterile Diamonite mortar and pestle and diluted in 50 mL vials with deep water collected from Site U1558 (collected on 28 June and 4 July 2022, ~4300 mbsl and filtered twice through 0.22  $\mu\text{m}$  pore size filter) to achieve a final volume of 40 mL. Samples will be incubated at 4°C for 6 months before shore-based analysis at Texas A&M University (USA).

### 12.2.2. Microbiological contamination monitoring

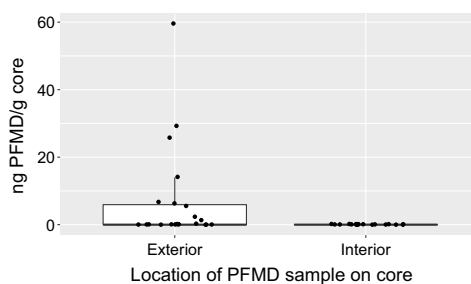
Circulating drilling fluid and mud are potential sources of contamination to cores collected for microbiological analyses (Sylvan et al., 2021). To determine the extent of contamination of the microbiology samples, the perfluorocarbon tracer perfluoromethyldecalin (PFMD) was injected into drilling fluid at a rate of 0.5 mL/min during circulation in Hole U1558D for the entirety of the hole. Samples from both the exterior and interior of whole rounds selected for microbiology analysis were collected to quantify the presence of PFMD. Ten exterior samples were additionally collected for PFMD analysis from rubble (core fragments <2 cm). Seven of the ten samples were taken in core intervals from which a microbiology sample was also collected, and three were taken from advances where no microbiology sample was taken (Tables **T40**, **T41**). These exterior rubble samples were chosen after the core was laid out in the splitting room, targeting rubble in the core catcher that was most likely in contact with drilling fluid and/or mud but not of high interest for further scientific analysis because of small size. For 12 of the whole-round cores where small rubble pieces were not available, a piece of the exterior of the rock was taken after the rock was rinsed and cleaned with ethanol, which may remove or dilute the PFMD but can also validate the cleaning process (Table **T41**).

An interior piece was also collected from the inside of every microbiology whole round for PFMD analysis to determine if any tracer infiltrated the interior of the cores. PFMD was detected on nearly half of the exterior samples (for the 23 tested samples, 4 samples were below detection level, 8 samples were 0 ng PFMD/g rock, and 11 samples were >0 ng PFMD/g rock) at an average concentration of 6.81 ng PFMD/g core and a median concentration of 0 ng PFMD/g rock (Figure **F115**; Table **T41**). The tracer was never detected in the interior microbiology samples, suggesting no or minimal contamination of the samples.

To characterize the microorganisms present in drilling fluid and also generate a database of potential contaminants, we collected one sample of drilling fluid from a drill pipe on the rig floor at the end of coring operations in Hole U1558D. Samples were collected for cell counts (1 mL of drilling fluid in 4 mL of 4% paraformaldehyde in 100 mM PBS), and 500 mL of drilling fluid was filtered onto one 0.22  $\mu\text{m}$  pore size 47 mm diameter filter and frozen at -80°C for shore-based molecular biology analysis.

**Table T41.** GC mass spectrometry measurements of PFMD tracer concentrations comparing concentrations on core exterior surfaces and whole-round interiors samples for microbiological analyses, Hole U1558D. [Download table in CSV format.](#)





**Figure F115.** PFMD tracer concentrations measured by gas chromatography comparing concentrations on core exterior surfaces with whole-round interiors for microbiological analyses, Hole U1558D.

## References

- Agnini, C., Fornaciari, E., Raffi, I., Catanzariti, R., Pälke, H., Backman, J., and Rio, D., 2014. Biozonation and biochronology of Paleogene calcareous nannofossils from low and middle latitudes. *Newsletters on Stratigraphy*, 47(2):131–181. <https://doi.org/10.1127/0078-0421/2014/0042>
- Alt, J.C., Honnorez, J., Laverne, C., and Emmermann, R., 1986. Hydrothermal alteration of a 1 km section through the upper oceanic crust, Deep Sea Drilling Project Hole 504B: mineralogy, chemistry and evolution of seawater-basalt interactions. *Journal of Geophysical Research: Solid Earth*, 91(B10):10309–10335. <https://doi.org/10.1029/JB091iB10p10309>
- Alt, J.C., and Teagle, D.A.H., 2003. Hydrothermal alteration of upper oceanic crust formed at a fast-spreading ridge: mineral, chemical, and isotopic evidence from ODP Site 801. *Chemical Geology*, 201(3):191–211. [https://doi.org/10.1016/S0009-2541\(03\)00201-8](https://doi.org/10.1016/S0009-2541(03)00201-8)
- Backman, J., Raffi, I., Rio, D., Fornaciari, E., and Pälke, H., 2012. Biozonation and biochronology of Miocene through Pleistocene calcareous nannofossils from low and middle latitudes. *Newsletters on Stratigraphy*, 45(3):221–244. <https://doi.org/10.1127/0078-0421/2012/0022>
- Baker, P.A., Gieskes, J.M., and Elderfield, H., 1982. Diagenesis of carbonates in deep-sea sediments; evidence from Sr/Ca ratios and interstitial dissolved Sr<sup>2+</sup> data. *Journal of Sedimentary Research*, 52(1):71–82. <https://doi.org/10.1306/212F7EE1-2B24-11D7-8648000102C1865D>
- Bennett, R.H., Fischer, K.M., Lavoie, D.L., Bryant, W.R., and Rezak, R., 1989. Porometry and fabric of marine clay and carbonate sediments: determinants of permeability. *Marine Geology*, 89(1–2):127–152. [https://doi.org/10.1016/0025-3227\(89\)90030-3](https://doi.org/10.1016/0025-3227(89)90030-3)
- Berggren, W.A., Aubry, M.P., and Hamilton, N., 1983. Neogene magnetobiostratigraphy of Deep Sea Drilling Project Site 516 (Rio Grande Rise, South Atlantic). In Barker, P.F., Carlson, R. L., Johnson, D. A., et al., *Initial Reports of the Deep Sea Drilling Project*. 72: Washington, DC (US Government Printing Office), 675–713. <https://doi.org/10.2973/dsdp.proc.72.130.1983>
- Bloemendal, J., King, J.W., Hall, F.R., and Doh, S.J., 1992. Rock magnetism of late Neogene and Pleistocene deep-sea sediments: relationship to sediment source, diagenetic processes, and sediment lithology. *Journal of Geophysical Research: Solid Earth*, 97(B4):4361–4375. <https://doi.org/10.1029/91JB03068>
- Bons, P.D., Elburg, M.A., and Gomez-Rivas, E., 2012. A review of the formation of tectonic veins and their microstructures. *Journal of Structural Geology*, 43:33–62. <https://doi.org/10.1016/j.jsg.2012.07.005>
- Bullard, E.C., 1939. Heat flow in South Africa. *Proceedings of the Royal Society of London, A: Mathematical and Physical Sciences*, 173(955):474–502. <https://doi.org/10.1098/rspa.1939.0159>
- Butler, R.F., 1992. *Paleomagnetism: Magnetic Domains and Geologic Terranes*: Oxford, England (Blackwell).
- Christeson, G., and Reece, R., 2020. Bathymetric site survey gridded data in support of IODP Expeditions 390 and 393, South Atlantic Transect (MGL1601, CREST). *Interdisciplinary Earth Data Alliance (IEDA)*. <https://doi.org/10.26022/IEDA/327528>
- Christeson, G.L., Goff, J.A., and Reece, R.S., 2019. Synthesis of oceanic crustal structure from two-dimensional seismic profiles. *Reviews of Geophysics*, 57(2):504–529. <https://doi.org/10.1029/2019RG000641>
- Christeson, G.L., Reece, R.S., Kardell, D.A., Estep, J.D., Fedotova, A., and Goff, J.A., 2020. South Atlantic transect: variations in oceanic crustal structure at 31°S. *Geochemistry, Geophysics, Geosystems*, 21(7):e2020GC009017. <https://doi.org/10.1029/2020GC009017>
- Coggon, R.M., Sylvan, J.B., Estes, E.R., Teagle, D.A.H., Reece, J., Williams, T.J., Christeson, G.L., Aizawa, M., Borrelli, C., Bridges, J.D., Carter, E.J., Dinarès-Turell, J., Estep, J.D., Gilhooly, W.P., III, Grant, L.J.C., Kaplan, M.R., Kempton, P.D., Lowery, C.M., McIntyre, A., Routledge, C.M., Slagle, A.L., Takada, M., Tamborrino, L., Wang, Y., Yang, K., Albers, E., Amadori, C., Belgrano, T.M., D'Angelo, T., Doi, N., Evans, A., Guérin, G.M., Harris, M., Hojnacki, V.M., Hong, G., Jin, X., Jonnalagadda, M., Kuwano, D., Labonte, J.M., Lam, A.R., Latas, M., Lu, W., Moal-Darrigade, P., Pekar, S.F., Robustelli Test, C., Ryan, J.G., Santiago Ramos, D., Shchepetkina, A., Villa, A., Wee, S.Y., Widlansky, S.J., Kurz, W., Prakasam, M., Tian, L., Yu, T., and Zhang, G., 2024a. Site U1556. In Coggon, R.M., Teagle, D.A.H., Sylvan, J.B., Reece, J., Estes, E.R., Williams, T.J., Christeson, G.L., and the Expedition 390/393 Scientists, *South Atlantic Transect. Proceedings of the International Ocean Discovery Program, 390/393: College Station, TX (International Ocean Discovery Program)*. <https://doi.org/10.14379/iodp.proc.390393.103.2024>

- Coggon, R.M., Teagle, D.A.H., Sylvan, J.B., Reece, J., Estes, E.R., Williams, T.J., Christeson, G.L., Aizawa, M., Albers, E., Amadori, C., Belgrano, T.M., Borrelli, C., Bridges, J.D., Carter, E.J., D'Angelo, T., Dinarès-Turell, J., Doi, N., Estep, J.D., Evans, A., Gilhooly, W.P., III, Grant, L.J.C., Guérin, G.M., Harris, M., Hojnacki, V.M., Hong, G., Jin, X., Jonnal-agadda, M., Kaplan, M.R., Kempton, P.D., Kuwano, D., Labonte, J.M., Lam, A.R., Latas, M., Lowery, C.M., Lu, W., McIntyre, A., Moal-Darrigade, P., Pekar, S.F., Robustelli Test, C., Routledge, C.M., Ryan, J.G., Santiago Ramos, D., Shchepetkina, A., Slagle, A.L., Takada, M., Tamborrino, L., Villa, A., Wang, Y., Wee, S.Y., Widlansky, S.J., Yang, K., Kurz, W., Prakasam, M., Tian, L., Yu, T., and Zhang, G., 2024b. Expedition 390/393 methods. In Coggon, R.M., Teagle, D.A.H., Sylvan, J.B., Reece, J., Estes, E.R., Williams, T.J., Christeson, G.L., and the Expedition 390/393 Scientists, South Atlantic Transect. Proceedings of the International Ocean Discovery Program, 390/393: College Station, TX (International Ocean Discovery Program). <https://doi.org/10.14379/iodp.proc.390393.102.2024>
- Coggon, R.M., Teagle, D.A.H., Sylvan, J.B., Reece, J., Estes, E.R., Williams, T.J., Christeson, G.L., Aizawa, M., Albers, E., Amadori, C., Belgrano, T.M., Borrelli, C., Bridges, J.D., Carter, E.J., D'Angelo, T., Dinarès-Turell, J., Doi, N., Estep, J.D., Evans, A., Gilhooly, W.P., III, Grant, L.J.C., Guérin, G.M., Harris, M., Hojnacki, V.M., Hong, G., Jin, X., Jonnal-agadda, M., Kaplan, M.R., Kempton, P.D., Kuwano, D., Labonte, J.M., Lam, A.R., Latas, M., Lowery, C.M., Lu, W., McIntyre, A., Moal-Darrigade, P., Pekar, S.F., Robustelli Test, C., Routledge, C.M., Ryan, J.G., Santiago Ramos, D., Shchepetkina, A., Slagle, A.L., Takada, M., Tamborrino, L., Villa, A., Wang, Y., Wee, S.Y., Widlansky, S.J., Yang, K., Kurz, W., Prakasam, M., Tian, L., Yu, T., and Zhang, G., 2024c. Expedition 390/393 summary. In Coggon, R.M., Teagle, D.A.H., Sylvan, J.B., Reece, J., Estes, E.R., Williams, T.J., Christeson, G.L., and the Expedition 390/393 Scientists, South Atlantic Transect. Proceedings of the International Ocean Discovery Program, 390/393: College Station, TX (International Ocean Discovery Program). <https://doi.org/10.14379/iodp.proc.390393.101.2024>
- Coggon, R.M., Teagle, D.A.H., Sylvan, J.B., Reece, J., Estes, E.R., Williams, T.J., Christeson, G.L., and the Expedition 390/393 Scientists, 2024d. Supplementary material, <https://doi.org/10.14379/iodp.proc.390393supp.2024>. In Coggon, R.M., Teagle, D.A.H., Sylvan, J.B., Reece, J., Estes, E.R., Williams, T.J., Christeson, G.L., and the Expedition 390/393 Scientists, South Atlantic Transect. Proceedings of the International Ocean Discovery Program, 390/393: College Station, TX (International Ocean Discovery Program).
- Dearing, J.A., Dann, R.J.L., Hay, K., Lees, J.A., Loveland, P.J., Maher, B.A., and O'Grady, K., 1996. Frequency-dependent susceptibility measurements of environmental materials. *Geophysical Journal International*, 124(1):228–240. <https://doi.org/10.1111/j.1365-246X.1996.tb06366.x>
- Donnelly, T.W., Thompson, G., and Salisbury, M.H., 1980. The chemistry of altered basalts at Site 417, Deep Sea Drilling Project Leg 51. In Donnelly, T., Francheteau, J., Bryan, W., Robinson, P., Flower, M., Salisbury, M., et al., Initial Reports of the Deep Sea Drilling Project. 51/52/53: Washington, DC (US Government Printing Office), 1319–1330. <https://doi.org/10.2973/dsdp.proc.515253.154.1980>
- Dunlea, A.G., Murray, R.W., Harris, R.N., Vasiliev, M.A., Evans, H., Spivack, A.J., and D'Hondt, S., 2013. Assessment and use of NGR instrumentation on the JOIDES Resolution to quantify U, Th, and K concentrations in marine sediment. *Scientific Drilling*, 15:57–63. <https://doi.org/10.2204/iodp.sd.15.05.2013>
- Estep, J., Reece, R., Kardell, D.A., Christeson, G.L., and Carlson, R.L., 2019. Seismic Layer 2A: evolution and thickness from 0- to 70-Ma crust in the slow-intermediate spreading South Atlantic. *Journal of Geophysical Research: Solid Earth*, 124(8):7633–7651. <https://doi.org/10.1029/2019JB017302>
- Estes, E.R., Williams, T., Midgley, S., Coggon, R.M., Sylvan, J.B., Christeson, G.L., Teagle, D.A.H., and the Expedition 390C Scientists, 2021. Expedition 390C Preliminary Report: South Atlantic Transect Reentry Systems. International Ocean Discovery Program. <https://doi.org/10.14379/iodp.pr.390C.2021>
- Fuchs, S., Norden, B., and the International Heat Flow Commission, 2021. The Global Heat Flow Database. GFZ Data Services. <https://doi.org/10.5880/figeo.2021.014>
- Gale, A., Dalton, C.A., Langmuir, C.H., Su, Y., and Schilling, J.-G., 2013. The mean composition of ocean ridge basalts. *Geochemistry, Geophysics, Geosystems*, 14(3):489–518. <https://doi.org/10.1029/2012GC004334>
- Gieskes, J.M., 1975. Chemistry of interstitial waters of marine sediments. *Annual Review of Earth and Planetary Sciences*, 3(1):433–453. <https://doi.org/10.1146/annurev.ea.03.050175.002245>
- Gradstein, F.M., Ogg, J.G., Schmitz, M.D., and Ogg, G.M. (Eds.), 2020. *The Geologic Time Scale 2020*: Amsterdam (Elsevier BV). <https://doi.org/10.1016/C2020-1-02369-3>
- Grove, T.L., Kinzler, R.J., and Bryan, W.B., 1992. Fractionation of mid-ocean ridge basalt (MORB). In Morgan, J.P., Blackman, D.K., and Sinton, J.M. (Eds.), *Mantle Flow and Melt Generation at Mid-Ocean Ridges*. *Geophysical Monograph*, 71: 281–310. <https://doi.org/10.1029/GM071p0281>
- Hamilton, E.L., 1976. Variations of density and porosity with depth in deep-sea sediments. *Journal of Sedimentary Research*, 46(2):280–300. <https://doi.org/10.1306/212F6F3C-2B24-11D7-8648000102C1865D>
- Harris, M., Coggon, R.M., Smith-Duque, C.E., Cooper, M.J., Milton, J.A., and Teagle, D.A.H., 2015. Channelling of hydrothermal fluids during the accretion and evolution of the upper oceanic crust: Sr isotope evidence from ODP Hole 1256D. *Earth and Planetary Science Letters*, 416:56–66. <https://doi.org/10.1016/j.epsl.2015.01.042>
- Hart, S.R., Erlank, A.J., and Kable, E.J.D., 1974. Sea floor basalt alteration: some chemical and Sr isotopic effects. *Contributions to Mineralogy and Petrology*, 44(3):219–230. <https://doi.org/10.1007/BF00413167>
- Hein, J.R., O'Neil, J.R., and Jones, M.G., 1979. Origin of authigenic carbonates in sediment from the deep Bering Sea. *Sedimentology*, 26(5):681–705. <https://doi.org/10.1111/j.1365-3091.1979.tb00937.x>
- Higgins, J.A., and Schrag, D.P., 2012. Records of Neogene seawater chemistry and diagenesis in deep-sea carbonate sediments and pore fluids. *Earth and Planetary Science Letters*, 357–358:386–396. <https://doi.org/10.1016/j.epsl.2012.08.030>
- Honnorez, J., 1981. The aging of the oceanic crust at low temperature. In Emiliani, C., *The oceanic lithosphere. The Sea: Ideas and Observations on Progress in the Study of the Seas*, 7: 525–588.
- Jelinek, V., 1981. Characterization of the magnetic fabric of rocks. *Tectonophysics*, 79(3–4):T63–T67. [https://doi.org/10.1016/0040-1951\(81\)90110-4](https://doi.org/10.1016/0040-1951(81)90110-4)

- Kardell, D.A., Christeson, G.L., Estep, J.D., Reece, R.S., and Carlson, R.L., 2019. Long-lasting evolution of Layer 2A in the western South Atlantic: evidence for low-temperature hydrothermal circulation in old oceanic crust. *Journal of Geophysical Research: Solid Earth*, 124(3):2252–2273. <https://doi.org/10.1029/2018JB016925>
- Kardell, D.A., Zhao, Z., Ramos, E.J., Estep, J., Christeson, G.L., Reece, R.S., and Hesse, M.A., 2021. Hydrothermal models constrained by fine-scale seismic velocities confirm hydrothermal cooling of 7–63 Ma South Atlantic crust. *Journal of Geophysical Research: Solid Earth*, 126(6):e2020JB021612. <https://doi.org/10.1029/2020JB021612>
- Kastner, M., 1999. Oceanic minerals: their origin, nature of their environment, and significance. *Proceedings of the National Academy of Sciences of the United States of America*, 96(7):3380–3387. <https://doi.org/10.1073/pnas.96.7.3380>
- Katz, M.E., Tjalsma, R.C., and Miller, K.G., 2003. Oligocene bathyal to abyssal benthic foraminifera of the Atlantic Ocean. *Micropaleontology*, 49(Suppl\_2):1–45. [https://doi.org/10.2113/49.Suppl\\_2.1](https://doi.org/10.2113/49.Suppl_2.1)
- Kelley, K.A., Kingsley, R., and Schilling, J.-G., 2013. Composition of plume-influenced mid-ocean ridge lavas and glasses from the Mid-Atlantic Ridge, East Pacific Rise, Galápagos spreading center, and Gulf of Aden. *Geochemistry, Geophysics, Geosystems*, 14(1):223–242. <https://doi.org/10.1002/ggge.20049>
- Kendrick, M.A., Hémond, C., Kamenetsky, V.S., Danyushevsky, L., Devey, C.W., Rodemann, T., Jackson, M.G., and Perfit, M.R., 2017. Seawater cycled throughout Earth's mantle in partially serpentinized lithosphere. *Nature Geoscience*, 10(3):222–228. <https://doi.org/10.1038/ngeo2902>
- King, D.J., Wade, B.S., Liska, R.D., and Miller, C.G., 2020. A review of the importance of the Caribbean region in Oligo-Miocene low latitude planktonic foraminiferal biostratigraphy and the implications for modern biogeochronological schemes. *Earth-Science Reviews*, 202:102968. <https://doi.org/10.1016/j.earscirev.2019.102968>
- Kirschvink, J.L., 1980. The least-squares line and plane and the analysis of palaeomagnetic data. *Geophysical Journal International*, 62(3):699–718. <https://doi.org/10.1111/j.1365-246X.1980.tb02601.x>
- Korenaga, T., and Korenaga, J., 2008. Subsidence of normal oceanic lithosphere, apparent thermal expansivity, and seafloor flattening. *Earth and Planetary Science Letters*, 268(1):41–51. <https://doi.org/10.1016/j.epsl.2007.12.022>
- Lam, A.R., Crundwell, M.P., Leckie, R.M., Albanese, J., and Uzel, J.P., 2022. Diachroneity rules the mid-latitudes: a test case using Late Neogene planktic foraminifera across the Western Pacific. *Geosciences*, 12(5):190. <https://doi.org/10.3390/geosciences12050190>
- Lam, A.R., and Leckie, R.M., 2020. Subtropical to temperate late Neogene to Quaternary planktic foraminiferal biostratigraphy across the Kuroshio Current Extension, Shatsky Rise, northwest Pacific Ocean. *PloS One*, 15(7):e0234351. <https://doi.org/10.1371/journal.pone.0234351>
- Le Bas, M.J., Le Maitre, R. W., Streckeisen, A., Zanettin, B., the IUGS Subcommittee on the Systematics of Igneous Rocks, 1986. A chemical classification of volcanic rocks based on the total alkali-silica diagram. *Journal of Petrology*, 27(3):745–750. <https://doi.org/10.1093/petrology/27.3.745>
- Le Roux, P.J., 2000. The geochemistry of selected mid-ocean ridge basalts from the Southern mid-Atlantic ridge (40°–55°S) [PhD dissertation]. University of Cape Town, Cape Town, South Africa. <http://hdl.handle.net/11427/4207>
- Marschall, H.R., Wanless, V.D., Shimizu, N., Pogge von Strandmann, P.A.E., Elliott, T., and Monteleone, B.D., 2017. The boron and lithium isotopic composition of mid-ocean ridge basalts and the mantle. *Geochimica et Cosmochimica Acta*, 207:102–138. <https://doi.org/10.1016/j.gca.2017.03.028>
- Martini, E., 1971. Standard Tertiary and Quaternary calcareous nannoplankton zonation. *Proceedings of the Second Planktonic Conference, Roma, 1970*:739–785.
- Marty, J.C., and Cazenave, A., 1989. Regional variations in subsidence rate of oceanic plates: a global analysis. *Earth and Planetary Science Letters*, 94(3):301–315. [https://doi.org/10.1016/0012-821X\(89\)90148-9](https://doi.org/10.1016/0012-821X(89)90148-9)
- Maxbauer, D.P., Feinberg, J.M., and Fox, D.L., 2016. MAX UnMix: a web application for unmixing magnetic coercivity distributions. *Computers & Geosciences*, 95:140–145. <https://doi.org/10.1016/j.cageo.2016.07.009>
- Michael, P.J., and Graham, D.W., 2015. The behavior and concentration of CO<sub>2</sub> in the suboceanic mantle: inferences from undegassed ocean ridge and ocean island basalts. *Lithos*, 236–237:338–351. <https://doi.org/10.1016/j.lithos.2015.08.020>
- Miller, M.D., Adkins, J.F., and Hodell, D.A., 2014. Rhizon sampler alteration of deep ocean sediment interstitial water samples, as indicated by chloride concentration and oxygen and hydrogen isotopes. *Geochemistry, Geophysics, Geosystems*, 15(6):2401–2413. <https://doi.org/10.1002/2014GC005308>
- Olson, P., Reynolds, E., Hinnov, L., and Goswami, A., 2016. Variation of ocean sediment thickness with crustal age. *Geochemistry, Geophysics, Geosystems*, 17(4):1349–1369. <https://doi.org/10.1002/2015GC006143>
- Parsons, B., and Sclater, J.G., 1977. An analysis of the variation of ocean floor bathymetry and heat flow with age. *Journal of Geophysical Research* (1896–1977), 82(5):803–827. <https://doi.org/10.1029/JB082i005p00803>
- Paulick, H., Münker, C., and Schuth, S., 2010. The influence of small-scale mantle heterogeneities on Mid-Ocean Ridge volcanism: evidence from the southern Mid-Atlantic Ridge (7°30'S to 11°30'S) and Ascension Island. *Earth and Planetary Science Letters*, 296(3–4):299–310. <https://doi.org/10.1016/j.epsl.2010.05.009>
- Pearce, J.A., and Cann, J.R., 1973. Tectonic setting of basic volcanic rocks determined using trace element analyses. *Earth and Planetary Science Letters*, 19(2):290–300. [https://doi.org/10.1016/0012-821X\(73\)90129-5](https://doi.org/10.1016/0012-821X(73)90129-5)
- Pearce, J.A., and Norry, M.J., 1979. Petrogenetic implications of Ti, Zr, Y, and Nb variations in volcanic rocks. *Contributions to Mineralogy and Petrology*, 69(1):33–47. <https://doi.org/10.1007/BF00375192>
- Pichler, T., Ridley, W.I., and Nelson, E., 1999. Low-temperature alteration of dredged volcanics from the Southern Chile Ridge: additional information about early stages of seafloor weathering. *Marine Geology*, 159(1–4):155–177. [https://doi.org/10.1016/S0025-3227\(99\)00008-0](https://doi.org/10.1016/S0025-3227(99)00008-0)
- Reece, R., Christeson, G., Amara, A., Estep, J., Greene, J., Koch, C., Henning, L., Worman, W., and Wright, A., 2016. CREST: Crustal Reflectivity Experiment southern transect South Atlantic multichannel seismic and ocean bottom

- seismometer experiment, 4 Jan–25 Feb 2016 Cruise Report. [http://www.iris.washington.edu/data/reports/2016/16-003/CREST\\_2016-01-04-2016-02-25\\_MGL1601\\_CruiseReport.pdf](http://www.iris.washington.edu/data/reports/2016/16-003/CREST_2016-01-04-2016-02-25_MGL1601_CruiseReport.pdf)
- Reece, R., and Estep, J., 2019. Processed MCS (PSTM) data from the Mid-Atlantic Ridge (MAR) to the Rio Grande Rise, South Atlantic Ocean, acquired by the R/V Marcus G. Langseth in 2016 (MGL1601) <https://doi.org/10.1594/IEDA/500255>
- Reekie, C.D.J., Jenner, F.E., Smythe, D.J., Hauri, E.H., Bullock, E.S., and Williams, H.M., 2019. Sulfide resorption during crustal ascent and degassing of oceanic plateau basalts. *Nature Communications*, 10(1):82. <https://doi.org/10.1038/s41467-018-08001-3>
- Ríos, A.F., Resplandy, L., García-Ibáñez, M.I., Fajar, N.M., Velo, A., Padin, X.A., Wanninkhof, R., Steinfeldt, R., Rosón, G., and Pérez, F.F., 2015. Decadal acidification in the water masses of the Atlantic Ocean. *Proceedings of the National Academy of Sciences*, 112(32):9950–9955. <https://doi.org/10.1073/pnas.1504613112>
- Sarmiento, J.L., Simeon, J., Gnanadesikan, A., Gruber, N., Key, R.M., and Schlitzer, R., 2007. Deep ocean biogeochemistry of silicic acid and nitrate. *Global Biogeochemical Cycles*, 21(1). <https://doi.org/10.1029/2006GB002720>
- Schrag, D.P., Higgins, J.A., Macdonald, F.A., and Johnston, D.T., 2013. Authigenic carbonate and the history of the global carbon cycle. *Science*, 339(6119):540–543. <https://doi.org/10.1126/science.1229578>
- Sclater, J.G., Jaupart, C., and Galson, D., 1980. The heat flow through oceanic and continental crust and the heat loss of the Earth. *Reviews of Geophysics*, 18(1):269–311. <https://doi.org/10.1029/RG018i001p00269>
- Shervais, J.W., 1982. Ti-V plots and the petrogenesis of modern and ophiolitic lavas. *Earth and Planetary Science Letters*, 59(1):101–118. [https://doi.org/10.1016/0012-821X\(82\)90120-0](https://doi.org/10.1016/0012-821X(82)90120-0)
- Shipboard Scientific Party, 1993. Site 896. In Alt, J.C., Kinoshita, H., Stokking, L.B., et al., *Proceedings of the Ocean Drilling Program, Initial Reports*, 148. College Station, TX (Ocean Drilling Program), 123–192. <https://doi.org/10.2973/odp.proc.ir.148.103.1993>
- Spinelli, G.A., Giambalvo, E.R., and Fisher, A.T., 2004. Sediment permeability, distribution, and influence on fluxes in oceanic basement. In Davis, E.E., and Elderfield, H. (Eds.), *Hydrogeology of the Oceanic Lithosphere*. Cambridge, UK (Cambridge University Press), 151–188.
- Straume, E.O., Gaina, C., Medvedev, S., Hochmuth, K., Gohl, K., Whittaker, J.M., Abdul Fattah, R., Doornenbal, J.C., and Hopper, J.R., 2019. GlobSed: updated total sediment thickness in the world's oceans. *Geochemistry, Geophysics, Geosystems*, 20(4):1756–1772. <https://doi.org/10.1029/2018GC008115>
- Sylvan, J.B., Estes, E.R., Bogus, K., Colwell, F.S., Orcutt, B.N., and Smith, D.C., 2021. Technical Note 4: Recommendations for microbiological sampling and contamination tracer use aboard the JOIDES Resolution following 20 years of IODP deep biosphere research. *International Ocean Discovery Program*. <https://doi.org/10.14379/iodp.tn.4.2021>
- Tarling, D.H., and Hrouda, F., 1993. *The Magnetic Anisotropy of Rocks*: London (Chapman and Hall).
- Teagle, D.A.H., Alt, J.C., Bach, W., Halliday, A.N., and Erzinger, J., 1996. Alteration of upper ocean crust in a ridge-flank hydrothermal upflow zone; mineral, chemical, and isotopic constraints from Hole 896A. In Alt, J.C., Kinoshita, H., Stokking, L.B., and Michael, P.J. (Eds.), *Proceedings of the Ocean Drilling Program, Scientific Results*. 148: College Station, TX (Ocean Drilling Program). <http://doi.org/10.2973/odp.proc.sr.148.113.1996>
- Teagle, D.A.H., Alt, J.C., and Halliday, A.N., 1998. Tracing the evolution of hydrothermal fluids in the upper oceanic crust: Sr-isotopic constraints from DSDP/ODP Holes 504B and 896A. In Mills, R.A., and Harrison, K. (Eds.), *Modern Ocean Floor Processes and the Geological Record*. Special Publication - Geological Society of London, 148: 81–97. <https://doi.org/10.1144/GSL.SP.1998.148.01.06>
- Turchyn, A.V., Bradbury, H.J., Walker, K., and Sun, X., 2021. Controls on the precipitation of carbonate minerals within marine sediments. *Frontiers in Earth Science*, 9:618311. <https://doi.org/10.3389/feart.2021.618311>
- van der Zwan, F.M., Devey, C.W., Hansteen, T.H., Almeev, R.R., Augustin, N., Frische, M., Haase, K.M., Basaham, A., and Snow, J.E., 2017. Lower crustal hydrothermal circulation at slow-spreading ridges: evidence from chlorine in Arctic and South Atlantic basalt glasses and melt inclusions. *Contributions to Mineralogy and Petrology*, 172(11):97. <https://doi.org/10.1007/s00410-017-1418-1>
- Von Damm, K.L., and Bischoff, J.L., 1987. Chemistry of hydrothermal solutions from the southern Juan de Fuca Ridge. *Journal of Geophysical Research: Solid Earth*, 92(B11):11334–11346. <https://doi.org/10.1029/JB092iB11p11334>
- Wade, B.S., Pearson, P.N., Berggren, W.A., and Pälike, H., 2011. Review and revision of Cenozoic tropical planktonic foraminiferal biostratigraphy and calibration to the geomagnetic polarity and astronomical time scale. *Earth-Science Reviews*, 104(1–3):111–142. <https://doi.org/10.1016/j.earscirev.2010.09.003>
- Yang, S., Humayun, M., and Salters, V.J.M., 2018. Elemental systematics in MORB glasses from the Mid-Atlantic Ridge. *Geochemistry, Geophysics, Geosystems*, 19(11):4236–4259. <https://doi.org/10.1029/2018GC007593>
- Yoder, H.S., Jr., and Tilley, C.E., 1962. Origin of basalt magmas: an experimental study of natural and synthetic rock systems. *Journal of Petrology*, 3(3):342–532. <https://doi.org/10.1093/petrology/3.3.342>
- Zijderveld, J.D.A., 1967. AC demagnetization of rocks: analysis of results. In Runcorn, S.K.C., Creer, K.M., and Collinson, D.W. (Eds.), *Methods in Palaeomagnetism*. *Developments in Solid Earth Geophysics*, 3: 254–286. <https://doi.org/10.1016/B978-1-4832-2894-5.50049-5>